UNIVERSITY OF NAPLES FEDERICO II

Polytechnic and Basic Sciences School

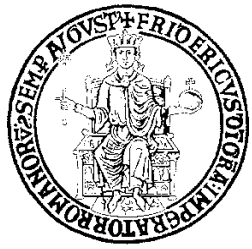

PHD THESIS IN CHEMICAL SCIENCES

XXXVIII CYCLE

Interaction between vanadium-based compounds and proteins

Tutor: Prof. Antonello Merlino Author: Maddalena Paolillo

Coordinator: Prof. Alessandra Napolitano

INDEX

FIGURES

CHAPTER 1

CHAPTER 2

APPENDIX A

CHAPTER 3

CHAPTER 4

CHAPTER 5

CHAPTER 6

TABLES

CHAPTER 2

CHAPTER 3

CHAPTER 4

CHAPTER 5

APPENDIX B

ABBREVIATIONS LIST

$[V^{IV}(Cp)_2(Cl)_2]$ or VDC bis(cyclopentadienyl)vanadium(IV) dichloride or vanadocene dichloride

$[V^{IV}O(acac)_2]$ bis(acetylacetonato)oxidovanadium(IV)

8-HQ 8-hydroxyquinolinato

apo-hTF metal-free human serum transferrin

BBOV bis((5-hydroxy-4-oxo-4H-pyran-2-yl)-methylbenzoato)oxidovanadium(IV)

BEOV or $[V^{IV}O(Etmalt)_2]$ bis(ethylmaltolato)oxidovanadium(IV)

Bipy bipyridine

BMOV or $[V^{IV}O(malt)_2]$ bis(maltolato)oxidovanadium(IV)

CCDC Cambridge Crystallographic Data Centre

CD circular dichroism

CRC colorectal cancer

$Cs_2[V^V_2O_4(lact)_2]\cdot 2H_2O$ dicaesium bis((μ_2-lactato)-dioxidovanadium(V)) dihydrate

$Cs_2[V^V_2O_4(mal)_2]\cdot 2H_2O$ dicaesium bis((μ_2-malato)-dioxidovanadium(V)) dihydrate

DFT density functional theory

Dipic dipicolinic acid or pyridine-2,6-dicarboxylic acid

DMSO dimethyl sulfoxide

e.d. electron density

EG ethylene glycol

EPR electron paramagnetic resonance

ESI-MS electrospray ionization mass spectrometry

FA formic acid

FBA fructose-1,6-bisphosphate aldolase

Fe_C-hTF monoferric form of human serum transferrin with the iron bound to the C-lobe only

H-bonds hydrogen bonds

Hdhp 1,2-dimethyl-3-hydroxy-4(1H)-pyridinone

Hempp 1-methyl-2-ethyl-3-hydroxy-4(1H)-pyridinone

HEPES 4-hydroxyethylpiperazine ethane sulfonic acid

HEWL hen egg white lysozyme

Hmpp 2-methyl-3-hydroxy-4(1H)-pyridinone

holo-hTF or Fe_NFe_C-hTF diferric human serum transferrin

HSA human serum albumin

hTF human serum transferrin

IC_{50} half maximal inhibitory concentration

IPOV isopolyvanadate

IR insulin receptor

Lact lactate

LMCT ligand-to-metal charge transfer

Mal malate

MBS multi-metal binding site

MeIm 1-methylimidazole

MIC minimum inhibitory concentration

NMR nuclear magnetic resonance

NTS N-terminal region

PAGE polyacrylamide gel electrophoresis

PBS Phosphate-Buffered Saline

PDB Protein Data Bank

PEG Polyethylene glycol

Phen phenatroline

PIPES 1,4-Piperazinediethanesulfonic acid

POV polyoxidovanadate

PTPase protein-tyrosine phosphatase

RMSD root mean square deviation

RNase A ribonuclease A

ROS reactive oxygen species

TFR transferrin receptor

TrpM tryptophan metabolites

UV-Vis UV-visible absorption spectroscopy

VC vanadium compound

VC1 dioxidovanadium(V) complex with furan-2-carboxylic acid (3-ethoxy-2-hydroxybenzylidene)hydrazide

VC2 dioxidovanadium(V) complex with (E)-N′-(1-(2-hydroxy-5-methoxyphenyl)ethylidene)furan-2-carbohydrazide

VC3 dioxidovanadium(V) complex with thiophene-2-carboxylic acid (3-ethoxy-2-hydroxybenzylidene)hydrazide

vdW van der Waals

Xant xanthurenic acid or 4,8-dihydroxyquinoline-2-carboxylic acid

XRD X-ray diffraction

CHAPTER 1

Introduction

1.1 Vanadium compounds in medicine

Vanadium compounds (VCs) have attracted growing interest in coordination chemistry due to their biological and catalytic properties.[1–8] Over the past decades, several studies have explored their potential therapeutic applications, including the treatment of diabetes, cancer, and various infectious, cardiovascular, and neurodegenerative diseases.[9–17] In particular, VCs have demonstrated anti-thrombotic, anti-hypertensive, anti-oxidant, and anti-atherosclerotic effects.[9–17] Furthermore, they exert anti-diabetic activity.[4,9,18–23] VCs modulate key metabolic enzymes, especially kinases and phosphatases, suggesting they could restore altered insulin signalling pathways. Several VCs have shown the ability to normalize glucose and lipid profiles in diabetic animal models, while clinical trials in humans have reported modest improvements in insulin sensitivity.[24–26] Although generally well-tolerated, some formulations have been associated with oxidative stress, even when administered as nutraceuticals.[24–26]

The insulin-like activity of V is mainly attributed to vanadate, which mimics phosphate in several enzymatic processes.[27–30] It can stimulate glucose uptake, enhance glycolysis, promote lipid synthesis, and suppress lipolysis. Vanadate also influences potassium transport, intracellular pH, and glycogen synthesis, particularly in liver, muscle, and adipose tissue. These effects are linked to its ability to substitute phosphate in the active sites of enzymes such as phosphatases, kinases, ATPases, and ribonucleases.[6,31]

The ability of vanadate to inhibit protein-tyrosine phosphatase (PTPase), an important enzyme that deactivates the insulin receptor by dephosphorylating its intracellular tyrosine residues, is particularly relevant in the context of diabetes treatment.[11] Vanadate prevents receptor dephosphorylation by binding the cysteinate residue in the active site of the enzyme, thereby sustaining its activation and promoting glucose transport into the cell, even in the absence of insulin.[11] A

simplified mechanism of this process, involving the allixin complex, is shown in Figure 1.1.

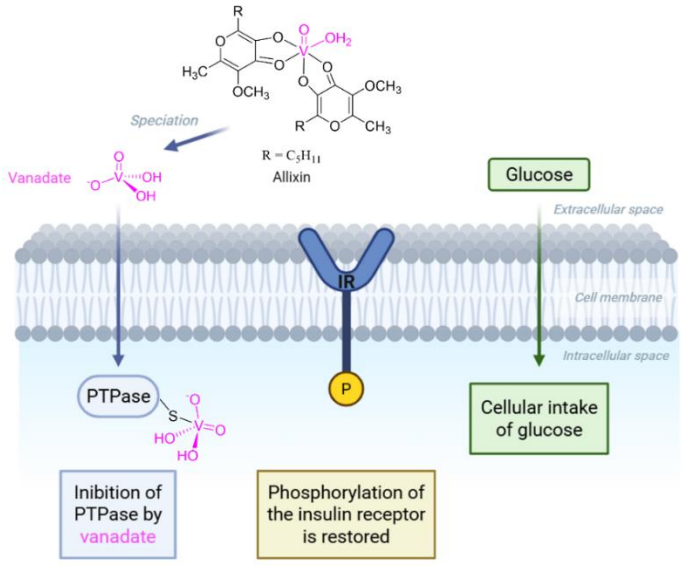

Figure 1.1 – Simplified mechanism of vanadate insulin-mimetic activity: the allixin complex partially converts to dihydrogenvanadate(V), which mimics phosphate, enters cells, inhibits PTPase, and restores insulin receptor phosphorylation, promoting glucose uptake.[11] Created with BioRender.com.

1.1.1 $V^{IV}O$ complexes with bidentate ligands

VCs can be broadly classified based on the oxidation state of the metal centre and on the nature of the organic ligands that coordinate the metal.

Oxidovanadium(IV) species of the type $[V^{IV}OL_2]$, where L is a bidentate monoanionic ligand, are the most studied VCs.[19,20,32–35]

Bis(maltolato)oxidovanadium(IV) (BMOV or $[V^{IV}O(malt)_2]$, Figure 1.2a) and bis(ethylmaltolato)oxidovanadium(IV) (BEOV or $[V^{IV}O(Etmalt)_2]$, Figure 1.2b) are widely recognized as reference compounds due to their well-established anti-diabetic properties. Studies from the 1990s showed that both BMOV and

BEOV are able to normalize glucose and lipid levels in diabetic animal models, with 2–3 times higher efficacy than $V^{IV}OSO_4$, and better tolerance compared to simple inorganic salts.[19] Their pharmacological activity was mainly attributed to efficient gastrointestinal absorption, facilitated by the neutral charge and optimal hydro/lipophilic balance, which allows passive diffusion through biological membranes.[23,36]

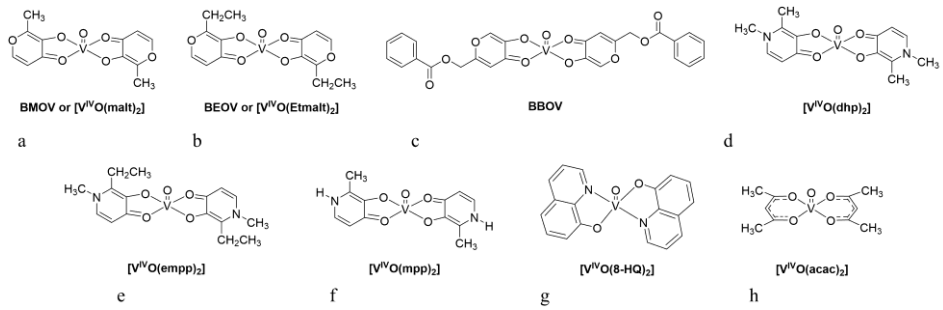

Figure 1.2 – Chemical structures of oxidovanadium(IV) species with bidentate ligands: a) BMOV or $[V^{IV}O(malt)_2]$, b) BEOV or $[V^{IV}O(Etmalt)_2]$, c) BBOV, d) $[V^{IV}O(dhp)_2]$, e) $[V^{IV}O(empp)_2]$, f) $[V^{IV}O(mpp)_2]$, g) $[V^{IV}O(8\text{-}HQ)_2]$, h) $[V^{IV}O(acac)_2]$.

BEOV (code AKP020) reached Phase I and II clinical trials.[19,20] Further development has been hampered by nephrotoxicity observed in some patients, financial difficulties faced by the sponsoring company (Akesis Pharmaceuticals), and patent expiration.[37,38]

In contrast, BMOV is still under investigation by CFM Pharma (code CFM10, commercial name Vanadis), entering Phase II trials for the treatment of myocardial infarction and secondary tissue damage due to trauma, such as burns.[32,39]

Research into $V^{IV}O$–pyrone complexes led to a "second generation" of derivatives. Species like BBOV (bis((5-hydroxy-4-oxo-4H-pyran-2-yl)-methylbenzoato)oxidovanadium(IV), Figure 1.2c) has attracted interest due to its significantly

lower oral toxicity, approximately half that of BMOV, and effective activity at doses 1000 times lower than BMOV.[40]

Another promising class of $V^{IV}O^{2+}$ complexes includes that formed with pyridinone ligands. Deferiprone (Hdhp, 1,2-dimethyl-3-hydroxy-4(1H)-pyridinone), a well-known iron chelator used in the treatment of thalassemia major,[41] has been investigated as the ligand in $[V^{IV}O(dhp)_2]$ (Figure 1.2d), a complex with antidiabetic activity.[42,43] $[V^{IV}O(empp)_2]$ (where Hempp is 1-methyl-2-ethyl-3-hydroxy-4(1H)-pyridinone, Figure 1.2e) and $[V^{IV}O(mpp)_2]$ (where Hmpp is 2-methyl-3-hydroxy-4(1H)-pyridinone, Figure 1.2f) have similarly high bioactivity.[44] In particular, $[V^{IV}O(empp)_2]$ strongly inhibits free fatty acid release with half maximal inhibitory concentration (IC_{50}) value significantly lower than $V^{IV}OSO_4$ and $[V^{IV}O(dhp)_2]$.[42] Some pyridinone-based complexes also show antiproliferative activity on malignant melanoma cell lines (A375 and CN-mel), inducing apoptosis and cell cycle arrest.[44]

Thanks to their dual anti-diabetic and anti-cancer properties, $V^{IV}O$−pyridinone complexes have been proposed as potential therapeutic agents for patients affected by both conditions.[45]

Other bioactive VCs have 8-hydroxyquinolinato (8-HQ) as a ligand. $[V^{IV}O(8\text{-}HQ)_2]$ (Figure 1.2g) and its derivatives possess anti-trypanosomal, anti-tubercular, and anti-cancer activities. These compounds have shown IC_{50} values below 1 μM and minimum inhibitory concentration (MIC) values in the low micromolar range.[46–50] $V^{IV}O$ complexes of 8-HQ hydrazones showed IC_{50} values below 6.3 μM in A375 melanoma cells, outperforming cisplatin (11.2 μM) on the same line.[51]

Bis(acetylacetonato)oxidovanadium(IV) or $[V^{IV}O(acac)_2]$ (Figure 1.2h) is probably the most studied VC.[52,53] It is more effective than $V^{IV}OSO_4$ in suppressing hepatic glycolysis in streptozotocin-induced diabetic rats.[52,54] $[V^{IV}O(acac)_2]$ enhances insulin receptor (IR) kinase activity more than other $V^{IV}O$ chelate

species.[55] It exhibits also notable anti-proliferative effects in human hepatoma HepG2 cells: it blocks the G1/S phase of the cell cycle progression via an activated extracellular signal-regulated kinase signal.[56] In human pancreatic cancer cell line AsPC-1 it induces cell cycle arrest at the G2/M phase and causes an increase of reactive oxygen species (ROS) levels.[57]

1.1.2 $V^{IV}O$ complexes with tridentate ligands

The coordination chemistry of V with multidentate ligands has gained increasing attention over the past decade due to its relevance in both catalysis[58,59] and medicinal applications.[58,60] Interest in these systems is further driven by their role as structural and functional models for vanadate-dependent haloperoxidases, vanadium nitrogenases, and other biologically active VCs.[61]

Among tridentate ligands, 8-HQ derivatives and related tryptophan metabolites (TrpM) such as kynurenine, xanthurenic, quinaldic, and 3- or 8-hydroxyquinolinic acids are of particular interest. Disruptions in tryptophan metabolism have been linked to colorectal cancer (CRC).[62] For instance, kynurenic and xanthurenic acids exhibit anti-oxidant properties in colon carcinoma cells.[63,64] Other metabolites, such as quinaldic acid and 8-hydroxyquinoline-2-carboxylic acid, demonstrate antiproliferative effects and can inhibit the growth of pathogenic colonic microflora.[65,66] These molecules display also anti-bacterial properties acting as non-competitive inhibitors of class II fructose-1,6-bisphosphate aldolase (FBA), an enzyme essential for Gram -positive and -negative bacteria survival.[67,68]

Based on these premises, the combination of 8-HQ derivatives biological activity with V pharmacological potential represents a promising strategy for the development of new V-based therapeutics.[69–73] An example of such a combination is the complex $[V^{IV}O(xant)(H_2O)_2]$, where xant is the xanthurenic acid (Figure 1.3a). Dipicolinic acid (dipic, or pyridine-2,6-dicarboxylic acid) is an ONO-donor ligand known for its amphiphilic character, low toxicity, and ability to stabilize

unusual oxidation states in metal complexes.[74,75] Dipic is naturally occurring and widely used in coordination chemistry to obtain water-soluble and biologically relevant compounds.[74] In this respect, oxidovanadium(IV) complexes of the type $[V^{IV}O(dipic)(H_2O)_2]$ (Figure 1.3b) or $[V^{IV}O(dipic)(N\cap N)]$ have been investigated for their anti-cancer properties.[76] The variation of the alkoxo chain length of $[V^{IV}O(OR)(dipic)(H_2O)]$ (R = Et, *n*-Pr, *n*-Bu) was found to modulate the compound cytotoxicity against MCF-7 breast cancer cells.[76,77] Moreover, the introduction of methyl or allyl substituents into imidazole ligands coordinated to $V^{IV}O$–dipic cores enhanced the anti-proliferative effects against Hep3B liver carcinoma cells.[74,76]

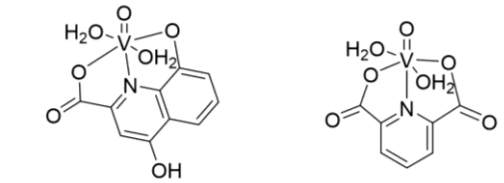

Figure 1.3 – Chemical structures of oxidovanadium(IV) species with tridentate ligands: a) $[V^{IV}O(xant)(H_2O)_2]$, b) $[V^{IV}O(dipic)(H_2O)_2]$.

1.1.3 Non-oxido V^{IV} complexes

Non-oxido V^{IV} complexes, also referred to as "bare" V species, are rare due to the high tendency of V to form terminal V=O bonds.[78–81] Their isolation requires strong ONS/SS/OS donor ligands able to compensate for the electron density normally provided by the oxo group.[78–80] Nevertheless these species offer unique reactivity patterns not observed in typical $V^{IV}O$, $V^{V}O$, or $V^{V}O_2$ systems, opening new opportunities for drug development.[4,82,83]

One of the earliest examples of a non-oxido VC with anti-cancer potential is the bis(cyclopentadienyl)vanadium(IV) dichloride or vanadocene dichloride ($[V^{IV}(Cp)_2(Cl)_2]$, VDC; Figure 1.4a), first reported in 1983 for its activity against Ehrlich ascites tumor.[84,85] A study on human testicular cancer cell lines (Tera-2 and Ntera-2) demonstrated that vanadocene derivatives are capable of inducing apoptosis within 24 hours.[84,86]

A potent derivative, the bis[(*p*-methoxybenzyl)cyclopentadienyl]vanadium(IV) dichloride (vanadocene Y; Figure 1.4b), exhibits an IC_{50} value of 3.0 μM against the LLC-PK (pig kidney epithelial) cell line, comparable to that of cisplatin under the same experimental conditions (IC_{50} = 3.3 μM).[23,87] More recently, a modified version of vanadocene Y, the diisoselenocyanate vanadocene Y (Figure 1.4c), has shown remarkable cytotoxicity against CAKI-1 human renal cancer cells, with nanomolar IC_{50} values.[84,88]

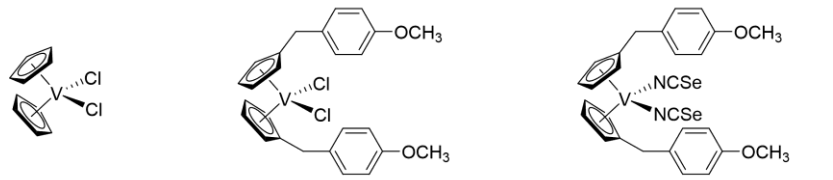

$[V^{IV}(Cp)_2(Cl)_2]$ or VDC **Vanadocene Y** **Diisoselenocyanate vanadocene Y**

a b c

Figure 1.4 – Chemical structures of non-oxido VCs: a) $[V^{IV}(Cp)_2(Cl)_2]$ or VDC, b) vanadocene Y, c) diisoselenocyanate vanadocene Y.

Additionally, the cytotoxic profiles of various methyl- and methoxy-substituted vanadocene derivatives have been evaluated against T-lymphocytic leukaemia MOLT-4 cells, further supporting the potential of vanadocene-based systems as anti-tumor agents.[84,89]

1.1.4 $V^{V}O_2$-hydrazonate complexes

In recent studies,[90–94] V^{V}-based species, including $V^{V}O$ and $V^{V}O_2$ complexes, have shown anti-cancer abilities primarily imputable to the interconversion between the +4 and +5 oxidation states, which promotes the generation of ROS.[32] Another important factor affecting their anti-tumour properties is the chemical nature of the ligands. Indeed, the choice of a specific ligand may influence the regulation of different metabolic pathways allowing, in this way, to investigate the binding of these VCs to biomolecules.[4,33,44,46,49,95–104] To this purpose, various oxidovanadium complexes with O- and N-donor ligands[10,11,13,32,95] have received great interest. Among them, aroylhydrazone-based ligands, which consist of a hydrazone moiety linked to a heterocyclic ring, have been widely used for the synthesis of bioactive VCs.[95,105] The structural features of the heterocycle have a notable impact on the selectivity and cytotoxicity of these compounds. Larger ring systems are generally associated with enhanced anti-cancer activity.[95,106,107] Within this class, the dioxidovanadium(V) complex with furan-2-carboxylic acid (3-ethoxy-2-hydroxybenzylidene)hydrazide (VC1, Figure 1.5a) exhibits cytotoxicity against various cancer cell lines, including HeLa.[95]

Structurally related analogues of VC1, such as those formed with (E)-N′-(1-(2-hydroxy-5-methoxyphenyl)ethylidene)furan-2-carbohydrazide (VC2, Figure 1.5b) and with thiophene-2-carboxylic acid (3-ethoxy-2-hydroxybenzylidene)hydrazide (VC3, Figure 1.5c) represent valuable systems for exploring the relationship between ligand structure and anti-cancer activity of VCs.

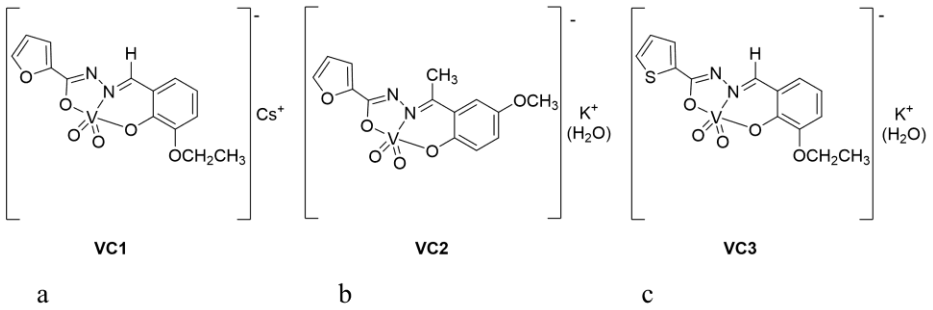

Figure 1.5 – Chemical structures of $V^{V}O_2$-hydrazonate complexes: a) VC1, b) VC2, c) VC3.

1.1.5 Dinuclear V^{V} complexes with *α*-hydroxycarboxylic acids

α-Hydroxycarboxylic acids are good ligands for new V-based drugs as they are involved in important metabolic pathways[108,109] such as the Krebs (citrate, isocitrate, malate), the Cori cycles (lactate) and the photorespiration (glycolate).[110,111] Given the biological relevance of both vanadates and *α*-hydroxycarboxylic acids, their mutual interactions have been intensively investigated.[110–115] Among these ligands, malic acid is a particularly intriguing candidate. In the pharmaceutical industry, it is used as a salt in the formulation for migraine medication almotriptan malate.[116] Due to its dicarboxylic nature, malic acid is also an excellent building block for the synthesis of homo- and heteropolymers.[116] The corresponding V^{V} complex, dicaesium bis((μ_2-malato)-dioxidovanadium(V)) dihydrate ($Cs_2[V^{V}_2O_4(mal)_2]\cdot 2H_2O$, Figure 1.6a), is a well-characterized dinuclear species.[117]

Lactic acid is another *α*-hydroxycarboxylic acid could be an ideal pharmaceutical candidate, owing to the fact that it is naturally occurring, hence not toxic in small scale, abundant, and cheap to produce.[118] VCs with lactic acid, like dicaesium bis((μ_2-lactato)-dioxidovanadium(V)) dihydrate ($Cs_2[V^{V}_2O_4(lact)_2]\cdot 2H_2O$, Figure 1.6b), are relevant in the broader context of V speciation in biological

fluids, particularly blood.[118] Understanding how V interacts with blood components is essential for predicting its behaviour under physiological conditions.

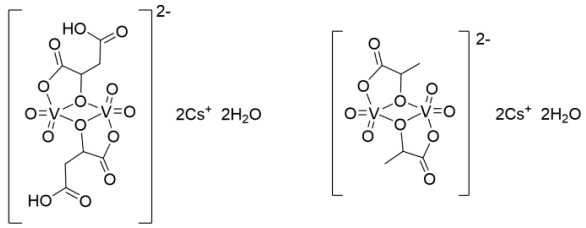

Figure 1.6 – Chemical structures of dinuclear V^V complexes with α-hydroxycarboxylic acids: a) $Cs_2[V^V_2O_4(mal)_2]\cdot 2H_2O$, b) $Cs_2[V^V_2O_4(lact)_2]\cdot 2H_2O$.

1.1.6 Polyoxovanadates

Polyoxidovanadates (POVs) are a class of vanadium compounds with a variety of interesting features. POVs can be employed in chemical engineering,[119] catalysis,[120] environmental chemistry,[121] material science,[122] biochemistry, biology, pharmacology, and medicine.[123,124,122,125–133] POVs can have a role as enzyme inhibitors[123,124,134–137] and in the treatment of diabetes mellitus, as insulin-enhancing agents,[123,138–140] and of Alzheimer disease as inhibitors of amyloid β-peptides aggregation.[123,141,142]

A wide variety of isopolyvanadates (IPOVs) has been characterized for their stability, like for example the species with tetrahedral coordination $[V^V_3O_9]^{3-}$ ($\{V_{3c}\}$, Figure 1.7c),[143,144] $[HV^V_4O_{12}]^{3-}$ ($\{V_{4c}\}$, Figure 1.7e)[144,145] and $[V^V_5O_{14}]^{3-}$ ($\{V_{5c}\}$, Figure 1.7g),[144,146] and those with octahedral V centres, $[V^V_{10}O_{28}]^{6-}$ ($\{V_{10}\}$, Figure 1.7h),[144,147] $[V^V_{12}O_{32}]^{4-}$,[144,148] $[V^V_{13}O_{34}]^{3-}$,[144,149] and $[V^V_{15}O_{42}]^{9-}$.[144,150]

The distribution and stability of these species are influenced by different physico-chemical parameters: pH, ionic strength, temperature, and vanadate concentration.[103,144,151]

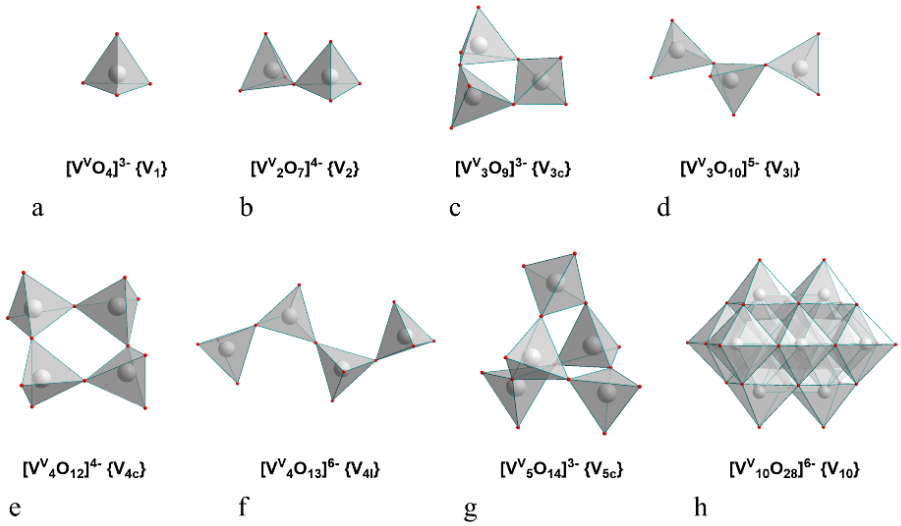

Figure 1.7 – Oxidovanadates and polyoxidovanadates structures: a) $[V^{V}O_4]^{3-}$ $\{V_1\}$, b) $[V^{V}_2O_7]^{4-}$ $\{V_2\}$, c) $[V^{V}_3O_9]^{3-}$ $\{V_{3c}\}$, d) $[V^{V}_3O_{10}]^{5-}$ $\{V_{3l}\}$, e) $[V^{V}_4O_{12}]^{4-}$ $\{V_{4c}\}$, f) $[V^{V}_4O_{13}]^{6-}$ $\{V_{4l}\}$, g) $[V^{V}_5O_{14}]^{3-}$ $\{V_{5c}\}$, h) decavanadate ($[V^{V}_{10}O_{28}]^{6-}$ $\{V_{10}\}$). In abbreviations the subscript "c" stands for "cyclic", "l" for "linear".

Figure 1.8 reports the different types of IPOVs in dependence of the pH. Polymers with one to five V atoms (Figure 1.7) are formed at pH > 6. Under acidic conditions, only a few species such as $\{V_{10}\}$ and the monomeric $[V^{V}O_2]^{+}$ are typically present (Figure 1.8).[144]

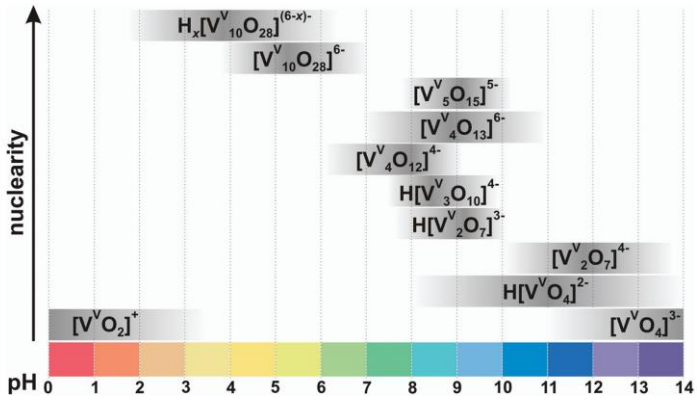

Figure 1.8 – Speciation of IPOVs in an aqueous solution with a total concentration of V more than 0.1 mM based on ref.[103,144,152–158] The darkest grey shading within each box indicates the highest relative concentration of the corresponding species within a given pH range. Boxes are arranged along the y-axis in order of increasing nuclearity. This arrangement does not imply that the species are dominating at a certain pH range. X in $H_x[V^V_{10}O_{28}]^{(6-x)}$ is 1–3 (N. I. Gumerova and A. Rompel, 2020).[144]

ESI-MS analyses of ammonium metavanadate $(NH_4)_3[V^VO_4]$ solutions at pH 4.5[144,159] and 6.0[144,160] revealed the presence of $\{V_{10}\}$, $[V^VO_4]^{3-}$ and novel POV ions, some of which are likely formed in the gas phase upon ionization.[144]

The structures of tri- and tetra- vanadate species in aqueous solution (Figure 1.7c-f) have been subject to long debate. Conflicting models proposed either cyclic or linear arrangements, with V in tetra- or penta-coordination.[144,161] It is now accepted that trivanadate $[V^V_3O_{10}]^{5-}$ ($\{V_{3l}\}$, Figure 1.7d) and tetravanadate $[V^V_4O_{13}]^{6-}$ ($\{V_{4l}\}$, Figure 1.7f) species can exist as linear forms in aqueous solution at pH < 10, as suggested by ^{51}V and ^{17}O NMR studies.[144,162] Linear species tend to polymerize during crystallization from aqueous solution, forming extended metavanadate chains $([V^VO_4]^{3-})_n$.[144]

The cyclic species such as $[V^V_3O_9]^{3-}$ (Figure 1.7c) and $[HV^V_4O_{12}]^{3-}$ (Figure 1.7e) have been isolated from non-aqueous solvents.[143–146]

{V_{10}} (Figure 1.7h) is stable for several days at neutral pH,[163] while under basic conditions, it gradually degrades into smaller oxidovanadates such as monomeric $[V^{V}O_4]^{3-}$ (Figure 1.7a), dimeric $[V^{V}_2O_7]^{4-}$ (Figure 1.7b), and tetrameric $[V^{V}_4O_{12}]^{4-}$ (Figure 1.7e), with a half-life time depending on concentration, ionic strength, and temperature.[144,164] At alkaline pH, {V_{10}} converts into colourless metavanadate species $H_x[V^{V}O_4]^{(3-x)}$ (x = 0–2). Near neutral pH, this transformation can take up to three weeks depending on experimental conditions.[144,165]

1.2 Protein metalation

Metal compounds can react with proteins forming different types of adducts. This process, known as protein metalation,[166–168] plays a crucial role in the transport, absorption, storage, toxicity, and mechanism of action of metal-based drugs.[166,169] Protein metalation is also essential for the design of protein-based metallodrug delivery systems[166,170–172] and artificial metalloenzymes.[166,173]

The extent and the nature of protein metalation are influenced by several factors, including the type of metal centres, physicochemical properties and concentrations of both protein and metal complex, pH, ionic strength, buffer composition, and presence of salts.[166] Being a very intricate process, research on protein metalation is of primary interest to identify the specific factors underlying their biological properties and side effects.[166,174–176]

1.2.1 Interaction between vanadium compounds and proteins

The interaction between VCs and proteins can be described in terms of binding site specificity and binding type, *i.e.* covalent and non-covalent.[177] Specific binding sites are regions of the protein with size, charge and hydro/lipophilic features that fit the metal moiety. The metal binding close to these sites can involve one or more than one residue, which can drive the formation the adducts via hydrogen bonds (H-bonds) and van der Waals interactions (vdW).[177]

In recent years, there has been much discussion in the literature concerning whether the moieties $[V^{IV}OL]/[V^{IV}OL_2]$ and $[V^{V}O_2L]/[V^{V}O_2L_2]$ can bind specific sites.[177,178] Binding depends on both the protein structure and the V ligands. Several binding modes are possible for $[V^{IV}OL]/[V^{IV}OL_2]$ and $[V^{V}O_2L]/[V^{V}O_2L_2]$ moieties, as summarized in Figure 1.9.

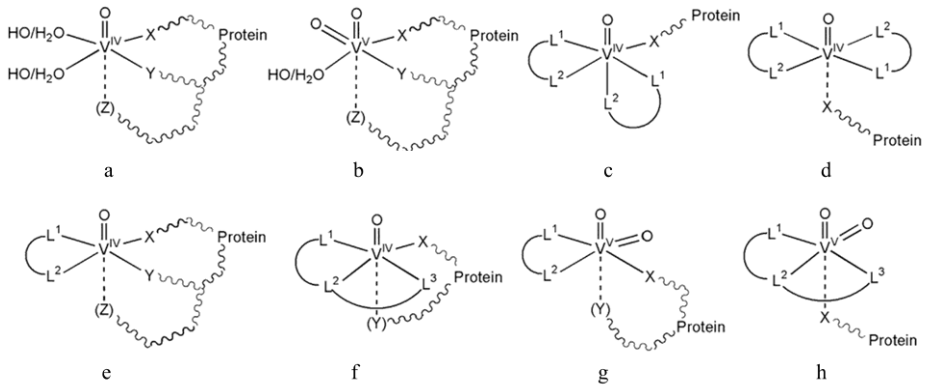

Figure 1.9 – General binding modes of a) $V^{IV}O^{2+}$, b) $V^{V}O_2^{+}$, c-f) $[V^{IV}OL_2]/[V^{IV}OL^{+}]$, and g-h) $[V^{V}O_2L]$. X, Y, and Z are the amino acid donors of the protein. The potential weak axial donor is represented between round parentheses.[177]

1.3 Protein metalation investigated by a combined approach: spectroscopic, spectrometric, and crystallographic studies

Determining the precise geometry of metal coordination and identifying the specific protein residues involved in binding is essential not only for understanding metal–protein recognition, but also for rational drug design. Indeed, the structural characterization of binding sites at atomic level supports structure-based approaches for developing new therapeutic agents. X-ray diffraction (XRD) from high-quality crystals is the most powerful and reliable technique for obtaining

detailed structural information on the interaction between metal-based drugs and proteins.[179]

XRD data provide crucial experimental evidence on the coordination geometry of the metal and the specific amino acid residues involved in metal recognition. However, in some cases, the electron density (e.d.) cannot allow for unambiguous assignment of the identity of the V-containing species bound to the protein.[180] In these cases, mass spectrometry, especially electrospray ionization mass spectrometry (ESI-MS), becomes a powerful complementary tool to characterize the metal–protein adducts and elucidate their composition in solution.[181,182]

The integration of X-ray crystallography with complementary biophysical techniques is essential to elucidate the molecular processes that occur before or upon the formation of V–protein adducts.[168] In particular, UV-Visible absorption spectroscopy (UV-Vis) and nuclear magnetic resonance (NMR) provide valuable insights into the behaviour of metal compounds in solution, in the absence and in the presence of proteins.[168] Circular dichroism (CD) and fluorescence spectroscopy allow to detect changes in the secondary and tertiary structure content, respectively, of proteins upon metal binding.[168]

1.4 Aim of the project

The aim of this PhD project was to characterize, from a structural point of view, the interaction between various VCs and proteins. The investigated VCs belonged to different vanadium oxidation states and chemical architectures, including $V^{IV}O$ complexes with bidentate ligands and tridentate ligands, $V^{V}O_2$-hydrazonate derivatives, and dinuclear V^{V} complexes with α-hydroxycarboxylic acids. These systems were chosen to obtain a comprehensive overview of how structural and electronic features could affect the interaction of VCs with proteins. Both model proteins (hen egg white lysozyme (HEWL) and ribonuclease A (RNase A))

and physiologically relevant proteins (human serum transferrin (hTF) and human serum albumin (HSA)) were used.

The model proteins were primarily selected for their well-established crystallization properties, enabling high-resolution structural studies, while hTF and HSA were studied for their potential role in the transport and distribution of VCs *in vivo*. A combined approach involving spectroscopic (UV-Vis, CD, fluorescence, ^{51}V NMR), spectrometric (ESI-MS), and crystallographic techniques was employed to investigate the binding behaviour of these VCs. While spectroscopic and spectrometric techniques provided insights into the stoichiometry and speciation of some adducts studied in this thesis, X-ray crystallography has been the primary technique used during the thesis.

CHAPTER 2

$V^{IV}O$ complexes containing bidentate ligands: the cases of $[V^{IV}O(empp)_2]$, $[V^{IV}O(dhp)_2]$, $[V^{IV}O(8\text{-}HQ)_2]$, and $[V^{IV}O(acac)_2]$

2.1 Introduction

$V^{IV}O^{2+}$ complexes exhibit promising pharmacological properties, particularly in the treatment of diabetes and cancer.

Among $V^{IV}O^{2+}$ complexes with anti-diabetic and anti-cancer properties, pyridinone-based species, such as $[V^{IV}O(empp)_2]$ (Figure 2.1a) and $[V^{IV}O(dhp)_2]$ (Figure 2.1b) have attracted considerable attention.[45] $V^{IV}O^{2+}$ complexes bearing 8-hydroxyquinolinato (8-HQ) as ligands, such as $[V^{IV}O(8\text{-}HQ)_2]$ (Figure 2.1c) and its derivatives, are relevant for their anti-trypanosomal, anti-tubercular, and anti-cancer activities,[46–50] $[V^{IV}O(acac)_2]$ (Figure 2.1d) shows strong insulin-mimetic properties and anti-proliferative effects in selected cancer cell lines.[52,53]

In this chapter, the interaction between $[V^{IV}O(empp)_2]$, $[V^{IV}O(dhp)_2]$, $[V^{IV}O(8\text{-}HQ)_2]$ and $[V^{IV}O(acac)_2]$ with the model protein HEWL and the interaction between $[V^{IV}O(acac)_2]$ and the physiologically relevant protein human transferrin is discussed.

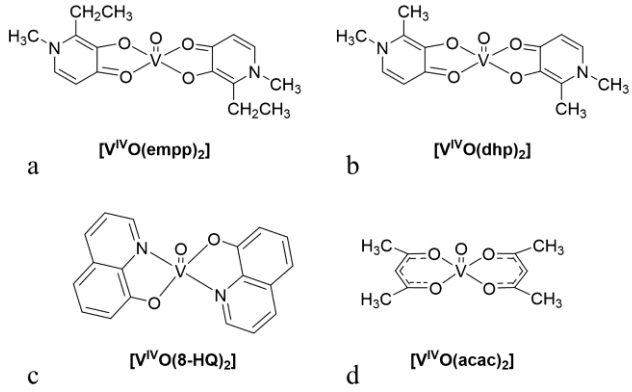

Figure 2.1 – Chemical structures of oxidovanadium(IV) species with bidentate ligands: a) $[V^{IV}O(empp)_2]$, b) $[V^{IV}O(dhp)_2]$, c) $[V^{IV}O(8\text{-}HQ)_2]$, d) $[V^{IV}O(acac)_2]$.

2.2 Interaction of $[V^{IV}O(empp)_2]$ with HEWL

The interaction between $[V^{IV}O(empp)_2]$ (Figure 2.1a) and HEWL was investigated using X-ray crystallography, supported by spectroscopic and spectrometric techniques (EPR and ESI-MS), which helped to characterize the species present in solution.

HEWL is frequently used as a model protein due to its small size, commercial availability with high purity grade, and suitability for structural and spectrometric studies.[33,166,183,184] Information gained using this model system has been useful to clarify the behaviour of several metallodrugs with physiologically relevant proteins such as serum albumin and transferrin.[166,167,184–186]

$[V^{IV}O(empp)_2]$ adopts a square pyramidal geometry in solid state,[187,188] whereas in aqueous solution it exists in equilibrium with *cis*-$[V^{IV}O(empp)_2(H_2O)]$, in which the oxido ligand and water molecule are in *cis* position.[188,189] Upon pH variation and V concentration reduction, different species like $[V^{IV}O(empp)_2]$, *cis*-$[V^{IV}O(empp)_2(H_2O)]$, and $[V^{IV}O(empp)(H_2O)_2]^+$ can interact with the protein.

This speciation strongly influences the way these complexes interact with HEWL, since different V-containing fragments can compete for protein binding sites, potentially resulting in distinct adducts and binding modes.

2.2.1 Crystallographic studies

To structurally characterize the interaction of $[V^{IV}O(empp)_2]$ with HEWL, a crystallographic study was carried out. Crystals of metal-free protein, grown under three different conditions, were exposed for 22-25 days to stabilizing solutions containing the mother liquors saturated with the VC. Then, these crystals were used to collect X-ray diffraction data (Table 2.1). The structure of three distinct V/HEWL adducts (structures A-C) were solved (Figure 2.2).

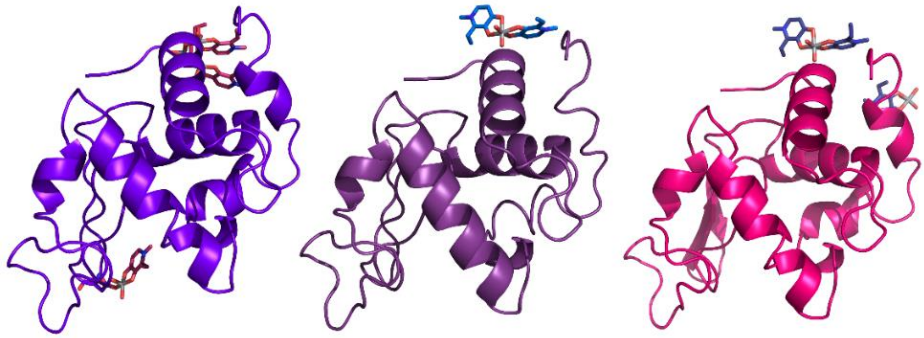

Figure 2.2 – Overall structures of the adducts formed upon reaction of $[V^{IV}O(empp)_2]$ with HEWL under different experimental conditions: a) structure A, derived from a crystal grown in 1.1 M sodium chloride, 0.1 M sodium acetate pH 4.0; b) structure B, derived from a crystal grown in 0.8 M succinic acid pH 7.0; c) structure C, derived from a crystal grown in 2.0 M sodium formate, 0.1 M HEPES pH 7.5. V atoms are in grey. Coordinates and structure factors were deposited in the Protein Data Bank (PDB) under the accession codes 8OM8, 8OMS, 8OMT.

In structure A (Figure 2.2a), derived from a crystal grown in 1.1 M sodium chloride and 0.1 M sodium acetate pH 4.0, the non-covalent binding of a cyclic trinuclear oxidovanadium(V) complex on the protein surface was observed (Figure 2.3a), together with the covalent binding of $[V^{IV}O(empp)(H_2O)]^+$ to the side chain of Asp48 (Figure 2.3b). Refinements suggest an occupancy value of 0.60 for these two V-containing fragments (Table 2.1).

The trinuclear oxidovanadium(V) complex has formula $[V^{V}_3O_6(empp)_3(H_2O)]$. An analogous species, $[V^{V}_3O_6(dhp)_3(H_2O)]$, has been isolated from the action of the methyl derivative of Hempp (Hdhp), KOH, and sodium metavanadate at pH 4.5,[190] and has been characterized in aqueous solution in the system V^V/Hdhp in the pH range 2.0-5.0.[191] This indicates that the oxidation of V^{IV} to V^V occurs under the investigated experimental conditions. This process

is likely promoted by the relatively high local V concentration reached during the soaking experiments and by crystal lattice environment, which acts as a chemical reaction vessel. Notably, the results previously obtained in a simple inorganic system were successfully reproduced in a complex biological system.

Table 2.1 – Data collection and refinement statistics for the structures A, B and C.

Data collection			
	Structure A	Structure B	Structure C
PDB code	8OM8	8OMS	8OMT
Crystallization condition	1.1 M sodium chloride, 0.1 M sodium acetate pH 4.0	0.8 M succinic acid pH 7.0	2.0 M sodium formate, 0.1 M HEPES pH 7.5
Soaking time	25 d	22 d	22 d
Space group	$P4_32_12$	$P4_32_12$	$P4_32_12$
a (Å)	78.41	77.59	77.13
b (Å)	78.41	77.59	77.13
c (Å)	37.02	37.58	37.26
Resolution range (Å)	55.44-1.08 (1.10-1.08)	38.80-1.10 (1.22-1.10)	38.56-1.08 (1.10-1.08)
Observations	1139882 (43874)	814761 (18987)	701425 (3107)
Unique reflections	50384 (2483)	46373 (2164)	40727 (820)
Completeness (%)	100.0 (100.0)	99.4 (95.0)	83.9 (34.0)
Redundancy	22.6 (17.7)	17.6 (8.8)	17.2 (3.8)
Rmerge (%)	0.045 (1.409)	0.051 (0.645)	0.043 (0.404)
Average I/σ(I)	33.2 (2.2)	28.8 (2.9)	36.5 (2.7)
$CC_{1/2}$	1.000 (0.744)	0.999 (0.867)	1.000 (0.829)
Anom. completeness (%)	99.9 (100.0)	99.1 (91.1)	83.8 (32.0)
Anom. Multiplicity	12.0 (9.2)	9.3 (4.8)	9.2 (2.1)
Refinement			
Resolution (Å)	55.26-1.08	38.80-1.10	38.56-1.10
N° reflections	43357	44373	38056
N° reflections in working set	1803	3090	1319
R-factor/Rfree	0.147/0.189	0.144/0.167	0.116/0.144
N° non-H atoms in the refinement	1311	1290	1317
B-factor overall ($Å^2$)	20.12	15.69	15.97
Estimated occupancy of $[(V^V_3O_6)(empp)_3(H_2O)]$ in structure A	0.60	–	–

Estimated occupancy of $[V^{IV}O(empp)(H_2O)]^+$ in structure A	0.60	–	–
B-factor of $[(V^{V}_3O_6)(empp)_3(H_2O)]$ in structure A (Å^2)	26.3 ± 2.7	–	–
B-factor of $[V^{IV}O(empp)(H_2O)]^+$ in structure A (Å^2)	23.24	–	–
Estimated occupancy of *cis*-$[V^{IV}O(empp)_2(H_2O)]$ in structure B	–	0.40	–
B-factor of *cis*-$[V^{IV}O(empp)_2(H_2O)]$ in structure B (Å^2)	–	17.14	–
Estimated occupancy of *cis*-$[V^{IV}O(empp)_2(H_2O)]$ in structure C	–	–	0.80
Estimated occupancy of $[V^{IV}O(empp)(H_2O)_2]^+$ in structure C	–	–	0.40
B-factor of *cis*-$[V^{IV}O(empp)_2(H_2O)]$ in structure C (Å^2)	–	–	14.51
B-factor of $[V^{IV}O(empp)(H_2O)_2]^+$ in structure C (Å^2)	–	–	37.39
Ramachandran values (%)			
Most favoured/Additional allowed	94.06/5.94	95.15/4.85	95.33/4.67
Outliers	0	0	0
RMSD from ideality			
RMSD bonds (Å)	0.022	0.021	0.024
RMSD angles (°)	2.967	2.691	3.029

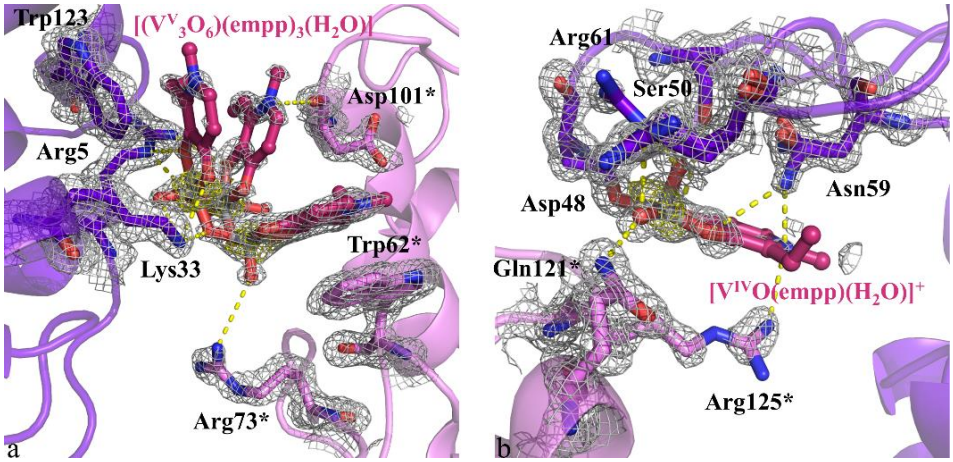

Figure 2.3 – V binding sites in structure A: a) non-covalent binding of $[(V^{V}_3O_6)(empp)_3(H_2O)]$; b) covalent coordination of $[V^{IV}O(empp)(H_2O)]^+$ to the side chain of Asp48. 2Fo-Fc e.d. maps are reported at 1.0 σ level in grey. Anomalous e.d. map is reported at 3.0 σ level in yellow. Atoms of symmetry related molecules are coloured in light violet and highlighted with *.

As reported for $[V^{V}_3O_6(dhp)_3(H_2O)]$ structure solved by Avecilla et al.,[190] one out of the three V^V atoms is penta-coordinated with a distorted square pyramidal geometry, while the other two V atoms adopt distorted octahedral coordination. Each V centre is bound by one oxido group, two O bridging ligands, and two empp(−) oxygen atoms. One of the two octahedral V atoms is also coordinated to a third oxygen from a second empp(−) anion, which bridges the two hexa-coordinated V^V centres; the second octahedral V^V completes its coordination sphere with a water molecule. Two out of the three empp(−) ligands show an equatorial-equatorial arrangement, with two oxygens in *cis* to V=O bond, while the third one occupies an equatorial and an axial position. The V=O bond distances are very similar (1.62−1.65 Å) and comparable to those experimentally observed in the analogous structure with dhp.[190] As expected, the V−OH_2 distance is slightly longer (2.03Å). The three V−O−V bond angles in the cyclic framework, involving

single bridging oxygen atoms, are very similar, with values close to 120°. The structure of trinuclear empp(−)-based cluster interacting with HEWL is shown in Figure 2.4.

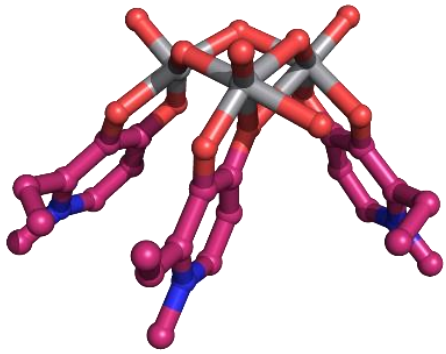

Figure 2.4 – Structure of the trinuclear cluster $[V^{V}_{3}O_{6}(empp)_{3}(H_{2}O)]$ formed by $[V^{IV}O(empp)_{2}]$ in the presence of HEWL in structure A. V atoms are in grey, empp(–) ligands are in hot pink, while oxygens are in red.

A detailed comparison of selected bond lengths and angles observed in $[V^{V}_{3}O_{6}(empp)_{3}(H_{2}O)]$ and in $[V^{V}_{3}O_{6}(dhp)_{3}(H_{2}O)]$ is provided in Table 2.2.

Table 2.2 – Selected bond lengths (Å) and angles (°) for $[V^{V}_{3}O_{6}(empp)_{3}(H_{2}O)]$ in its adduct with HEWL, and comparison with the values found in single crystals of $[V^{V}_{3}O_{6}(dhp)_{3}(H_{2}O)]$.[a]

	$[V^{V}_{3}O_{6}(empp)_{3}(H_{2}O)]$	**$[V^{V}_{3}O_{6}(dhp)_{3}(H_{2}O)]$** [b]
Bond	**Bond lengths (Å)**	**Bond lengths (Å)**
V(1)-O(1)	1.65	1.599(3)
V(1)-O(6)	1.76	1.794(3)
V(1)-O(4)	1.99	1.817(3)
V(1)-O(7)	1.94	1.980(4)
V(1)-O(8)	1.79	2.008(4)
V(1)-O(12)	2.29	2.450(3)
V(2)-O(2)	1.62	1.613(4)
V(2)-O(4)	1.93	1.795(3)
V(2)-O(5)	1.81	1.824(4)
V(2)-O(9)	1.97	1.962(3)
V(2)-O(10)	1.75	2.004(4)
V(3)-O(3)	1.62	1.609(4)
V(3)-O(5)	1.82	1.813(3)
V(3)-O(6)	1.98	1.857(3)
V(3)-O(11)	1.81	1.909(3)
V(3)-O(12)	2.05	2.204(3)
V(3)-O(1W)	2.03	2.180(4)
O(7)-C(1)	1.30	1.433(7)
O(8)-C(7)	1.30	1.259(7)
O(9)-C(8)	1.30	1.325(5)
O(10)-C(14)	1.30	1.310(6)
O(11)-C(15)	1.30	1.336(5)
O(12)-C(21)	1.30	1.309(5)
Angles	**Angle values (°)**	**Angle values (°)**

O(1)-V(1)-O(6)	99.18	103.03(17)
O(1)-V(1)-O(4)	100.32	103.18(17)
O(6)-V(1)-O(4)	88.53	93.88(15)
O(1)-V(1)-O(7)	97.94	102.01(17)
O(6)-V(1)-O(7)	89.25	90.56(17
O(4)-V(1)-O(7)	161.73	152.69(16)
O(1)-V(1)-O(8)	95.30	100.36(18)
O(6)-V(1)-O(8)	165.30	156.20(15)
O(4)-V(1)-O(8)	86.40	84.93(17)
O(7)-V(1)-O(8)	91.25	80.33(19)
O(1)-V(1)-O(12)	168.78	176.19(17)
O(6)-V(1)-O(12)	70.13	74.47(12)
O(4)-V(1)-O(12)	83.23	78.40(12)
O(7)-V(1)-O(12)	78.96	76.89(13)
O(8)-V(1)-O(12)	95.55	82.04(13)
O(4)-V(2)-O(9)	172.33	153.53(15)
O(5)-V(2)-O(9)	81.44	88.57(14)
O(2)-V(2)-O(10)	97.42	102.7(2)
O(4)-V(2)-O(10)	88.15	86.67(15)
O(5)-V(2)-O(10)	156.85	152.79(15)
O(9)-V(2)-O(10)	86.30	79.36(14)
O(3)-V(3)-O(5)	103.61	102.16(19)
O(3)-V(3)-O(6)	109.38	105.34(17)
O(5)-V(3)-O(6)	91.93	92.03(14)
O(3)-V(3)-O(11)	92.71	95.80(16)
O(5)-V(3)-O(11)	93.33	100.14(14)
O(6)-V(3)-O(11)	155.37	152.82(14)
O(3)-V(3)-O(12)	173.73	172.09(16)
O(5)-V(3)-O(12)	82.37	83.65(14)

O(6)-V(3)-O(12)	71.88	79.86(13)
O(2)-V(2)-O(4)	94.34	103.26(18)
O(2)-V(2)-O(5)	102.52	103.6(2)
O(4)-V(2)-O(5)	101.45	94.01(15)
O(2)-V(2)-O(9)	91.93	101.69(17)
V(3)-O(12)-V(1)	97.01	84.98(10)
O(11)-V(3)-O(12)	85.00	77.54(12)
V(2)-O(4)-V(1)	112.20	125.61(18)
V(3)-O(5)-V(2)	119.40	120.39(17)
V(1)-O(6)-V(3)	120.79	119.22(17)

[a] Structure reported in Avecilla, F.; Geraldes, Carlos F. G. C.; Castro, M. Margarida C. A. A New Trinuclear Oxovanadium(V) Complex with DMPP Ligands − Synthesis and Structural Characterization in the Solid State and in Aqueous Solution. *Eur. J. Inorg. Chem*. **2001**, *2001*, 3135-3142. [b] Standard deviations in parenthesis.

The binding of $[V^{V}_{3}O_6(empp)_3(H_2O)]$ to HEWL is stabilized by stacking interactions of the two empp(−) ligands, which are almost parallel to each other, with the side chain of Trp123, and by hydrogen bonds with the side chains of Arg5 and Lys33, water molecules, the side chains of Arg73 and Asp101 from a symmetry-related molecule and stacking interaction with Trp62 from a symmetry-related molecule (Figure 2.3a).

The $[V^{IV}O(empp)(H_2O)]^+$ fragment in structure A is coordinated to the side chain of Asp48 and is held in its position by hydrogen bonds formed with Ser50, Asn59, and Arg61 side chains, water molecules, and with Gln121 and Asp125 side chains from a symmetry-related molecule (Figure 2.3b). This agrees with ESI-MS and EPR results (see Appendix A, Interaction of $[V^{IV}O(empp)_2]$ with HEWL: mass spectrometric studies, and Interaction of $[V^{IV}O(empp)_2]$ with HEWL: electron paramagnetic resonance studies).

In structure B (Figure 2.2b), derived from crystals grown in 0.8 M succinic acid pH 7.0, non-covalent binding of *cis*-$[V^{IV}O(empp)_2(H_2O)]$ on the protein surface was found (occupancy = 0.40). This V-containing fragment is non-covalently bound to HEWL through hydrogen bonds with N main chain atoms of Arg5, Cys6, and Glu7 (Figure 2.5), water molecules, and Arg14 side chain from a symmetry-related molecule. This agrees with EPR data (see Appendix A, Interaction of $[V^{IV}O(empp)_2]$ with HEWL: electron paramagnetic resonance studies).

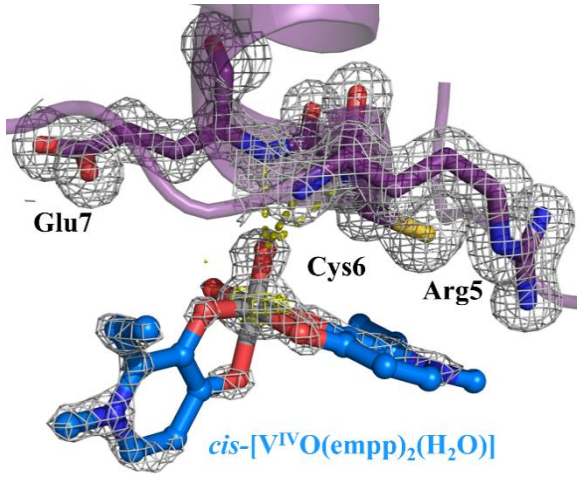

Figure 2.5 – V binding site in structure B: non-covalent binding of *cis*-$[V^{IV}O(empp)_2(H_2O)]$. 2Fo-Fc e.d. maps are reported at 1.0 σ level in grey. Anomalous e.d. map is reported at 3.0 σ level in yellow.

The structure C was derived from a crystal grown in 2.0 M sodium formate and 0.1 M HEPES pH 7.5 (Figure 2.2c). In this structure, the non-covalent binding of *cis*-$[V^{IV}O(empp)_2(H_2O)]$ fragment (occupancy = 0.80) was observed (Figure 2.6a), together with the non-covalent binding of $[V^{IV}O(empp)(H_2O)_2]^+$ (occupancy = 0.40). This additional V-containing fragment forms hydrogen bonds with Arg125 side chain and water molecules (Figure 2.6b). The simultaneous binding of *cis*-$[V^{IV}O(empp)_2(H_2O)]$ and $[V^{IV}O(empp)(H_2O)]^+$ to HEWL was also confirmed by ESI-MS measurements (see Appendix A, Interaction of $[V^{IV}O(empp)_2]$ with HEWL: mass spectrometric studies).

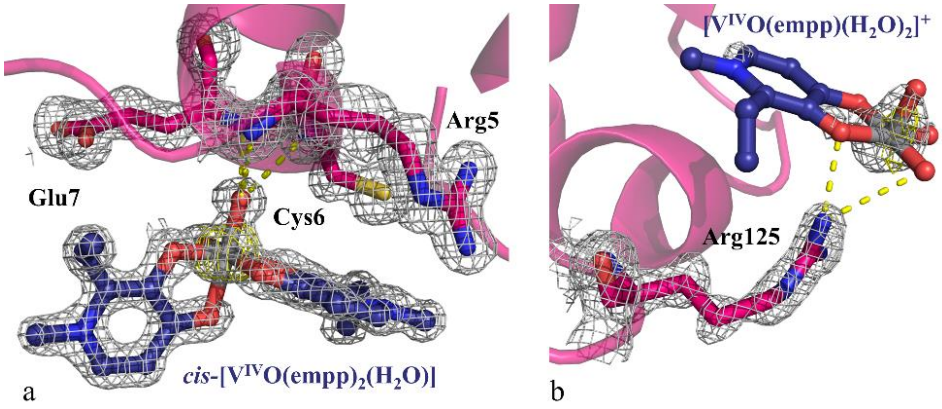

Figure 2.6 – V binding site in structure C. Non- covalent binding of a) *cis*-$[V^{IV}O(empp)_2(H_2O)]$ and b) $[V^{IV}O(empp)(H_2O)_2]^+$. 2Fo-Fc e.d. maps are reported at 1.0 σ level in grey. Anomalous e.d. map is reported at 3.0 σ level in yellow.

In conclusion, crystallographic data provide insights into the role of HEWL interaction in the speciation of $[V^{IV}O(empp)_2]$. Under the investigated experimental conditions, $[V^{IV}O(empp)(H_2O)]^+$, $[V^{IV}O(empp)(H_2O)_2]^+$, *cis*-$[V^{IV}O(empp)_2(H_2O)]$ derived from the reaction $[V^{IV}O(empp)_2] + H_2O \rightleftarrows$ *cis*-$[V^{IV}O(empp)_2(H_2O)]$ and $[V^{V}{}_3O_6(empp)_3(H_2O)]$ can bind the protein.

Notably, even though in aqueous solution $[V^{IV}O(empp)_2]$ and *cis*-$[V^{IV}O(empp)_2(H_2O)]$ are in equilibrium between each other, no binding of $[V^{IV}O(empp)_2]$ is detected. For *cis*-$[V^{IV}O(empp)_2(H_2O)]$ only the isomer with two equatorial phenolate-O is revealed and only the enantiomer *OC*-6−24-Λ (Figure 2.7) interacts with HEWL.

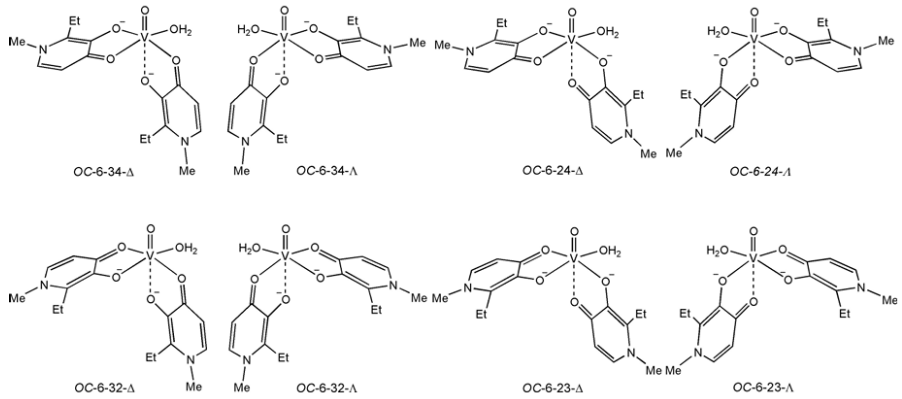

Figure 2.7 – Isomers/enantiomers of *cis*-$[V^{IV}O(empp)_2(H_2O)]$ complex formed after the dissolution of $[V^{IV}O(empp)_2]$ in aqueous solution.

The simultaneous binding of multiple V-containing fragments to HEWL suggests that these species may distribute among different protein sites with comparable affinity. This dynamic behaviour could be relevant for understanding the transport mechanisms and potential mode of action of this class of V-based drugs. Moreover, the results highlight that the species isolated in the solid state and characterized by XRD may strongly depend on the experimental conditions.

2.3 Interaction of $[V^{IV}O(dhp)_2]$ with HEWL

The interaction of $[V^{IV}O(dhp)_2]$ (Figure 2.1b) with proteins has been already studied in solution, using potentiometric (pH titrations), spectroscopic (EPR) and spectrometric (ESI-MS) methods.[192] EPR and pH titrations have demonstrated that $[V^{IV}O(dhp)_2]$ interacts with human serum albumin and transferrin.[192] The interaction of $[V^{IV}O(dhp)_2]$ with HEWL has been studied using ESI-MS.[33] In aqueous solution from pH 5.0 to 8.0, the complex exists as a mixture of *cis*-$[V^{IV}O(dhp)_2(H_2O)]$ (*cis*-octahedral) and $[V^{IV}O(dhp)_2]$ (square pyramidal).[33] Mass spectra have revealed that $[V^{IV}O(dhp)(H_2O)]^+$ and $[V^{IV}O(dhp)_2]$ can bind the protein when in $[V^{IV}O(dhp)_2]$/HEWL 3:1 molar ratio. A peak (14870 Da) attributed

to an adduct formed by HEWL with both these species has been also found. When the $[V^{IV}O(dhp)_2]$/HEWL molar ratio is 5:1 two molecules of $[V^{IV}O(dhp)_2]$ can bind the protein.[33]

To complement these findings, X-ray crystallographic studies were carried out. Understanding the interaction of $[V^{IV}O(dhp)_2]$ with proteins is essential to clarify how structural and electronic features of this complex influence recognition by biological macromolecules and to provide insights into the potential mechanism of action of this V-based drug.

2.3.1 Crystallographic studies

To identify the residues involved in the interactions with the V-containing fragments derived by $[V^{IV}O(dhp)_2]$ that bind HEWL according to ESI MS experiments, crystals of the metal-free protein were grown in 1.1 M sodium chloride, 0.1 M sodium acetate pH 4.0 and then were exposed for 7 days to a saturated solution of $[V^{IV}O(dhp)_2]$. High resolution X-ray diffraction data were collected on two HEWL crystals treated with $[V^{IV}O(dhp)_2]$ (1.10-1.11 Å resolution). Data collection and refinement statistics are reported in Table 2.3.

Table 2.3 – Data collection and refinement statistics for the structures A and B.

Data collection		
	Structure A	Structure B
Crystallization condition	1.1 M sodium chloride, 0.1 M sodium acetate at pH 4.0	1.1 M sodium chloride, 0.1 M sodium acetate at pH 4.0
Soaking time	7 d	7 d
Space group	$P4_32_12$	$P4_32_12$
a (Å)	78.41	77.59
b (Å)	78.41	77.59
c (Å)	37.02	37.58
Resolution range (Å)	55.20-1.10 (1.12-1.10)	55.55-1.10 (1.11-1.10)
Observations	1027650 (37961)	1082006 (36072)
Unique reflections	46635 (2310)	48322 (2357)
Completeness (%)	100.0 (100.0)	99.9 (99.4)
Redundancy	22.0 (16.4)	22.4 (15.3)
Rmerge (%)	0.044 (1.108)	0.057 (1.258)
Average I/σ(I)	32.2 (2.6)	29.4 (2.4)
$CC_{1/2}$	1.000 (0.853)	0.999 (0.770)
Anom. completeness (%)	100.0 (100.0)	100.0 (99.6)
Anom. Multiplicity	11.6 (8.5)	11.8 (7.9)
Refinement		
Resolution (Å)	55.20-1.11	55.55-1.10
N° reflections	44259	45400
N° reflections in working set	3242	3296
R-factor/Rfree	0.131/0.156	0.134/0.161
N° non-H atoms in the refinement	1367	1332
B-factor overall ($Å^2$)	20.36	18.61
Estimated occupancy of $[V^{IV}O(H_2O)_3]^+$	0.60	0.50
Estimated occupancy of $[(V^{V}O(dhp)_2)_2O]$ in structure A	0.70	-

Estimated occupancy of $[(V^{V}O(dhp)_2)(V^{V}O(dhp)(H_2O)_2)O]^+$ in structure B	-	0.50
B-factor of $[V^{IV}O(H_2O)_3]^+$ (Å^2)	24.25	22.80
B-factor of $[(V^{V}O(dhp)_2)_2O]$ in structure A (Å^2)	22.9±1.4	-
B-factor of $[(V^{V}O(dhp)_2)(V^{V}O(dhp)(H_2O)_2)O]^+$ in structure B (Å^2)	-	24.1±1.7
Ramachandran values (%)		
Most favoured/Additional allowed	96.81/3.19	94.90/5.10
Outliers	0	0
RMSD from ideality		
RMSD bonds (Å)	0.025	0.023
RMSD angles (°)	2.946	2.674

Surprisingly, in both refined structures, $[V^{IV}O(dhp)_2]$ and $[V^{IV}O(dhp)(H_2O)]^+$ were not found. This could be due to the difference in the experimental conditions used to collect ESI-MS spectra and to produce the adducts within the protein crystals. However, interesting interactions between V-containing fragments and protein residues were observed. In particular, in the first structure (structure A, Figure 2.8), the covalent binding of $[V^{IV}O(H_2O)_3]^+$ to the Asp48 side chain (Figure 2.9a) and the non-covalent interaction of the dinuclear oxidovanadium(V) complex $[(V^{V}O(dhp)_2)_2O]$ (Figure 2.9b) to protein surface residues were detected. In this structure, refinements suggest occupancy = 0.60 and 0.70 for the two V-containing fragments, respectively.

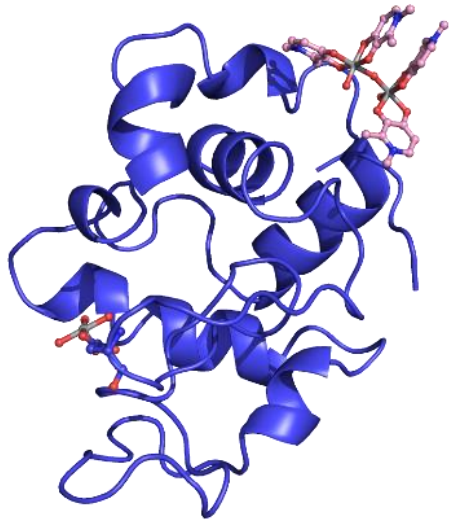

Figure 2.8 – Overall structure of the adduct formed upon reaction of $[V^{IV}O(dhp)_2]$ with HEWL (structure A). V atoms are in grey.

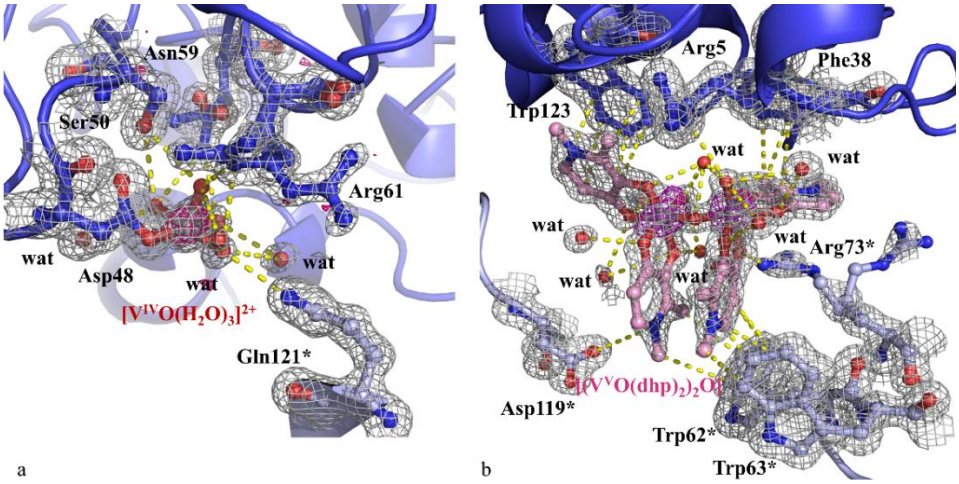

Figure 2.9 – V binding sites in the structure A: a) covalent binding of $[V^{IV}O(H_2O)_3]^+$ to the Asp48 side chain; b) non-covalent binding of $[(V^{V}O(dhp)_2)_2O]$ to protein surface residues. 2Fo-Fc e.d. maps are reported at 1.0 σ level in grey. Anomalous e.d. map is reported at 3.0 σ level in pink. Atoms of symmetry related molecules are coloured in light blue and highlighted with *. Arg73 adopts two alternative conformations.

Regarding the binding of $[V^{IV}O(H_2O)_3]^+$ fragment coordinated to the side chain of Asp48 (Figure 2.9a), it should be noted that the three water molecules and the OD2 atom of the Asp are on a plane, while the V=O group is on the top of the square pyramid. The O of the V=O group forms a hydrogen bond with the side chain of Arg61, which adopts two different conformations in the crystal, and the side chain of Ser50. The water molecules that are coordinated to the V centres are hydrogen bonded to the side chains of Ser50, Asn59, Arg61 and Gln121 from a symmetry related molecule and to other water molecules that in turns are directly linked to the side chains of Thr47, Arg61, Trp62, to the main chain N atom of Thr47 and Asp48, the side chain of Gln121 from a symmetry-related molecule and to the main chain N atom of Gly126 from a symmetry-related molecule.

The dinuclear oxidovanadium(V) complex $[(V^{V}O(dhp)_2)_2O]$ found on HEWL surface (Figure 2.9b) has been previously identified by Jakusch et al.,[191] but its 3D

structure has been never reported before. The presence of this structure in our crystals indicates an oxidation of the V centre that could play a significant role in the formation of the dimetallic compound. The formation of this structure could be also promoted by the relatively high local V concentration due to the soaking experiments. The presence of the protein or the crystal lattice environment could also play a role in the stabilization of this dimeric species.

The $[(V^{V}O(dhp)_2)_2O]$ complex consists of a dinuclear oxovanadium(V) complex with four anionic dhp ligands, one oxygen atom bridging the two metal centers, each one of which is coordinated to one oxo group. The two V atoms adopt a slightly distorted octahedral geometry. In Figure 2.10, atomic numbering scheme related to the $[(V^{V}O(dhp)_2)_2O]$ structure is reported.

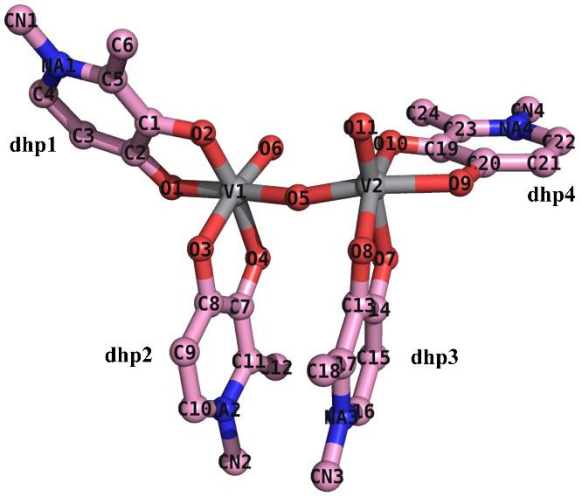

Figure 2.10 – Structure of $[(V^{V}O(dhp)_2)_2O]$ showing the atomic numbering scheme.

Bond lengths and angles of this structure are listed in Table 2.4. Values are in the expected range. In the structure, the two dhp ligands dhp2 and dhp3 stack to each other and are almost parallel (angle between the planes of the two ligands = 14.1°). Stacking is also involved in the stabilization of the $[(V^{V}O(dhp)_2)_2O]$

binding to HEWL. Indeed, dhp1 is almost parallel to the side chain of Trp123 (angle between the two planes = 6.7°) and dhp4 is almost parallel to the guanidinium group of the Arg73 side chain (angle between the two planes = 7.3°). The $[(V^{V}O(dhp)_2)_2O]$ structure also forms many other interactions with the protein. Dhp4 forms hydrophobic interactions with the Phe38 side chain, while dhp3 with the side chains of Trp62 and Trp63 from a symmetry-related molecule. Hydrogen bonds are also involved in the recognition of $[(V^{V}O(dhp)_2)_2O]$ by HEWL. Indeed, O11 is hydrogen bonded to the NE atom of Arg5, NA2 forms a hydrogen bond with the OD1 atom of Asp119 from a symmetry-mate, and O7 forms a hydrogen bond with the NH1 of Arg73. The oxygen atoms of the complex are also in contact with several water molecules that in turn are linked to several different protein atoms.

Similar results have been obtained in structure B. However, in this structure the non-covalent binding of $[(V^{V}O(dhp)_2)(V^{V}O(dhp)(H_2O)_2)O]^{+}$ (occupancy = 0.50) on the protein surface was found (Figure 2.11). This V-containing fragment was probably obtained by the replacement of a dhp group (dhp4) by two water molecules (see Table 2.4 for bond length and angle values). This replacement could be favoured by the close contacts of the dhp ligand to the side chain of Arg73 from a symmetry-related molecule, which changes its conformation when compared to structure A (see Figure 2.11 vs Figure 2.9b), where it adopts two alternative conformations.

Table 2.4 – Selected bond lengths (Å) and angles (°) for $[(V^{V}O(dhp)_2)_2O]$ and $[(V^{V}O(dhp)_2)(V^{V}O(dhp)(H_2O)_2)O]^{+}$.

Bond lengths (Å)		
	$[(V^{V}O(dhp)_2)_2O]$ (structure A)	**$[(V^{V}O(dhp)_2)(V^{V}O(dhp)(H_2O)_2)O]^{+}$ (structure B)**
V(1)-O(1)	1.95	1.96
V(1)-O(2)	1.73	1.71
V(1)-O(3)	1.86	1.77
V(1)-O(4)	1.95	1.94
V(1)-O(5)	1.89	1.82
V(1)-O(6)	1.72	1.72
V(2)-O(5)	1.83	1.79
V(2)-O(7)	2.08	2.03
V(2)-O(8)	1.89	1.78
V(2)-O(9)	1.93	1.75
V(2)-O(10)	2.00	1.95
V(2)-O(11)	1.73	1.76
Bond angles (°)		
O(1)-V(1)-O(2)	87.56	86.31
O(1)-V(1)-O(3)	93.78	94.16
O(1)-V(1)-O(4)	86.29	88.74
O(1)-V(1)-O(5)	177.26	178.10
O(1)-V(1)-O(6)	88.00	84.63
O(2)-V(1)-O(3)	93.62	91.89
O(2)-V(1)-O(4)	170.95	174.36
O(2)-V(1)-O(5)	92.92	91.79
O(2)-V(1)-O(6)	94.46	91.46
O(3)-V(1)-O(4)	80.18	85.75
O(3)-V(1)-O(5)	83.50	85.86
O(3)-V(1)-O(6)	171.79	176.36

O(4)-V(1)-O(5)	92.91	93.15
O(4)-V(1)-O(6)	91.96	90.78
O(5)-V(1)-O(6)	94.65	95.46
O(5)-V(2)-O(7)	77.30	78.54
O(5)-V(2)-O(8)	92.98	92.40
O(5)-V(2)-O(9)	159.48	165.27
O(5)-V(2)-O(10)	85.93	84.60
O(5)-V(2)-O(11)	104.80	100.82
O(7)-V(2)-O(8)	79.07	81.52
O(7)-V(2)-O(9)	85.29	92.22
O(7)-V(2)-O(10)	81.88	84.41
O(7)-V(2)-O(11)	172.50	179.11
O(8)-V(2)-O(9)	94.30	97.61
O(8)-V(2)-O(10)	160.68	165.93
O(8)-V(2)-O(11)	93.58	99.14
O(9)-V(2)-O(10)	80.89	83.08
O(9)-V(2)-O(11)	93.87	88.28
O(10)-V(2)-O(11)	105.36	94.93
V(1)-O(5)-V(2)	161.87	165.95

O(9) and O(10) in the structure of $[(V^{V}O(dhp)_2)(V^{V}O(dhp)(H_2O)_2)O]^{+}$ are the oxygen of the two water molecules replacing the dhp4 of $[(V^{V}O(dhp)_2)_2O]$.

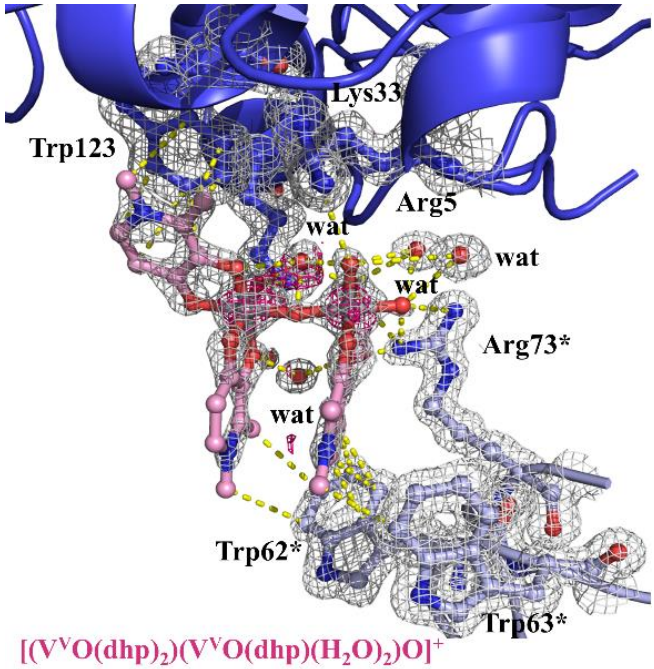

Figure 2.11 – The $[(V^{V}O(dhp)_2)(V^{V}O(dhp)(H_2O)_2)O]^+$ binding site in the structure B. 2Fo-Fc e.d. maps are reported at 1.0 σ level in grey. Anomalous e.d. map is reported at 3.0 σ level in pink. Atoms of symmetry related molecules are coloured in light blue and highlighted with *.

In conclusion, crystallographic data reveals the binding of $[V^{IV}O(dhp)_2]$ derivatives to HEWL. Under the investigated experimental condition, the *cis*-octahedral $[V^{IV}O(dhp)_2(H_2O)]$ complex and the square pyramidal $[V^{IV}O(dhp)_2]$, were not found in the structures. However, $[V^{IV}O(H_2O)_3]^+$, $[(V^{V}O(dhp)_2)_2O]$ and $[(V^{V}O(dhp)_2)(V^{V}O(dhp)(H_2O)_2)O]^+$, derived from the hydrolysis of $[(V^{V}O(dhp)_2)_2O]$, bind the protein.

Overall, these results highlight the importance of structural studies on VC–protein interactions, as they allow the identification of unexpected molecular species that could also form in the cellular environment. Notably, the presence of proteins can alter the speciation of active $[V^{IV}OL_2]$ compounds, which may lose

one or more ligands before or after binding. Moreover, proteins can provide a scaffold for the formation and stabilization of dinuclear or even trinuclear V-containing complexes.

2.4 Interaction of $[V^{IV}O(8\text{-}HQ)_2]$ with HEWL

Previous studies on the interaction of $[V^{IV}O(8\text{-}HQ)_2]$ (Figure 2.1c) with proteins have shown that this complex can form different V-containing species in solution, whose stability is influenced by pH and ligand substitution equilibria.[193]

To gain further insight into the binding behaviour of $[V^{IV}O(8\text{-}HQ)_2]$ with proteins, the interaction with HEWL was investigated using an integrated approach combining X-ray crystallography with complementary spectroscopic (UV-vis, EPR), spectrometric (ESI-MS), and computational methods. This strategy was aimed at characterizing the nature of the V-containing fragments bound to the protein and at understanding how solution conditions, such as pH, affect the species involved.

2.4.1 Crystallographic studies

Crystals of the adducts formed upon reaction of HEWL with $[V^{IV}O(8\text{-}HQ)_2]$ were obtained by soaking strategy, exposing metal-free protein crystals to a solution containing $[V^{IV}O(8\text{-}HQ)]$, under two different experimental conditions using ethylene glycol or sodium formate as precipitants (Table 2.5).

Table 2.5 – Data collection and refinement statistics for the structures A and B.

Data collection		
	Structure A	Structure B
PDB code	8RTJ	8RTK
Crystallization condition	20% ethylene glycol, 0.6 M sodium nitrate, 0.1 M sodium acetate pH 4.5	2.0 M sodium formate, 0.1 M HEPES pH 7.5
Soaking time	50 d	22 d
Space group	$P4_32_12$	$P4_32_12$
a (Å)	78.14	77.08
b (Å)	78.14	77.08
c (Å)	37.52	37.53
Resolution range (Å)	55.25-1.27 (1.30-1.27)	38.54-1.21 (1.23-1.21)
Observations	730862 (37257)	651773 (19279)
Unique reflections	30889 (1522)	35157 (1693)
Completeness (%)	99.9 (100.0)	100.0 (100.0)
Redundancy	23.7 (24.5)	18.5 (11.4)
Rmerge (%)	0.038 (1.629)	0.048 (1.037)
Average I/σ(I)	36.5 (2.2)	27.9 (2.3)
$CC_{1/2}$	1.000 (0.844)	1.000 (0.787)
Anom. completeness (%)	100.0 (100.0)	100.0 (99.8)
Anom. Multiplicity	12.6 (12.8)	9.9 (6.0)
Refinement		
Resolution (Å)	55.24-1.27	38.54-1.21
N° reflections	29498	33319
N° reflections in working set	2012	2426
R-factor/Rfree	0.174/0.197	0.173/0.192
N° non-H atoms in the refinement	1248	1284
B-factor overall ($Å^2$)	23.33	19.81
Estimated occupancy of $[V^{IV}O(8\text{-}HQ)(H_2O)]^+$	0.60	-

Estimated occupancy of V	0.60	-
B-factor of $[V^{IV}O(8\text{-}HQ)(H_2O)]^+$ ($Å^2$)	45.63	-
B-factor of V ($Å^2$)	55.31	-
Estimated occupancy of $[V^{IV}O(8\text{-}HQ)_2(H_2O)]$	-	0.50
Estimated occupancy of $V^{V}O_2^+$	-	0.30
Estimated occupancy of $V^{IV}O^{2+}$	-	0.30
Estimated occupancy of $V^{IV}O^{2+}$	-	0.30
B-factor of $[V^{IV}O(8\text{-}HQ)_2(H_2O)]$ ($Å^2$)	-	34.12
B-factor of $V^{V}O_2^+$ ($Å^2$)	-	20.63
B-factor of $V^{IV}O^{2+}$ ($Å^2$)	-	24.14
B-factor of $V^{IV}O^{2+}$ ($Å^2$)	-	33.64
Ramachandran values (%)		
Most favoured/Additional allowed	94.78/5.22	96.15/3.85
Outliers	0	0
RMSD from ideality		
RMSD bonds (Å)	0.015	0.015
RMSD angles (°)	2.010	2.193

It has been verified that, under these conditions, the VC remains stable in the absence and in the presence of HEWL (see the UV-vis spectra shown in Figure 2.12).

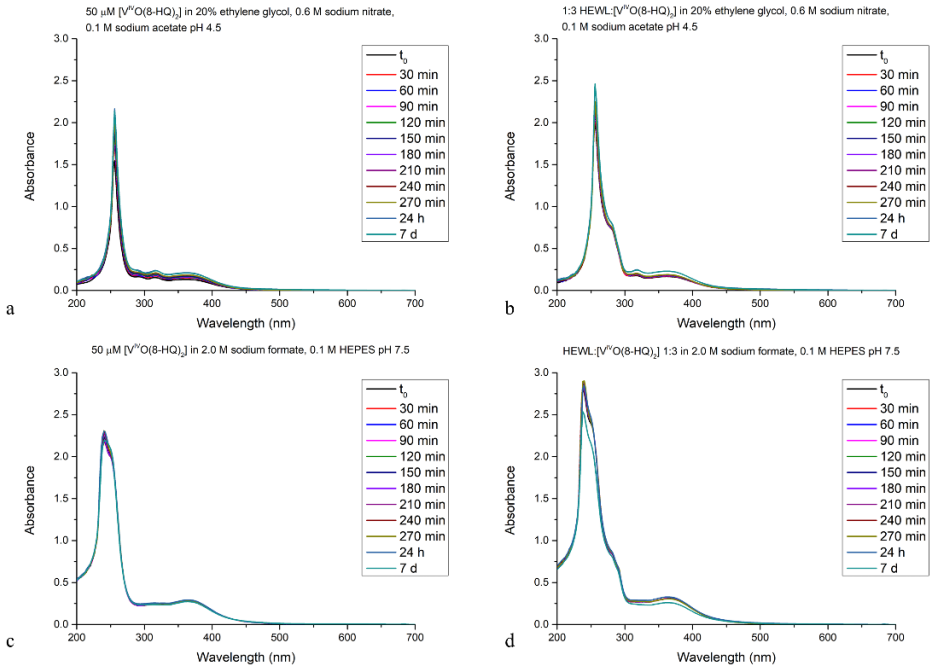

Figure 2.12 – UV-vis spectra as a function of time of a) $[V^{IV}O(8\text{-}HQ)_2]$ and of b) $[V^{IV}O(8\text{-}HQ)_2]$ collected in the presence of HEWL using a 3/1 vanadium-to-protein molar ratio (protein and V concentrations were 16.7 and 50 μM, respectively) in 20% ethylene glycol, 0.6 M sodium nitrate, 0.1 M sodium acetate at pH 4.5; UV-vis spectra as a function of time of c) $[V^{IV}O(8\text{-}HQ)_2]$ and of d) $[V^{IV}O(8\text{-}HQ)_2]$ collected in the presence of HEWL using a 3/1 vanadium-to-protein molar ratio (protein and V concentrations were 16.7 and 50 μM, respectively) in 2.0 M sodium formate, 0.1 M HEPES pH 7.5.

The structure of the adduct formed in crystals of HEWL grown in ethylene glycol (structure A) was solved using data collected using a crystal of the protein

exposed to the VC for 50 days (Figure 2.13). Data collection, refinement and model statistics are reported in Table 2.5.

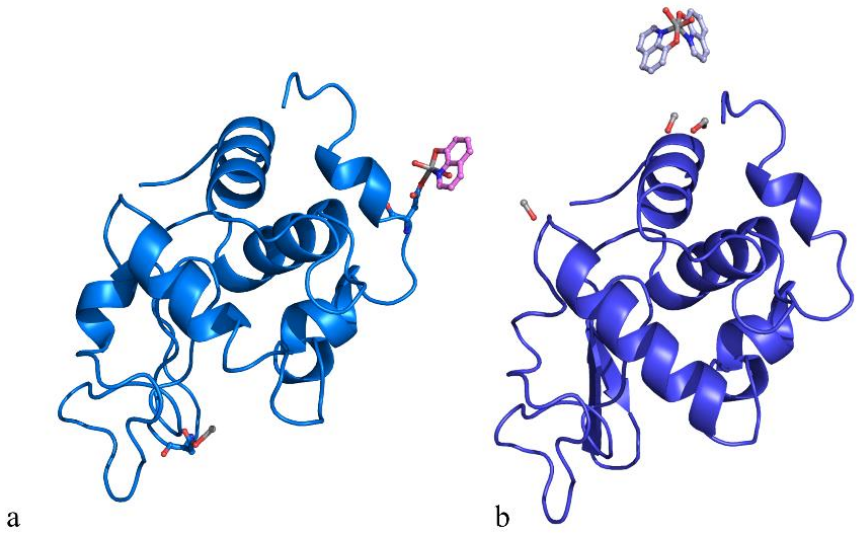

Figure 2.13 – Overall structures of the adducts formed upon reaction of: a) $[V^{IV}O(8\text{-}HQ)_2]$ with HEWL from crystals grown in 20% ethylene glycol, 0.6 M sodium nitrate, 0.1 M sodium acetate pH 4.5 (structure A, PDB code 8RTJ) and b) in 2.0 M sodium formate, 0.1 M HEPES pH 7.5 (structure B, PDB code 8RTK). V atoms are in grey.

The e.d. maps are well defined in correspondence of main chain and side chain protein atoms. Carbon alpha (Cα) atom root mean square deviation (RMSD) from the structure of metal-free protein used as starting model (PDB code 193L[194]) is 0.21 Å, suggesting that the binding of the VC does not significantly affect HEWL structure. In the structure A, a $[V^{IV}O(8\text{-}HQ)(H_2O)]^+$ fragment (occupancy = 0.60) was found close to the side chain of Asp119 (Figure 2.14a).

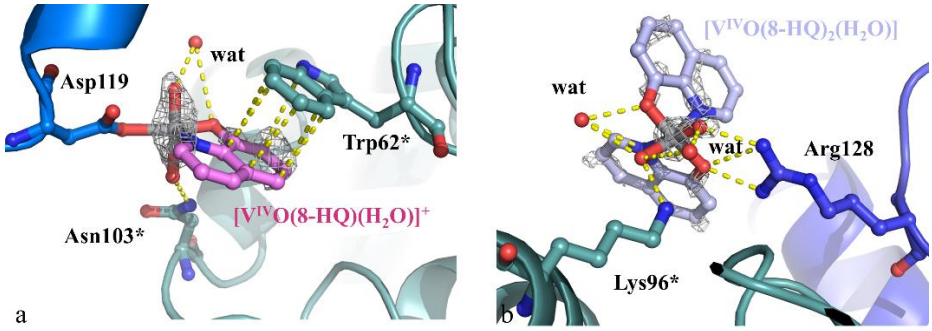

Figure 2.14 – V binding sites in the structures of the adducts formed when HEWL crystals are exposed to $[V^{IV}O(8\text{-HQ})_2]$. a) Covalent binding of $[V^{IV}O(8\text{-HQ})(H_2O)]^+$ to the side chain of Asp119 in crystals of the adduct formed in the structure A and b) non-covalent binding of $[V^{IV}O(8\text{-HQ})_2(H_2O)]$ in crystals of the adduct formed in the structure B. Omit Fo-Fc e.d. maps are reported at 2.5 σ level in grey. Atoms of symmetry related molecules are coloured in green and highlighted with *.

EPR results agree with this interpretation and a V oxidation state of +4 (see Appendix A, Interaction of $[V^{IV}O(8\text{-HQ})_2]$ with HEWL: electron paramagnetic resonance studies). In this site, the V centre shows a slightly distorted pentacoordinate geometry, retaining the oxido-O atom and one of the original 8-HQ ligands and completing its coordination sphere with the OD2 atom of Asp119 side chain and a water molecule (Figure 2.14a). In this fragment one of the two original 8-HQ ligands dissociates and is replaced by two water molecules that, in turn, can be substituted by protein atoms, in this case by carboxylate-O of Asp119 side chain. The adduct is stabilized by a hydrogen bonding network involving a water molecule and the side chain of Asn103* from a symmetry related molecule and stacks against the side chain of Trp62* from a symmetry mate.

Notably, the stabilization of a metal–protein adduct by a second protein molecule through π–π interaction is rarely reported in the literature,[195,196] and it is often overlooked in the characterization and description of the adducts formed with metal-derived fragment. This interaction was also confirmed by computational

studies (see Appendix A, Interaction of $[V^{IV}O(8\text{-}HQ)_2]$ with HEWL: computational studies).

According to Martinez and Iverson,[197] π–π interactions between aromatic rings can be classified as "face-to-face" or "edge-to-face". In the "face-to-face" arrangement, the centroid-to-centroid distance is typically < 4.0 Å and the angle between the aromatic rings is < 30°. In contrast, an "edge-to-face" interaction is characterized by a distance between the centroids < 5.5 Å and an angle between the planes in the range 60-120°. In our structure, the centroid-to-centroid distance is 3.8 Å and the angle between the planes is 6.5°, suggesting a "face-to-face" interaction.

In addition to these interactions, the oxygens of the V coordination sphere form hydrogen bonds with water molecules that in turn are hydrogen bonded to surrounding protein residues. In the $[V^{IV}O(8\text{-}HQ)(H_2O)]^+$ fragment the V=O(oxido) is 1.67 Å, consistent with the expected range value (1.57-1.65 Å);[198] the V–O(8-HQ) and V–N(8-HQ) distances are 1.76 and 1.96 Å, respectively; the V–OD2(Asp119) bond is 2.25 Å, while the V–OH_2 distance is 1.95 Å.

An additional V binding site, with occupancy 0.60 and low density in the anomalous difference e.d. map, was identified close to the side chain of Asp48 with a V–OD2 atom distance of 2.39 Å (Figure 2.15).

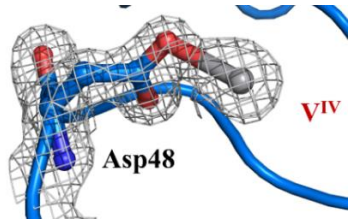

Figure 2.15 – Additional V binding site in the structure A: the V is covalently bonds to the side chain of Asp48. The V atom is in grey. 2Fo-Fc e.d. map is reported at 1.0 σ level in grey.

Soaking of HEWL crystals grown in 2.0 M sodium formate, 0.1 M HEPES pH 7.5 with an excess of $[V^{IV}O(8\text{-}HQ)_2]$ for 22 days resulted in a V-HEWL adduct crystals where the VC is not covalently bound to the protein (structure B, Figure 2.13b). In the absence of the protein, $[V^{IV}O(8\text{-}HQ)_2]$ is stable under the experimental conditions, as suggested by pH-potentiometry and EPR,[199] and confirmed by time-dependent UV-vis analysis (Figure 2.12c,d). Crystals of the adduct diffract X-rays at 1.21 Å resolution and all protein atoms are clearly defined in the electron density maps. Data collection and refinement statistics for this structure are reported in Table 2.5.

In the adduct, the non-covalent binding of $[V^{IV}O(8\text{-}HQ)_2(H_2O)]$ is observed (Figure 2.14b), in agreement with the EPR data (see Appendix A, Interaction of $[V^{IV}O(8\text{-}HQ)_2]$ with HEWL: electron paramagnetic resonance studies). The geometry of this species is *cis*-octahedral, with two phenoxido-O, one quinoline-N and one water-O donors in the equatorial plane plus another quinoline-N *trans* to the V=O bond. This indicates that, in aqueous solution, the original square pyramidal $[V^{IV}O(8\text{-}HQ)_2]$ complex converts into an hexacoordinate species (Figure 2.14b). The V=O distance is 1.67 Å, the two V–O(8-HQ) are 1.76 Å and 1.75 Å, the V–N(8-HQ) has a value of 1.96 Å, while the V–OH_2 bond length is 1.95 Å. The observed difference between V=O and V–OH_2 distances together with the EPR signal (see Appendix A, Interaction of HEWL with $[V^{IV}O(8\text{-}HQ)_2]$: electron paramagnetic resonance studies) confirm the +4 oxidation state. The HEWL–$[V^{IV}O(8\text{-}HQ)_2(H_2O)]$ adduct is stabilized by various hydrogen bonds involving water molecules, the side chains of Arg128 and of Lys96* from a symmetry related molecule (Figure 2.14b).

In the structure, additional V-containing fragments, whose formula cannot be easily determined from the e.d. maps and interpreted as two $V^{IV}O^{2+}$ and one $V^{V}O_2^{+}$ (Figure 2.16), were also found non-covalently bound to HEWL surface.

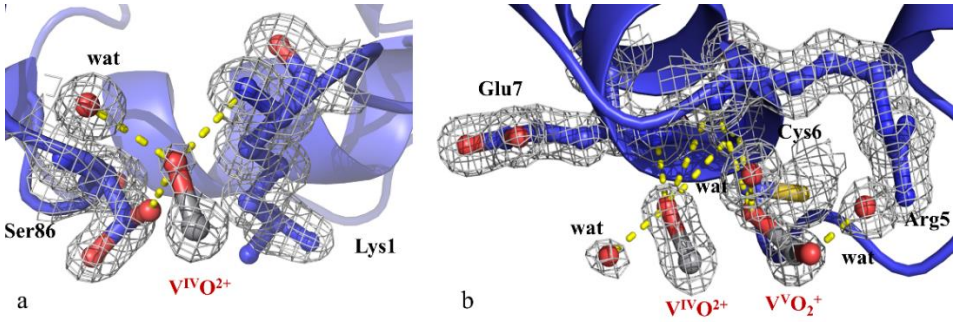

Figure 2.16 – Additional V binding sites in the structure B: a) the V-containing fragment interpreted as $V^{IV}O^{2+}$ forms hydrogen bonds with a water molecule, the side chain of Ser86 and N main chain atom of Lys1; b) non-covalent interactions of a V-containing fragment interpreted as $V^{IV}O^{2+}$ and of an alternative $V^{V}O_2^{+}$ group with protein atoms of residue Arg5, Cys6 and Glu7 and solvent molecules. V atoms are in grey. 2Fo–Fc e.d. map is reported at 1.0 σ level in grey.

One of the V-containing fragment, described as $V^{IV}O^{2+}$, forms hydrogen bonds with water molecules, the main chain N of Lys1 and the side chain OG atom of Ser86 (Figure 2.16a), while the other one interacts with a water molecule and main chain atoms of Arg5, Cys6, and Glu7. The last V-containing species is alternative to a $V^{V}O_2^{+}$ ion that interacts with water molecules and atoms from Arg5 and Cys6 residues (Figure 2.16b).

In conclusion, the stabilization of the formed adducts is due not only to hydrogen bonds but also to π–π interactions, as observed for the HEWL–$[V^{IV}O(8\text{-}HQ)(H_2O)]^{+}$ adduct involving Asp119. Notably, this stabilization also involves Trp62* from another protein molecule, a behaviour already seen in other systems, such as the HEWL–oxaliplatin adduct.[196] For $[V^{IV}O(8\text{-}HQ)(H_2O)]^{+}$, the interaction is facilitated by contacts between the aromatic rings of tryptophan and 8-hydroxyquinolinato. Although it is not yet clear whether this type of protein–protein stabilization can promote metal complex-protein recognition in solution, ESI-MS and surface plasmon resonance data on the HEWL–oxaliplatin system suggest that

it is possible.[195] These findings indicate that the contacts observed in the crystal can provide valuable insights into protein–protein interactions that may have a real biological role in solution.

2.5 Interaction of $[V^{IV}O(acac)_2]$ with hTF

Serum transferrin (hTF) is an 80 kDa human plasma single-chain glycoprotein that plays a key role in iron homeostasis by sequestrating and transporting Fe^{3+} ion throughout the body.[200–203] The hTF folding consists of two lobes, denoted as N- (residues 1-331) and C-lobe (residues 339-679), each able to bind iron.[204] As a result, four hTF forms coexist in the serum: the metal-free (apo-hTF), the diferric (holo-hTF or Fe_NFe_C-hTF), and two monoferric forms, where Fe^{3+} is bound to the C-lobe (Fe_C-hTF) or to the N-lobe only (Fe_N–hTF);[205] the percent amount is *ca*. 39%, 27%, 23% and 11%, respectively.[206] The iron binds His249, Asp63, Tyr95 and Tyr188 in the N-lobe and/or His585, Asp392, Tyr426 and Tyr517 in the C-lobe.[204] The Fe^{3+} binding to both the N- and the C-lobe is associated with a conformation variation: the iron-free lobes adopt an open conformation, while their holo forms have a closed conformation.[207,208]

It has been demonstrated that hTF is able to bind vanadate(V)[209] and $V^{IV}O^{2+}$ and that this protein is the major $V^{IV}O^{2+}$ scavenger in the serum.[210–214] The potential role of hTF as a V delivery system into cells has been extensively studied.[9,37,209–217] Previous results have suggested that V ions can occupy the Fe^{3+} binding sites of hTF, even in the presence of high HSA concentrations, although hTF appears to inhibit rather than enhance the biological activity of VCs.[218]

Structural models, based on the X-ray structure of the iron-bound N-lobe of hTF, indicate that $V^{IV}O^{2+}$ may coordinate with Tyr188, Asp63, His249, and a carbonate ion that facilitates iron binding, with the V centre positioned near Tyr95.[211] Similar coordination has been proposed for V^{3+} and $V^{V}O_2^{+}$, while V^{V} might bind

hTF without the need for a synergistic anion. Despite these insights, direct structural evidence of V binding sites on hTF is still lacking.

To address this gap and characterize the binding of $[V^{IV}O(acac)_2]$ (Figure 2.1d) to hTF at the structural level, the structures of the adducts that this vanadium compound form with the monoferric form of hTF with the iron bound to the C-lobe only (Fe_C-hTF) were solved.

2.5.1 Crystallographic studies

X-ray diffraction data were collected on many Fe_C-hTF crystals exposed to 5 mM $[V^{IV}O(acac)_2]$ dissolved in DMSO (final DMSO concentration <10%) in collaboration with Dr. Andrea Pica, ALPX, Grenoble, France. Fe_C-hTF crystals were grown in 15% (w/v) PEG 3350, 16% (v/v) glycerol, 8 mM disodium malonate, and 150 mM Na-PIPES pH 6.5, starting from an apo protein sample dissolved in 10 mM Na-HEPES pH 7.5 and 20mM sodium bicarbonate. The apo protein was then incubated with ammonium iron sulphate to obtain the Fe_C-hTF form. Since the results obtained using the other data collections are essentially the same as those presented here, only data collected using the crystal that diffracted X-rays at the highest resolution are reported (Table 2.6). Diffraction data were also collected on crystals of V-free Fe_C-hTF and V-free protein treated with DMSO (Table 2.6).

Crystals of the adduct are isomorphous to those of the V-free protein, with and without DMSO, showing only minor differences in their unit cell parameters.

Table 2.6 – Data collection and refinement statistics.

Data collection			
	$[V^{V}_2O_6]_N$Fe$_C$-hTF	Fe$_C$-hTF	Fe$_C$-hTF with DMSO
PDB code	9RTB	9RTF	9RTH
Crystallization condition	15% (w/v) PEG 3350, 16% (v/v) glycerol, 8 mM disodium malonate, 150 mM Na-PIPES pH 6.5	15% (w/v) PEG 3350, 16% (v/v) glycerol, 8 mM disodium malonate, 150 mM Na-PIPES pH 6.5	15% (w/v) PEG 3350, 16% (v/v) glycerol, 8 mM disodium malonate, 150 mM Na-PIPES pH 6.5
Soaked compound	5mM $[V^{IV}O(acac)_2]$ dissolved in DMSO (final DMSO concentration <10%)	-	10% DMSO
Soaking time	5h	-	72h
Space group	$C222_1$	$C222_1$	$C222_1$
a (Å)	136.13	138.15	137.10
b (Å)	157.70	158.03	156.78
c (Å)	107.22	107.62	107.11
Resolution range (Å)	78.85-1.93 (2.17-1.93)	104.01-2.16 (2.35-2.16)	74.32-2.52 (2.77-2.52)
Observations	585795 (26804)	381020 (14028)	302818 (17413)
Unique reflections	47778 (2389)	47443 (2372)	26234 (1312)
Completeness (%)	95.0 (79.6)	92.8 (53.0)	90.4 (54.9)
Redundancy	12.3 (11.2)	8.0 (5.9)	11.5 (13.3)
Rmerge (%)	0.147 (1.499)	0.272 (3.435)	0.273 (2.141)
Average I/σ(I)	11.2 (2.0)	6.2 (1.6)	9.1 (1.4)
$CC_{1/2}$	0.998 (0.788)	0.985 (0.263)	0.992 (0.596)
Anom. completeness (%)	94.9 (79.3)	92.4 (50.6)	90.0 (54.1)
Anom. Multiplicity	6.4 (5.8)	4.2 (3.2)	6.1 (7.0)
Refinement			
Resolution (Å)	103.15-1.93	104.01-2.16	103.20-2.52
N° reflections	45441	45069	24911
N° reflections in working set	138	99	30
R-factor/Rfree	0.186/0.235	0.185/0.232	0.177/0.260

N° non-H atoms in the refinement	5785	5636	5409
B-factor overall (Å^2)	37.38	38.43	40.24
Estimated occupancy of $[V^V_2O_6]^{2-}$	0.70	-	-
B-factor of $[V^V_2O_6]^{2-}$ (Å^2)	36±12	-	-
Ramachandran values (%)			
Most favoured/Additional allowed	91.6/6.1	90.3/6.5	88.5/7.4
Outliers	2.3	3.2	4.1
RMSD from ideality			
RMSD bonds (Å)	0.008	0.010	0.009
RMSD angles (°)	1.286	1.630	1.645

The structures obtained from these crystals were refined at a resolution higher than those of all the known models of Fe_C-hTF reported in the PDB. The overall conformation of Fe_C-hTF in the adduct is not significantly affected by the V binding: Cα RMSD between the three structures here solved is within the range 0.27-0.33 Å.

In the structure of the adduct, refined at 1.9 Å resolution (Figure 2.17), binding of a $[V^{V}_2O_6]^{2-}$ species was clearly observed.

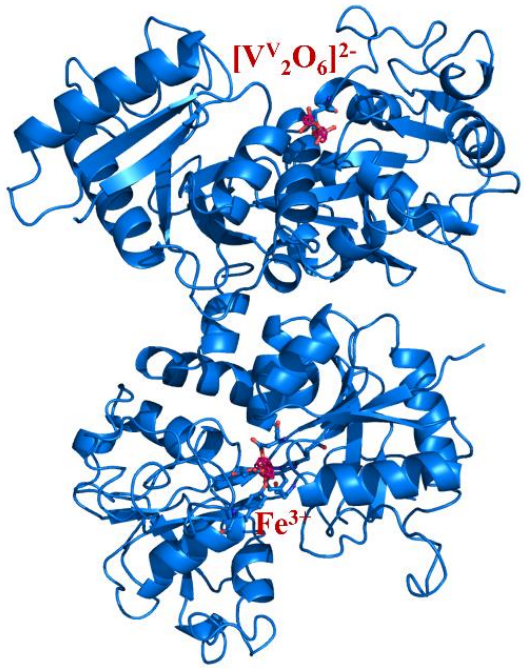

Figure 2.17 – Overall structure of the adduct formed by $[V^{IV}O(acac)_2]$ with Fe_C-hTF. Anomalous difference e.d. map showing the position of two V atoms in the N-lobe and of Fe^{3+} in the C-lobe are depicted in pink at 3.0 σ value.

This species can be described as a divanadate(V) anion, $[V^{V}_2O_7]^{4-}$, in which one oxygen atom is replaced by the phenolate oxygen of Tyr188 (Figure 2.18a).

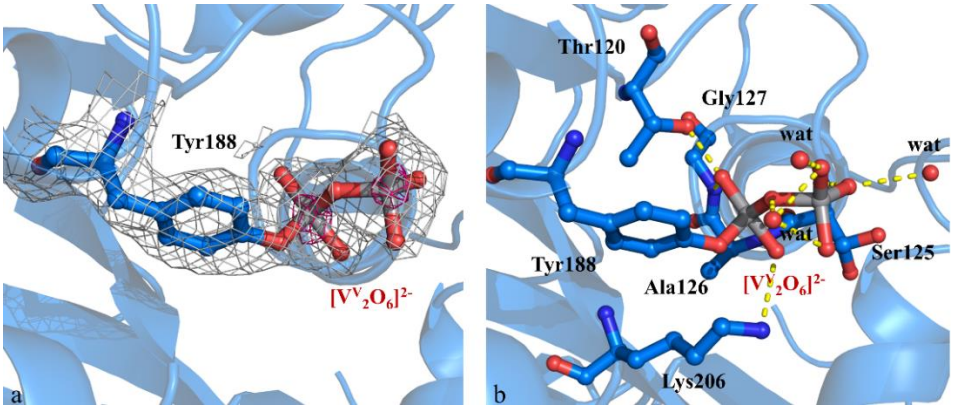

Figure 2.18 – a) Details of the V binding site in the structure of the adduct formed when $[V^{IV}O(acac)_2]$ reacts with Fe_C-hTF at solid state. The structure shows the binding of $[V^{V}_{2}O_6]^{2-}$ to the side chain of Tyr188. 2Fo-Fc e.d. maps are reported at 1.0 σ level in grey. Anomalous difference e.d. map showing the position of the two V atoms in the N-lobe is depicted in pink at 3.0 σ value. b) Hydrogen bonds formed by $[V^{V}_{2}O_6]^{2-}$ with OG1 atom of Thr120, the N atom of Ser125 (whose side chain adopts two different conformations), the N atom of Ala126, the N atom of Gly127, NZ atom of Lys206 and water molecules.

Notably, the formation of a POV from $[V^{IV}O(acac)_2]$ has previously been observed in crystal structures of its adducts with HEWL.[219–221]

As expected,[222] Fe^{3+} is found close to the side chains of Asp392, Tyr426, Tyr517, and His585 in the C-lobe and is also coordinated by a malonate ion, which acts as a synergistic anion (Figure 2.19).

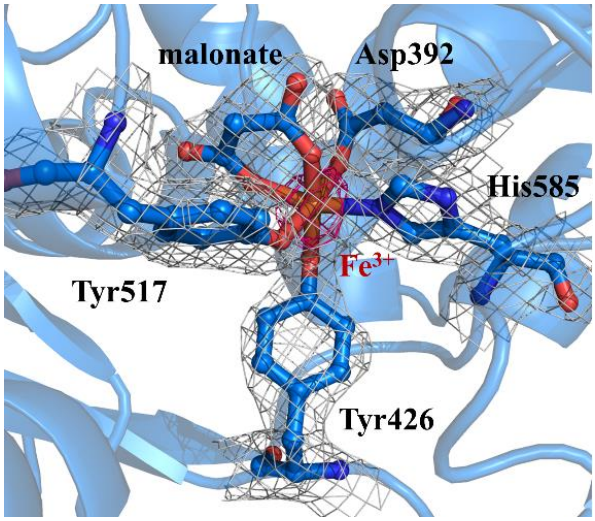

Figure 2.19 – Structural details of the Fe^{3+} binding site in the solid-state structure of the adduct formed upon reaction of $[V^{IV}O(acac)_2]$ with Fe_C-hTF, where transferrin is coordinated to the VC. The Fe^{3+} ion is in the C-lobe, near the side chains of Asp392, Tyr426, Tyr517, and His585, and is also coordinated by a malonate ion. The 2Fo-Fc e.d. map is shown in grey at the 1.0 σ level, while the anomalous difference e.d. map highlighting the Fe^{3+} position is shown in pink at 3.0 σ.

Unrestrained distance between the O donor atom of Tyr188 and V centre is 1.75 Å, close to the expected value. V^V-O distances are in the range 1.7-2.0 Å.

The formation of $[V^V_2O_6]^{2-}$ can be explained by the dissociation of $[V^{IV}O(acac)_2]$ to obtain the $V^{IV}O^{2+}$ ion, which is then oxidized to $[H_2V^VO_4]^-$ at pH 7.5. Subsequently, $[H_2V^VO_4]^-$ dimerizes to form $[V^V_2O_7]^{4-}$ which reacts with hTF. A model calculation, based on the thermodynamic stability constants of vanadium(V) species in aqueous solution,[223] allows the determination of the chemical form of V^V at pH 7.5 and with concentration between 0.01 and 100 mM (Figure 2.20).

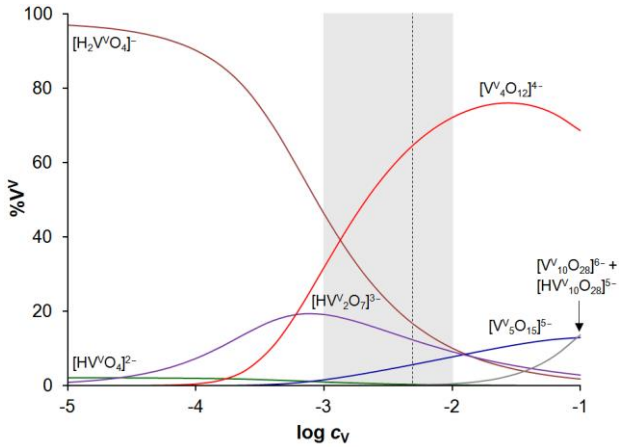

Figure 2.20 – Speciation of vanadium(V) in aqueous solution at pH 6.5 from 10 μM to 100 mM concentration (C_V). For the x axis a logarithmic scale was used. The concentration 5 mM is indicated by the dotted line, while the range 1-10 mM by the gray background. The thermodynamic stability constants of the inorganic V^V anions were taken from ref [223]. Data obtained in collaboration with Prof. Eugenio Garribba from University of Sassari.

Notably, at the V concentration used in the crystallographic experiments (5 mM) and within the range of 1-10 mM, divanadate(V) anions with various protonation degrees ($[H_2V^V_2O_7]^{2-}$ and $[HV^V_2O_7]^{3-}$) are present in solution at pH 7.5. However, these are minor species compared to $[V^V_4O_{12}]^{4-}$ and $[H_2V^VO_4]^-$. This means that Fe_C-hTF stabilizes divanadate(V) through covalent bond and a network of secondary interactions, as revealed by X-ray crystallography. Indeed, $[V^V_2O_6]^{2-}$ is held in position by hydrogen bonds formed with the OG1 atom of Thr120, the N atom of Ser125, whose side chain adopts two different conformations, the N atom of Ala126, the N atom of Gly127, the NZ atom of Lys206 and several water molecules (Figure 2.18b). The Fourier difference e.d. maps close to the Tyr188 side chain in the crystals of the V-free protein, with and without DMSO, show peaks attributable to water molecules (Figure 2.21), supporting the assignment of the e.d. map in the adduct to $[V^V_2O_6]^{2-}$.

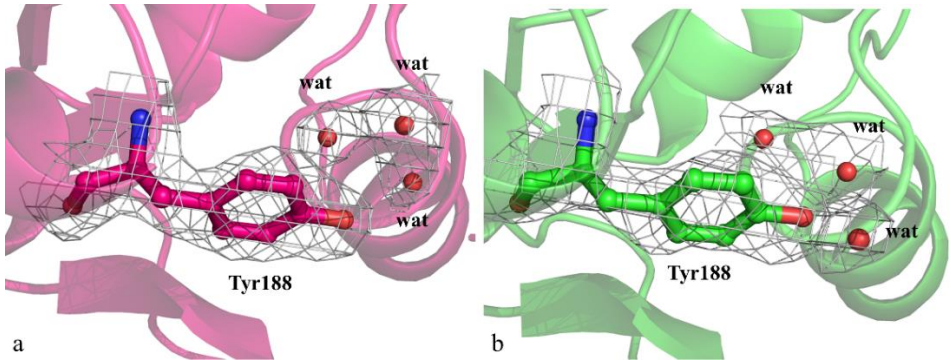

Figure 2.21 – 2Fo-Fc e.d. map reported at 1.0 σ level in grey close to the Tyr188 side chain of the a) V-free Fe_C-hTF (*i.e.* the negative control without DMSO) and of the b) V-free Fe_C-hTF treated with DMSO, used as a negative control for the hTF structure treated with $[V^{IV}O(acac)_2]$.

Remarkably, the atoms of $[V^V_2O_6]^{2-}$ are not in contact with the side chains of Asp63 and His249, as previously suggested for the $V^{IV}O^{2+}$ and $V^VO_2^+$ ions bound to the side chain of Tyr188, based on the structure of the closed form of the N-lobe only.[211] This observation indicates that, at least at the solid state, the binding of this V-containing fragment to Tyr188 in the iron binding site does not induce the conformational variation of the N-lobe that occurs upon Fe^{3+} binding. Such conformational changes are required to bring Tyr188, Asp63 and His249 in proximity, allowing their simultaneous coordination to a metal ion. Further support comes from a detailed comparison between the conformations of the N-lobes in the $[V^V_2O_6]_NFe_C$-hTF adduct and in the V-free Fe_C-hTF structures here solved, with and without DMSO. The angles required to superimpose the N2 region of the N-lobe after the superimposition of the N1 region of the same lobe fall within the range 0.5-0.7°, indicating that the overall conformation of the N-lobe remains largely unchanged upon binding of the V-containing fragment. Previous studies suggested that V^{3+} binding to the iron site induces the same conformational

changes as Fe^{3+} binding.[37] In contrast, $V^{V}_{N}V^{V}_{C}$-hTF adduct adopts the open form, which has low affinity for TFR (transferrin receptor).[177,224]

Since the structure of $[V^{V}_{2}O_{6}]_{N}Fe_{C}$-hTF closely resembles that of Fe_{C}-hTF, it is expected that, in the presence of $[V^{IV}O(acac)_{2}]$, this hTF form could be still able to bind the TF receptor. To verify this, Fe_{C}-hTF has been treated with $[V^{IV}O(acac)_{2}]$ in solution (hereafter denoted as V/Fe_{C}-hTF) and the binding to the TFR ectodomain has been evaluated using polyacrylamide non-denaturing gel electrophoresis in comparison to Fe_{C}-hTF alone (Figure 2.22), following the approach described in a previous work.[225] This experiment was performed in collaboration with Professor Delia Picone's research group from University of Naples Federico II.

On the gel, the monoferric hTF forms, untreated (lane 1) and treated with $[V^{IV}O(acac)_{2}]$ (lane 2), migrate differently from TFR (lane 3), due to their different charge/size ratio. The binding of the two Fe_{C}-hTF forms to TFR can be observed incubating each protein with the receptor (samples in lanes 4 and 5, respectively) and comparing the electrophoretic mobility with Fe_{C}-hTF (lane 4), V/Fe_{C}-hTF (lane 5) and TFR alone (lane 3). As seen in Figure 2.22, the bands of the monoferric forms in lanes 1 and 2 disappear when incubated with TRF (lanes 4 and 5). Currently, two bands with a slightly different electrophoretic mobility from that observed for TFR alone (lane 3) are observed in lanes 4 and 5, indicating that both Fe_{C}-hTF and V/Fe_{C}-hTF form a complex with TFR. This suggests that V/Fe_{C}-hTF is still able to bind TFR.

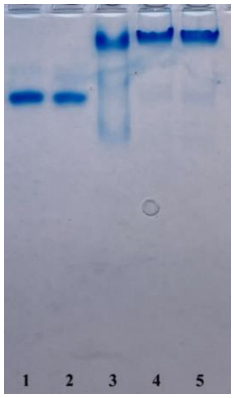

Figure 2.22 – Non-denaturing gel electrophoresis of: Fe_C-hTF (lane 1), V/Fe_C-hTF, obtained incubating Fe_C-hTF for 1 day with $[V^{IV}O(acac)_2]$ (lane 2), TFR (lane 3), TFR incubated with Fe_C-hTF for 24 h in a 1:1 molar ratio (lane 4), and TFR incubated with V/Fe_C-hTF for 24 h in a 1:1 molar ratio (lane 5). This experiment was performed in collaboration with Professor Delia Picone's research group from University of Naples Federico II.

In conclusion, here the first crystal structure of human serum transferrin with a VC is reported. X-ray crystallography data show that $[V^V_2O_6]^{2-}$ binds Tyr188 of the N-lobe in the monoferric Fe_C-hTF, without altering the protein conformation, confirming previous suggestions of Tyr188 involvement in $V^{IV}O^{2+}$ recognition.[211,213] The results indicate that, at least *in vitro*, Fe_C-hTF stabilizes low-nuclearity vanadate species such as $[V^V_2O_7]^{4-}$, in contrast with HEWL, which promotes the formation of POV including $[V_4O_{12}]^{4-}$, $[V_{15}O_{33}(H_2O)]^{+}$, $[V_{15}O_{36}(H_2O)]^{5-}$, $[V_{20}O_{54}(NO_3)]^{n-}$, $[V_{20}O_{51}(H_2O)]^{n-}$.[219–221] These results highlight, for the first time at the structural level, how hTF can stabilize divanadate(V) species, providing a key insight into V/protein interactions relevant for the biological activity of V-based compounds.

2.6 Comparison of the behaviour of $[V^{IV}O(empp)_2]$, $[V^{IV}O(dhp)_2]$, $[V^{IV}O(8\text{-}HQ)_2]$, $[V^{IV}O(acac)_2]$ and other $[V^{IV}OL_2]$ potential drugs

Structural analysis of the adducts formed by $[V^{IV}OL_2]$ compounds and HEWL deposited into the Protein Data Bank[34,35,219,220,226,227] reveals variability in the V-containing fragments, their localization, occupancy and microenvironment. The adducts were obtained by the soaking method under different experimental conditions, with a pH value ranging from 4.0 to 7.5. V centres and their ligands have occupancy in the range 0.25-1.00.[34,35,219,220,226,227]

Our recent studies have shown that small changes in experimental conditions, such as pH, ionic strength, or buffer composition, can alter the nature of the adducts formed between the same VC and proteins.[35,227,219,220]

VCs can generate various ions, like $[V^{IV}O(H_2O)_3]^{2+}$, $[V^{IV}O(H_2O)_4]^{2+}$, $[V^{IV}O]^{2+}$, $[V^{V}O_2]^{+}$, $[V^{IV}OL(H_2O)]^{+}$, $[V^{IV}OL(H_2O)_2]^{+}$.[35] Alternatively, they can remain as $[V^{IV}OL_2]$ or can form dinuclear ($[(V^{V}O(dhp)_2)_2O]$ and $[(V^{V}O(dhp)_2)(V^{V}O(dhp)(H_2O)_2)O]^{+}$) or trinuclear ($[V^{V}_3O_6(empp)_3(H_2O)]$) species upon oxidation of V from +4 to +5 or even POVs ($[V^{V}_4O_{12}]^{4-}$, $[V_{20}O_{54}(NO_3)]^{n-}$, $[V^{V}_7V^{IV}_8O_{36}(OH_2)]^{5-}$, $[V^{V}_7V^{IV}_8O_{33}(OH_2)]^{+}$, $[V_{20}O_{51}(OH_2)]^{n-}$, $[V^{V}_7V^{IV}_8O_{36}(Cl)]^{6-}$).[219–221,228] Unexpected reaction products can also form: for example, upon rearrangement and ring cleavage of the maltol ligand, BMOV interacts with HEWL creating a cross-linked dimer which involves Lys1 side chain and coordinates to Asp87 of a second protein molecule.[227] This structural rearrangement, resembling a post-translational modification, highlights the complex, and sometimes unpredictable, reactivity of VCs with proteins.[227]

The binding of VCs to proteins can occur both covalently or non-covalently.[35,219–221,227] Indeed, the V-containing ions coordinated to HEWL side chains preferentially interact with negatively charged residues (Asp18, Glu35, Asp48,

Asp52, Asp87, Asp101, Asp119 and the C-terminal carboxylate), while the neutral compound $[V^{IV}OL_2]$ can bind both Asp (Asp52) and Asn (Asn65) side chains. His15, which has been found to bind different metals,[186,229–231] is not involved in VC recognition.

Non-covalent interactions were observed for neutral species $[V^{IV}OL_2(H_2O)]$[35] and for both positively ($[V^{IV}O]^{2+}$, $[V^{V}O_2]^{+}$, $[V^{IV}OL(H_2O)_2]^{+}$, $[V^{IV}OL(H_2O)_3]^{+}$)[35] and negatively charged species ($[V_4O_{12}]^{4-}$ and $[V_{15}O_{36}(OH_2)]^{5-}$ are observed bound to HEWL, $[V_{15}O_{36}(Cl)]^{6-}$ is observed bound to human H-chain Ferritin).[219,220,228] Non-covalent interactions are guided by hydrogen bonds formed by metal ligands with the main chain and side chain atoms of Lys1, Val2, Arg5, Cys6, Glu7, Tyr20, Arg21, Lys33, Ser86, Lys96, Arg73, Arg74, Gln121, Arg125, Arg128. In both covalent and non-covalent binding, the V-compound/protein recognition can be helped by symmetry-related molecules.[219,220,227] Cross-linked protein dimers bridged by V-containing fragments were observed in multiple crystal structures.[35,219,220,227]

In conclusion, $[V^{IV}OL_2]$ compounds react differently with HEWL even under similar conditions, producing a variety of V-containing fragments with different binding modes and occupancies. Reactivity depends on the nature and stability of the ligands: strongly coordinating ligands favour non-covalent interactions, whereas more labile ligands allow covalent binding. Stabilizing interactions, including hydrogen bonding, hydrophobic, and π–π interactions, play a key role in V recognition and may influence the transport of V-based drugs in biological systems. Notably, the comparison with the studies on Fe_C-hTF indicates that the protein environment can strongly affect V speciation. While HEWL and human H-chain ferritin promote formation of higher-nuclearity POVs, Fe_C-hTF stabilizes low-nuclearity species, such as $[V^{V}_2O_6]^{2-}$, highlighting the importance of studying multiple protein targets to understand the potential biological activity of VCs.

2.7 Materials and methods

Crystallization, adduct formation, data collection, structure resolution and refinement

HEWL (concentration = 13 mg/mL, 0.9 mM) was crystallized using the hanging drop vapour diffusion method in:

- 1.1 M sodium chloride, 0.1 M sodium acetate pH 4.0
- 20% ethylene glycol, 0.6 M sodium nitrate, 0.1 M sodium acetate pH 4.5
- 0.8 M succinic acid pH 7.0
- 2.0 M sodium formate, 0.1 M HEPES pH 7.5

Crystals grew within 1-2 days at 20°C (Figure 2.23).

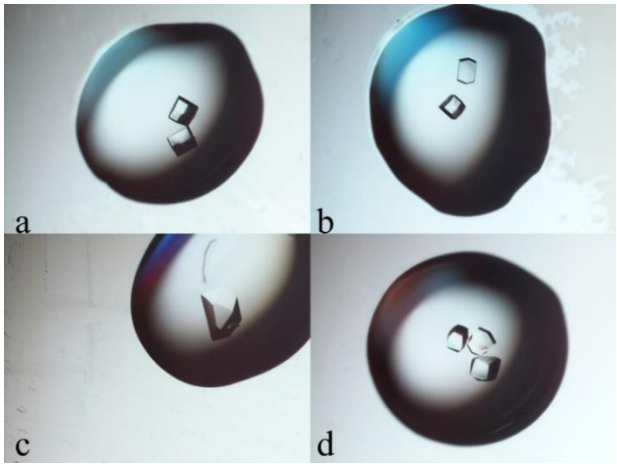

Figure 2.23 – HEWL crystals grown in a) 1.1 M sodium chloride, 0.1 M sodium acetate pH 4.0; b) 20% ethylene glycol, 0.6 M sodium nitrate, 0.1 M sodium acetate pH 4.5; c) 0.8 M succinic acid pH 7.0; d) 2.0 M sodium formate, 0.1 M HEPES pH 7.5.

Pre-formed HEWL crystals were then exposed to stabilizing solutions containing the mother liquor saturated with $[V^{IV}O(empp)_2]$, $[V^{IV}O(dhp)_2]$ and $[V^{IV}O(8\text{-}HQ)_2]$ for a soaking time in a range of 7-50 days. X-ray diffraction data

collections were carried out on several crystals at 100 K on Beamline XRD2 at Elettra synchrotron, Trieste, Italy. Crystals were cryoprotected using a solution of reservoir containing 25% glycerol. Data processing and scaling were performed using Global Phasing autoPROC pipeline.[232] HEWL crystals belong to the space group $P4_32_12$ and present a single protein molecule in the asymmetric unit. The structures were solved by Molecular Replacement using Phaser program from CCP4 suite[233] and the structure deposited in the PDB 193L[194] as template. Refmac5 was used for refinement.[234] Model building was carried out using Coot.[235] In all the structures, V atom position was validated using anomalous difference e.d. maps. The final models show R-factor and Rfree values in the range of 0.116-0.174 and 0.144-0.197, respectively. Ligand positions were restrained to guide geometry optimization. Figures were generated using PyMol (www.pymol.org). The structure validation of the final models was performed using the PDB validation server.[236] Coordinates and structure factors of the structures of HEWL with $[V^{IV}O(empp)_2]$ and $[V^{IV}O(8\text{-}HQ)_2]$ were deposited in the PDB under the accession codes 8OM8, 8OMS, 8OMT, 8RTJ and 8RTK.

Fe_C-hTF crystals were grown by sitting drop vapour diffusion method using 15% (w/v) PEG 3350, 16% (v/v) glycerol, 8 mM disodium malonate, and 150 mM Na-PIPES pH 6.5, as a reservoir, and the apo-hTF sample (from Sigma-Aldrich, ref. T4382, concentration = 30 mg/mL, 0.4 mM) dissolved in 10 mM Na-HEPES pH 7.5, 20 mM sodium bicarbonate and then incubated with ammonium iron sulphate to obtain the Fe_C-hTF form. Data collections were performed on several crystals of Fe_C-hTF treated with 5 mM $[V^{IV}O(acac)_2]$ dissolved in DMSO (final DMSO concentration < 10%) at SOLEIL Synchrotron (beamtime at Proxima1 beamline) and bioMAX beamline at MAXIV laboratory. Phases were obtained by Molecular Replacement using Phaser from CCP4 suite,[233] and the structure of Fe_C-hTF deposited in the PDB with code 4X1B,[222] without ligands and water molecules, as a template. The structures were isotropically refined using

Refmac5.[234] Fourier difference (2Fo-Fc and Fo-Fc) and anomalous difference electron density maps were used to evaluate the presence of vanadium atoms. Model building and inspection of the electron density maps were carried out using Coot.[235] Coordinates and structure factors of the structures were deposited in the PDB under the accession codes 9RTB, 9RTF and 9RTH.

UV-visible absorption spectroscopy

The stability of $[V^{IV}O(8\text{-}HQ)_2]$ in 20% ethylene glycol, 0.6 M sodium nitrate, 0.1 M sodium acetate pH 4.5 and in 2.0 M sodium formate, 0.1 M HEPES pH 7.5 was studied by UV-vis absorption spectroscopy, using a Jasco V750 spectrophotometer. Spectra of $[V^{IV}O(8\text{-}HQ)_2]$ (concentration = 50 μM) were recorded in the absence and in the presence of HEWL (1:3 protein to metal molar ratio) at room temperature as a function of time. The following parameters were used: data pitch 1.0 nm, bandwidth 2.0 nm, scan speed 400 nm min^{-1}, and quartz cuvette with 1.0 cm path length.

Non denaturing gel electrophoresis experiments

The ability of Fe_C-hTF to recognize and bind TFR, even after treatment with $[V^{IV}O(acac)_2]$, was evaluated by non-denaturing (native) polyacrylamide gel electrophoresis (PAGE). Fe_C-hTF at a concentration of 100 μM was incubated with $[V^{IV}O(acac)_2]$ at 20°C in a 1:1 protein:metallodrug molar ratio. After the incubation with the metallodrug for 24 h, V/Fe_c-hTF and Fe_c-hTF were incubated with TFR in a 1:1 protein:receptor molar ratio at 20°C for 24 h. Then, 9 μL of each sample was loaded on a 6% polyacrylamide gel for the separation, using 25 mM TRIS/glycine pH 8.4 as running buffer. The gel was run for 3.5 h at a constant voltage of 100 V, at 4°C and stained using Coomassie Brilliant Blue G-250. This procedure has been already used in the past to evaluate the binding of cisplatin/hTF adduct with TFR.[225]

Appendix A

Interaction of $[V^{IV}O(empp)_2]$ with HEWL: mass spectrometry studies

ESI-MS spectra in positive-ion mode were measured from freshly prepared solutions containing: (i) HEWL at pH 4.0 and 7.0; (ii) a 2:1 $[V^{IV}O(empp)_2]$/HEWL mixture (50 μM V concentration) at both pH values. Spectra are reported in Figure A.1.

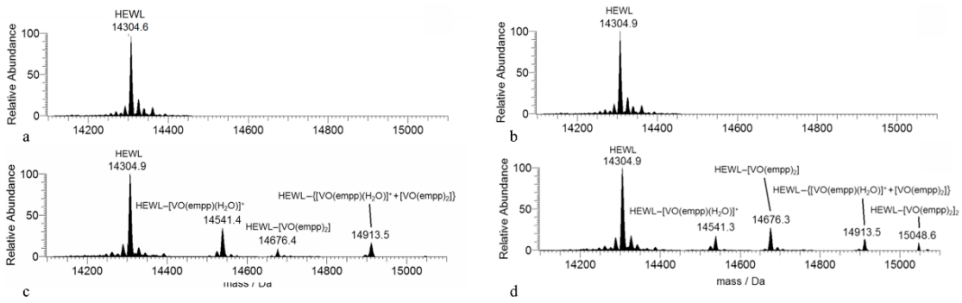

Figure A.1 – Deconvoluted positive-ion mode spectra recorded on the system containing $[V^{IV}O(empp)_2]$ and HEWL. a) Free protein at pH 4.0; b) free protein at pH 7.0; c) $[V^{IV}O(empp)_2]$/HEWL 2/1 at pH 4.0 with a V concentration of 50 μM; d) $[V^{IV}O(empp)_2]$/HEWL 2/1 at pH 7.0 with a V concentration of 50 μM. Data obtained in collaboration with Prof. Eugenio Garribba from University of Sassari.

In the metal-free HEWL spectra, the major peak at 14304.6 Da at pH 4.0 (14304.9 Da at pH 7.0) corresponds to the native protein, accompanied by signals arising from adducts with Na^+ ions and water molecules (Figure A.1a,b). In the presence of $[V^{IV}O(empp)_2]$, the ESI-MS profiles change when pH changes. At pH 4.0 (Figure A.1c), three main adducts are detected: (i) HEWL−$[V^{IV}O(empp)(H_2O)]^+$ at 14541.4 Da; (ii) HEWL−$[V^{IV}O(empp)_2]$ at 14676.4 Da; (iii) a mixed adduct HEWL−{$[V^{IV}O(empp)(H_2O)]^+$ + $[V^{IV}O(empp)_2]$} at 14915.3 Da.

At pH 7.0 (Figure A.1d), an additional species appears at 15048.6 Da, assigned to HEWL−$[V^{IV}O(empp)_2]_2$, while the intensity of the HEWL−$[V^{IV}O(empp)_2]$ decreases.

These data allow several conclusions to be depicted: (i) pH raise favours the protein binding of $[V^{IV}O(empp)_2]$ over $[V^{IV}O(empp)]^+$; (ii) the $[V^{IV}O(empp)]^+$ fragment retains a coordinated water molecule; (iii) both V-containing fragments with one or two empp(−) ligands can bind simultaneously to the protein; (iv) the adduct with $[V^{IV}O(empp)]^+$ is still observed at pH 7.0; (v) all detected adducts involve V^{IV} species which would generate $V^{IV}O^{2+}$ fragments readily distinguishable by mass; (vi) no signals corresponding to dinuclear or trinuclear V species were detected under these conditions.

Interaction of $[V^{IV}O(empp)_2]$ with HEWL: electron paramagnetic resonance studies

High-field region of the anisotropic EPR spectra (Figure A.2) were recorded at 120 K and pH 7.0.

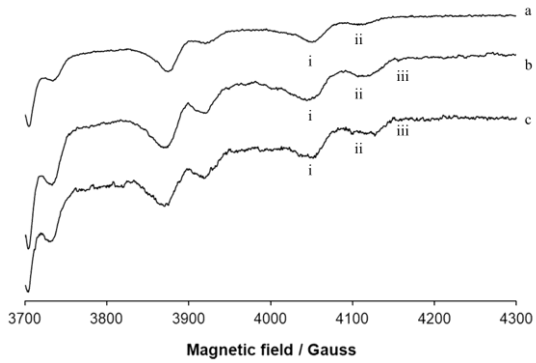

Figure A.2 – High-field region of the anisotropic X-band EPR spectra recorded at 120 K and pH 7.0 in an aqueous solution containing: a) $[V^{IV}O(empp)_2]$; b) $[V^{IV}O(empp)_2]$/HEWL 2/1; c) $[V^{IV}O(empp)_2]$/HEWL 1/2. V concentration is 1.0 mM. The M_I = 7/2 resonances of $[V^{IV}O(empp)_2]$, *cis*-$[V^{IV}O(empp)_2]$, and of the adduct

HEWL−$[V^{IV}O(empp)]^+$ with a covalent binding are indicated with i, ii, and iii, respectively. The interaction of $[V^{IV}O(empp)_2]$ (i) and *cis*-$[V^{IV}O(empp)_2]$ (ii) with HEWL could be non-covalent since this does not change the spin Hamiltonian parameters, while that of $[V^{IV}O(empp)]^+$ could be covalent. Data obtained in collaboration with Prof. Eugenio Garribba from University of Sassari.

The EPR spectrum shown in trace (a) of Figure A.2 was recorded for $[V^{IV}O(empp)_2]$ dissolved in water using HEPES as buffer at pH 7.0. Two species were identified in solution: $[V^{IV}O(empp)_2]$ (i) and *cis*-$[V^{IV}O(empp)_2(H_2O)]$ (ii), which coexist in equilibrium. The corresponding spin Hamiltonian parameters, g factor and hyperfine coupling constant on z axis (g_z and A_z), are consistent with literature data:[188] for species (i), $g_z = 1.953$ and $A_z = 158 \times 10^{-4}$ cm^{-1}; for species (ii), $g_z = 1.943$ and $A_z = 168 \times 10^{-4}$ cm^{-1}.

In the presence of HEWL (traces b and c, Figure A.2), the same signals were detected, indicating that $[V^{IV}O(empp)_2]$ and *cis*-$[V^{IV}O(empp)_2(H_2O)]$ interact non-covalently with the protein. This is supported by the fact that the EPR parameters remain unchanged, suggesting the absence of direct coordination to protein donor atoms. Notably, no additional signals were observed in the 3960–4100 G region suggesting that the covalent binding does not occur. This contrasts with previous observations for *cis*-$[V^{IV}O(malt)_2]$, which forms a V^{IV}–O(Asn) bond with HEWL as confirmed by X-ray crystallography.[35] The larger steric hindrance and/or lower stabilization through secondary interactions such as hydrogen bonds or van der Waals contacts in the case of $[V^{IV}O(empp)_2]$ may explain these results.

However, a resonance at 4130 G (species iii in Figure A.2), with $g_z \approx 1.942$ and $A_z \approx 173 \times 10^{-4}$ cm^{-1}, suggests the formation of a third species, likely $[V^{IV}O(empp)(H_2O)]^+$, coordinated to HEWL. The simultaneous presence of both $[V^{IV}O(empp)_2]$ and $[V^{IV}O(empp)(H_2O)]^+$ cannot be excluded.

Overall, the EPR data are consistent with the speciation observed by ESI-MS (Figure A.1), supporting the coexistence of multiple non-covalently interacting V^{IV} fragments in solution.

Interaction of $[V^{IV}O(8\text{-}HQ)_2]$ with HEWL: mass spectrometry studies

The deconvoluted ESI-MS(+) spectrum recorded at pH 4.5 on a solution containing $[V^{IV}O(8\text{-}HQ)_2]$ and HEWL at 2:1 molar ratio and V concentration of 100 μM is shown in Figure A.3a.

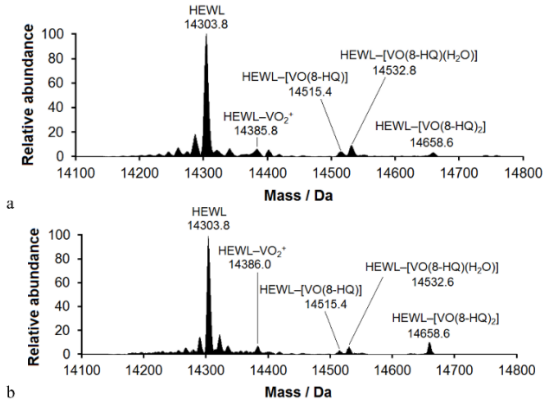

Figure A.3 – Deconvoluted ESI-MS(+) spectrum recorded on the system containing $[V^{IV}O(8\text{-}HQ)_2]$ and HEWL with 2:1 molar ratio at a) pH 4.5, b) pH 7.5 and a V concentration of 100 μM. Data obtained in collaboration with Prof. Eugenio Garribba from University of Sassari.

The major signal at 14303.8 Da corresponds to the free protein and is surrounded by the peaks of the adducts with Na^+ ion. Beside this, the signals of other species were observed: HEWL–$V^{V}O_2$ at 14385.8 Da, HEWL–$[V^{IV}O(8\text{-}HQ)]$ at 14515.4, HEWL–$[V^{IV}O(8\text{-}HQ)(H_2O)]$ at 14532.8 and HEWL–$[V^{IV}O(8\text{-}HQ)_2]$ at 14658.6 Da.

Overall, the results indicate that, under these experimental conditions, $[V^{IV}O(8\text{-HQ})]$/$[V^{IV}O(8\text{-HQ})(H_2O)]$ and $[V^{IV}O(8\text{-HQ})_2]$, with V in the +4 oxidation state, are formed. Based on these data, it is not possible to discriminate if the binding is covalent or non-covalent, because one or more aqua ligands could be lost from $[V^{IV}O(8\text{-HQ})(H_2O)_2]^+$ and $[V^{IV}O(8\text{-HQ})_2(H_2O)]$ during the mass spectra recording. Furthermore, the detection of HEWL–$V^{V}O_2$ adducts suggests that at least a part of the sample loses both anionic ligands to generate the $V^{IV}O^{2+}$ ion which can be oxidized to $V^{V}O_2^+$ (Figure A.4).

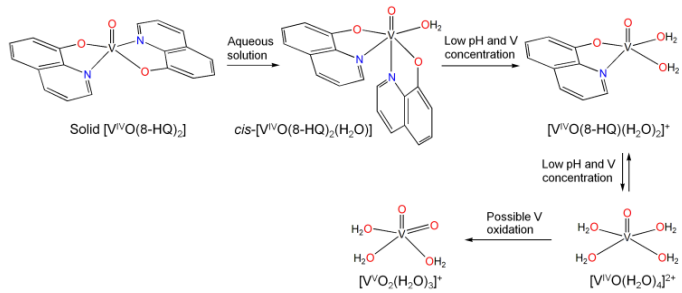

Figure A.4 – Possible transformation of $[V^{IV}O(8\text{-HQ})_2]$ in aqueous solution. Only the most stable isomer of cis-$[V^{IV}O(8\text{-HQ})_2(H_2O)]$, with two equatorial phenoxido-O, is shown.

The mass spectrum recorded at pH 7.5 (Figure A.3b) appears to be very similar to that at pH 4.5 (Figure A.3a) and the peaks of HEWL–$V^{V}O_2$ at 14385.8 Da, HEWL–$[V^{IV}O(8\text{-HQ})]$ at 14515.4 Da, HEWL–$[V^{IV}O(8\text{-HQ})(H_2O)]$ at 14532.6 Da, and HEWL–$[V^{IV}O(8\text{-HQ})_2]$ at 14658.6 Da were observed. The only relevant difference is the increase of the relative amount of HEWL–$[V^{IV}O(8\text{-HQ})_2]$ compared to HEWL–$[V^{IV}O(8\text{-HQ})]$ and HEWL–$[V^{IV}O(8\text{-HQ})(H_2O)]$. It agrees with the variation of the percent concentration of 1:1 and 1:2 $V^{IV}O$:8-HQ complexes by changing the pH from 4.5 to 7.5.

Interaction of [$V^{IV}O(8\text{-}HQ)_2$] with HEWL: electron paramagnetic resonance studies

The EPR spectrum recorded on the [$V^{IV}O(8\text{-}HQ)_2$]/HEWL system with 2:1 molar ratio metallodrug to protein at 298 K and pH 4.5 (Figure A.5) reveals the superimposition of two different signals, one isotropic and another anisotropic.

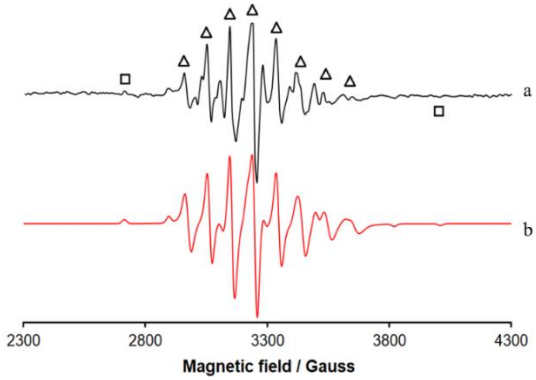

Figure A.5 – a) Experimental X-band EPR spectrum recorded at 298 K on an aqueous solution containing [$V^{IV}O(8\text{-}HQ)_2$] and HEWL with 2:1 molar ratio, pH 4.5 with a V concentration of 8.0×10^{-4} M and b) simulated spectrum with WINEPR SimFonia software.[237] The spectrum was simulated overlapping the signals of two species: HEWL–[$V^{IV}O(8\text{-}HQ)(H_2O)]^+$ adduct and [$V^{IV}O(8\text{-}HQ)_2(H_2O)$]. The triangles indicate the eight isotropic resonances of [$V^{IV}O(8\text{-}HQ)_2(H_2O)$] and the squares the M_I = -7/2, 7/2 anisotropic resonances of HEWL–[$V^{IV}O(8\text{-}HQ)(H_2O)]^+$. Data obtained in collaboration with Prof. Eugenio Garribba from University of Sassari.

These results show that two V-containing species are present in solution and interact with HEWL both non-covalently and covalently under the experimental conditions used. The isotropic EPR signal was simulated with $g_{iso} \sim 1.970$ and $A_{iso} \sim 89 \times 10^{-4}$ cm^{-1}, while the anisotropic spectrum with $g_{x,y,z} \sim \{1.984, 1.984, 1.944\}$ and $A_{x,y,z} \sim \{57, 57, 168\} \times 10^{-4}$ cm^{-1}. The A_z value is slightly lower than that reported for [$V^{IV}O(8\text{-}HQ)(H_2O)_2]^+$ (around $(169–170) \times 10^{-4}$ cm^{-1}),[199] suggesting

the presence of a stronger equatorial donor than water. It has the same value found for the adduct of $[V^{IV}O(8\text{-HQ})(H_2O)]^+$ with RNase A at pH 5.0 (168.2×10^{-4} cm^{-1}),[50] indicating that the protein donor could be a carboxylate group from Asp or Glu. Therefore, the adduct should have the formula HEWL–$[V^{IV}O(8\text{-HQ})(H_2O)]$, consistent with the ESI-MS data (Figure A.3). The g_{iso} and A_{iso} values of the isotropic signal match those expected for $[V^{IV}O(8\text{-HQ})_2(H_2O)]$ and suggest that its interaction with HEWL is not strong enough to trap the V species at the binding site within the EPR timescale. These findings also indicate that the oxidation of V^{IV} to V^{V} does not occur quickly in solution and agree with the speciation at pH 4.5.

The EPR spectrum recorded at pH 7.5 (Figure A.6) is less resolved than the one at pH 4.5 and is difficult to interpret.

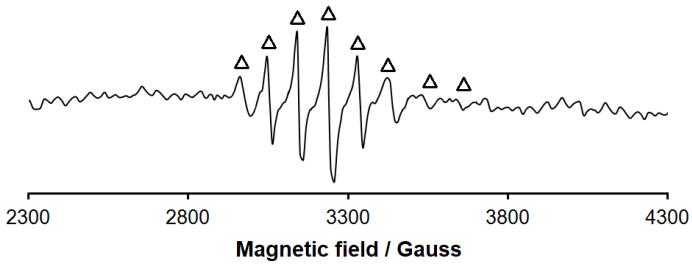

Figure A.6 – Experimental X-band EPR spectrum recorded at 298 K on an aqueous solution containing $[V^{IV}O(8\text{-HQ})_2]$ and HEWL with 2:1 molar ratio, pH 7.5 and a V concentration of 8.0×10^{-4} M. The triangles indicate the eight isotropic resonances of $[V^{IV}O(8\text{-HQ})_2(H_2O)]$. Data obtained in collaboration with Prof. Eugenio Garribba from University of Sassari.

The isotropic signal from $[V^{IV}O(8\text{-HQ})_2(H_2O)]$ is still observed, while the anisotropic features assigned to the covalent adduct HEWL–$[V^{IV}O(8\text{-HQ})(H_2O)]$ seems to be absent. However, the low signal-to-noise ratio prevents a clear assignment.

Still, the presence of the isotropic signal near physiological pH confirms that $[V^{IV}O(8\text{-}HQ)_2(H_2O)]$ interacts weakly and non-covalently with the protein.

Interaction of $[V^{IV}O(8\text{-}HQ)_2]$ with HEWL: computational studies

The covalent binding of the V-containing fragment $[V^{IV}O(8\text{-}HQ)(H_2O)]^+$ to HEWL was studied optimizing in a first step the structure of $[V^{IV}O(8\text{-}HQ)(H_2O)_2]^+$ with a density functional theory (DFT) approach and in a second one simulating the coordinative interaction of $[V^{IV}O(8\text{-}HQ)(H_2O)]^+$ with the protein by molecular docking.

The structure of $[V^{IV}O(8\text{-}HQ)(H_2O)]^+$ was DFT-optimized with Gaussian 09[238] and shown that two penta-coordinate enantiomers are possible, clockwise *SPY-5-13-C*-$[V^{IV}O(8\text{-}HQ)(H_2O)_2]^+$ and anticlockwise *SPY-5-13-A*-$[V^{IV}O(8\text{-}HQ)(H_2O)_2]^+$ (Figure A.7).

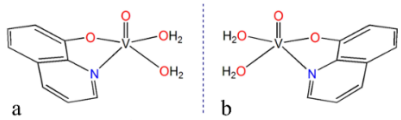

Figure A.7 – The two possible enantiomers of $[V^{IV}O(8\text{-}HQ)(H_2O)_2]^+$: a) clockwise *SPY-5-13-C*-$[V^{IV}O(8\text{-}HQ)(H_2O)_2]^+$ and b) anticlockwise *SPY-5-13-A*-$[V^{IV}O(8\text{-}HQ)(H_2O)_2]^+$.

Then, docking simulations were applied to investigate the molecular reasons why the binding of $[V^{IV}O(8\text{-}HQ)(H_2O)]^+$ to HEWL occurs at the Asp119 residue and not at other potential binding sites such as Glu35, Asn46, Asp48 and Asp52.

In the crystallographic structure, the V atom of $[V^{IV}O(8\text{-}HQ)(H_2O)]^+$ coordinates the side chain of Asp119 and the V containing fragment interacts with two residues from a symmetric related protein molecule, Trp62*and Asn103* (Figure 2.14). These residues are exposed to the solvent, but at solid state or when the

protein–protein interactions are relevant, they stabilize the binding of the metal fragment.

To assess the effect of the crystal lattice or, in general, of protein–protein interactions on the binding of $[V^{IV}O(8\text{-HQ})(H_2O)]^+$ to the protein, two different docking approaches were applied: i) an ensemble docking, denoted as "classic model", which uses one metal-containing fragment and three superimposed crystallographic structures of HEWL (PDB codes 2LYZ,[239] 8RTJ, and 8RTK); ii) a docking, denoted as "symmetry mate model", which uses one metal-containing fragment with two symmetry-related protein chains from the structure A with PDB code 8RTJ. This calculation was carried out to model the crystal lattice or protein–protein interactions.

The "classic model" results suggest that for each of the two metal-containing ligands, 100% of the solutions were located within the HEWL active site pocket. Specifically, the clockwise *SPY-5-13-C*-$[V^{IV}O(8\text{-HQ})(H_2O)]^+$ enantiomer was found to bind to the carboxylate-O of Glu35, while the anticlockwise *SPY-5-13-A*-$[V^{IV}O(8\text{-HQ})(H_2O)]^+$ to the carboxylate-O of Asp52 (Figure A.8a).

Thus, protein–protein stabilization must be invoked to explain the experimental data. The docking calculations was carried out using the "symmetry mate model" *i.e.* using two symmetry related protein chains and the V-containing fragment in the calculations. The simulations that restrict the search around Asp119 residue reproduced the experimental outcome for the case of *SPY-5-13-A*-$[V^{IV}O(8\text{-HQ})(H_2O)]^+$, and, in a lesser extent, for *SPY-5-13-C*-$[V^{IV}O(8\text{-HQ})(H_2O)]^+$. For both enantiomers, the coordination of the V centre to the carboxylate-O of Asp119 is observed (Figure A.8b).

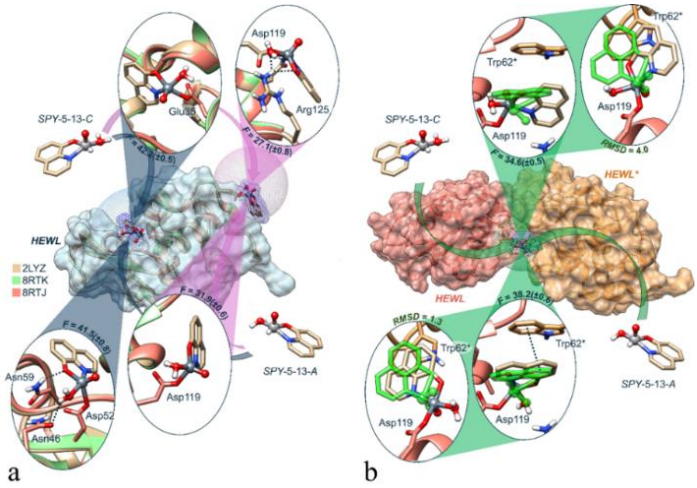

Figure A.8 – a) Docking results for the "classic model": best poses for *SPY-5-13-C*-$[V^{IV}O(8\text{-HQ})(H_2O)]^+$ in the HEWL pocket with Glu35 and Asp119 (top) and best poses for *SPY-5-13-A*-$[V^{IV}O(8\text{-HQ})(H_2O)]^+$ in the active HEWL pocket with Asp52 and with solvent exposed Asp119 residue (bottom). b) Docking results for the "symmetry mate model": best poses from two different points of view for *SPY-5-13-C*-$[V^{IV}O(8\text{-HQ})(H_2O)]^+$ (top) and for *SPY-5-13-A*-$[V^{IV}O(8\text{-HQ})(H_2O)]^+$ (bottom). The crystallographic structure of $[V^{IV}O(8\text{-HQ})(H_2O)]^+$ is displayed for comparison in green. Data obtained in collaboration with Prof. Eugenio Garribba from University of Sassari.

This sustains that the crystal packing could have a significant role in the experimentally observed interaction of Asp119 residue with $[V^{IV}O(8\text{-HQ})(H_2O)]^+$, favouring π–π contact with Trp62* which stabilizes the adduct.

Materials and methods

ESI-MS measurements

The solutions for ESI-MS studies were prepared in LC-MS grade water dissolving $[V^{IV}O(empp)_2]$ and $[V^{IV}O(8\text{-HQ})_2]$ and HEWL to reach a vanadium-to-protein molar ratio of 2:1 and a V concentration of 50 and 100 μM respectively.

The pH of the solution was 4.0 or 7.0 for [$V^{IV}O(empp)_2$] and 4.5 for [$V^{IV}O(8\text{-}HQ)_2$]. ESI-MS spectra in positive ion mode were recorded after the preparation of the solutions with a Q Exactive™ Plus Hybrid Quadrupole-Orbitrap™ (Thermo Fisher Scientific) mass spectrometer in the m/z range 300-4500 and accumulated for at least 5 min to increase the signal-to-noise ratio; the resolution was as high as possible (140000 in arbitrary units). The experimental parameters were: flow rate of infusion into the ESI chamber 5.00 μL/min; spray voltage 2300 V; capillary temperature 250°C; sheath gas 10 (arbitrary units); auxiliary gas 3 (arbitrary units); sweep gas 0 (arbitrary units); probe heater temperature 50°C. ESI-MS spectra were analysed with Thermo Xcalibur 3.0.63 software (Thermo Fisher Scientific) and the average deconvoluted monoisotopic masses were obtained with the software Unidec 4.4.0.[240]

EPR measurements

The EPR spectra were measured in water at pH 7.0 on solutions containing [$V^{IV}O(empp)_2$] alone or [$V^{IV}O(empp)_2$] and HEWL at several molar ratios. 0.1 M HEPES was employed to buffer the solutions. The spectra were recorded at 120 K with an X-band Bruker EMX spectrometer with this instrumental setting: microwave frequency 9.40 GHz; microwave power 20 mW; modulation frequency 100 kHz; modulation amplitude 4.0 G; time constant 81.9 ms; sweep time 335.5 s; resolution 4096 points. To increase the signal-to-noise ratio, signal averaging was used.[213] The number of scans for the high-field regions of the spectra was 5 or 10.

The EPR spectra were measured in water at pH 4.5 on solutions containing [$V^{IV}O(8\text{-}HQ)_2$] and HEWL with a vanadium-to-protein molar ratio of 2:1 and a V concentration of 8.0×10^{-4} M. All the spectra were recorded at 298 K with an X-band Varian E-9 spectrometer equipped with variable temperature unit. The microwave frequency was 9.15 GHz, microwave power 20 mW, time constant 0.5 s,

modulation frequency 100 kHz, modulation amplitude 0.4 mT. The spectra were simulated with WINEPR SimFonia software.[237]

DFT structure optimizations and docking calculations

The DFT optimization of $[V^{IV}O(8\text{-HQ})(H_2O)_2]^+$ was performed with Gaussian 09,[238] using the B3LYP functional[241] and the Grimme's D3 correction[242] with basis set 6-31G(d,p) for main group elements and SDD plus f-functions[243] for vanadium. The SMD continuum method was used to model the water environment.[244] Covalent docking of $[V^{IV}O(8\text{-HQ})(H_2O)_2]^+$ with HEWL was performed using the CCDC GOLD software[245] implementing the scoring function GoldScore, 50 genetic algorithm (GA) automatic runs per ligand, minimum 1 × 105 operations, early termination disabled. Any other parameter was set as default. GOLD and GoldScore parameter files were modified as described by Sciortino et al. for the implementation of GOLD with metal-containing ligands.[246]

The results of these studies were successfully published in:

G. Ferraro, **M. Paolillo**, G. Sciortino, E. Garribba, A. Merlino. "Multiple and variable binding of pharmacologically active Bis(maltolato)oxidovanadium (IV) to lysozyme." Inorg. Chem. 61, (2022), 16458-16467. DOI: https://doi.org/10.1021/acs.inorgchem.2c02690

G. Ferraro, **M. Paolillo**, G. Sciortino, F. Pisanu, E. Garribba, A. Merlino. "Implications of Protein Interaction in the Speciation of Potential $V^{IV}O$–Pyridinone Drugs." Inorg. Chem. 62, (2023), 8407-8417. DOI: https://doi.org/10.1021/acs.inorgchem.3c01041

M. Paolillo, G. Ferraro, F. Pisanu, J.D. Maréchal, G. Sciortino, E. Garribba, A. Merlino "Protein-Protein Stabilization in $V^{IV}O$/8-Hydroxyquinoline–Lysozyme Adducts". Chem. Eur. J. (2024), e202401712. DOI: https://doi.org/10.1002/chem.202401712

M. Paolillo, G. Ferraro, I. Cipollone, E. Garribba, M. Monti, A. Merlino "Unexpected in *crystallo* reactivity of the potential drug bis(maltolato)oxidovanadium (IV) with lysozyme". Inorg. Chem. Front., 11, (2024), 6307-6315. DOI: 10.1039/D4QI01528B

and under revision:

A.S. Banneville, R. Lucignano, **M. Paolillo**, V. Cuomo, M. Chino, G. Ferraro, D. Picone, E. Garribba, I. Cornaciu-Hoffmann, A. Pica, A. Merlino "First crystal structure of an adduct formed upon reaction of a vanadium compound with human serum transferrin". Commun. Chem., under revision

CHAPTER 3

$V^{IV}O$ complexes with tridentate ligands: the cases of $[V^{IV}O(xant)(H_2O)_2]$, and $[V^{IV}O(dipic)(H_2O)_2]$

3.1 Introduction

The coordination chemistry of vanadium with multidentate ligands is relevant for both catalytic[58,59] and medicinal applications.[58,60] Among tridentate ligands, 8-HQ derivatives and related tryptophan metabolites, such as xanthurenic acid (xant), are of particular interest because of their anti-oxidant and anti-cancer properties.[63,64] The combination of the biological activity of 8-HQ derivatives with the pharmacological potential of V, as in the case of $[V^{IV}O(xant)(H_2O)_2]$ (Figure 3.1a), represents a promising strategy for the development of new V-based therapeutic agents.[69–73] Another relevant ligand is dipicolinic acid (dipic), an ONO-donor ligand known for its amphiphilic character, low toxicity, and ability to stabilize unusual vanadium oxidation states.[74,75] Dipic is naturally occurring and widely used in coordination chemistry to obtain water-soluble and biologically relevant complexes,[74] such as $[V^{IV}O(dipic)(H_2O)_2]$ (Figure 3.1b), which have been investigated for their anti-cancer properties.

Importantly, the stability and geometry of these complexes strongly influence their gastrointestinal absorption, plasma transport, cellular uptake, and ultimately their interaction with proteins, which plays a key role in their bioavailability and potential therapeutic activity.[15]

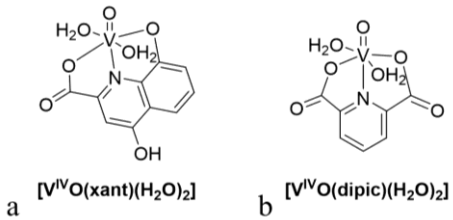

Figure 3.1 – Chemical structures of oxidovanadium(IV) species with tridentate ligands: a) $[V^{IV}O(xant)(H_2O)_2]$, b) $[V^{IV}O(dipic)(H_2O)_2]$.

3.2 Interaction of $[V^{IV}O(xant)(H_2O)_2]$ with HSA

Among the plasma proteins, HSA plays a key role in the transport and distribution of V species *in vivo* due to its high concentration and strong binding affinity.[247] HSA can bind V^{IV} ions at several binding sites, including the primary site in the N-terminal region (NTS), the multi-metal binding site (MBS or site A), non-specific sites involving His-N, Asp/Glu-O, or carbonyl-O atoms (sites B), and weak O-donor sites (sites C).[248]

The potential interaction between HSA and the $V^{IV}O$ complex formed by xanthurenic acid, $[V^{IV}O(xant)(H_2O)_2]$ (Figure 3.1a), was investigated by UV-vis absorption and fluorescence measurements. The possible involvement of histidine residues in the binding process was also evaluated.

3.2.1 UV-visible absorption spectroscopy

First, the stability of the complex under different experimental conditions was studied. UV-vis absorption spectra of $[V^{IV}O(xant)(H_2O)_2]$ (20 μM) were collected over 24 h in: 100% DMSO (Figure 3.2a), 0.4% DMSO - 99.6% PBS (Figure 3.2b), and water (Figure 3.2c). The spectrum of $[V^{IV}O(xant)(H_2O)_2]$ in DMSO indicates that, under this condition, the V compound is not stable over time. Indeed, an isosbestic point at 286 nm is observed, suggesting either a slow decomposition of the complex or ligand exchange processes. Notably, the absorption band at 341 nm increases in intensity, while the band at 266 nm gradually decreases over time (Figure 3.2a), further supporting this hypothesis. This finding indicates that the complex should not be dissolved in DMSO for further studies. In contrast, under the other conditions the complex is stable for 24 h. In particular, in 0.4% DMSO - 99.6% PBS pH 7.4 (Figure 3.2b) and in milli-Q water (Figure 3.2c), only minor changes in absorbance are observed.

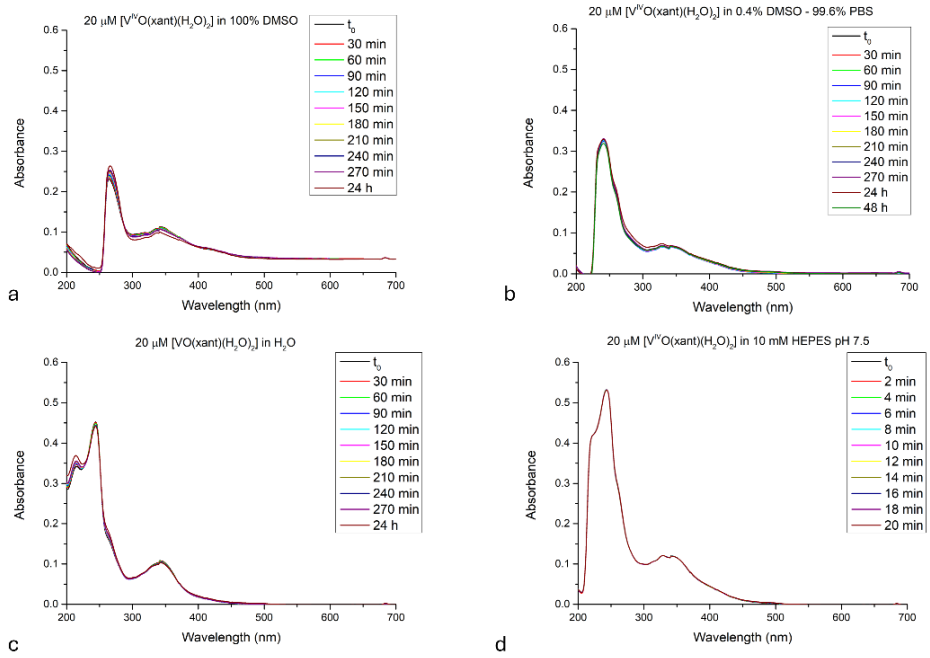

Figure 3.2 – UV-vis spectra as a function of time of $[V^{IV}O(xant)(H_2O)_2]$ (20 μM) in a) 100% DMSO, b) 0.4% DMSO - 99.6% PBS, c) water and d) 10 mM HEPES pH 7.5.

Then, a titration of the complex with increasing amounts of 1-methylimidazole (MeIm) in 10 mM HEPES pH 7.5 was performed (Figure 3.3). Under this condition the complex remains stable during the experiment (Figure 3.2d). MeIm has been frequently studied as model for the coordination of histidine side chain to metals (His-N).[192,249–251] When MeIm binds to $V^{IV}O$ complexes with *cis*-octahedral geometry, it forms ternary species with *cis*-$[V^{IV}O(L)_2(MeIm)]$ composition.[192] As the concentration of MeIm increases, a progressive rise in absorbance at 214 nm is observed. This is due to the intrinsic absorbance of MeIm (λ_{max} = 216 nm). Moreover, a slight red shift of this band, from 214 nm to 216 nm, becomes evident after the final addition, suggesting a potential interaction between MeIm and this VC. Complementary EPR measurements also support this interaction, although these data are not included in the thesis.

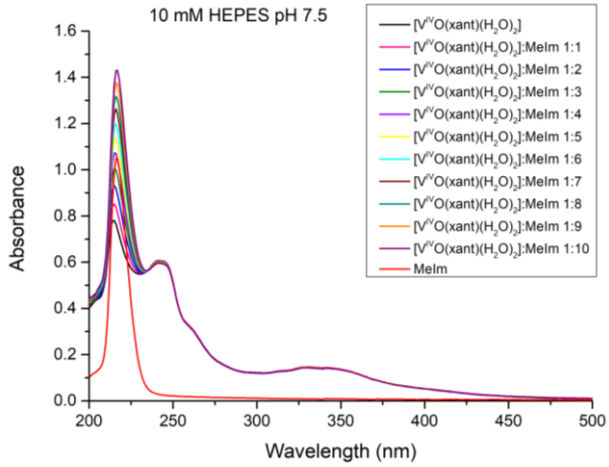

Figure 3.3 – UV-vis spectrum of $[V^{IV}O(xant)(H_2O)_2]$ (20 µM) in 10 mM HEPES pH 7.5 upon titration with an increasing concentration of MeIm.

3.2.2 Fluorescence spectroscopy

The fluorescence spectra of HSA (1.4 µM) in 10 mM HEPES pH 7.5 in the presence of increasing concentrations of $[V^{IV}O(xant)(H_2O)_2]$ were registered to analyse the binding of the compound to the protein (Figure 3.4). Measurements were carried out upon excitation at 280 nm and 295 nm to monitor changes in the environment of the Tyr and Trp or Trp alone. Progressive addition of the VC to the protein results in a marked decrease in fluorescence intensity. These spectral changes suggest that $[V^{IV}O(xant)(H_2O)_2]$ interacts with HSA.

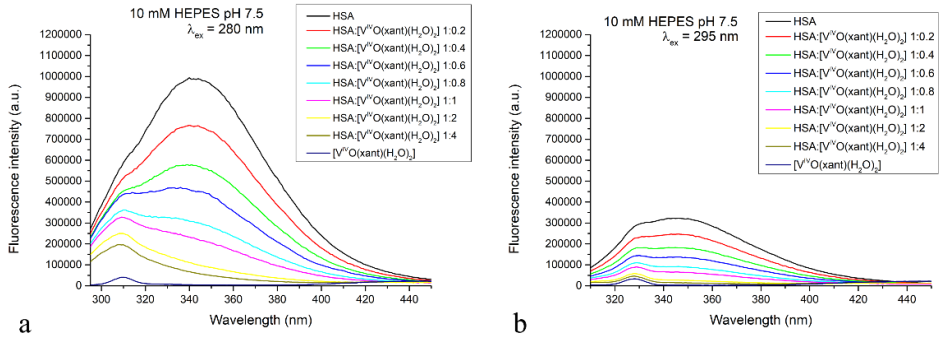

Figure 3.4 – Fluorescence emission spectra of HSA in 10 mM HEPES pH 7.5 upon titration with an increasing concentration of $[V^{IV}O(xant)(H_2O)_2]$. Spectra were collected using a) λ_{exc} = 280 nm and b) λ_{exc} = 295 nm.

The spectroscopic data suggest that HSA could bind $[V^{IV}O(xant)(H_2O)_2]$ through a His side chain.

Although preliminary, these findings justify further studies combining high-resolution structural techniques and biological assays to better clarify the interaction mode and evaluate the pharmacological potential of this compound.

3.3 Interaction of $[V^{IV}O(xant)(H_2O)_2]$ with HEWL

To gain deeper insights into the interaction of $[V^{IV}O(xant)(H_2O)_2]$ with proteins, the binding of this potential V-based drug to HEWL was investigated using a multi-technique approach based on spectroscopic techniques (UV-vis, fluorescence and CD) and X-ray crystallography.

3.3.1 UV-visible absorption spectroscopy

UV-vis absorption spectroscopy was employed to investigate the stability of $[V^{IV}O(xant)(H_2O)_2]$ (concentration = 63 μM) over time, in the absence and in the presence of HEWL (protein-to-VC molar ratio 1:3), in solutions containing: i) 1.1

M sodium chloride, 0.1 M sodium acetate pH 4.0 (Figure 3.5a,b); ii) 20% ethylene glycol, 0.6 M sodium nitrate, 0.1 M sodium acetate pH 4.0 (Figure 3.5c,d) ; iii) 14% PEG 8000, 0.1 M sodium citrate, 0.05 M sodium cacodylate pH 6.5 (Figure 3.5e,f); iv) 0.8 M succinic acid pH 7.0 (Figure 3.5g,h); v) 2.0 M sodium formate, 0.1 M HEPES pH 7.5 (Figure 3.5i,j). These experimental conditions were used to grow HEWL crystals then treated with $[V^{IV}O(xant)(H_2O)_2]$. Under these conditions the complex exhibits stability in the absence and in the presence of HEWL (Figure 3.5).

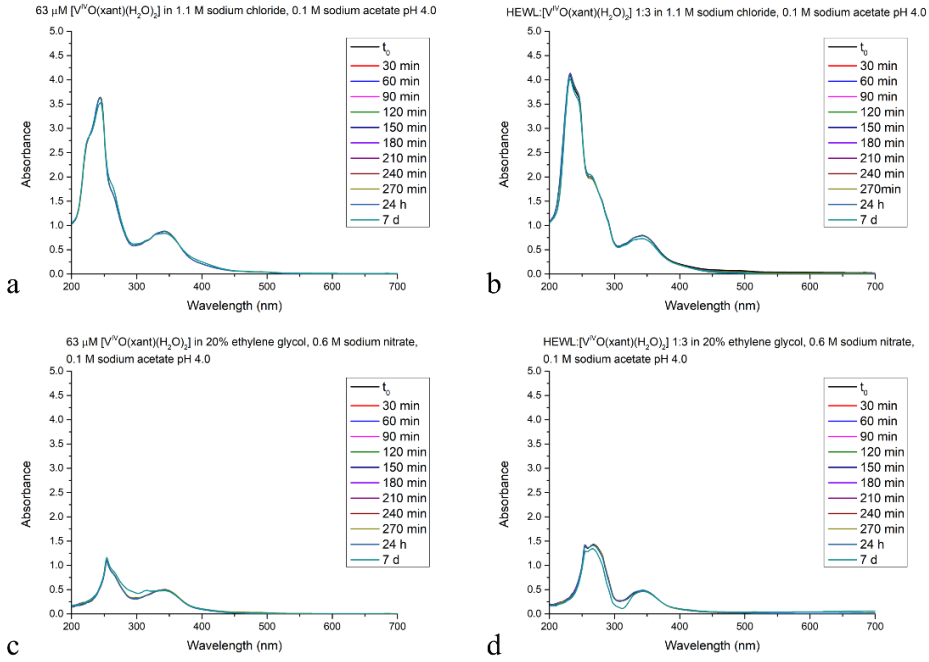

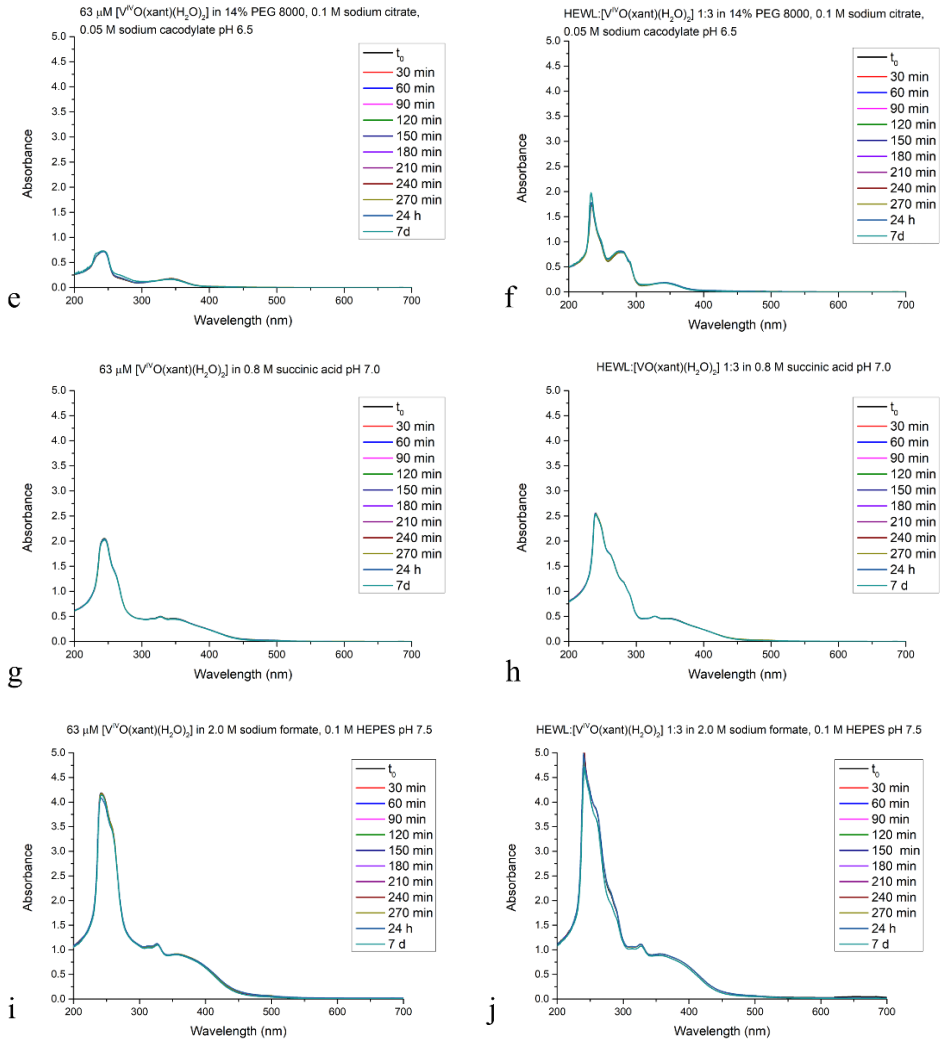

Figure 3.5 – UV-vis spectra as a function of time of [$V^{IV}O(xant)(H_2O)_2$] (63 μM) were collected in a,c,e,g,i) the absence and in b,d,f,h,j) the presence of HEWL (21 μM) using a 3:1 VC-to-protein molar ratio in a,b) 1.1 M sodium chloride and 0.1 M sodium acetate pH 4.0, c,d) 20% ethylene glycol, 0.6 M sodium nitrate, 0.1 M sodium acetate pH 4.0, e,f) 14% PEG 8000, 0.1 M sodium citrate, 0.05 M sodium cacodylate pH 6.5, g,h) 0.8 M succinic acid pH 7.0, i,j) 2.0 M sodium formate, 0.1 M HEPES pH 7.5.

3.3.2 Fluorescence studies

Fluorescence can be used to monitor the metallodrug binding to HEWL since the protein possesses six Trp residues. Indeed, Trp emission is sensitive to structural variations induced by metal compound binding. The fluorescence spectra of HEWL (protein concentration = 1.4 μM) in the buffer used in the conditions i-v reported in the previous paragraph in the presence of increasing concentrations of $[V^{IV}O(xant)(H_2O)_2]$ are collected, upon excitation at 280 and 295 nm, respectively (Figure 3.6). The addition of $[V^{IV}O(xant)(H_2O)_2]$ to HEWL results decrease of protein emission upon increasing of vanadium concentration. This suggests that the compound interacts with the protein. The quenching is not associated with a change in the maximum emission wavelength, indicating that the recognition of $[V^{IV}O(xant)(H_2O)_2]$ by HEWL occurs without significantly altering the protein tertiary structure.

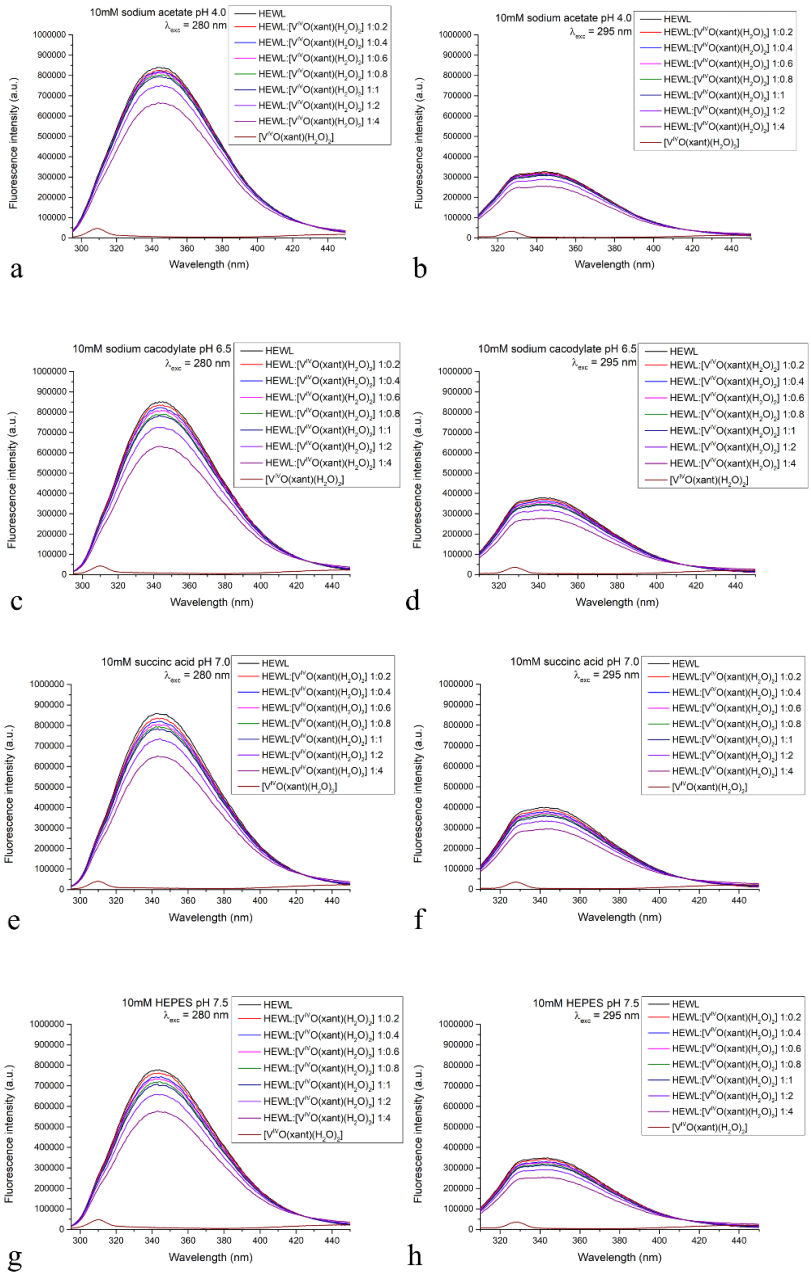

Figure 3.6 – Fluorescence emission spectra of HEWL in a,b) 10 mM sodium acetate pH 4.0, c,d) 10 mM sodium cacodylate pH 6.5, e,f) 10 mM succinic acid pH 7.0, g,h) 10 mM HEPES pH 7.5 were recorded upon titration with a solution of $[V^{IV}O(xant)(H_2O)_2]$.

Spectra were collected using λ_{exc} = 280 nm (panels a,c,e and g) and 295 nm (panels b,d,f and h).

3.3.3 Circular dichroism

To evaluate the effect of $[V^{IV}O(xant)(H_2O)_2]$ binding on HEWL secondary structure content, circular dichroism spectroscopy was used. HEWL far UV-CD spectra (concentration = 7.0 μM), in the absence and in the presence of the VC at protein to metal molar ratios of 1:1, 1:3, and 1:5, were collected in the same buffers used for fluorescence experiments after 24 h (Figure 3.7a,d,g and j), 48 h (Figure 3.7d,e,h and k), and 7 days (Figure 3.7c,f,i and l) of incubation.

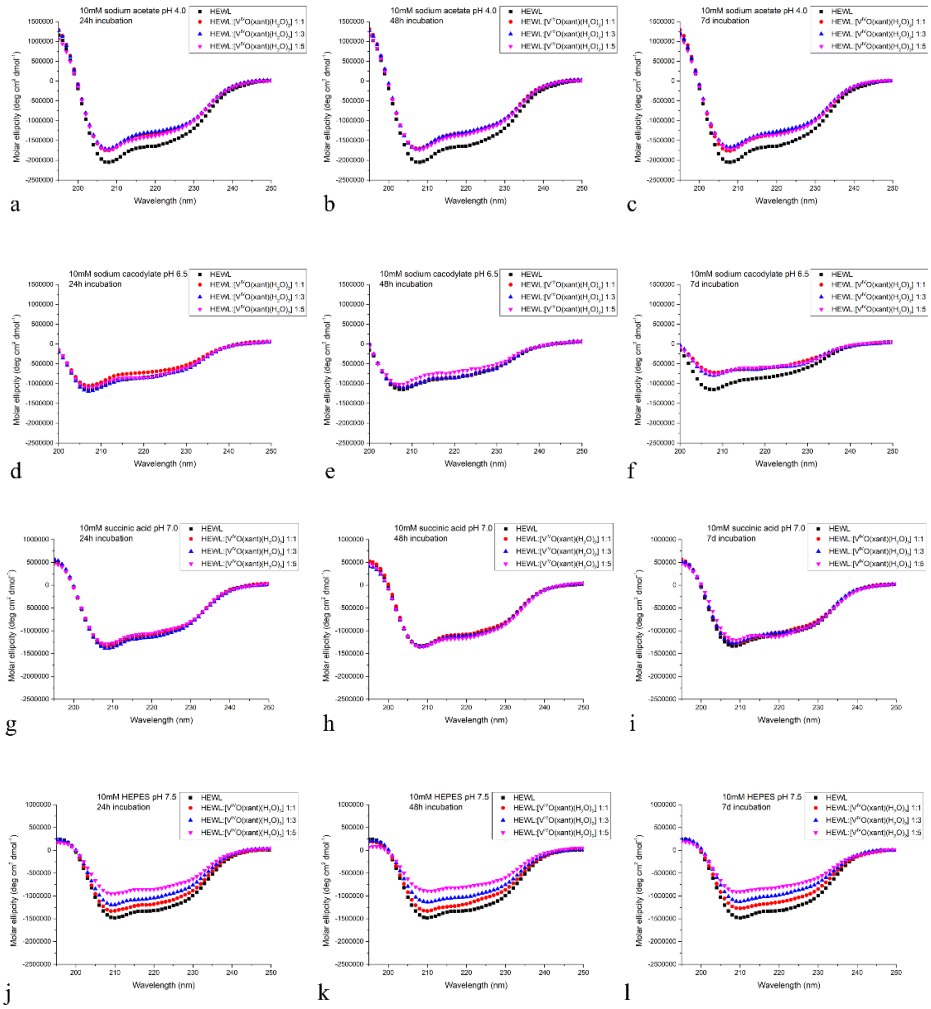

Figure 3.7 – Far-UV CD spectra of HEWL (concentration = 7.0 μM) incubated for a,d,g,j) 24 h, b,e,h,k) 48 h and c,f,i,l) 7 d in the presence of $[V^{IV}O(xant)(H_2O)_2]$ in 10 mM sodium acetate pH 4.0 (panels a-c), in 10 mM sodium cacodylate pH 6.5 (panels d-f), in 10 mM succinic acid pH 7.0 (panels g-i) and in 10 mM HEPES pH 7.5 (panels j-l) at protein-to-VC molar ratio = 1:1 (red), 1:3 (blue) and 1:5 (violet). CD of metal-free protein is in black.

The analysis of HEWL spectral profiles indicates that the secondary structure content does not change in 10 mM sodium acetate at pH 4.0 (Figure 3.7a-c) and in 10 mM succinic acid pH 7.0 (Figure 3.7g-i). A slight reduction in the α-helical content or a subtle rearrangement in the local environment of the peptide bonds is observed in 10 mM HEPES pH 7.5 (Figure 3.7j-l) and, just after 7 days of incubation, in 10 mM sodium cacodylate pH 6.5 (Figure 3.7d-f). This behaviour indicates that, under these conditions, the protein adopts a slightly different conformation upon VC binding.

Overall, these findings demonstrate that the interaction between HEWL and $[V^{IV}O(xant)(H_2O)_2]$ is influenced by buffer composition and pH.

3.3.4 Crystallographic studies

Crystals of the metal-free protein were thus grown in the crystallization conditions above mentioned and then exposed to stabilizing solutions containing the mother liquors saturated with $[V^{IV}O(xant)(H_2O)_2]$ for 7 days. X-ray diffraction data were collected on these crystals at resolution within the range 1.11-1.48 Å. Structures were refined with R-factor and Rfree values within the range 0.131-0.198 and 0.171-0.229, respectively. Data collection and refinement statistics are reported in Table 3.1.

Table 3.1 – Data collection and refinement statistics for the structures A-E.

Data collection					
	Structure A	Structure B	Structure C	Structure D	Structure E
Crystallization condition	1.1 M sodium chloride, 0.1 M sodium acetate pH 4.0	20% ethylene glycol, 0.6 M sodium nitrate, 0.1 M sodium acetate pH 4.0	14% PEG 8000, 0.1 M sodium citrate, 0.05 M sodium cacodylate pH 6.5	0.8 M succinic acid pH 7.0	2.0 M sodium formate, 0.1 M HEPES pH 7.5
Soaking time	7 d	7 d	7 d	7 d	7 d
Space group	$P4_32_12$	$P4_32_12$	$P4_32_12$	$P4_32_12$	$P4_32_12$
a (Å)	77.81	77.55	76.71	76.98	76.30
b (Å)	77.81	77.55	76.71	76.98	76.30
c (Å)	36.47	36.40	37.16	37.46	37.08
Resolution range (Å)	55.02-1.38 (1.40-1.38)	54.84-1.48 (1.50-1.48)	54.24-1.34 (1.36-1.34)	38.49-1.11 (1.13-1.11)	53.95-1.24 (1.26-1.24)
Observations	288446 (8647)	251734 (12046)	511343 (23496)	954762 (23095)	238040 (3386)
Unique reflections	23746 (1168)	19377 (952)	23777 (1246)	44655 (2085)	30993 (1322)
Completeness (%)	100.0 (99.6)	100.0 (100.0)	92.6 (100.0)	99.5 (94.3)	98.4 (85.8)
Redundancy	12.1 (7.4)	13.0 (12.7)	21.5 (18.9)	21.4 (11.1)	7.7 (2.6)
Rmerge (%)	0.093 (2.946)	0.087 (4.226)	0.078 (6.554)	0.048 (0.989)	0.108 (0.778)
Average I/σ(I)	10.2 (0.5)	10.7 (0.6)	18.7 (0.5)	30.6 (2.3)	10.8 (2.1)
$CC_{1/2}$	0.994 (0.364)	0.996 (0.349)	1.000 (0.355)	1.000 (0.739)	0.995 (0.407)
Anom. completeness (%)	100.0 (99.6)	100.0 (100.0)	92.0 (100.0)	99.6 (94.0)	94.1 (59.6)
Anom. Multiplicity	6.5 (3.9)	7.0 (6.7)	11.6 (9.9)	11.3 (5.8)	4.2 (1.7)
Refinement					
Resolution (Å)	55.02-1.38	54.84-1.50	54.24-1.39	38.52-1.11	53.95-1.24
N° reflections	19145	15597	19129	42504	29328
N° reflections in working set	367	194	448	2947	1736
R-factor/Rfree	0.195/0.218	0.198/0.229	0.180/0.224	0.131/0.171	0.175/0.204
N° non-H atoms in the refinement	1172	1121	1188	1288	1280

B-factor overall (Å^2)	27.47	32.48	23.73	19.95	13.51
Estimated occupancy of $[V^{V}O_2(xant)]^-$ (1) in structure A	0.60	-	-	-	-
Estimated occupancy of $[V^{V}O_2(xant)]^-$ (2) in structure A	0.50	-	-	-	-
Estimated occupancy of $[V^{V}O_2(xant)]^-$ (3) in structure A	0.50	-	-	-	-
Estimated occupancy of $[(V^{V}O_2(xant))_2(V^{IV}O(H_2O)_2)_2]^{2+}$ in structure A	0.85	-	-	-	-
Estimated occupancy of $[V^{V}O_2(xant)]^-$	-	0.60	0.50	0.50	0.50
B-factor of $[V^{V}O_2(xant)]^-$ (1) in structure A (Å^2)	33.49	-	-	-	-
B-factor of $[V^{V}O_2(xant)]^-$ (2) in structure A (Å^2)	58.78	-	-	-	-
B-factor of $[V^{V}O_2(xant)]^-$ (3) in structure A (Å^2)	60.10	-	-	-	-
B-factor of $[(V^{V}O_2(xant))_2(V^{IV}O(H_2O)_2)_2]^{2+}$ in structure A (Å^2)	28.7±1.7	-	-	-	-
B-factor of $[V^{V}O_2(xant)]^-$ (Å^2)	-	44.92	26.44	19.48	16.21
Ramachandran values (%)					
Most favoured/Additional allowed	96.06/3.94	93.55/6.45	93.91/6.09	94.83/5.17	95.28/4.72
Outliers	1	0	0	0	0
RMSD from ideality					
RMSD bonds (Å)	0.011	0.009	0.013	0.017	0.013
RMSD angles (°)	2.253	1.775	1.954	2.341	2.206

The folding of HEWL in the five structures is almost identical to that of the metal free protein (RMSD of the Cα atoms is within the range 0.24-0.37 Å). Thus, the binding of the metal-containing fragments to the protein does not alter its overall conformation.

In the first structure (structure A, Figure 3.8a), obtained from crystals grown in 1.1 M sodium chloride, 0.1 M sodium acetate pH 4.0, and refined at 1.38 Å resolution to R-factor/Rfree values of 0.195/0.218, three species with [VO_2(xant)] composition and an additional V-containing fragment were found on the protein surface (Figure 3.8a).

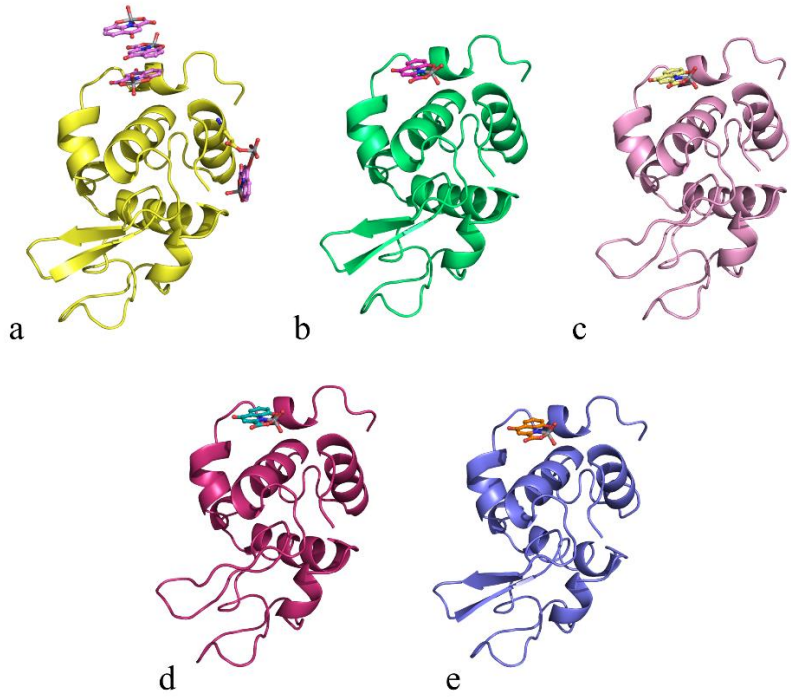

Figure 3.8 – Overall structure of the adduct formed upon reaction of [$V^{IV}O$(xant)$(H_2O)_2$] with HEWL from crystals grown in: a) 1.1 M sodium chloride, 0.1 M sodium acetate pH 4.0 (structure A), b) 20% ethylene glycol, 0.6 M sodium nitrate, 0.1 M sodium acetate pH 4.0 (structure B), c) 14% PEG 8000, 0.1 M sodium citrate, 0.05 M sodium cacodylate pH

6.5 (structure C), d) 0.8 M succinic acid pH 7.0 (structure D), e) 2.0 M sodium formate, 0.1 M HEPES pH 7.5 (structure E). Vanadium atoms are in grey.

The three species with composition $[VO_2(xant)]$, named (1), (2) and (3), occupy a cavity formed at the interface between two symmetry-related molecules binding non-covalently to the protein (Figure 3.8). They are close to each other and have an occupancy = 0.60, 0.50 and 0.50, respectively. In these three V moieties, the geometry of the V centre is intermediate between a square pyramid and a trigonal bipyramid and differs from that of $[V^{IV}O(xant)(H_2O)_2]$, in which the V centre has an octahedral geometry. Actually, a species with formula $[VO_2(xant)]$, bearing a V in the oxidation state +5, has been already reported in literature as product of the reaction of 4,8-dihydroxyquinoline-2-carboxylic acid and NH_4VO_3.[252] Thus, the V-fragments bound to HEWL were assigned to the $[V^{V}O_2(xant)]^-$ ion previously isolated.[252] In particular, $[V^{V}O_2(xant)]^-$ is a *cis*-VO_2 structural unit coordinated to the two O atoms and the N atom of the tridentate xant ligand, with the V centre adopting the penta-coordinated geometry. Selected geometrical parameters of $[V^{V}O_2(xant)]^-$ ions bound to HEWL are reported in Table 3.2, compared with the values observed in the $[V^{V}O_2(xant)]^-$ ion from literature.

Looking at the X-ray structure in detail, $[V^{V}O_2(xant)]^-$ (1) forms π–π stacking interactions with Trp123 side chain and $[V^{V}O_2(xant)]^-$ (2), and hydrogen bonds with water molecules and with the side chain of Asp119 from a symmetry mate (Figure 3.9). $[V^{V}O_2(xant)]^-$ (2) is hydrogen-bonded with the O atom of Ala122, the side chain of Arg125, the N atom of Asp119 from a symmetry related molecule (Figure 3.9) and interacts also with $[V^{V}O_2(xant)]^-$ (3). Finally, $[V^{V}O_2(xant)]^-$ (3) forms hydrogen bonds with a water molecule and with the side chains of Asn103, Asn106, Arg112 from a symmetry related molecule (Figure 3.9).

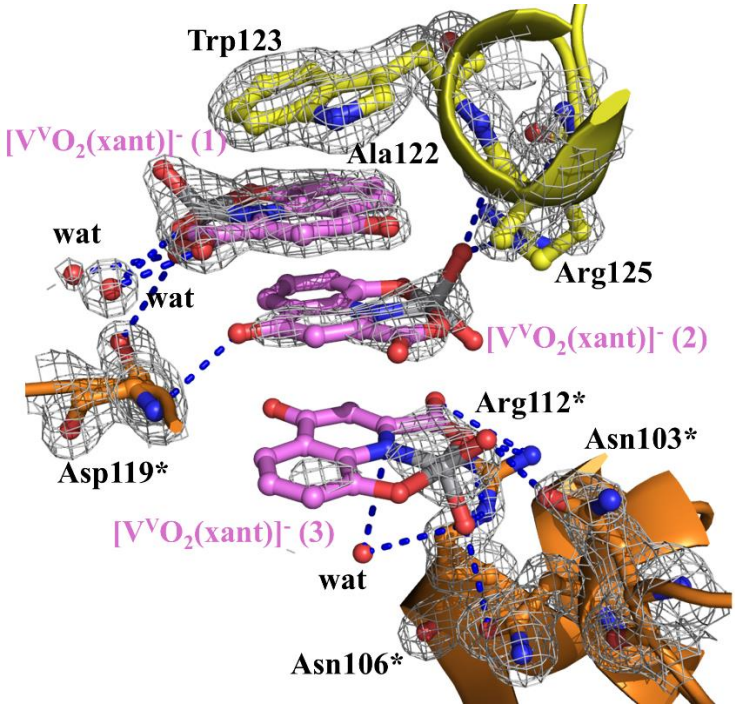

Figure 3.9 – V binding sites in the structure A: non-covalent binding of three $[V^{V}O_2(xant)]^-$ ions to protein surface residues. 2Fo-Fc e.d. maps are reported at 1.0 σ level in grey. Residues from symmetry related molecules are highlighted with an asterisk (*) and coloured in orange.

The three $[V^{V}O_2(xant)]^-$ ions are almost parallel to each other. The angles formed by the planes of xant ligands and the side chain of Trp123 are within the range 9.6-17.1° (Table 3.3). π–π interactions between the *cis*-dioxidovanadium(V) complexes have been also observed in the crystal structure of $[V^{V}O_2(xant)]^-$.[252]

Table 3.2 – Selected bond lengths and angles for the $[V^{V}O_2(xant)]^-$ complexes observed in the structures A, B, C, D and E compared with the values for the isolated $[V^{V}O_2(xant)]^-$ complex reported in literature.[252]

	$[V^{V}O_2(xant)]^-$ reported in literature[252]	First (1) $[V^{V}O_2(xant)]^-$ observed in the structure A	Second (2) $[V^{V}O_2(xant)]^-$ observed in the structure A	Third (3) $[V^{V}O_2(xant)]^-$ observed in the structure A	$[V^{V}O_2(xant)]^-$ observed in the structure B	$[V^{V}O_2(xant)]^-$ observed in the structure C	$[V^{V}O_2(xant)]^-$ observed in the structure D	$[V^{V}O_2(xant)]^-$ observed in the structure E
O5–V1–O6 (°)	109.9(2)	102.98	108.45	114.06	103.54	110.58	109.43	114.69
N1–V1–O2 (°)	76.2(1)	77.61	75.55	75.40	76.96	75.85	76.97	75.22
N1–V1–O4 (°)	75.2(1)	81.42	85.89	86.10	82.89	83.00	79.48	79.82
V–O(carboxylate) (Å)	1.995(2)	1.80	1.81	1.80	1.82	1.81	1.84	1.82
V–N(pyridine) (Å)	2.023(3)	1.86	1.85	1.85	1.86	1.86	1.88	1.86
V–O(hydroxide) (Å)	2.010(2)	2.12	2.12	2.12	2.12	2.11	2.09	2.11

Table 3.3 – Angles formed by the planes of the xant ligands and with the side chain of Trp123.

Angles formed by the planes of $[V^{V}O_2(xant)]^-$ (1) and $[V^{V}O_2(xant)]^-$ (2)	Angles formed by the planes of $[V^{V}O_2(xant)]^-$ (2) and $[V^{V}O_2(xant)]^-$ (3)	Angles formed by the planes of $[V^{V}O_2(xant)]^-$ (1) in the structure A and Trp123	Angles formed by the planes of $[V^{V}O_2(xant)]^-$ in the structure B and Trp123	Angles formed by the planes of $[V^{V}O_2(xant)]^-$ in the structure C and Trp123	Angles formed by the planes of $[V^{V}O_2(xant)]^-$ in the structure D and Trp123	Angles formed by the planes of $[V^{V}O_2(xant)]^-$ in the structure E and Trp123
1.4°	10.2°	17.1°	14.9°	12.4°	14.4°	9.6°

The fourth metal-containing fragment is covalently attached to the protein, close to the side chain of Glu7 (Figure 3.10). Inspection of anomalous difference e.d. map in this position suggests the presence of four V atoms (occupancy = 0.85), two of them belonging to a symmetry related molecule. The first V centre adopts a distorted octahedral geometry and thus could be in the oxidation state +4. It is attached to the OE2 atom of Glu7 side chain and is coordinated by three oxygen atoms, the O atom of the xant ligand and one oxygen atom that is in turn linked to the second V centre from a symmetry mate. The distances between V and O suggest that one of the three oxygens forms a double bond with the vanadium centre. The second V centre adopts the same geometry and structure of the three $[V^{V}O_2(xant)]^-$ ions that are non-covalently attached to the protein and thus it should be in the oxidation state +5. This V atom completes its coordination sphere with two oxygen atoms and the tridentate ligand. One of two coordinating oxygen atoms is shared with the first V centre from a symmetry mate. This peculiar arrangement leads to the formation of a mixed valence tetrametallic species that bridges two protein molecules (Figure 3.11). This species interacts with the side chains of Lys1, His15, the main chain N of Ile88 and the side chain of Asp87 from a symmetry related molecule (Figure 3.10).

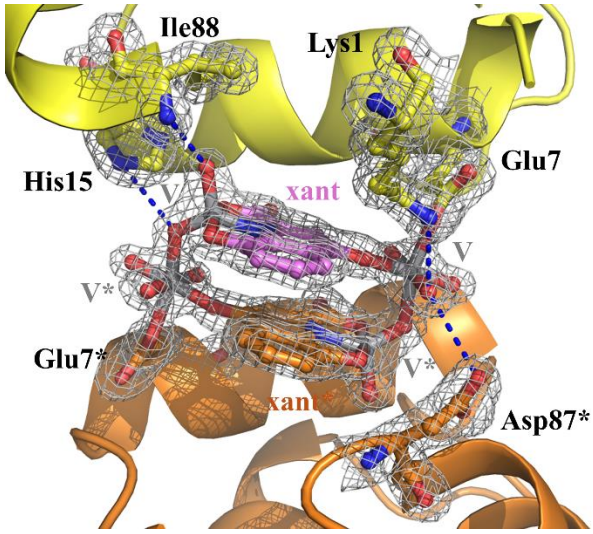

Figure 3.10 – Additional V binding site in the structure A: covalent binding of a tetrametallic species derived by $[V^{IV}O(xant)(H_2O)_2]$ to HEWL. 2Fo-Fc e. d. maps are reported at 1.0 σ level in grey. Residues from symmetry related molecules are highlighted with an asterisk (*) and coloured in orange.

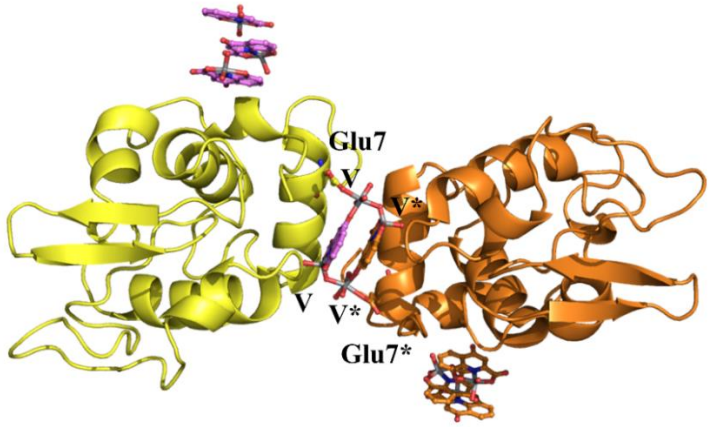

Figure 3.11 – Structure of the cross-linked HEWL dimer formed in the crystals of the protein exposed to $[V^{IV}O(xant)(H_2O)_2]$. The symmetry related molecule is coloured in orange. Glu7 from the symmetry-related molecule is highlighted as *.

In the other structures, obtained in 20% ethylene glycol, 0.6 M sodium nitrate, 0.1 M sodium acetate pH 4.0 (structure B), 14% PEG 8000, 0.1 M sodium citrate, 0.05 M sodium cacodylate pH 6.5 (structure C), 0.8 M succinic acid pH 7.0 (structure D) and 2.0 M sodium formate and 0.1 M HEPES pH 7.5 (structure E) only one $[V^{V}O_2(xant)]^-$ ion was observed (Figure 3.8b-e). It occupies almost the same position in the structures B-E and has on occupancy in the range 0.50-0.60 (Table 3.1). The V complex binding site in these structures is close to that of the first $[V^{V}O_2(xant)]^-$ ion observed in the structure A (Figure 3.12).

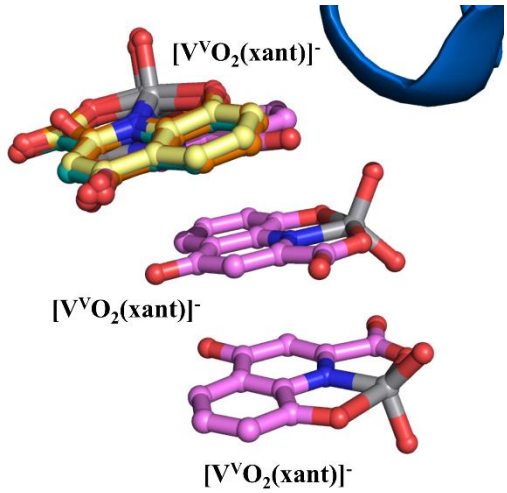

Figure 3.12 – Structural superimposition between the structures of $[V^{V}O_2(xant)]^-$ ions found in the structures A (light violet), B, C, D and E.

Selected bond lengths and angles for the $[V^{V}O_2(xant)]^-$ ions observed in the structures B, C, D and E are reported in Table 3.2. The absence of the second and third $[V^{V}O_2(xant)]^-$ ions in the structures B, C, D and E is due to a conformational variation of Arg125 side chain that adopts a conformation that is not compatible with the binding of the second $[V^{V}O_2(xant)]^-$ complex of the structure A (Figure 3.9 vs Figure 3.13).

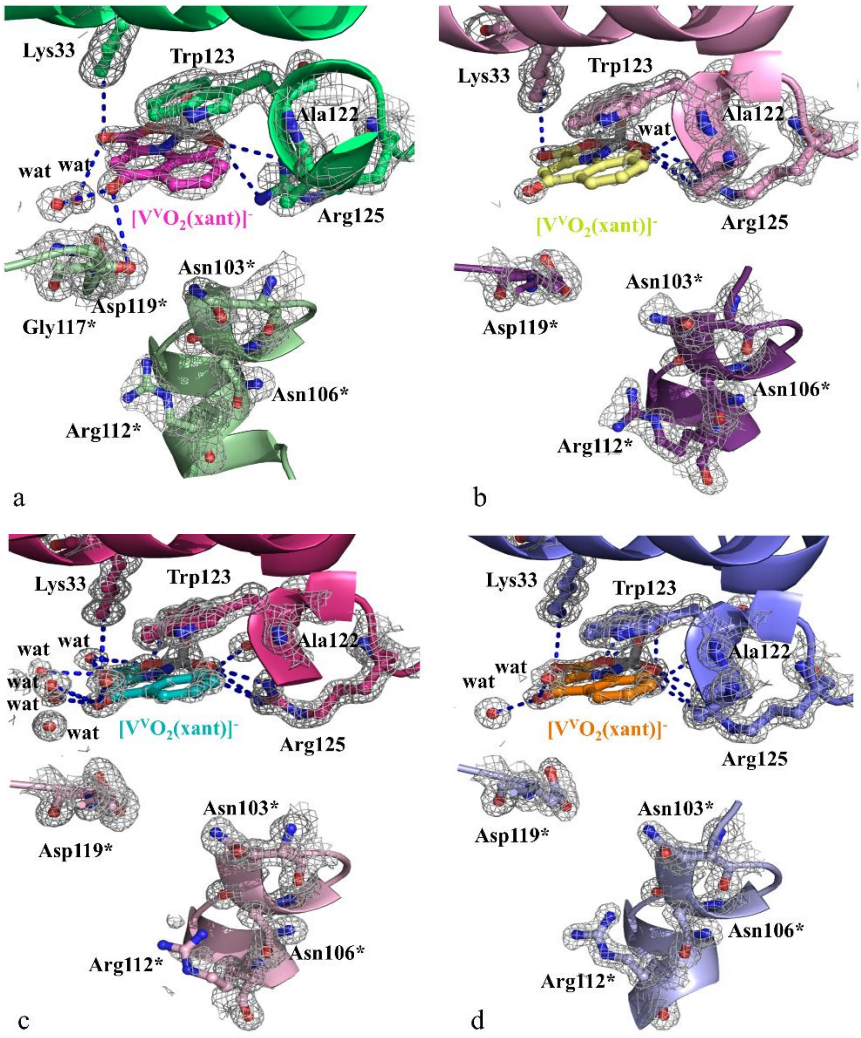

Figure 3.13 – 2Fo-Fc electron density maps of the $[V^{V}O_2(xant)]^-$ ion observed in: a) the structure B, b) the structure C, c) the structure D and d) the structure E are reported at 1.0 σ level in grey. Residues from symmetry related molecules are highlighted with an asterisk (*).

In the structures B, C, D and E, $[V^{V}O_2(xant)]^-$ forms hydrogen bonds with the side chains of Lys33, Arg125, water molecules and π–π stacking interactions with Trp123 side chain (Figure 3.13).

In conclusion, X-ray crystallography shows that HEWL interacts with $[V^{IV}O(xant)(H_2O)_2]$ derivatives. In particular, one or three $[V^{V}O_2(xant)]^-$ ions, formed upon oxidation of the V centre, non-covalently bind the protein, while an unexpected (and never reported before) mixed valence tetrametallic species ($[V^{V}O_2(xant))_2(V^{IV}O(H_2O)_2)_2]^{2+}$) covalently binds to the side chain of Glu7 of two symmetry-related molecules. These findings indicate that i) binding of $[V^{IV}O(xant)(H_2O)_2]$ derivatives to the model protein HEWL does not alter the overall structure of the protein, ii) the V atom of $[V^{IV}O(xant)(H_2O)_2]$ can oxidize, iii) non-covalent binding to HEWL of $[V^{V}O_2(xant)]^-$ can occur; iv) HEWL can bind three $[V^{V}O_2(xant)]^-$ that are stacked to each other simultaneously, iii) the structure of $[V^{IV}O(xant)(H_2O)_2]$ can be sensibly modified in the presence of proteins forming mixed valence supramolecular species, like $[(V^{V}O_2(xant))_2(V^{IV}O(H_2O)_2)_2]^{2+}$, which can cross-link protein molecules.

Overall, these results provide crucial insights into the reactivity of V-based complexes suggesting their possible behaviour in biological environments and represent a key step toward understanding their mechanism of action as therapeutic agents.

3.4 Interaction of $[V^{IV}O(dipic)(H_2O)_2]$ with HEWL

With the aim of clarifying how the nature of the ligand influences recognition of $V^{IV}O$ complexes with tridentate ligands by proteins, the interaction of $[V^{IV}O(dipic)(H_2O)_2]$ (Figure 3.1b) with HEWL was studied. Dipic is an ONO-donor ligand that is able to stabilize unusual V oxidation states, making its derivatives attractive as potential bioactive species.[74,75]

3.4.1 Mass spectrometry studies

First, in solution behaviour of $[V^{IV}O(dipic)(H_2O)_2]$ was investigated by ESI-MS in negative mode, recording spectra in pure H_2O, and acetonitrile/methanol + 1% H_2O, a mixture that ensures a good ionization (Figure 3.14). In aqueous solution (Figure 3.14a), the spectrum shows a distribution of vanadium-containing species with one, two, or three metal centres, including $[V^{V}O_2(dipic)]^-$, $[V^{IV}O(dipic)_2{}^{2-} + H^+]^-$, $[V^{IV}V^{V}O_3(dipic)_2]^-$ and $[V^{V}{}_3O_4(dipic)_3]^-$ (Table 3.4). In acetonitrile/methanol + 1% H_2O (Figure 3.14b), most of the species detected in water are still observed (Table 3.4), except for $[V^{IV}O(dipic)_2{}^{2-} + H^+]^-$, which is absent.

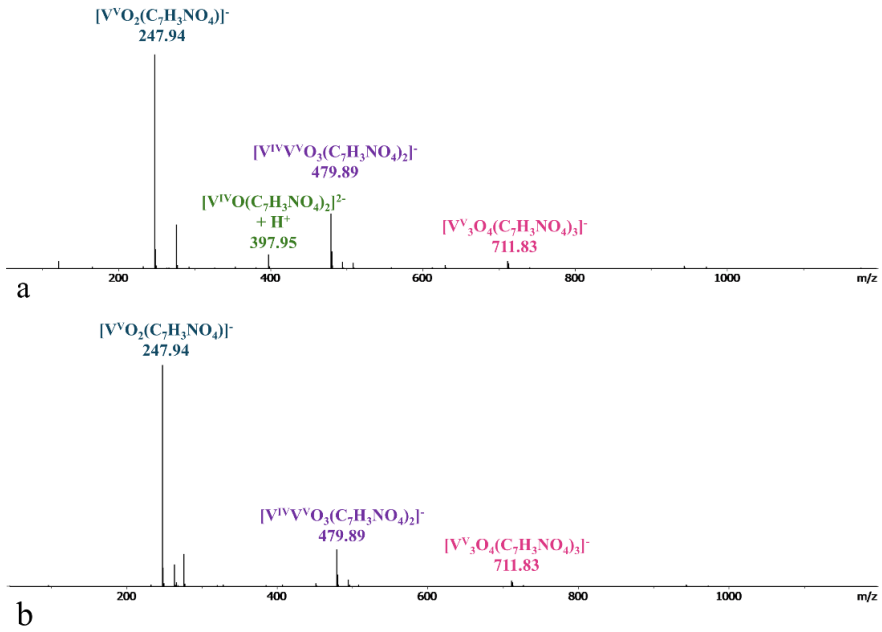

Figure 3.14 – ESI mass spectrum of $[V^{IV}O(dipic)(H_2O)_2]$ (~ 100 μM) in a) H_2O and in b) acetonitrile/methanol + 1% H_2O. The spectra were recorded in negative ion mode within the m/z range of 0 to 1200, and the spectrometer was calibrated using the standard tunemix (Bruker Daltonik GmbH, timsTOF Pro User Manual, Bremen, Germany) to

ensure an accuracy of approximately 5 ppm in the m/z region of 45-1800. These studies were carried out under the supervision of Prof. Annette Rompel from University of Vienna.

The formation of dimeric V–dipic species in solution is not unexpected, since these VCs are known to form multinuclear architectures, including dimers and even higher-order oligomers.[253–258] The detection of such species in the ESI-MS spectra thus reflects the intrinsic propensity of dipicolinate ligands to stabilize multinuclear V assemblies, a feature that may also play a role in their reactivity with proteins.

Table 3.4 – Experimental and calculated m/z values for $[V^{IV}O(dipic)(H_2O)_2]$ dissolved in H_2O and in ACN/MeOH + 1% H_2O, recorded in negative ion mode using ESI-MS.

In H_2O		
Observed species	**Experimental m/z**	**Simulated m/z**
$[V^{V}O_2(C_7H_3NO_4)]^-$	247.94 248.94	247.94 248.94
$[V^{IV}O(C_7H_3NO_4)_2]^{2-} + H^+$	397.96 398.96 399.96	397.96 398.96 399.96
$[V^{IV}V^{V}O_3(C_7H_3NO_4)_2]^-$	479.89 480.89 481.89	479.89 480.89 481.89
$[V^{V}_3O_4(C_7H_3NO_4)_3]^-$	711.83 712.83 713.84	711.83 712.83 713.84
In ACN/MeOH + 1% H_2O		
Observed species	**Experimental m/z**	**Simulated m/z**
$[V^{V}O_2(C_7H_3NO_4)]^-$	247.94 248.94	247.94 248.94
$[V^{IV}V^{V}O_3(C_7H_3NO_4)_2]^-$	397.96 398.96 399.96	397.96 398.96 399.96
$[V^{V}_3O_4(C_7H_3NO_4)_3]^-$	479.89 480.89 481.89	479.89 480.89 481.89

The positive-ion mode ESI-MS spectrum of HEWL (concentration = 13 mg/mL, 0.9 mM) diluted 1:100 in acetonitrile/H_2O (9/1) + 1% formic acid (FA) was recorded to determine the exact protein mass. Deconvolution of the spectrum, which estimates protein mass from the distribution of multiply charged ions, yields a predominant peak at 14304.9 Da (Figure 3.15a), in agreement with the expected value for the metal-free protein. In the presence of $[V^{IV}O(dipic)(H_2O)_2]$ at a 1:1 protein to metal compound molar ratio, the spectrum displays two major peaks: one at 14304.9 Da, corresponding to metal-free HEWL, and the other at 14553.8 Da, which can be assigned to $[V^{V}O_2(dipic)]^-$–HEWL adduct (Figure 3.15b).

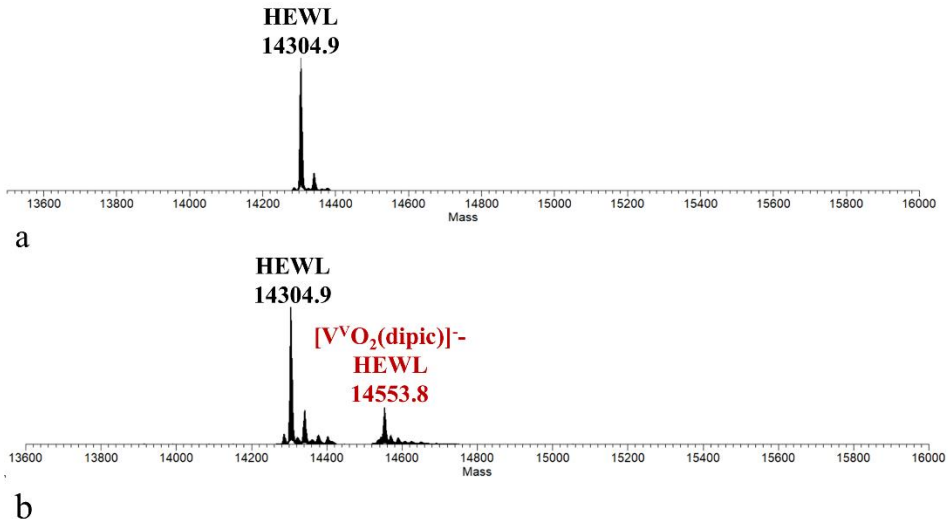

Figure 3.15 – Deconvoluted ESI-MS spectra of a) HEWL (concentration = 13 mg/mL) and b) of the system containing $[V^{IV}O(dipic)(H_2O)_2]$:HEWL in 1:1 molar ratio. Both samples were diluted 1:100 in acetonitrile/H_2O (9/1) + 1% FA. Mass is in Da. These studies were carried out under the supervision of Prof. Annette Rompel from University of Vienna.

3.4.2 Crystallographic studies

To obtain the structure of the adduct that the protein forms with $[V^{IV}O(dipic)(H_2O)_2]$, HEWL crystals were grown in two different crystallization conditions and then were exposed to stabilizing solutions containing mother liquors saturated with the metal compound for 7 days. X-ray diffraction data were collected on several crystals at resolution within the range 1.12-1.34 Å. Data collection and refinement statistics are reported in Table 3.5.

In structure A (Figure 3.16a), obtained from data collected on crystals grown in 1.1 M sodium chloride, 0.1 M sodium acetate pH 4.0, several V-containing species were detected, in agreement with the ESI-MS data (Figure 3.14).

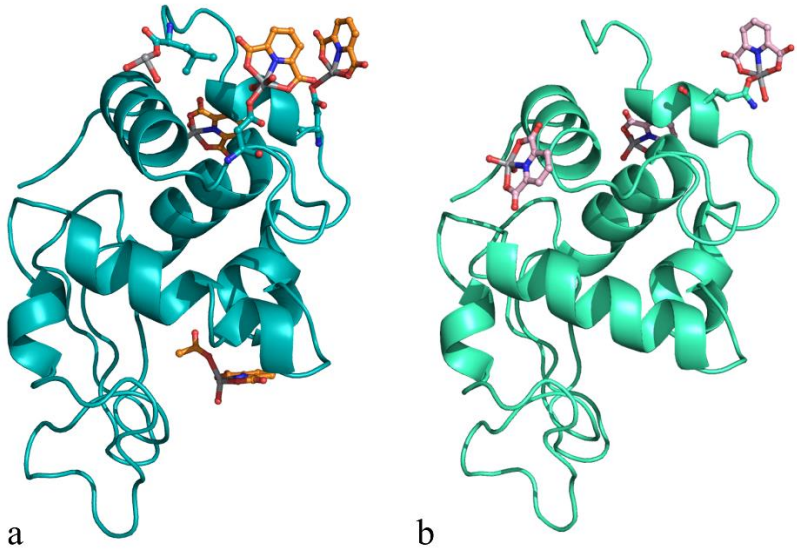

Figure 3.16 – Overall structure of the adduct formed upon reaction of $[V^{IV}O(dipic)(H_2O)_2]$ with HEWL from crystals grown in a) 1.1 M sodium chloride, 0.1 M sodium acetate at pH 4.0 (structure A), b) 20% ethylene glycol, 0.6 M sodium nitrate, 0.1 M sodium acetate at pH 4.0 (structure B). Vanadium atoms are in grey.

Table 3.5 – Data collection and statistics for the structures A and B.

Data collection		
	Structure A	Structure B
Crystallization condition	1.1 M sodium chloride, 0.1 M sodium acetate pH 4.0	20% ethylene glycol, 0.6 M sodium nitrate, 0.1 M sodium acetate pH 4.0
Soaking time	7 d	7 d
Space group	$P4_32_12$	$P4_32_12$
a (Å)	78.00	77.10
b (Å)	78.00	77.10
c (Å)	36.97	37.41
Resolution range (Å)	34.88-1.12 (1.14-1.12)	38.55-1.34 (1.37-1.34)
Observations	1008376 (38616)	303896 (7644)
Unique reflections	44109 (2149)	25659 (1243)
Completeness (%)	100.0 (100.0)	100.0 (100.0)
Redundancy	22.9 (18.0)	11.8 (6.1)
Rmerge (%)	0.053 (1.265)	0.116 (2.114)
Average I/σ(I)	29.9 (2.4)	7.8 (0.5)
$CC_{1/2}$	0.999 (0.812)	0.998 (0.378)
Anom. completeness (%)	100.0 (100.0)	100.0 (99.2)
Anom. Multiplicity	12.2 (9.3)	6.3 (3.2)
Refinement		
Resolution (Å)	34.88-1.12	38.55-1.39
N° reflections	41948	20144
N° reflections in working set	3053	342
R-factor/Rfree	0.146/0.182	0.209/0.248
N° non-H atoms in the refinement	1316	1215
B-factor overall ($Å^2$)	23.37	24.28
Estimated occupancy of $[V^VO_2(dipic)]^-$	0.80	0.40
Estimated occupancy of $[V^VO(dipic)(CH_3COO)]$ in structure A	0.70	-
Estimated occupancy of $[V^{IV}O(dipic)]$ in structure A	0.95	-
Estimated occupancy of $[V^{IV}O(dipic)(H_2O)]$ in structure A	0.80	-

Estimated occupancy of V in structure A	0.20	-
B-factor of $[V^{V}O_2(dipic)]^-$ ($Å^2$)	48.48	32.45
B-factor of $[V^{V}O(dipic)(CH_3COO)]$ ($Å^2$) in structure A	42.75	-
B-factor of $[V^{IV}O(dipic)]$ ($Å^2$) in structure A	93.39	-
B-factor of $[V^{IV}O(dipic)(H_2O)]$ ($Å^2$) in structure A	37.64	-
B-factor of V($Å^2$) in structure A	23.61	-
Estimated occupancy of $[V^{V}O_2(dipic)]^-$ in structure B	-	0.50
Estimated occupancy of $[V^{IV}O(dipic)(H_2O)]$ in structure B	-	0.90
B-factor of $[V^{V}O_2(dipic)]^-$ ($Å^2$) in structure B	-	38.99
B-factor of $[V^{IV}O(dipic)(H_2O)]$ ($Å^2$) in structure B	-	39.66
Ramachandran values (%)		
Most favoured/Additional allowed	96.43/3.57	93.22/6.78
Outliers	0	0
RMSD from ideality		
RMSD bonds (Å)	0.019	0.010
RMSD angles (°)	2.491	1.733

In particular, a [VO_2(dipic)] unit and a [$V^{V}O$(dipic)(CH_3COO)] species were found non-covalently bound to the protein surface (Figure 3.16a), while [$V^{IV}O$(dipic)(H_2O)], [$V^{IV}O$(dipic)] and an additional V-containing fragment were found covalently bound to the protein (Figure 3.16a). In the [VO_2(dipic)] unit, the V centre adopts a distorted geometry, intermediate between trigonal bipyramidal and square pyramidal. This suggests an oxidation of the V centre from +4 to +5 and the formation of the [$V^{V}O_2$(dipic)]$^-$ ion. In this ion (occupancy = 0.70), the distorted equatorial plane is occupied by the N atom of dipic and by the two O atoms of the VO_2 group, while two carboxylate oxygen atoms of dipic occupy the axial positions. This species establishes π–π stacking interactions with the side chain of Trp123 and hydrogen bonds with water molecules as well as with the side chain NE atom of Arg5 and NH2 atom of Arg125 (Figure 3.17a).

[$V^{V}O$(dipic)(CH_3COO)] (occupancy = 0.70) has one oxygen atom of the VO_2 group replaced by an O of an acetate ion from the crystallization medium (Figure 3.17b). This complex interacts through hydrogen bonds with the O atom of Ala107, the OD1 and OD2 atoms of Asp101, NE1 atom of Trp108, water molecules, and a [$V^{IV}O$(dipic)] unit from a symmetry related molecule (Figure 3.17b). The two covalently bound species ([$V^{IV}O$(dipic)(H_2O)] (occupancy = 0.80) and [$V^{IV}O$(dipic)] (occupancy = 0.95)) are coordinated to the side chains of Asp18 and Asp119 (V–O distances are in both cases equal to 2.01 Å).

[$V^{IV}O$(dipic)(H_2O)] displays an octahedral geometry stabilized by hydrogen bonds with the side chain of Asn19 and water molecules (Figure 3.17c). The coordinative binding of [$V^{IV}O$(dipic)] to Asp119 is stabilized by hydrogen bonds with a water molecule and with [$V^{V}O$(dipic)(CH_3COO)] from a symmetry-related molecule, and by π–π stacking interactions with Trp62 from a symmetry-mate (Figure 3.17d).

The last covalently bound V-containing fragment is attached to the C-terminal carboxylate of Leu129 at the interface between two symmetry-related molecules

(Figure 3.17e). This species completes its coordination sphere with three water molecules and mediates the formation of covalently linked HEWL dimers. It forms hydrogen bonds with the O atom of Ala10 and water molecules.

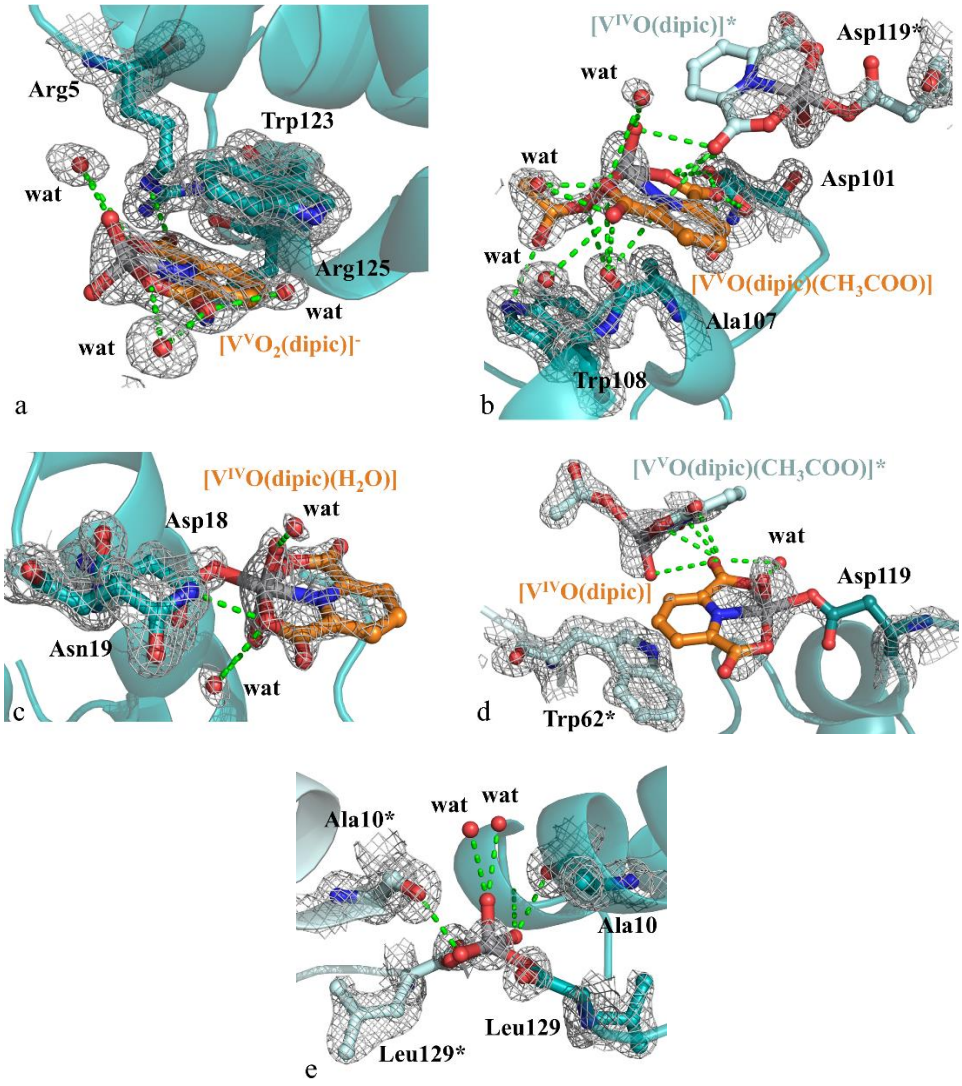

Figure 3.17 – V binding sites in the structure A: non-covalent binding of a) $[V^{V}O_2(dipic)]^-$ and b) $[V^{V}O(dipic)(CH_3COO)]$ to protein surface residues; covalent binding of c) $[V^{IV}O(dipic)(H_2O)]$ to the side chain of Asp18, d) $[V^{IV}O(dipic)]$ to the side chain of

Asp119 and e) V atom to the C-terminal carboxylate. 2Fo-Fc e.d. maps are reported at 1.0 σ level in grey. Residues from symmetry related molecules are highlighted with an asterisk (*) and coloured in pale cyan.

Three V-containing species were detected in structure B (Figure 3.16b), obtained from data collected on crystals grown in 20% ethylene glycol, 0.6 M sodium nitrate, 0.1 M sodium acetate pH 4.0. In particular, two $[V^{V}O_2(dipic)]^-$ unit (occupancy = 0.40 and 0.50 respectively) are non-covalently bound to the protein (Figure 3.18a,b). The first one occupies the same position of the equivalent species observed in the structure A: it establishes π–π stacking interactions with the side chain of Trp123 and hydrogen bonds with water molecules, nitrate anions from the crystallization condition, the NH1 atom of Arg125, and also with the O atom of Gly117 and the H_2O of a $[V^{IV}O(dipic)(H_2O)]$ from a symmetry-related molecule (Figure 3.18a). The second $[V^{V}O_2(dipic)]^-$ ion is held in its position by hydrogen bonds formed with the side chain of Arg14, that adopts two different conformations, water molecules and with the N atom of Arg128 from a symmetry-related molecule (Figure 3.18b).

The third V-containing species observed in structure B is a $[V^{IV}O(dipic)(H_2O)]$ moiety (occupancy = 0.90), that can be described as the starting compound with a water molecule replaced by the side chain OE1 atom of Gln121. $[V^{IV}O(dipic)(H_2O)]$ occupies almost the same position adopted by $[V^{IV}O(dipic)]$ in the structure A (Figure 3.19). Notably, the observed V–OE1 distance is 2.73 Å, a value significantly higher than expected. However, this value could be affected by the scarce electron density map in correspondence of the side chain of the Gln121. The binding at this site is stabilized by hydrogen bonds with water molecules, with the side chain of Asp119, and with the O atom of the VO_2 group of a $[V^{V}O_2(dipic)]^-$ ion from a symmetry-related molecule. A further

stabilizing interaction comes from π–π stacking with Trp62 from a symmetry-mate (Figure 3.18c).

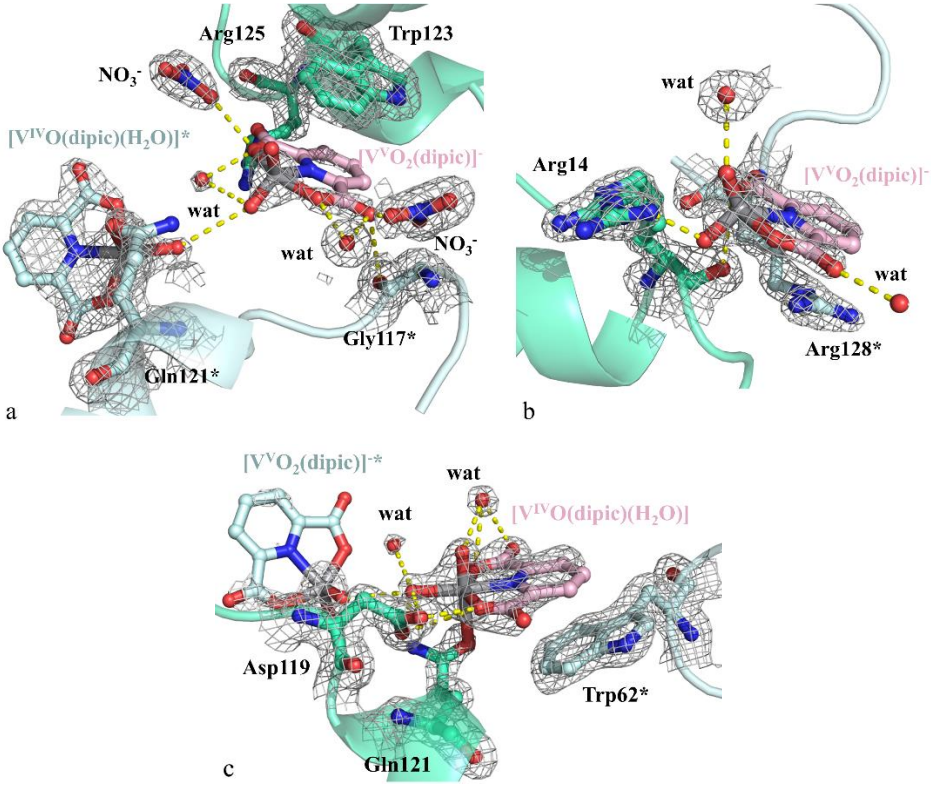

Figure 3.18 – V binding sites in the structure B: covalent binding of a) $[V^{IV}O(dipic)(H_2O)]$ to the side chain of Gln121, and non-covalent binding of two b,c) $[V^VO_2(dipic)]^-$ ions to protein surface residues. 2Fo-Fc e.d. maps are reported at 1.0 σ level in grey. Residues from symmetry related molecules are highlighted with an asterisk (*) and are coloured in pale cyan.

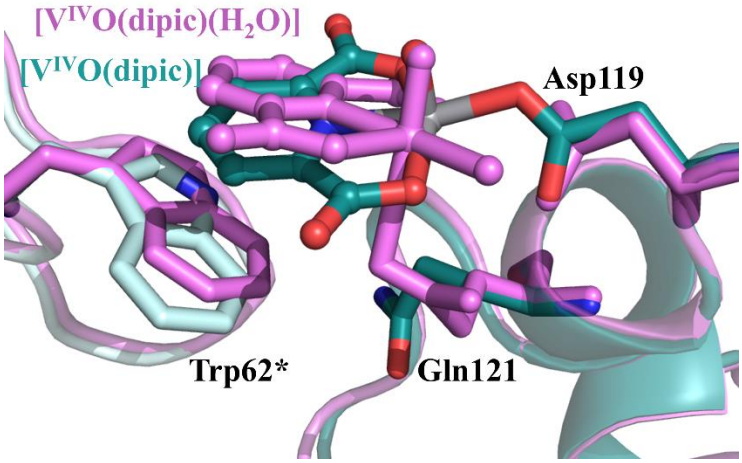

Figure 3.19 – Superimposition of the V-containing fragments that are bound close to Asp119 and Gln121 in the structures A ([$V^{IV}O$(dipic)], deep teal)) and B ([$V^{IV}O$(dipic)(H_2O)], violet), respectively. Asterisk (*) indicates residues from symmetry-related molecules.

In conclusion, mass spectrometry and X-ray crystallography results indicate that HEWL can interact with multiple [$V^{IV}O$(dipic)(H_2O)$_2$]-derived species. Upon oxidation, [$V^{V}O_2$(dipic)]$^-$ and the acetate-containing derivative [$V^{V}O$(dipic)(CH_3COO)] are stabilized through non-covalent contacts, while [$V^{IV}O$(dipic)(H_2O)], [$V^{IV}O$(dipic)] and an additional V-containing fragment establish covalent bonds with different protein residues. Remarkably, the use of different crystallization conditions leads to different results. Indeed, the comparison between the structures A and B shows that the V-containing fragments derived by [$V^{IV}O$(dipic)(H_2O)$_2$] show distinct distributions and orientations on the structure of the protein (Figure 3.17d and Figure 3.18c). These differences are influenced both by local rearrangements of protein side chains and by crystallization medium components (nitrate, acetate, water molecules).

3.5 Interaction of $[V^{IV}O(dipic)(H_2O)_2]$ with RNase A

RNase A represents a well-established model system in metalation studies due to its small size, high stability, and the presence of well-defined binding pockets that make it particularly suitable for probing metal–protein interactions.[50,186,259] Its biological relevance as an enzyme involved in RNA cleavage adds further interest, since alterations in its activity upon metal binding may provide valuable clues about possible biological effects of VCs.[50,186,259]

The binding of $[V^{IV}O(dipic)(H_2O)_2]$ to RNase A can therefore offer complementary information to that obtained with HEWL.

3.5.1 Crystallographic studies

Monoclinic crystals of RNase A with two protein molecules in the asymmetric unit, denoted as molecule A and molecule B, were grown in 22% PEG 4K, 0.01 M sodium citrate pH 5.1 and subsequently exposed to stabilizing solutions saturated with $[V^{IV}O(dipic)(H_2O)_2]$ for 6 days. X-ray diffraction data were collected on one of these crystals at 1.80 Å resolution. Data collection and refinement statistics are reported in Table 3.6.

Table 3.6 – Data collection and refinement statistics.

Data collection	
	Structure of RNase A treated with $[V^{IV}O(dipic)(H_2O)_2]$
Crystallization condition	22% PEG 4K, 0.01 M sodium citrate pH 5.1
Soaking time	6 d
Space group	*C2*
a (Å)	100.19
b (Å)	32.21
c (Å)	68.89
α/β/γ (°)	90.0/91.4/90.0
Resolution range (Å)	41.00-1.80 (1.83-1.80)
Observations	102584 (5369)
Unique reflections	18977 (1017)
Completeness (%)	90.9 (99.8)
Redundancy	5.4 (5.3)
Rmerge (%)	0.137 (2.139)
Average I/σ(I)	7.4 (0.7)
$CC_{1/2}$	0.996 (0.333)
Anom. completeness (%)	88.5 (98.6)
Anom. Multiplicity	2.9 (2.7)
Refinement	
Resolution (Å)	41.00-1.80
N° reflections	15891
N° reflections in working set	276
R-factor/Rfree	0.244/0.278
N° non-H atoms in the refinement	1987
B-factor overall ($Å^2$)	29.12
Estimated occupancy of $[V^{IV}O(dipic)(H_2O)]$	0.75
B-factor of $[V^{IV}O(dipic)(H_2O)]$ ($Å^2$)	20.42
Ramachandran values (%)	
Most favoured/Additional allowed	93.44/6.56
Outliers	6
RMSD from ideality	
RMSD bonds (Å)	0.007
RMSD angles (°)	1.524

Inspection of the electron density maps reveals that the V complex binds to molecule A, while molecule B remains unaltered. The comparison of the structures of molecules A and B furnishes a detailed picture of the structural modifications associated with the V complex binding. The superimposition of the two protein molecules in the asymmetric unit of the adduct indicates that the binding of the VC induces only small variations in the structure of the protein. In fact, the two molecules present RMSD of the Cα atom of 0.67 Å.

Inspection of the electron density maps indicates the presence of only one V centre bound to the protein. Metalation occurs at the C-terminal tail of chain A, where the terminal carboxylate replaces a water ligand of $[V^{IV}O(dipic)(H_2O)_2]$ (occupancy = 0.75), resulting in the formation of a covalent adduct (Figure 3.20a). This binding is stabilized by hydrogen bonds involving the main chain N atom and the ND1 atom of His105, water molecules, and the side chain OG1 atom of Thr3 from a symmetry-related molecule (Figure 3.20b).

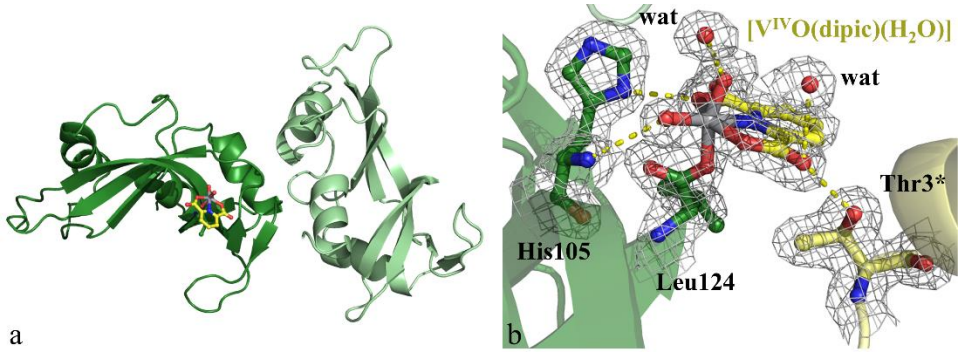

Figure 3.20 – a) Overall structure of the adduct formed upon reaction of $[V^{IV}O(dipic)(H_2O)_2]$ with RNase A. b) Covalent binding of $[V^{IV}O(dipic)(H_2O)]$ to the C-terminal carboxylate. 2Fo-Fc e.d. maps are reported at 1.0 σ level in grey. Amino acid residues from symmetry related molecules are highlighted with an asterisk (*) and coloured in yellow.

Although only one binding site was identified, this result is highly informative. The observation that C-terminal carboxylate acts as an anchoring group suggests that exposed terminal residues can play a central role in stabilizing V species.

Overall, this study provides preliminary but significant insights into how V–protein recognition can occur in different structural protein contexts and contributes to a broader understanding of the possible modes of action of VCs in biological environments.

3.6 $[V^{IV}O(xant)(H_2O)_2]$ vs $[V^{IV}O(dipic)(H_2O)_2]$

The interaction of VCs with proteins is strongly influenced by the chemical nature of the ligands, which modulates both their stability in solution and their reactivity in the protein environment. A comparison between $[V^{IV}O(xant)(H_2O)_2]$ and $[V^{IV}O(dipic)(H_2O)_2]$ illustrates how different tridentate ligands can lead to marked differences in the binding to the protein.

In 1.1 M sodium chloride, 0.1 M sodium acetate pH 4.0, $[V^{IV}O(xant)(H_2O)_2]$ undergoes oxidation to $[V^{V}O_2(xant)]^-$ species, which non-covalently bind HEWL forming supramolecular species of up to three molecules. Moreover, $[V^{IV}O(xant)(H_2O)_2]$ speciation leads to the formation of an unprecedented mixed-valence tetrametallic species, $[(V^{V}O_2(xant))_2(V^{IV}O(H_2O)_2)_2]^{2+}$, which binds covalently the Glu7 from two symmetry-related molecules. $[V^{IV}O(dipic)(H_2O)_2]$ gives rise to a different pattern of interactions. Indeed, it can form V-moieties that interact with proteins through covalent and non-covalent interactions. Notably, in the case $[V^{IV}O(dipic)(H_2O)_2]$, multinuclear species like those formed by $[V^{IV}O(xant)(H_2O)_2]$ are not observed. Upon oxidation, $[V^{V}O_2(dipic)]^-$ and the acetate-containing derivative $[V^{V}O(dipic)(CH_3COO)]$ establish hydrogen bonds and π–π stacking contacts with specific residues of the protein. At the same time, $[V^{IV}O(dipic)(H_2O)]$ and $[V^{IV}O(dipic)]$ fragments covalently bind to Asp18 and

Asp119, respectively, while a low-occupancy V atom coordinates to the C-terminal carboxylate of Leu129, promoting protein dimerization.

In 20% ethylene glycol, 0.6 M sodium nitrate and 0.1 M sodium acetate pH 4.0, $[V^{IV}O(xant)(H_2O)_2]$ undergoes oxidation to form a $[V^{V}O_2(xant)]^-$ species, which non-covalently binds HEWL, while $[V^{IV}O(dipic)(H_2O)_2]$ forms three V-containing species: two $[V^{V}O_2(dipic)]^-$ unit non-covalently bound to the protein and a $[V^{IV}O(dipic)(H_2O)]$ moiety, that can be described as the starting VC with a water molecule replaced by the side chain of Gln121.

Overall, the comparison between $[V^{IV}O(xant)(H_2O)_2]$ and $[V^{IV}O(dipic)(H_2O)_2]$ underscores the diverse chemical reactivity of VCs upon protein binding and how this behaviour is affected by the structural features of different VC ligands. While $[V^{IV}O(xant)(H_2O)_2]$ tends to oxidize, stack, and self-assemble into unusual multinuclear species, $[V^{IV}O(dipic)(H_2O)_2]$ forms a broader range of non-covalent and covalent adducts strongly dependent on crystallization conditions. These findings suggest the structural adaptability of VCs in biological environments, a property that may be crucial for their pharmacological action.

3.7 Materials and methods

UV-visible absorption spectroscopy

Spectra of $[V^{IV}O(xant)(H_2O)_2]$ (concentration = 20 μM) were collected over time at room temperature in:

- DMSO 100%
- 0.4% DMSO - 99.6% PBS pH 7.4
- Milli-Q water
- 10 mM HEPES pH 7.5

Additionally, it was titrated with MeIm in 10 mM HEPES buffer at pH 7.5. During titration, increasing molar ratios of V complex to MeIm were employed:

1:1, 1:2, 1:3, 1:4, 1:5, 1:6, 1:7, 1:8, 1:9, and 1:10. After each addition, the samples were stirred and allowed to equilibrate for 2 minutes prior to data acquisition.

Spectra of $[V^{IV}O(xant)(H_2O)_2]$ (concentration = 63 μM) were also collected over time at room temperature in:

- 1.1 M sodium chloride, 0.1 M sodium acetate pH 4.0
- 20% ethylene glycol, 0.6 M sodium nitrate, 0.1 M sodium acetate pH 4.0
- 14% PEG 8000, 0.1 M sodium citrate, 0.05 M sodium cacodylate pH 6.5
- 0.8 M succinic acid pH 7.0
- 2.0 M sodium formate, 0.1 M HEPES pH 7.5

in the absence and presence of HEWL (protein to metal molar ratio 1:3).

All measurements were collected employing a Jasco V750 spectrophotometer using the following parameters: wavelength range of 700-200 nm, data interval of 1.0 nm, bandwidth of 2.0 nm, and scan speed of 400 nm min^{-1}. Each measurement was performed at least twice independently in duplicate using a quartz cuvette with a path length of 1.0 cm.

Circular dichroism

Far UV-CD spectra of HEWL, in the absence and presence of $[V^{IV}O(xant)(H_2O)_2]$, were registered in the 250-190 nm range using a Jasco J-1500 spectropolarimeter equipped with a Peltier thermostatic cell. Spectra were registered using a protein concentration of 7 μM and different concentrations of the VCs (1:1, 1:3, and 1:5 protein-to-metal ratio) on samples of the protein incubated for 24 hours, 48 hours, and 7 days with the VC. Spectra were acquired in i) 10 mM sodium acetate pH 4.0, ii) 10 Mm sodium cacodylate pH 6.5, iii) 10 mM succinic acid pH 7.0, iv) 10 mM HEPES pH 7.5 using a quartz cell with a path length of 0.1 cm. Additional experimental parameters were: data pitch of 1.0 nm, bandwidth of 1.0 nm, scanning speed of 50 nm per minute, response time of 2.0

seconds, and a temperature of 25°C. Each spectrum was generated by averaging three scans, and each measurement was performed twice.

Fluorescence

A HORIBA Fluoromax-4 spectrofluorometer, equipped with a thermostat bath and a 1 cm path length cuvette, was employed to record fluorescence spectra of a HSA solution (concentration = 1.4 μM) titrated with a 60.0 μM aqueous solution of $[V^{IV}O(xant)(H_2O)_2]$ at 25°C in 10 mM HEPES pH 7.5.

Additionally, HEWL solution (concentration = 1.4 μM) titrated with $[V^{IV}O(xant)(H_2O)_2]$ at 25°C in i) 10 mM sodium acetate pH 4.0, ii) 10 mM sodium cacodylate pH 6.5, iii) 10 mM succinic acid pH 7.0, iv) 10 mM HEPES pH 7.5. To collect the spectra, a HEWL solution at a concentration of 1.4 μM was titrated with a solution of the VC dissolved in water at a concentration of 60 μM.

The protein was excited at 280 nm (to monitor Tyr and Trp emission) and 295 nm (to monitor Trp emission exclusively) and spectra were registered between 295 and 450 nm and between 310 and 450 nm, respectively. Various protein-to-VC molar ratios were achieved during titration: 1:0.2, 1:0.4, 1:0.6, 1:0.8, 1:1, 1:2, and 1:4. Solutions were stirred and allowed to equilibrate for 5 minutes before recording the spectra. Self-absorbance and inner-filter effects were limited since at the used concentrations the VC has an ignorable absorbance. Emission spectra of the VC at 5.6 μM, *i.e.* the highest concentration reached during the titration, were also registered as control. Each measurement was repeated twice.

Mass spectrometry

Mass spectra of the $[V^{IV}O(dipic)(H_2O)_2]$ (concentration ~ 100 μM) were collected in H_2O, and acetonitrile/methanol + 1% H_2O in negative mode on timsTOF flex LC-MS System supplied by Bruker Daltonics Ltd. The spectra were recorded in positive and negative ion mode within the m/z range of 0 to 1200, and the

spectrometer was calibrated using the standard tunemix (Bruker Daltonik GmbH, timsTOF Pro User Manual, Bremen, Germany) to ensure an accuracy of approximately 5 ppm in the m/z region of 45-1800. Spectra were analysed using Bruker Daltonics Data Analysis 4.0 software. Other settings: capillary voltage: 2500 V, nebulizer: 0.3 Bar, dry gas flow: 3.0 L/min (Nitrogen), dry heater Temperature: 200°C, flow rate: 3 µL/min.

Mass spectra of HEWL (concentration = 13 mg/mL, 0.9 mM in distilled water) in the absence and in the presence of the $[V^{IV}O(dipic)(H_2O)_2]$ (HEWL:VC molar ratio 1:1) were collected after diluting the sample 1:100 in acetonitrile/H_2O (9/1) + 1% formic acid (FA) in positive mode on timsTOF flex LC-MS System supplied by Bruker Daltonics Ltd. Spectra were deconvoluted using MagTran software. Other settings: capillary voltage: 3500 V, nebulizer: 0.3 Ba, dry gas flow: 3.0 L/min (Nitrogen), dry heater Temperature: 200°C, mass range: 300-3000 m/z.

Crystallization, adduct formation, data collection, structure resolution and refinement

HEWL (concentration = 13 mg/mL, 0.9 mM) was crystallized using the hanging drop vapour diffusion method in:

- 1.1 M sodium chloride, 0.1 M sodium acetate pH 4.0
- 20% ethylene glycol, 0.6 M sodium nitrate, 0.1 M sodium acetate pH 4.0
- 14% PEG 8000, 0.1 M sodium citrate, 0.05 M sodium cacodylate pH 6.5
- 0.8 M succinic acid pH 7.0
- 2.0 M sodium formate, 0.1 M HEPES pH 7.5

Pre-formed HEWL crystals were then exposed to stabilizing solutions containing the mother liquor saturated with $[V^{IV}O(xant)(H_2O)_2]$ and $[V^{IV}O(dipic)(H_2O)_2]$ for a soaking time of 7 days and were cryopreserved for X-ray diffraction by transfer into a solution consisting of 70 % reservoir solution and

30 % glycerol. The crystals were then fished with a nylon loop, rapidly cooled in liquid nitrogen and then sent to synchrotron. X-ray diffraction data were collected at the ID23–1 beamline of European Synchrotron Radiation Facility (ESRF), Grenoble (France), except for the HEWL crystals treated with $[V^{IV}O(xant)(H_2O)_2]$ in 14% PEG 8000, 0.1 M sodium citrate, 0.05 M sodium cacodylate pH 6.5, whose data were collected at the XRD2 Beamline at Elettra synchrotron, Trieste (Italy). Crystals diffract at high resolution (1.11-1.48 Å) at 100 K. Data processing and scaling were performed using Global Phasing autoPROC pipeline.[232] HEWL crystals belong to the space group $P4_32_12$ and present a single protein molecule in the asymmetric unit. The structures were solved by the Molecular Replacement method using the Phaser program from CCP4 suite[233] and the structure 193L[194] as template. Refmac5 was used for refinement.[234] Model building was carried out using Coot.[235] In all the structures, V atom position was validated using anomalous difference e.d. maps. The final models show R-factor and Rfree values in the range of 0.131-0.211 and 0.171-0.248 respectively. Ligand positions were restrained to guide geometry optimization. Figures were generated using PyMol (www.pymol.org). The structure validation of the final models was performed using the PDB validation server.[236]

RNase A (concentration = 22 mg/mL, 1.6 mM) was crystallized using the hanging drop vapour diffusion method in 22% PEG 4K, 0.01 M sodium citrate pH 5.1. Crystals grew in 2 weeks at 20°C. Metal-free RNase A crystals were exposed to a solution of the reservoir saturated with $[V^{IV}O(dipic)(H_2O)_2]$ for 7 days. X-ray diffraction data were collected at the XRD2 Beamline at Elettra synchrotron, Trieste (Italy). Crystals diffract at 1.80 Å resolution at 100 K. Data processing and scaling were performed using Global Phasing autoPROC pipeline.[232] HEWL crystals belong to the space group *C*2. The structures were solved by the Molecular Replacement method using the Phaser program from CCP4 suite[233] and the structure 1JVT[260] as template. Refmac5 was used for refinement.[234] Model building

was carried out using Coot.[235] In all the structures, V atom position was validated using anomalous difference e.d. maps. The final models show R-factor and Rfree values 0.246/0.278 respectively. Ligand positions were restrained to guide geometry optimization. Figures were generated using PyMol (www.pymol.org). The structure validation of the final models was performed using the PDB validation server.[236]

CHAPTER 4

$V^{V}O_2$-hydrazonate complexes: the cases of VC1, VC2 and VC3

4.1 Introduction

Among the various families of dioxidovanadium(V) compounds, aroylhydrazone-based complexes emerge as promising systems due to their structural versatility and potential biological relevance.[95,105] Within this class, VC1 (Figure 4.1a) has attracted considerable attention due to its cytotoxic activity against several cancer cell lines;[95] VC2 (Figure 4.1b), a structural analogue of VC1 is designed to explore the impact of ligand substitution on biological activity; VC3 (Figure 4.1c), differing from VC1 for the replacement of an oxygen atom with sulphur, provides a system to assess how this structural change can affect protein binding and cytotoxicity.

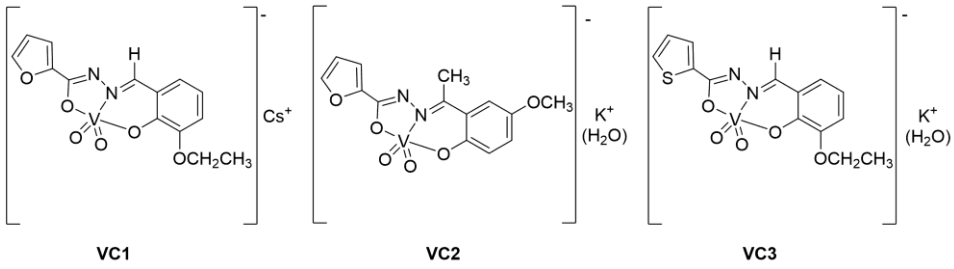

Figure 4.1 – Chemical structures of $V^{V}O_2$-hydrazonate complexes: a) VC1, b) VC2, c) VC3.

4.2 Interaction of VC1 and VC2 with HEWL

The molecular basis of the mechanism of action of V-based drugs is only partially understood, and literature lacks structural studies on the interaction of dioxidovanadium(V) aroylhydrazone complexes with proteins.

To fill this gap, the reaction of VC1 (Figure 4.1a) and VC2 (Figure 4.1b) with HEWL was investigated using a combination of spectroscopic (UV-vis

spectroscopy, fluorescence, CD) and crystallographic techniques, to evaluate the interaction in solution and in solid state.

4.2.1 UV-vis absorption spectroscopy

First, to verify VC1 and VC2 stability in the chosen experimental conditions, in the absence (Figure 4.2a,c) and in the presence of HEWL (Figure 4.2b,d), UV-vis absorption spectra were collected in a solution containing 1.1 M sodium chloride and 0.1 M sodium acetate pH 4.0.

VC1 spectrum shows peaks at 225, 336 and 407 nm and a shoulder between 270 and 290 nm (Figure 4.2a). The strong absorption band at 407 nm can be attributed to ligand-to-metal charge transfer (LMCT) transitions, while the peak at 336 nm likely arises from a ligand-centred transition.[95] The overlap of the spectra collected over time indicates that VC1 is not completely stable under these experimental conditions. In particular, the appearance of an isosbestic point at 275 nm, after 24 h incubation, suggests the occurrence of hydrolysis or decomposition, according to the equilibrium reactions: $[V^{V}O_2(L^1)]^- + 2H^+ \rightleftarrows V^{V}O_2^+ + H_2L^1$ and $V^{V}O_2^+ + 2H_2O \rightleftarrows H_2V^{V}O_4^- + 2H^+$ (where H_2L^1 is the furan-2-carboxylic acid (3-ethoxy-2-hydroxybenzylidene)hydrazide ligand). These reactions are favoured by acid pH which prompts $(L^1)^{2-}$ protonation and consequent complex dissociation. These data are in contrast with previous findings about VC1 stability in pure water, in Tris-HCl at pH 7.4, and in DMSO,[95] and underline the influence of the experimental environment on the compound integrity.

A similar behaviour is observed in the presence of HEWL (Figure 4.2c).

VC2 spectrum is characterized by four peaks at 220, 297, 320, and 379 nm (Figure 4.2b). Given its structural similarity to VC1, the band at 379 nm is attributed to a LMCT transition, while the others correspond to ligand-centred transitions. Over time, the peak at 220 nm remains stable, while that at 297 nm disappears after 24 h. The peaks at 320 and 379 nm significantly decrease in intensity

over time just after 24 h. Interestingly, the spectrum collected after 24 h reveals the presence of a new peak at 254 nm, which becomes well-resolved after 6 days. This behaviour suggests partial VC2 decomposition.

In the presence of HEWL, VC2 spectral profile has a similar trend (Figure 4.2d) suggesting that decomposition reactions are induced by the experimental conditions and not by interaction with the protein.

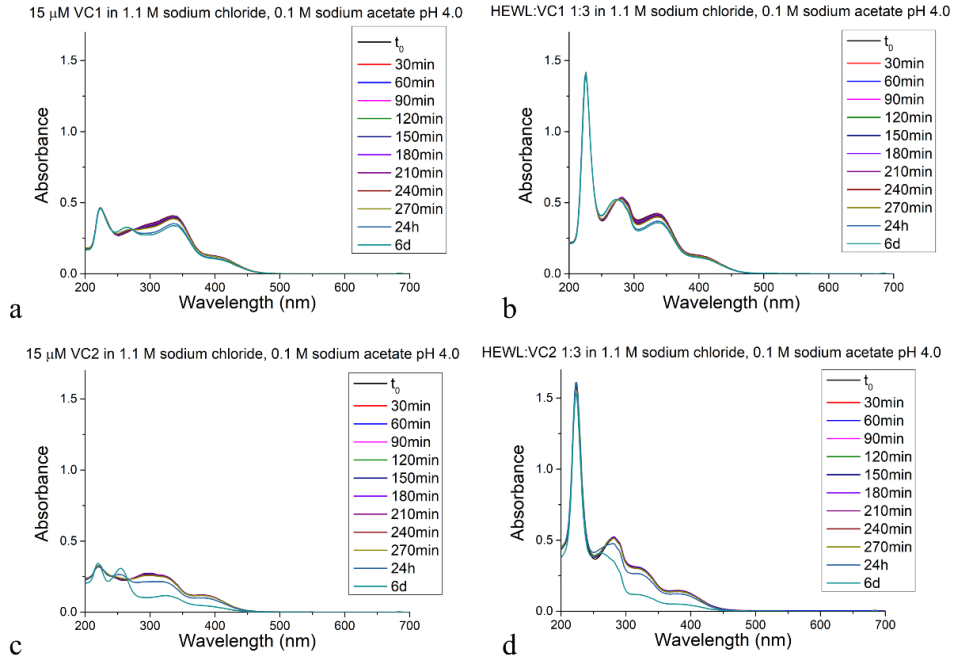

Figure 4.2 – UV-vis spectra as a function of time of a,b) VC1 and c,d) VC2 in 1.1 M sodium chloride and 0.1 M sodium acetate at pH 4.0. In panels b and d the spectra of the compounds are collected in the presence of HEWL using a 3:1 VC-to-protein molar ratio (protein and VC concentrations were 5 and 15 μM, respectively).

4.2.2 Circular dichroism

To assess the effect of VC1 and VC2 binding on HEWL secondary structure content, far-UV CD spectra of the protein were recorded in the absence and in the

presence of the two VCs at 1:1, 1:3, and 1:5 protein to metal molar ratios. Measurements were carried out in 10 mM sodium acetate pH 4.0 after 24 h (Figure 4.3a,d), 48 h (Figure 4.3b,e), and 6 d (Figure 4.3c,f) of incubation. The collected CD spectra are almost superimposable, indicating that VC1 and VC2 binding to HEWL does not affect protein folding.

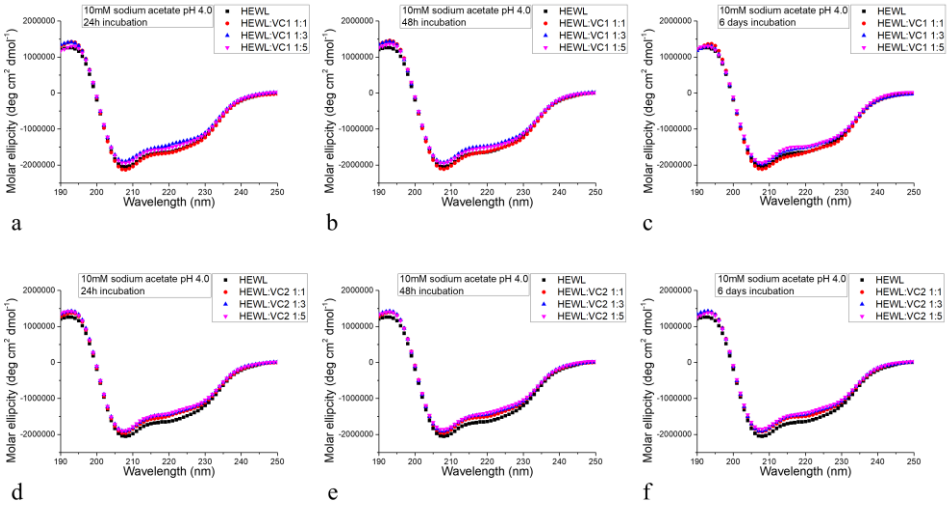

Figure 4.3 – Far-UV CD spectra of HEWL (concentration = 7.0 µM) incubated for a,d) 24 h, b,e) 48 h, c,f) 6 d in the presence of a-c) VC1 and d-f) VC2 in 10 mM sodium acetate pH 4.0 at protein-to-VC molar ratio = 1:1 (red), 1:3 (blue) and 1:5 (violet). CD of metal-free protein is in black.

4.2.3 Fluorescence spectroscopy

To evaluate a possible effect of VC binding on the tertiary structure of HEWL, fluorescence spectroscopy was used. Fluorescence spectra of HEWL (concentration = 1.4 µM) were collected in 10 mM sodium acetate pH 4.0 in the presence of increasing concentrations of VC1 and VC2 (Figure 4.4) upon excitation at 280 and 295 nm, respectively. The addition of both VCs to HEWL results in a

concentration-dependent decrease in the protein fluorescence intensity, suggesting the occurrence of VC-HEWL interaction.

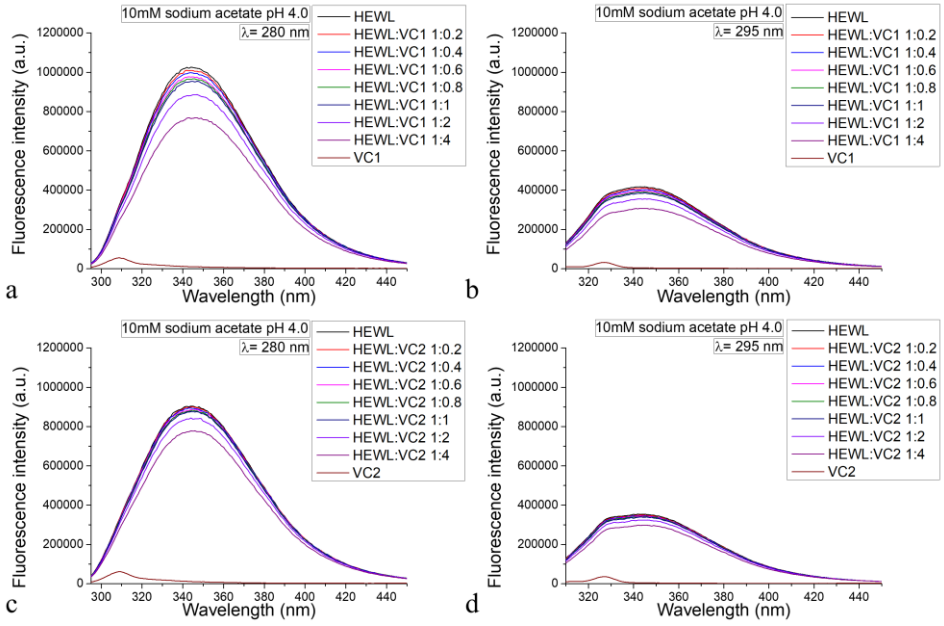

Figure 4.4 – Fluorescence emission spectra of HEWL in 10 mM sodium acetate pH 4.0 upon titration with a solution of a,b) VC1 and c,d) VC2. Spectra were collected using a,c) λ_{exc} = 280 nm and b,d) λ_{exc} = 295 nm.

4.2.4 Crystallographic Studies

Crystals of the metal-free protein, grown in 1.1 M sodium chloride and 0.1 M sodium acetate pH 4.0, were exposed for 6 days to stabilizing solutions containing the mother liquor saturated with VC1 and VC2 (Figure 4.5), respectively. Data collection and refinement statistics are reported in Table 4.1.

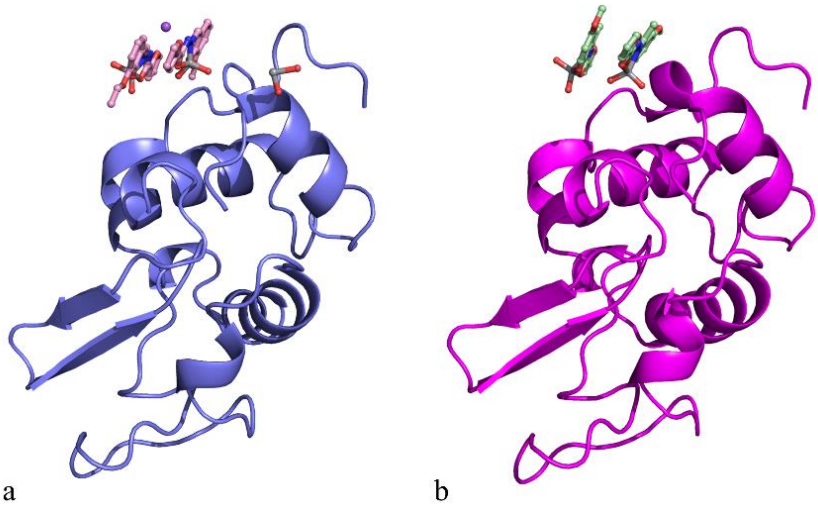

Figure 4.5 – Overall structures of the adducts formed upon reaction with HEWL of a) VC1 and b) VC2. V atoms are in grey. Coordinates and structure factors were deposited in the PDB under the accession codes 9GOG and 9GOK.

Table 4.1 – Data collection and refinement statistics.

Data collection		
	Structure of HEWL treated with VC1	Structure of HEWL treated with VC2
PDB code	9GOG	9GOK
Crystallization condition	1.1 M sodium chloride, 0.1 M sodium acetate pH 4.0	1.1 M sodium chloride, 0.1 M sodium acetate pH 4.0
Soaking time	6 d	6 d
Space group	$P4_32_12$	$P4_32_12$
a (Å)	76.85	76.67
b (Å)	76.85	76.67
c (Å)	36.84	36.80
Resolution range (Å)	54.34-1.24 (1.26-1.24)	38.34-1.18 (1.20-1.18)
Observations	832405 (40283)	657340 (5752)
Unique reflections	32110 (1555)	34130 (1027)
Completeness (%)	100.0 (100.0)	92.1 (55.8)
Redundancy	25.9 (25.9)	19.3 (5.6)
Rmerge (%)	0.085 (6.381)	0.080 (1.726)
Average I/σ(I)	15.0 (0.4)	16.1 (0.6)
$CC_{1/2}$	0.999 (0.412)	0.999 (0.376)
Anom. completeness (%)	100.0 (100.0)	91.7 (54.7)
Anom. Multiplicity	13.8 (13.5)	10.3 (3.0)
Refinement		
Resolution (Å)	54.34-1.24	38.34-1.18
N° reflections	30200	29112
N° reflections in working set	2102	244
R-factor/Rfree	0.203/0.256	0.159/0.221
N° non-H atoms in the refinement	1244	1258
B-factor overall ($Å^2$)	24.68	22.00
Estimated occupancy of $V^VO_2^+$	0.70	-
Estimated occupancy of VC1 (1)	0.70	-
Estimated occupancy of VC1 (2)	0.70	-

B-factor of $V^{V}O_2^+$ (Å^2)	38.35	-
B-factor of VC1 (1) (Å^2)	33.92	-
B-factor of VC1 (2) (Å^2)	41.52	-
Estimated occupancy of VC2 (1)	-	0.60
Estimated occupancy of VC2 (2)	-	0.60
B-factor of VC2 (1) (Å^2)	-	36.37
B-factor of VC2 (2) (Å^2)	-	75.42
Ramachandran values (%)		
Most favoured/Additional allowed	92.59/7.41	94.78/5.22
Outliers	0	0
RMSD from ideality		
RMSD bonds (Å)	0.014	0.017
RMSD angles (°)	1.860	2.302

Binding of VC1 to HEWL

In the structure of HEWL in the presence of VC1 (Figure 4.5a) non-covalent binding of a $V^{V}O_2^+$ ion (occupancy = 0.70) and of two VC1 molecules (occupancy = 0.70) to the protein was observed. The $V^{V}O_2^+$ ion forms hydrogen bonds with the main chain atoms of Cys6 and Glu7 (Figure 4.6a), while the two VC1 molecules, named VC1 (1) and VC1 (2), interact with each other to form a dimeric assembly (Figure 4.6b). The coexistence of both $[V^{V}O_2(L^1)]^-$ and $V^{V}O_2^+$ species is consistent with the partial VC1 decomposition suggested by the UV-vis spectra (Figure 4.2a,b).

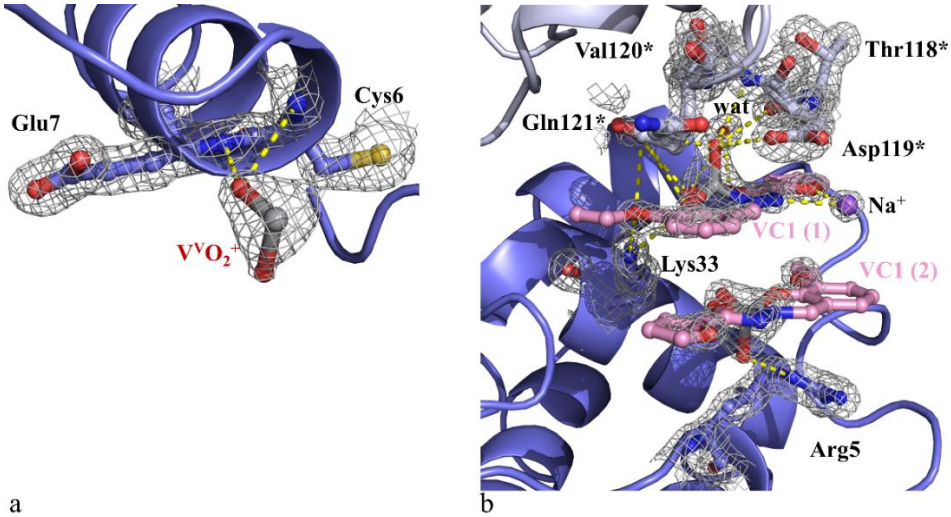

Figure 4.6 – Vanadium binding sites in the structure of the adduct formed upon reaction of HEWL with VC1. a) Interaction of the $V^{V}O_2^+$ group with protein atoms, b) supramolecular association of the two VC1 molecules and their interaction with protein atoms. 2Fo-Fc e.d. maps are contoured at 1.0 σ level and depicted in grey.

VC1 (1) forms hydrogen bonds with water molecules, the NZ atom of Lys33 and the O atom of Thr118. Additional interactions involve the N atom of Val120, the OD1 atom of Asp119, and the NE2 atom of Gln121 from a symmetry related

molecule (Figure 4.6b, Table 4.2). VC1 (2) forms a hydrogen bond with the NE atom of Arg5 (Figure 4.6b, Table 4.2).

Table 4.2 – Interactions between VCs and protein atoms and their distances (Å).

Hydrogen bond		
Donor	Acceptor	distance (Å)
O1 VC1 (1)	NZ Lys33	3.4
O1 VC1 (1)	NE2 Gln121*	3.5
O2 VC1 (1)	OH_2	3.1
O3 VC1 (1)	NZ Lys33	3.0
O3 VC1 (1)	NE2 Gln121*	3.2
O4 VC1 (1)	OD1 Asp119*	3.7
O4 VC1 (1)	NE2 Gln121*	3.3
O5 VC1 (1)	OH_2	3.6
O4 VC1 (2)	NE Arg5	3.0
O1 VC2 (1)	NZ Lys33	3.7
O2 VC2 (1)	OH_2	3.1
O5 VC2 (1)	OH_2	2.8
O6 VC2 (1)	O Gln117*	3.2
O4 VC2 (2)	OH_2	3.1
O4 VC2 (2)	OH_2	3.5
O5 VC2 (2)	NZ Lys33	2.5
N1 VC2 (2)	OH_2	2.9
N2 VC2 (2)	OH_2	3.5
Non-covalent interactions		
O4 VC1 (1)	O Thr118*	3.5
O4 VC1 (1)	N Val120*	3.1
O6 VC1 (1)	Na^+	2.3
N2 VC1 (1)	Na^+	3.2
O4 VC2 (1)	O Thr118*	3.7
O4 VC2 (1)	N Val120*	3.2
O4 VC2 (1)	N Gln121*	3.5

In the two VC1 molecules, the V^V centre is penta-coordinated and completes its coordination sphere with the tridentate ligand and two O atoms. Selected geometrical parameters of VC1 molecules bound to HEWL are listed in Table 4.3 in comparison with the values found in single crystals of VC1 and of its analogues denoted as **2** (*i.e.*, $K[V^VO_2(L^1)]\cdot 2H_2O$)[95] and **3** (*i.e.*, $K[V^VO_2(L^x)]\cdot 2H_2O$, where L^x is the derivative of L^1 with a pyridine instead a furan ring).[95]

Table 4.3 – Selected bond lengths (Å) and angles (°) for VC1 and VC2 in their adducts with HEWL. Values are compared with those found in single crystals of VC1 and its analogues **2** and **3**.

	VC1 (1)/HEWL[a]	VC1 (2)/HEWL[a]	VC2 (1)/HEWL[b]	VC2 (2)/HEWL[b]	VC1 [95 c]	**2** [95 c,d]	**3** [95 c,e]
Bond	Length (Å)	Length (Å)	Length (Å)	Length (Å)	Length (Å)	Length (Å)	Length (Å)
V–O1	1.92	1.92	1.91	1.92	1.921(3)	1.9036(15)	1.9179(13)
V–O2	2.00	2.00	2.00	2.00	1.999(3)	1.9765(15)	1.9797(13)
V–O4	1.64	1.63	1.64	1.65	1.632(3)	1.6234(16)	1.6206(13)
V–O5	1.65	1.65	1.65	1.65	1.651(3)	1.6466(16)	1.6370(13)
V–N1	2.13	2.12	2.13	2.14	2.134(3)	2.1405(18)	2.1376(15)
N1–N2	1.40	1.40	1.41	1.40	1.405(4)	1.404(2)	1.404(2)
N1–C7	1.30	1.30	1.31	1.30	1.302(5)	1.295(3)	1.295(2)
N2–C8	1.30	1.30	1.31	1.30	1.297(5)	1.303(3)	1.306(2)
C1–O1	1.32	1.32	1.32	1.32	1.318(5)	1.330(3)	1.324(2)
C8–O2	1.31	1.31	1.31	1.31	1.307(4)	1.306(3)	1.297(2)
Angle	Value (°)	Value (°)	Value (°)	Value (°)	Value (°)	Value (°)	Value (°)
O1–V–O2	137.66	133.33	141.61	139.88	148.29(11)	148.42(6)	152.29(5)
O1–V–O4	107.47	115.10	102.78	104.63	106.00(12)	104.28(7)	102.30(6)
O1–V–O5	97.02	87.14	97.90	91.53	95.41(12)	93.97(7)	95.91(6)
O1–V–N1	81.18	79.41	80.41	81.77	82.18(11)	82.52(7)	82.93(5)
O2–V–O4	109.41	108.48	110.60	112.96	100.48(13)	101.98(7)	99.95(6)
O2–V–O5	88.23	89.91	86.76	88.27	91.52(12)	93.10(7)	91.79(6)
O2–V–N1	71.36	73.54	76.26	73.32	73.41(11)	73.67(6)	73.75(5)
O4–V–O5	111.57	114.18	112.24	110.43	110.11(14)	110.30(9)	109.94(7)
O4–V–N1	102.28	105.55	98.95	109.12	107.39(12)	105.73(8)	111.09(6)
O5–V–N1	144.83	140.08	148.20	140.30	141.54(13)	143.51(8)	138.21(7)

[a] VC1 (1) and VC1 (2) indicate the two molecules bound to HEWL forming the dimeric assembly. [b] VC2 (1) and VC2 (2) indicate the two molecules bound to HEWL forming the dimeric assembly. [c] Data from ref. [95] with errors in parenthesis. [d] The complex **2** is $K[V^{V}O_2(L^1)]\cdot 2H_2O$. [e] The complex **3** is $K[V^{V}O_2(L^x)]\cdot 2H_2O$, where L^x is the derivative of L^1 with a pyridine instead a furan ring on the hydrazonate moiety.

The VC1 molecules in the dimer are almost parallel. Their orientation is stabilized by face-to-face π–π stacking interactions, with a centroid-to-centroid distance of 4.79 Å and an interplanar angle of 6.0°.

The formation of the dimeric VC1 assembly in HEWL crystals (Figure 4.7d) is consistent with dioxidovanadium(V) complexes of aroylhydrazones tendency to form oligomeric species in solid state (Figure 4.7a-c).[95]

In the structures of VC1 and its analogues deposited in the Cambridge Crystallographic Data Centre (CCDC),[95] different cations (A = K^+ and Cs^+) mediate the supramolecular association by A···N/O interactions. For instance, in the structure of compound **2**,[95] where three molecules are observed in the asymmetric unit, a K^+ ion is coordinated to phenoxide O1, ethoxy O3, oxido O5 atom, two water molecules, imine N2 atom and furyl O6 atom from a second molecule of **2** and oxido O5 atom from a third molecule of **2** (Figure 4.7a). In the structure of **3**, four molecules are present in the asymmetric unit (Figure 4.7b).[95] Here, a K^+ ion is coordinated to the oxido O4, two water molecules of the first molecule of **3**, oxido O5 atoms from the second and third molecules of **3**, and a symmetry-related water molecule, the phenoxide O1, ethoxy O3 atom of the second molecule of **3** (Figure 4.7b). Finally, in the structure of VC1,[95] a Cs^+ ion is coordinated to enolate O2 and oxide O5 of VC1, phenoxide O1 and oxido O5 atoms of another VC1 molecule, furyl O6, and imine N2 atoms of a third VC1 system, and an oxide O6 atom of a fourth VC1 unit (Figure 4.7c). In the HEWL-VC1 adduct, a peak in the e.d. map was found close to the furyl O6 and imine N2 atoms of one VC1 unit. This was attributed to Na^+ ions from the crystallization condition (Figure 4.7d).

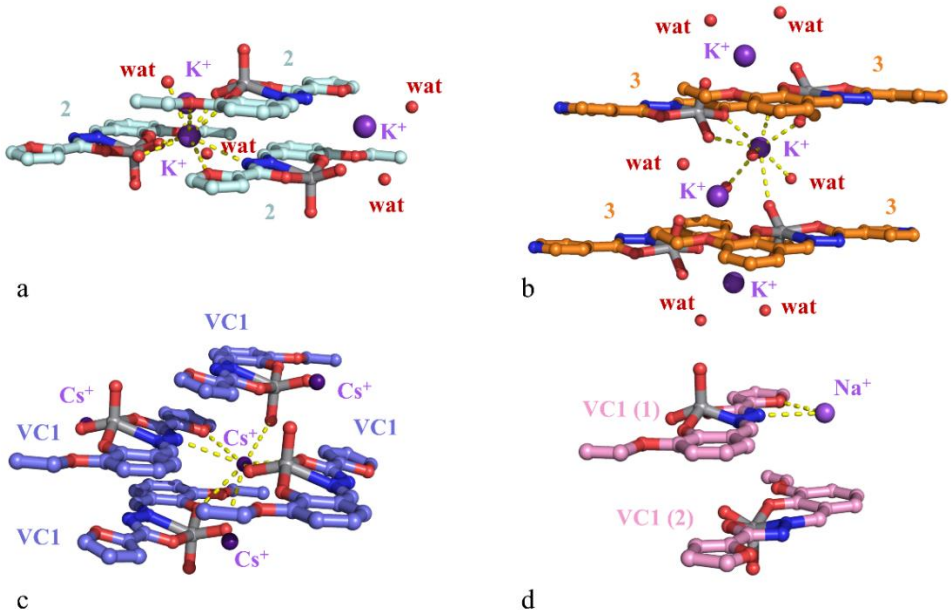

Figure 4.7 – Supramolecular association of a) **2**, b) **3** and c) VC1 in the structures deposited in the CCDC under the accession codes DAKKEJ,[95] DAKKIN,[95] and DAKKOT,[95] respectively. d) VC1 supramolecular association in the adduct formed by the VC with HEWL.

Binding of VC2 to HEWL

The structure of HEWL in complex with VC2 (Figure 4.5b) reveals the non-covalent binding of two VC2 molecules (occupancy = 0.60) to the protein surface. Similarly to VC1, the two VC2 molecules, denoted as VC2 (1) and VC2 (2), interact with each other to form a dimeric assembly. However, in this case, the e.d. maps are less defined when compared to the e.d. observed in the structure of HEWL treated with VC1. VC2 (1) forms hydrogen bonds with the side chain of Lys33, water molecules, the O atoms of Gly117 and Thr118, and N atoms of Val120 and Gln121 from a symmetry related molecule (Figure 4.8, Table 4.2). VC2 (2) forms hydrogen bonds with the side chain of Lys33 and water molecules (Figure 4.8, Table 4.2). Also in this case, the V^V species is penta-coordinated with

the two oxido O and tridentate hydrazone ligands bound to the V centre. No ions are detected close to the VC2 molecules. Selected geometrical parameters of VC2 bound to HEWL are reported in Table 4.3. The two VC2 molecules in the dimer have an intramolecular centroid-to-centroid distance of 4.73 Å and form an inter-planar angle of 12.3°.

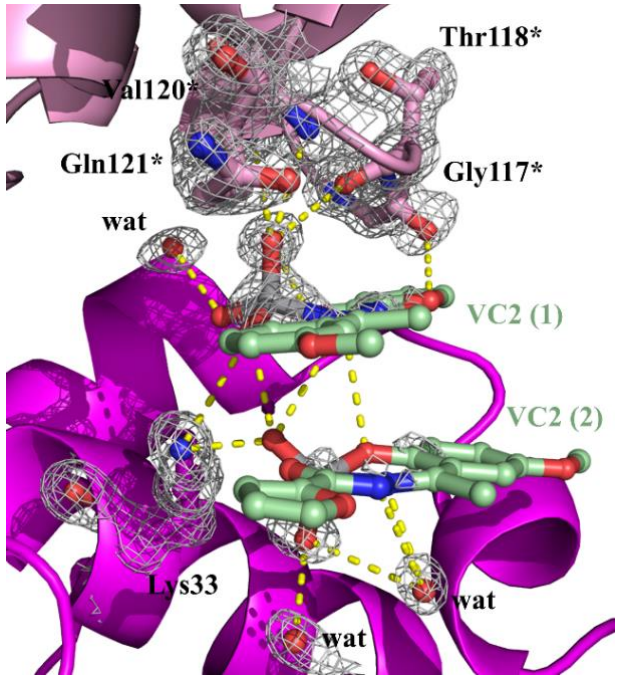

Figure 4.8 – Non-covalent binding of the supramolecular association of VC2 to HEWL. 2Fo-Fc e.d. maps are reported at 1.0 σ level in grey.

Although VC1 and VC2 share similar structures (Figure 4.1a,b), the dimers they form and interact with HEWL, are different to each other. Indeed, after superimposing VC1 (1) and VC2 (1), the best fit for the remaining VC molecules (VC2 (2) and VC1 (2)) requires a further rotation and translation. In particular, VC2 (2) should be translated of x = 3.98 Å, y = 2.78 Å, z = -7.30 Å and rotated of 57.60° to best superimpose VC1 (2) (Figure 4.9).

Despite these local differences, the overall position of the dimeric assemblies with respect to the protein surface remains similar. Indeed, after superimposition of HEWL structures, VC2 (1) should be translated of x = 3.30 Å, y = -2.17 Å, z = 2.79 Å and rotated of 133.86° to best fit VC1 (1), while VC2 (2) should be translated of x = 7.47 Å y = 1.08 Å z = -4.42 Å and rotated of 69.97° to best fit VC1 (2).

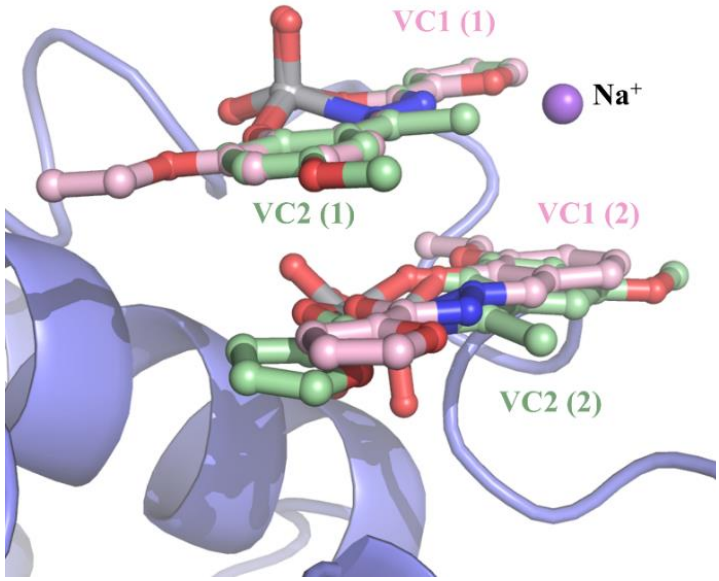

Figure 4.9 – Structural superimposition of one molecule of VC1 (1) (pink) and one molecule of VC2 (1) (green).

4.3 Interaction of VC3 with HEWL

To further investigate the interaction with proteins of dioxidovanadium(V) complexes with aroylhydrazone ligands, a third compound, VC3 (Figure 4.1c), was used.

The interaction between VC3 and HEWL was studied following the same experimental strategy used for VC1 and VC2.

4.3.1 UV-vis absorption spectroscopy

Over time stability of VC3, both in the absence (Figure 4.10a) and in the presence of HEWL (Figure 4.10b), was evaluated in a solution containing 1.1 M sodium chloride and 0.1 M sodium acetate pH 4.0 by UV-Vis absorption spectroscopy.

In the spectrum of VC3 (Figure 4.10a), peaks appear at 223, 339, and 410 nm, along with a shoulder between 280 and 300 nm. The peak at 220 nm remains stable over time, whereas the shoulder disappears after 24 hours. The absorption band at 339 nm can be attributed, as in previous cases, to spin-allowed ligand-centred $\pi \rightarrow \pi^*$ transitions, while the peak at 410 nm corresponds to a LMCT transition. Notably, after 24 h, a new peak emerges at 265 nm. The spectral overlap suggests that VC3 is not completely stable under the examined experimental conditions.

In the presence of HEWL (Figure 4.10b), four peaks are detected at 228, 278, 340, and 410 nm. The peaks at 228 and 410 nm remain stable over time, whereas the intensity of the remaining two peaks slightly increases up to 24 h and then slightly decreases after 7 d.

Overall, the UV-Vis profile of VC3 in the absence and in the presence of HEWL closely resembles that of VC1, indicating similar electronic properties and supporting a comparable behaviour in solution.

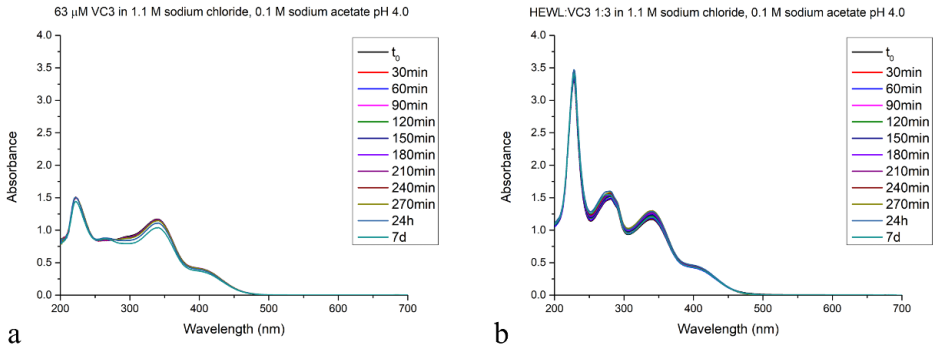

Figure 4.10 – a) UV−Vis spectrum as a function of time of VC3 in 1.1 M sodium chloride and 0.1 M sodium acetate pH 4.0. b) UV−Vis spectrum of the compound collected in the presence of HEWL using a 3:1 V compound-to-protein molar ratio (protein and VC3 concentrations were 21 and 63 µM, respectively).

4.3.2 Circular dichroism

CD spectra of the protein were then recorded in the absence and presence of VC3 at protein to metal molar ratios of 1:1, 1:3, and 1:5. Measurements were carried out in 10 mM sodium acetate pH 4.0 after 24 h (Figure 4.11a), 48 h (Figure 4.11b), and 7 d (Figure 4.11c) of incubation. The spectra were nearly identical, indicating that the secondary structure of HEWL remains unchanged upon binding of the VC.

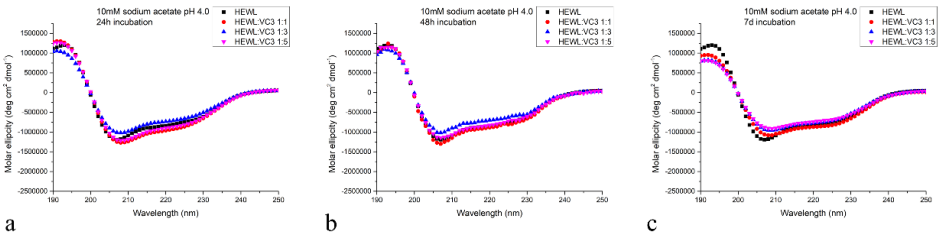

Figure 4.11 – Far-UV CD spectra of HEWL (concentration = 7.0 µM) incubated for a) 24 h, b) 48 h, c) 7 d in the presence of VC3 in 10 mM sodium acetate pH 4.0 at protein-to-V

molar ratio = 1:1 (red), 1:3 (blue) and 1:5 (violet). The CD spectra of metal-free protein are in black.

4.3.3 Fluorescence spectroscopy

Fluorescence spectra of HEWL in 10 mM sodium acetate pH 4.0, recorded upon excitation at 280 (Figure 4.12a) and 295 nm (Figure 4.12b), were recorded in the presence of increasing concentrations of VC3. The addition of VC3 leads to a concentration-dependent quenching of the intrinsic emission of HEWL, confirming the interaction of the VC to the protein.

The absence of a shift in the maximum emission wavelength suggests that the binding does not induce significant alterations in the tertiary structure of the protein.

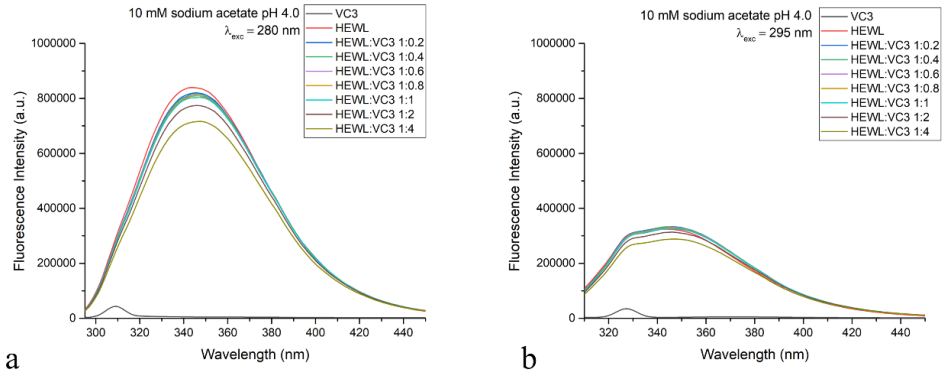

Figure 4.12 – Fluorescence emission spectra of HEWL in 10 mM sodium acetate pH 4.0 upon titration with VC3. Spectra were collected using a) λ_{exc} = 280 nm and b) λ_{exc} = 295 nm.

4.3.4 Crystallographic Studies

To obtain atomic-level insights into the interaction of VC3 with HEWL, a crystal of the metal-free protein, grown in 1.1 M sodium chloride and 0.1 M

sodium acetate pH 4.0, was exposed for two days to a stabilizing solution containing the mother liquor saturated with VC3. The overall structure of the protein, showing the non-covalent binding of two VC3 molecules (occupancy = 0.70) on its surface, is shown in Figure 4.13. Data collection and refinement statistics are reported in Table 4.4.

Table 4.4 – Data collection and refinement statistics.

Data collection	
	Structure of HEWL treated with VC3
PDB code	9S2A
Crystallization condition	1.1 M sodium chloride, 0.1 M sodium acetate pH 4.0
Soaking time	2 d
Space group	$P4_32_12$
a (Å)	76.57
b (Å)	76.57
c (Å)	36.73
Resolution range (Å)	38.29-1.31 (1.33-1.31)
Observations	549653 (30212)
Unique reflections	24505 (1297)
Completeness (%)	91.1 (100.0)
Redundancy	22.4 (23.3)
Rmerge (%)	0.099 (6.702)
Average I/σ(I)	13.3 (0.5)
$CC_{1/2}$	0.999 (0.326)
Anom. completeness (%)	90.8 (100.0)
Anom. Multiplicity	12.0 (12.2)
Refinement	
Resolution (Å)	38.28-1.37
N° reflections	19291
N° reflections in working set	603
R-factor/Rfree	0.195/0.233
N° non-H atoms in the refinement	1177
B-factor overall ($Å^2$)	27.59
Estimated occupancy of VC3 (1)	0.70
Estimated occupancy of VC3 (2)	0.70
B-factor of VC3 (1) ($Å^2$)	41.94
B-factor of VC3 (2) ($Å^2$)	80.57
Ramachandran values (%)	
Most favoured/Additional allowed	92.24/7.76
Outliers	0
RMSD from ideality	
RMSD bonds (Å)	0.012
RMSD angles (°)	1.817

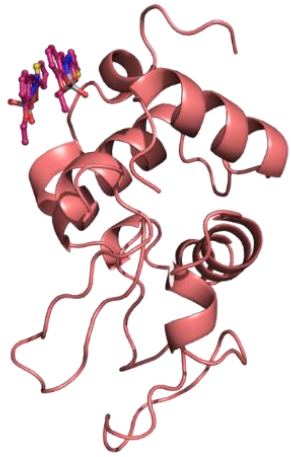

Figure 4.13 – Overall structure of the adducts formed upon reaction of HEWL with VC3. Vanadium atoms are in grey. Coordinates and structure factors were deposited in the PDB under the accession code 9S2A.

As observed when HEWL crystals were treated with VC1 and VC2, two VC3 molecules, labelled VC3 (1) and VC3 (2), interact with each other to form a dimeric assembly. VC3 (1) establishes hydrogen bonds with water molecules and the NZ atom of the Lys33 side chain and interacts with the N atom of Val120 from a symmetry-related molecule (Figure 4.14). VC3 (2) forms hydrogen bonds with the NZ atom of the Lys33 side chain (Figure 4.14) and forms a favourable interaction between sulphur and π aromatic systems (S/π interaction) with the side chain of Trp123, with an angle of 88.9° between the planes of the ligand and the Trp123 side chain.

The two VC molecules forming the dimeric assembly are nearly parallel to each other. This assembly is stabilized by a face-to-face π–π stacking interaction, characterized by a centroid-to-centroid distance of 4.40 Å and an interplanar angle of 16.7° between the ligands.

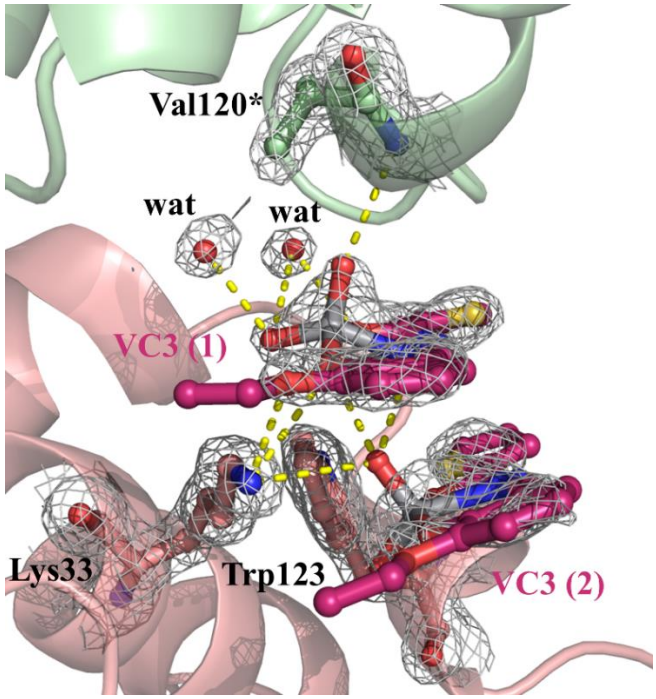

Figure 4.14 – Binding sites of vanadium compound in the structure of the adduct formed upon reaction of HEWL with VC3. The interaction of the supramolecular association of the two VC3 molecules and their interaction with protein atoms are highlighted. 2Fo-Fc e.d. maps are contoured at a 1.0 σ level and depicted in grey. Asterisk (*) refers to atoms from symmetry-related molecules (coloured in green).

Although VC1 and VC3 share similar chemical architectures (Figure 4.1a,c), the dimeric assemblies display a different orientation. After superimposing VC1 (1) and VC3 (1) (Figure 4.15), optimal overlap of the remaining molecules, VC3 (2) and VC1 (2), requires an additional rotation and translation. Specifically, VC3 (2) needs to be translated by x = -8.08 Å, y = -36.64 Å, z = 9.07 Å and rotated by 117.21° to best superimpose VC1 (2).

The thiophene ring in VC3(2) is positioned on the opposite side compared to the furan ring of VC1(2). This rearrangement is likely driven by a favourable S/π interaction between the thiophene ring of VC3(2) and the side chain of Trp123.

Despite this local reorientation, the overall position of the dimeric assemblies relative to the protein surface remains similar. Indeed, after superimposing the HEWL structures, VC3 (1) must be translated by x = 1.40 Å, y = -0.56 Å, z = 0.71 Å and rotated of 138.35° to best fit VC1 (1), while VC3 (2) should be translated of x = -9.59 Å y = -36.14 Å z = 8.60 Å and rotated of 125.20° to best fit VC1 (2).

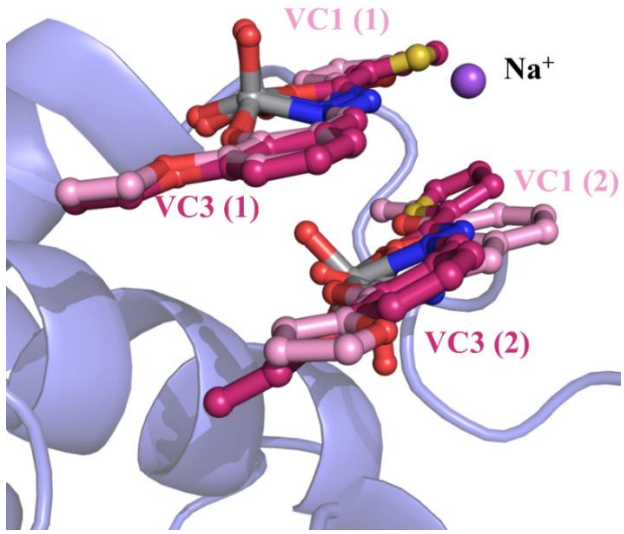

Figure 4.15 – Structural superimposition of one molecule of VC1 (1) (pink) and one molecule of VC3 (1) (magenta).

4.4 VC1, VC2 and VC3 binding to HEWL: structural comparison

The three oxidovanadium(V) complexes with aroylhydrazone ligands (VC1, VC2, and VC3) show similar interaction patterns with HEWL, although differences in the ligand structure affect how they bind and organize in the crystal.

The binding involves non-covalent interactions, such as hydrogen bonds and π–π stacking between the aromatic parts of the ligands and the indole rings of tryptophan residues on the protein surface. These complexes do not alter the overall protein structure and tend to associate into dimers or small aggregates in the crystal, stabilized by π–π interactions and positioned close to basic residues like Lys33 and Arg125. In the case of VC3, there is also a S/π interaction with Trp123.

Overall, these results show that small differences in the ligand structure can significantly influence the binding mode and self-assembly of vanadium(V) complexes on the protein, helping to understand how ligand design can affect the interaction of V-based compounds with biological targets.

The X-ray structures of HEWL with VC1, VC2 and VC3 contribute to expanding the limited number of available X-ray structures of V^{V}–protein adducts available in literature and provide a structural basis for understanding how V-based drugs may interact with proteins. Such knowledge is essential for the design of stable, water-soluble VCs and for better assessing their potential impact on biological functions and therapeutic activity.

4.5 Materials and methods

UV-vis absorption spectroscopy

Spectra of VC1 (concentration = 15 μM), VC2 (concentration = 15 μM) and VC3 (concentration = 63 μM) were collected over time at room temperature in a solution of 1.1 M sodium chloride and 0.1 M sodium acetate pH 4.0, in the absence and presence of HEWL (protein to metal molar ratio 1:3), employing a Jasco V750 spectrophotometer and using the following parameters: wavelength range of 700-200 nm, data interval of 1.0 nm, bandwidth of 2.0 nm, and scan speed of 400 nm min^{-1}. Each measurement was performed at least twice independently in duplicate using a quartz cuvette with a path length of 1.0 cm.

Circular dichroism

Far UV-CD spectra of HEWL, in the absence and presence of VC1, VC2 and VC3 were registered in the 250-190 nm range using a Jasco J-1500 spectropolarimeter equipped with a Peltier thermostatic cell. Spectra were registered using a protein concentration of 7 μM and different concentrations of the VCs (1:1, 1:3, and 1:5 protein-to-metal ratio) on samples of the protein incubated for 24 h, 48 h, and 6 days with VC1 and VC2 and for 24 h, 48 h, and 7 days with VC3. Spectra were acquired in 10 mM sodium acetate pH 4.0 using a quartz cell with a path length of 0.1 cm. Additional experimental parameters were: data pitch of 1.0 nm, bandwidth of 1.0 nm, scanning speed of 50 nm min^{-1}, response time of 2.0 s, and a temperature of 25°C. Each spectrum was generated by averaging three scans, and each measurement was performed twice.

Fluorescence

A HORIBA Fluoromax-4 spectrofluorometer, equipped with a thermostat bath and a 1 cm path length cuvette, was employed to record fluorescence spectra of HEWL both in the absence and presence of VC1, VC2 and VC3 at 25°C in 10 mM sodium acetate pH 4.0. To collect the spectra, a HEWL solution at a concentration of 1.4 μM was titrated with a solution of each VC dissolved in water at a concentration of 60.0 μM. The protein was excited at 280 nm (to monitor Tyr and Trp emission) and 295 nm (to monitor Trp emission exclusively) and spectra were registered between 295 and 450 nm and between 310 and 450 nm, respectively. Increasing protein-to-VC molar ratios were achieved during titration: 1:0.2, 1:0.4, 1:0.6, 1:0.8, 1:1, 1:2, and 1:4. Solutions were stirred and allowed to equilibrate for 5 min before recording the spectra. Self-absorbance and inner-filter effects were limited since at the used concentrations the VCs have an ignorable absorbance. Emission spectra of the VCs at 5.6 μM, *i.e.* the highest concentration reached

during the titration, were also registered as control. Each measurement was repeated twice.

Crystallization, adduct formation, data collection, structure resolution and refinement

HEWL (concentration = 13 mg/mL, 0.9 mM) was crystallized using the hanging drop vapour diffusion method in 1.1 M sodium chloride, 0.1 M sodium acetate pH 4.0. Native HEWL crystals were then exposed to stabilizing solutions containing the mother liquor saturated with the VCs. After 6 days (in the case of VC1 and VC2) and 2 days of soaking (in the case of VC3) HEWL crystals were cryoprotected with a solution consisting of 70 % reservoir solution and 30 % glycerol, fished with a nylon loop, flash-cooled in liquid nitrogen and sent to synchrotrons. X-ray diffraction data on HEWL crystals treated with VC1 were collected at the ID23–1 beamline of European Synchrotron Radiation Facility (ESRF), Grenoble (France), while data for the HEWL crystals treated with VC2 and VC3 were collected at the XRD2 Beamline at Elettra synchrotron, Trieste (Italy). Crystals diffracted X-ray at a resolution in the range 1.18-1.31 Å. Data processing and scaling were performed using Global Phasing autoPROC pipeline.[232] The structures were solved by Molecular Replacement method using the Phaser program from CCP4 suite[233] and the structures deposited in the PDB 193L[194] as template. Refmac5 was used for refinement.[234] Model building was carried out using Coot.[235] In all the structures, V atom position was validated using anomalous difference e.d. maps. The final models show R-factor and Rfree values in the range of 0.159-0.203 and 0.221-0.256 respectively. Ligand positions were restrained to guide geometry optimization. Figures were generated using PyMol (www.pymol.org). The structure validation of the final models was performed using the PDB validation server.[236] Coordinates and structure factors were deposited in the PDB under the accession codes 9GOG, 9GOK and 9S2A.

Translation vectors and angles of rotation after structure superimposition were calculated using Superpose routine of the CCP4 package.[261]

Centroid-to-centroid distance and interplanar angle were calculated using ChimeraX.[262]

The results of this study were successfully published on:

M. Paolillo, G. Ferraro, G. Sahu, P. Das Pattanayak, E. Garribba, S. Halder, R. Ghosh, B. Mondal, P. B. Chatterjee, R. Dinda, A. Merlino. "Interaction of $V^{V}O_2$– hydrazonates with lysozyme" J. Inorg. Biohem. 264, (2025), 112787. DOI: https://doi.org/10.1016/j.jinorgbio.2024.112787

and submitted for publication:

D. Mohapatra, P. D. Pattanayak, W. Kaminsky, **M. Paolillo**, G. Tito, G. Ferraro, A Merlino, R. Dinda. "Binding of Aqueous-stable, Lipophilic, Anticancer $V^{V}O_2$ Metallodrugs with Biological Molecules: X-ray Structures of the Adduct of the V^{V}–hydrazonato Complex with Hen Egg White Lysozyme". Submitted for publication

CHAPTER 5

Dinuclear V^V complexes: the cases of $Cs_2[V^V_2O_4(mal)_2]\cdot 2H_2O$ and $Cs_2[V^V_2O_4(lact)_2]\cdot 2H_2O$

5.1 Introduction

α-Hydroxycarboxylic acids represent an important class of biologically relevant ligands for vanadium-based drug development. They participate in fundamental metabolic pathways, such as the citric acid and Cori cycles, and possess versatile coordination sites capable of stabilizing various metal oxidation states.[108–111]

Among the *α*-hydroxycarboxylic acids, malic and lactic acid are particularly noteworthy.[116,118] Both molecules contain a hydroxyl and at least one carboxylate group able to coordinate V centres, giving rise to well-defined dinuclear dioxidovanadium(V) species. Their corresponding dimetallic V^V complexes, $Cs_2[V^V_2O_4(mal)_2]\cdot 2H_2O$ (Figure 5.1a) and $Cs_2[V^V_2O_4(lact)_2]\cdot 2H_2O$ (Figure 5.1b), are soluble compounds that provide valuable models for studying the aqueous chemistry of V^V complexes. These systems offer a framework for exploring how these ligands modulate V speciation and its interaction with proteins.

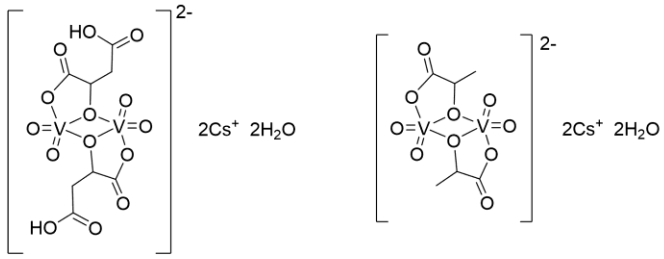

Figure 5.1 – Chemical structures of dinuclear V^V complexes with *α*-hydroxycarboxylic acids: a) $Cs_2[V^V_2O_4(mal)_2]\cdot 2H_2O$, b) $Cs_2[V^V_2O_4(lact)_2]\cdot 2H_2O$.

5.2 Interaction of $Cs_2[V^V_2O_4(mal)_2]\cdot 2H_2O$ with HEWL

Structural studies on the interaction between proteins and dinuclear V^V complexes of general formula $[V^V_2O_4(L)_2]$ are still missing in literature.

The dinuclear dioxidovanadium(V) complex $Cs_2[V^V_2O_4(mal)_2]\cdot 2H_2O$ (Figure 5.1a) provides an ideal model to investigate the interaction of dimetallic VCs with proteins. For this reason, its behaviour in aqueous solution, at room and physiological temperatures, and its interaction with HEWL were examined.

5.2.1 ^{51}V NMR studies

The behaviour of $Cs_2[V^V_2O_4(mal)_2]\cdot 2H_2O$ in solution was investigated by NMR spectroscopy. ^{51}V NMR spectra of the compound (concentration = 5 mM) in D_2O and under the conditions used to obtain its adduct with HEWL (1.1 M sodium chloride, 0.1 M sodium acetate pH 4.0 and 10% D_2O) were collected in the absence and in the presence of the protein (concentration = 13 mg/mL, 0.9 mM) (Figure 5.3 and Figure 5.4). Spectra were recorded after 1 hour and 7 days of incubation at RT (Figure 5.3), and after 42 hours and 7 days of incubation at 37°C (Figure 5.4).

The solution chemistry of vanadium(V) complexes with α-hydroxycarboxylates (L^{2-}) has been extensively studied by ^{51}V NMR.[110,113,114,118,181,263,264] These studies revealed the formation of several V species, among which the most relevant are $[V^V_2O_4(L)_2]^{2-}$ and $[V^V_2O_5(L)]^{2-}$. Literature data report the high stability of a group of dinuclear V^V compounds bearing α-hydroxycarboxylates. Examples are the compounds based on malate (mal), lactate (lact) and mandelate.[110,118] $[V^V_2O_4(mal)_2]^{2-}$ consists of two equivalent coordination centres, characterized by ^{51}V NMR signal at around –533 ppm. On the contrary, the two signals at –551 ppm and at –533 ppm were attributed to $[V^V_2O_5(mal)]^{2-}$, due to its non-equivalent V centres. Additional signals are observed at: –561 ppm, attributed to $H_2V^VO_4^-$ (V_1); –574 ppm, arising from $H_2V^V_2O_7^{2-}$ (V_2); and –579 ppm, due to $V^V_4O_{12}^{4-}$

(V_4). Signals that are in the ranges –525 to –514 ppm, –507 to –497 ppm, and –425 to –423 correspond to the V_A, V_B, and V_C centres of $[H_xV^V_{10}O_{28}]^{(6-x)-}$ (V_{10}, x = 0-3) in Figure 5.2, respectively. These chemical shifts vary depending on the protonation state of the decavanadate species. Signals at approximately –517 and –502 ppm have also been attributed to $[V^VO_2(mal)(H_2O)]^-$ and $[V^VO_2(mal)(OH)]^{2-}$, respectively.[110,113,114,118,181,263–266]

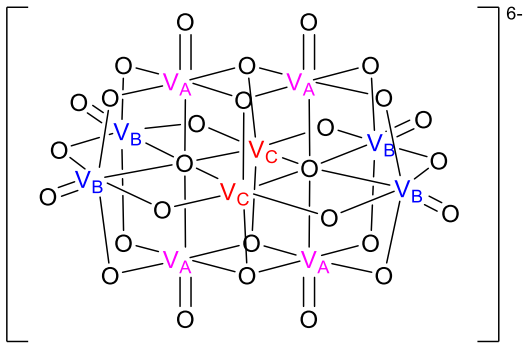

Figure 5.2 – V_A, V_B, and V_C centres in $[V^V_{10}O_{28}]^{6-}$.

The spectra of $Cs_2[V^V_2O_4(mal)_2]\cdot 2H_2O$ collected at RT reveal the presence of $[V^V_2O_4(mal)_2]^{2-}$ (signal at ~–534 ppm), $[V^V_2O_5(mal)]^{2-}$ (signals at ~–538 ppm, -545 ppm), V_{10} (signals at ~–425 ppm, –502 ppm, –520 ppm) under all the investigated experimental conditions. Peak integration analysis suggests that the percentage of V_{10} in the various solutions increases over time. A small amount (~ 1%) of V_{10} is observed in the presence of HEWL (Figure 5.3, Table 5.1).

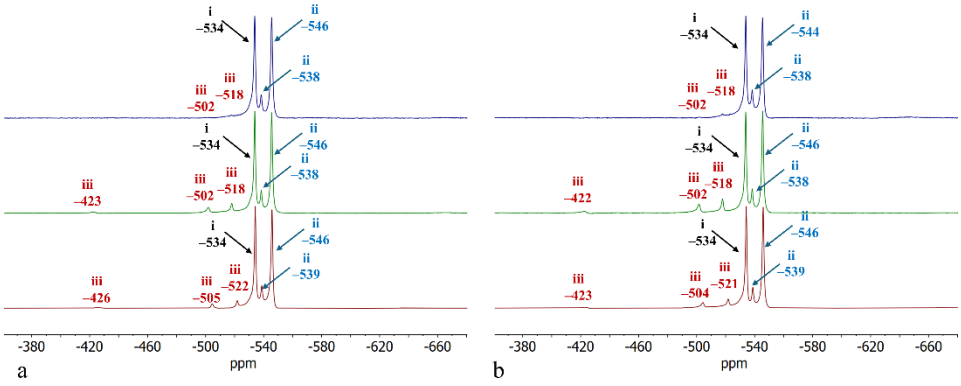

Figure 5.3 – ^{51}V NMR spectra measured at RT after a) 1 h and b) 7 d of incubation of $Cs_2[V^V_2O_4(mal)_2]\cdot 2H_2O$ (5 mM) dissolved in D_2O (red lines); in 1.1 M sodium chloride, 0.1 M sodium acetate pH 4.0 and 10% D_2O (green lines); and in 1.1 M sodium chloride, 0.1 M sodium acetate pH 4.0 and 10% D_2O in presence of HEWL (13 mg/mL) (blue lines). i indicates $[V^V_2O_4(mal)_2]^{2-}$, ii $[V^V_2O_5(mal)]^{2-}$ and iii V_{10}. These studies were carried out under the supervision of Prof. Annette Rompel from University of Vienna.

The spectra collected at 37°C show similar results, suggesting the presence in solution of $[V^V_2O_4(mal)_2]^{2-}$ (signal at ~–534 ppm), $[V^V_2O_5(mal)]^{2-}$ (signals at ~–538 and –545 ppm), and V_{10} (signals at ~–425 ppm, –502 ppm, and –520 ppm) also at physiological temperature. Notably, the percentage of the V_{10} increases after 7 days of incubation in the absence of protein, while its formation is precluded at 37°C in the presence of HEWL (Figure 5.4, Table 5.2). This is in contrast with recent results indicating that HEWL could stabilize decavanadate and other larger POVs, like V_{15} and V_{20}, also at physiological temperature.[219–221,267]

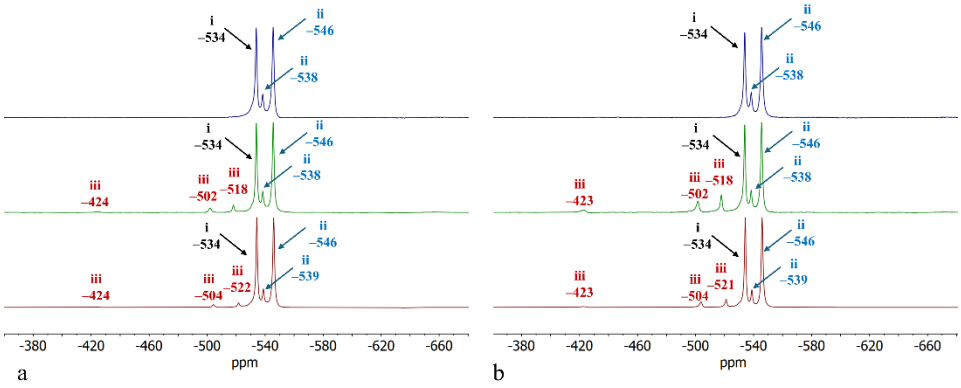

Figure 5.4 – ^{51}V NMR spectra measured at 37°C after a) 42 h and b) 7 d of incubation of $Cs_2[V^V_2O_4(mal)_2]\cdot 2H_2O$ (5 mM) dissolved in D_2O (red lines); in 1.1 M sodium chloride, 0.1 M sodium acetate pH 4.0 and 10% D_2O (green lines); and in 1.1 M sodium chloride, 0.1 M sodium acetate pH 4.0 and 10% D_2O in presence of HEWL (13 mg/mL) (blue lines). i indicates $[V^V_2O_4(mal)_2]^{2-}$, ii $[V^V_2O_5(mal)]^{2-}$ and iii V_{10}. These studies were carried out under the supervision of Prof. Annette Rompel from University of Vienna.

Table 5.1 – Chemical shifts in ^{51}V NMR spectra measured in triplicate at RT after 1 h and 7 d of incubation of $Cs_2[V^V_2O_4(mal)_2]\cdot 2H_2O$ (5 mM) dissolved in (i) D_2O; (ii) 1.1 M sodium chloride, 0.1 M sodium acetate pH 4.0 and 10% D_2O; and (iii) 1.1 M sodium chloride, 0.1 M sodium acetate pH 4.0 and 10% D_2O in presence of HEWL (13 mg/mL). The relative content of species was calculated based on the integration of ^{51}V signals. Signals were assigned based on literature data.[110,113,114,263–265,268] [a]

5 mM $Cs_2[V^V_2O_4(mal)_2]\cdot 2H_2O$ in D_2O (after 1 h at RT)											
^{51}V chemical shift (ppm)			**Species**	**References**	**Integration (%)**			**Sum**			**Aver-age ± SD (%)**
Sample 1	**Sample 2**	**Sample 3**			**Sample 1**	**Sample 2**	**Sample 3**	**Sample 1**	**Sample 2**	**Sample 3**	
–423	–426	–425	V_{10}	110,263	0.6	0.5	0.5	6.2	5.9	6.1	6.1 ± 0.2
–504	–505	–505	V_{10} (or VL^-)	110,113,114,263,264,268	1.9	1.8	1.8				
–522	–522	–522	V_{10} (or VL^{2-})	110,113,114,263,264,268	3.7	3.6	3.8				
–534	–534	–534	$V_2L_2^{2-}$	110,113,114,263,264,268	43.1	42.6	43.4	43.1	42.6	43.4	43.0 ± 0.4
–539	–539	–539	V_2L^{2-} (or $V_3L_2^{3-}$)	110,113,114,263–265,268	10.6	10.6	9.9	50.8	51.6	50.5	51.0 ± 0.6
–546	–546	–546	V_2L^{2-} (or $V_3L_2^{3-}$)	110,113,114,263–265,268	40.2	41.0	40.6				
5 mM $Cs_2[V^V_2O_4(mal)_2]\cdot 2H_2O$ in 0.1 M NaOAc pH 4.0, 1.1 M NaCl, 10% D_2O (after 1 h at RT)											
^{51}V chemical shift (ppm)			**Species**	**References**	**Integration (%)**			**Sum**			**Aver-age ± SD (%)**
Sample 1	**Sample 2**	**Sample 3**			**Sample 1**	**Sample 2**	**Sample 3**	**Sample 1**	**Sample 2**	**Sample 3**	
–423	–424	–424	V_{10}	110,263	0.6	0.5	0.5	7.6	8.3	9.3	8.4 ± 0.9
–502	–502	–502	V_{10}	110,113,114,263,264,268	3.0	3.1	3.5				

			(or VL^{-})								
–518	–518	–518	V_{10} (or VL^{2-})	110,113,114,263,264,268	4.0	4.7	5.3				
–534	–534	–534	$V_2L_2^{2-}$	110,113,114,263,264,268	42.8	43.0	44.3	42.8	43.0	44.3	43.4 ± 0.8
–538	–538	–538	V_2L^{2-} (or $V_3L_2^{3-}$)	110,113,114,263–265,268	9.9	9.1	9.9	49.7	48.7	46.5	48.3 ± 1.6
–546	–545	–545	V_2L^{2-} (or $V_3L_2^{3-}$)	110,113,114,263–265,268	39.8	39.6	36.6				
5 mM $Cs_2[V^{V}_2O_4(mal)_2]\cdot 2H_2O$ + 13 mg/mL HEWL in 0.1 M NaOAc pH 4.0, 1.1 M NaCl, 10% D_2O (after 1 h at RT)											
^{51}V chemical shift (ppm)			**Species**	**References**	**Integration (%)**			**Sum**			**Aver-age ± SD (%)**
Sample 1	**Sample 2**	**Sample 3**			**Sample 1**	**Sample 2**	**Sample 3**	**Sample 1**	**Sample 2**	**Sample 3**	
–502	–502	–502	V_{10} (or VL^{-})	110,113,114,263,264,268	0.2	0.2	0.1	2.0	0.7	0.9	1.2 ± 0.7
–518	–518	–518	V_{10} (or VL^{2-})	110,113,114,263,264,268	1.8	0.5	0.8				
–534	–534	–534	$V_2L_2^{2-}$	110,113,114,263,264,268	44.7	45.1	43.4	44.7	45.1	43.4	44.4 ± 0.9
–538	–538	–538	V_2L^{2-} (or $V_3L_2^{3-}$)	110,113,114,263–265,268	11.1	10.6	11.1	53.3	54.2	55.7	54.4 ± 1.2
–546	–546	–546	V_2L^{2-} (or $V_3L_2^{3-}$)	110,113,114,263–265,268	42.2	43.6	44.6				
5 mM $Cs_2[V^{V}_2O_4(mal)_2]\cdot 2H_2O$ in D_2O (after 7 d at RT)											
^{51}V chemical shift (ppm)			**Species**	**References**	**Integration (%)**			**Sum**			**Aver-age**
Sample 1	**Sample 2**	**Sample 3**			**Sample 1**	**Sample 2**	**Sample 3**	**Sample 1**	**Sample 2**	**Sample 3**	

											± SD (%)
–424	–423	–425	V_{10}	[110,263]	0.5	0.5	0.1	6.7	9.0	5.9	7.2 ± 1.6
–504	–504	–505	V_{10} (or VL^{-})	[110,113,114,263,264,268]	2.1	3.4	2.1				
–521	–521	–522	V_{10} (or VL^{2-})	[110,113,114,263,264,268]	4.1	5.1	3.7				
–534	–534	–534	$V_2L_2^{2-}$	[110,113,114,263,264,268]	42.6	41.5	43.1	42.6	41.5	43.1	42.4 ± 0.8
–539	–539	–539	V_2L^{2-} (or $V_3L_2^{3-}$)	[110,113,114,263–265,268]	9.5	8.6	9.9	50.7	49.5	51.0	50.4 ± 0.8
–543	–546	–546	V_2L^{2-} (or $V_3L_2^{3-}$)	[110,113,114,263–265,268]	41.2	40.9	41.1				
5 mM $Cs_2[V^V_2O_4(mal)_2]\cdot 2H_2O$ in 0.1 M NaOAc pH 4.0, 1.1 M NaCl, 10% D_2O (after 7 d at RT)											
^{51}V chemical shift (ppm)			**Species**	**References**	**Integration (%)**			**Sum**			**Aver-age ± SD (%)**
Sample 1	**Sample 2**	**Sample 3**			**Sample 1**	**Sample 2**	**Sample 3**	**Sample 1**	**Sample 2**	**Sample 3**	
–423	–422	–424	V_{10}	[110,263]	1.0	0.9	0.9	10.8	11.5	9.3	10.5 ± 1.1
–502	–502	–502	V_{10} (or VL^{-})	[110,113,114,263,264,268]	4.6	4.8	3.5				
–518	–518	–518	V_{10} (or VL^{2-})	[110,113,114,263,264,268]	5.2	5.8	4.9				
–534	–534	–534	$V_2L_2^{2-}$	[110,113,114,263,264,268]	40.2	40.7	40.6	40.2	40.7	40.6	40.5 ± 0.2
–538	–538	–538	V_2L^{2-} (or $V_3L_2^{3-}$)	[110,113,114,263–265,268]	10.4	9.8	11.1	49.1	47.8	50.1	49 ± 1.2
–546	–546	–543	V_2L^{2-}	[110,113,114,263–265,268]	38.7	38.0	39.0				

			(or $V_3L_2^{3-}$)								
5 mM $Cs_2[V^V_2O_4(mal)_2]\cdot 2H_2O$ + 13 mg/mL HEWL in 0.1 M NaOAc pH 4.0, 1.1 M NaCl, 10% D_2O (after 7 d at RT)											
^{51}V chemical shift (ppm)			**Species**	**References**	**Integration (%)**			**Sum**			**Aver-age ± SD (%)**
Sample 1	**Sample 2**	**Sample 3**			**Sample 1**	**Sample 2**	**Sample 3**	**Sample 1**	**Sample 2**	**Sample 3**	
–502	–501	–501	V_{10} (or VL^-)	110,113,114,263,264,268	0.3	0.6	0.6	2.1	2.7	1.3	2.0 ± 0.7
–518	–518	–518	V_{10} (or VL^{2-})	110,113,114,263,264,268	1.8	2.1	0.7				
–534	–534	–534	$V_2L_2^{2-}$	110,113,114,263,264,268	43.0	44.8	39.6	43.0	44.8	39.6	42.4 ± 2.7
–538	–538	–538	V_2L^{2-} (or $V_3L_2^{3-}$)	110,113,114,263–265,268	12.4	11.1	13.1	55.0	52.5	59.2	55.6 ± 3.4
–544	–545	–546	V_2L^{2-} (or $V_3L_2^{3-}$)	110,113,114,263–265,268	42.6	41.4	46.1				

[a] L indicates mal^{2-} ligand, VL^- indicates $[V^VO_2(mal)(H_2O)]^-$, VL^{2-} $[V^VO_2(mal)(OH)]^{2-}$, $V_2L_2^{2-}$ $[V^V_2O_4(mal)_2]^{2-}$, V_2L^{2-} $[V^V_2O_5(mal)]^{2-}$ and $V_3L_2^{3-}$ $[V^V_3O_7(mal)_2]^{3-}$.

Table 5.2 – Chemical shifts in ^{51}V NMR spectra measured in triplicate at 37°C after 42 h and 7 d of incubation of $Cs_2[V^V_2O_4(mal)_2]\cdot 2H_2O$ (5 mM) dissolved in (i) D_2O; (ii) 1.1 M sodium chloride, 0.1 M sodium acetate pH 4.0 and 10% D_2O; and (iii) 1.1 M sodium chloride, 0.1 M sodium acetate pH 4.0 and 10% D_2O in presence of HEWL (13 mg/mL). The content of species was calculated based on integration of ^{51}V signals. Signals were assigned based on the literature data.[110,113,114,263–265,268] [a]

5 mM $Cs_2[V^V_2O_4(mal)_2]\cdot 2H_2O$ in D_2O (after 42 h at 37°C)											
^{51}V chemical shift (ppm)			**Species**	**References**	**Integration (%)**			**Sum**			**Average ± SD (%)**
Sample 1	**Sample 2**	**Sample 3**			**Sample 1**	**Sample 2**	**Sample 3**	**Sample 1**	**Sample 2**	**Sample 3**	
–424	–425	–425	V_{10}	[110,263]	0.3	0.1	0.3	4.0	1.8	3.6	3.1 ± 1.2
–504	–505	–504	V_{10} (or VL^-)	[110,113,114,263,264,268]	1.4	0.7	1.2				
–522	–522	–522	V_{10} (or VL^{2-})	[110,113,114,263,264,268]	2.3	1.0	2.1				
–534	–534	–534	$V_2L_2^{2-}$	[110,113,114,263,264,268]	41.3	41.8	42.9	41.3	41.8	42.9	42.0 ± 0.8
–539	–539	–539	V_2L^{2-} (or $V_3L_2^{3-}$)	[110,113,114,263–265,268]	10.0	10.1	9.7	54.7	56.5	53.6	54.9 ± 1.5
–546	–546	–546	V_2L^{2-} (or $V_3L_2^{3-}$)	[110,113,114,263–265,268]	44.7	46.4	43.9				
5 mM $Cs_2[V^V_2O_4(mal)_2]\cdot 2H_2O$ in 0.1 M NaOAc pH 4.0, 1.1 M NaCl, 10% D_2O (after 42 h at 37°C)											
^{51}V chemical shift (ppm)			**Species**	**References**	**Integration (%)**			**Sum**			**Average ± SD (%)**
Sample 1	**Sample 2**	**Sample 3**			**Sample 1**	**Sample 2**	**Sample 3**	**Sample 1**	**Sample 2**	**Sample 3**	
–424	–424	–424	V_{10}	[110,263]	0.5	0.5	0.5	5.8	5.3	5.7	5.6 ± 0.3
–502	–502	–502	V_{10}	[110,113,114,263,264,268]	2.2	1.9	2.1				

			(or VL^{-})								
–518	–518	–518	V_{10} (or VL^{2-})	110,113,114,263,264,268	3.1	2.9	3.1				
–534	–534	–534	$V_2L_2^{2-}$	110,113,114,263,264,268	40.1	41.3	40.8	40.1	41.3	40.8	40.7 ± 0.6
–538	–538	–538	V_2L^{2-} (or $V_3L_2^{3-}$)	110,113,114,263–265,268	10.8	9.6	11.1	54.0	53.4	53.6	53.7 ± 0.3
–546	–546	–546	V_2L^{2-} (or $V_3L_2^{3-}$)	110,113,114,263–265,268	43.2	43.8	42.5				
5 mM $Cs_2[V^V_2O_4(mal)_2]\cdot 2H_2O$ + 13 mg/mL HEWL in 0.1 M NaOAc pH 4.0, 1.1 M NaCl, 10% D_2O (after 42 h at 37°C)											
^{51}V chemical shift (ppm)			**Species**	**References**	**Integration (%)**			**Sum**			**Aver-age ± SD (%)**
Sample 1	**Sample 2**	**Sample 3**			**Sample 1**	**Sample 2**	**Sample 3**	**Sample 1**	**Sample 2**	**Sample 3**	
–534	–534	–534	$V_2L_2^{2-}$	110,113,114,263,264,268	43.8	44.2	44.3	43.8	44.2	44.3	44.1 ± 0.3
–538	–538	–538	V_2L^{2-} (or $V_3L_2^{3-}$)	110,113,114,263–265,268	12.5	12.3	11.9	56.3	55.8	55.6	55.9 ± 0.3
–546	–546	–546	V_2L^{2-} (or $V_3L_2^{3-}$)	110,113,114,263–265,268	43.8	43.5	43.7				
5 mM $Cs_2[V^V_2O_4(mal)_2]\cdot 2H_2O$ in D_2O (after 7 d at 37°C)											
^{51}V chemical shift (ppm)			**Species**	**References**	**Integration (%)**			**Sum**			**Aver-age ± SD (%)**
Sample 1	**Sample 2**	**Sample 3**			**Sample 1**	**Sample 2**	**Sample 3**	**Sample 1**	**Sample 2**	**Sample 3**	
–423	–423	–424	V_{10}	110,263	0.7	0.7	0.8	7.0	7.7	8.7	7.8 ± 0.9
–504	–504	–504	V_{10} (or VL^{-})	110,113,114,263,264,268	3.0	3.3	3.1				

–521	–521	–521	V_{10} (or VL^{2-})	110,113,114,263,264,268	3.3	3.7	4.8				
–534	–534	–534	$V_2L_2^{2-}$	110,113,114,263,264,268	39.5	39.0	41.4	39.5	39.0	41.4	40.0 ± 1.3
–539	–539	–539	V_2L^{2-} (or $V_3L_2^{3-}$)	110,113,114,263–265,268	8,6	8,7	9,6	53.5	53.4	49.8	52.2 ± 2.1
–546	–546	–546	V_2L^{2-} (or $V_3L_2^{3-}$)	110,113,114,263–265,268	44,9	44,7	40,2				
5 mM $Cs_2[V^V_2O_4(mal)_2]\cdot 2H_2O$ in 0.1 M NaOAc pH 4.0, 1.1 M NaCl, 10% D_2O (after 7 d at 37°C)											
^{51}V chemical shift (ppm)			**Species**	**References**	**Integration (%)**			**Sum**			**Aver-age ± SD (%)**
Sample 1	**Sample 2**	**Sample 3**			**Sample 1**	**Sample 2**	**Sample 3**	**Sample 1**	**Sample 2**	**Sample 3**	
–422	–426	–423	V_{10}	110,263	1.6	1.9	1.7	14.8	15.5	14.8	15.0 ± 0.4
–502	–502	–502	V_{10} (or VL^{-})	110,113,114,263,264,268	5.9	6.4	6.0				
–518	–518	–518	V_{10} (or VL^{2-})	110,113,114,263,264,268	7.3	7.2	7.1				
–534	–534	–534	$V_2L_2^{2-}$	110,113,114,263,264,268	37.0	36.1	36.1	37.0	36.1	36.1	36.4 ± 0.5
–538	–538	–538	V_2L^{2-} (or $V_3L_2^{3-}$)	110,113,114,263–265,268	10.3	10.3	10.4	48.3	48.4	49.1	48.6 ± 0.4
–541	–546	–546	V_2L^{2-} (or $V_3L_2^{3-}$)	110,113,114,263–265,268	38.0	38.1	38.7				
5 mM $Cs_2[V^V_2O_4(mal)_2]\cdot 2H_2O$ + 13 mg/mL HEWL in 0.1 M NaOAc pH 4.0, 1.1 M NaCl, 10% D_2O (after 7 d at 37°C)											
^{51}V chemical shift (ppm)			**Species**	**References**	**Integration (%)**			**Sum**			**Aver-age**
Sample 1	**Sample 2**	**Sample 3**			**Sample 1**	**Sample 2**	**Sample 3**	**Sample 1**	**Sample 2**	**Sample 3**	

											± SD (%)
–534	–534	–534	$V_2L_2^{2-}$	110,113,114,263,264,268	43.7	41.5	41.4	43.7	41.5	41.4	42.2 ± 1.3
–538	–538	–538	V_2L^{2-} (or $V_3L_2^{3-}$)	110,113,114,263–265,268	14.2	13.2	13.5	56.3	58.4	58.7	57.8 ± 1.3
–545	–546	–546	V_2L^{2-} (or $V_3L_2^{3-}$)	110,113,114,263–265,268	42.1	45.2	45.2				

[a] L indicates mal^{2-} ligand, VL^{-} indicates $[V^{V}O_2(mal)(H_2O)]^{-}$, VL^{2-} $[V^{V}O_2(mal)(OH)]^{2-}$, $V_2L_2^{2-}$ $[V^{V}_2O_4(mal)_2]^{2-}$, V_2L^{2-} $[V^{V}_2O_5(mal)]^{2-}$ and $V_3L_2^{3-}$ $[V^{V}_3O_7(mal)_2]^{3-}$.

5.2.2 Mass spectrometry studies

The behaviour of the $Cs_2[V^V_2O_4(mal)_2]\cdot 2H_2O$ in solution was further examined by electrospray ionization mass spectrometry (ESI-MS) in both positive (Figure 5.5) and negative (Figure 5.6) ion modes, using H_2O, and acetonitrile/methanol + 1% H_2O as solvents.

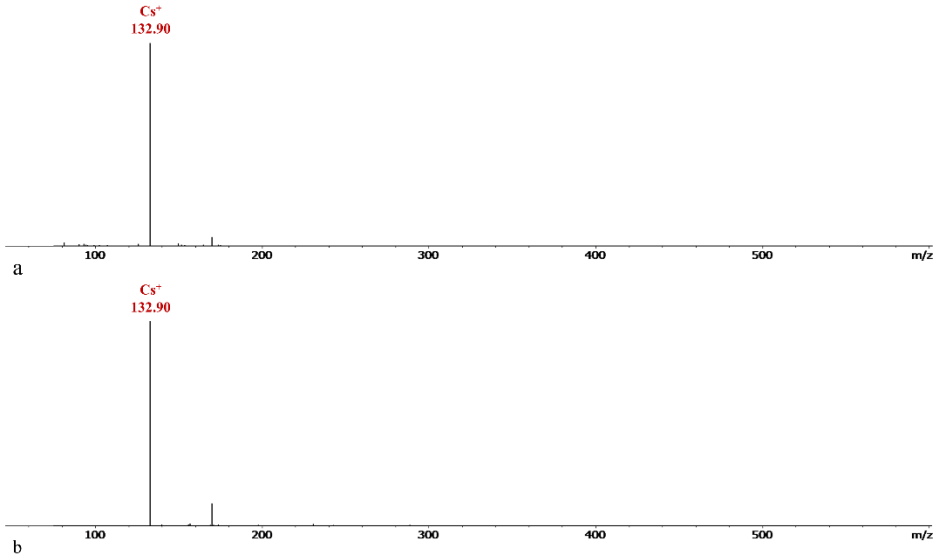

Figure 5.5 – ESI mass spectrum of $Cs_2[V^V_2O_4(mal)_2]\cdot 2H_2O$ (~ 100 μM) in a) H_2O and in b) acetonitrile/methanol + 1% H_2O. The spectra were recorded in positive ion mode within the m/z range of 90 to 600, and the spectrometer was calibrated using the standard tunemix (Bruker Daltonik GmbH, timsTOF Pro User Manual, Bremen, Germany) to ensure an accuracy of approximately 5 ppm in the m/z region of 45-1800. These studies were carried out under the supervision of Prof. Annette Rompel from University of Vienna.

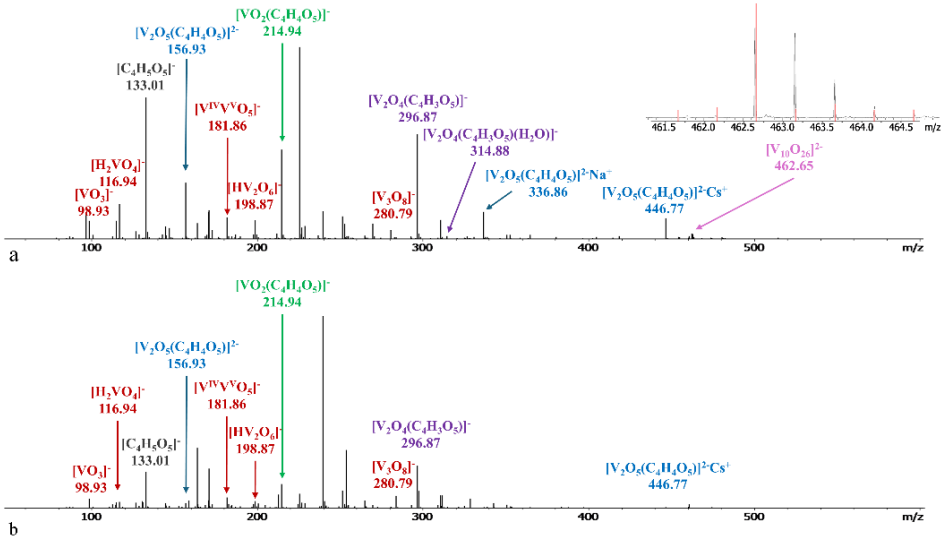

Figure 5.6 – ESI mass spectrum of $Cs_2[V^V_2O_4(mal)_2]\cdot 2H_2O$ (~ 100 µM) in a) H_2O and in b) acetonitrile/methanol + 1% H_2O. The spectra were recorded in negative ion mode within the m/z range of 90 to 600, and the spectrometer was calibrated using the standard tunemix (Bruker Daltonik GmbH, timsTOF Pro User Manual, Bremen, Germany) to ensure an accuracy of approximately 5 ppm in the m/z region of 45-1800. In the case of $[V^V_{10}O_{26}]^{2-}$, the overlap between the experimental (black) and simulated (red) envelopes is depicted in the insert. These studies were carried out under the supervision of Prof. Annette Rompel from University of Vienna.

In negative-ion mode, the spectrum recorded in H_2O (Figure 5.6a) reveals a variety of singly and doubly charged species. Among the singly charged ions, protonated and unprotonated vanadates such as $[V^VO_3]^-$, $[H_2V^VO_4]^-$, $[V^{IV}V^VO_5]^-$, $[HV^V_2O_6]^-$ and $[V^V_3O_8]^-$ were detected, together with the monoanionic malate ligand $[C_4H_5O_5]^-$ (*i.e.*, $[mal^{2-} + H^+]^-$). Several VCs with one or two V centres were also identified: $[V^VO_2(mal)]^-$, $[V^V_2O_4(mal) - H^+]^-$, and $[V^V_2O_4(mal)(H_2O) - H^+]^-$. The only doubly charged species identified contains two V centres: $[V^V_2O_5(mal)]^{2-}$. Additionally, the $[V^V_{10}O_{26}]^{2-}$, a decavanadate anion with two oxido ligands less than the canonical $[V^V_{10}O_{28}]^{6-}$, was observed (Table 5.3). When

the analysis was repeated in acetonitrile/methanol + 1% H_2O (Figure 5.6b), most of the species observed in aqueous solution were confirmed (Table 5.3). Notably, the decavanadate species was absent under this condition.

Table 5.3 – Experimental and calculated m/z values for $Cs_2[V^V_2O_4(mal)_2]\cdot 2H_2O$ dissolved in H_2O and in ACN/MeOH + 1% H_2O, recorded in negative ion mode using ESI-MS.

In H_2O		
Observed species	**Experimental m/z**	**Simulated m/z**
$[V^VO_3]^-$	98.93	98.93
$[H_2V^VO_4]^-$	116.94	116.94
$[mal^{2-} + H^+]^-$	133.01 134.02	133.01 134.02
$[V^V_2O_5(mal)]^{2-}$	156.93 157.44 157.94	156.93 157.44 157.94
$[V^{IV}V^VO_5]^-$	181.86	181.86
$[HV^V_2O_6]^-$	198.87	198.87
$[V^VO_2(mal)]^-$	214.94 215.94	214.94 215.94
$[V^V_3O_8]^-$	280.79	280.79
$[V^V_2O_4(mal) - H^+]^-$	296.87 297.87	296.87 297.87
$[V^V_2O_4(mal)(H_2O) - H^+]^-$	314.88 315.88	314.88 315.88
$[V^V_2O_5(mal)^{2-} + Na^+]^-$	336.86 337.86	336.86 337.86
$[V^V_2O_5(mal)^{2-} + Cs^+]^-$	446.77 447.78	446.77 447.78
$[V^V_{10}O_{26}]^{2-}$	462.16 462.65 463.16 463.66 464.16 464.65	462.16 462.65 463.16 463.66 464.16 464.65
In ACN/MeOH + 1% H_2O		
Observed species	**Experimental m/z**	**Simulated m/z**
$[V^VO_3]^-$	98.93	98.93
$[H_2V^VO_4]^-$	116.94	116.94
$[mal^{2-} + H^+]^-$	133.01 134.02	133.01 134.02

$[V^{V}_2O_5(mal)]^{2-}$	156.93 157.44 157.94	156.93 157.44 157.94
$[V^{IV}V^{V}O_5]^-$	181.86	181.86
$[HV^{V}_2O_6]^-$	198.87	198.87
$[V^{V}O_2(mal)]^-$	214.94 215.94	214.94 215.94
$[V^{V}_3O_8]^-$	280.79	280.79
$[V^{V}_2O_4(mal) - H^+]^-$	296.87 297.87	296.87 297.87
$[V^{V}_2O_5(mal)^{2-} + Cs^+]^-$	446.77 447.78	446.77 447.78

The positive-ion mode ESI-MS spectrum of HEWL (concentration = 13 mg/mL, 0.9 mM) diluted 1:100 in acetonitrile/H_2O (9/1) + 1% FA was recorded. The raw spectrum, which reconstructs the protein mass from the distribution of multiply charged ions, yielded an intense peak at 14,304.9 Da, consistent with the expected value for metal-free HEWL (Figure 5.7a). The positive-ion mode ESI-MS spectrum was then recorded after dissolving HEWL in the presence of $Cs_2[V^{V}_2O_4(mal)_2]\cdot 2H_2O$ (VC:HEWL molar ratio = 1:1) diluted 1:100 in acetonitrile/H_2O (9/1) + 1% FA (Figure 5.7b). The spectrum shows two main peaks: at 14304.9 Da (metal-free protein) and at 15268.2 Da, the latter attributed to the $[H_6V^{V}_{10}O_{28}]$–HEWL adduct. These findings provide direct evidence that decavanadate is present in solution under the chosen experimental conditions and can bind the protein. As indicated in previous studies,[269] the protonated species $[H_6V^{V}_{10}O_{28}]$ is expected to be the dominant form of decavanadate.

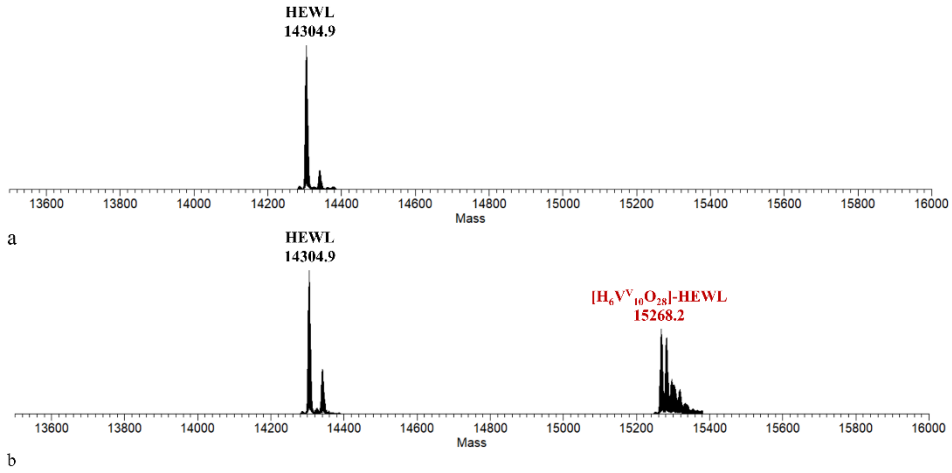

Figure 5.7 – Deconvoluted ESI-MS spectra of a) HEWL (concentration = 13 mg/mL) and b) of the system containing $Cs_2[V^V_2O_4(mal)_2]\cdot 2H_2O$:HEWL in 1:1 molar ratio. Both samples were diluted 1:100 in acetonitrile/H_2O + 1% FA. Mass is in Da. These studies were carried out under the supervision of Prof. Annette Rompel from University of Vienna.

5.2.3 Crystallographic studies at cryogenic temperature

X-ray diffraction data were collected at 100 K on two crystals of HEWL grown in 1.1 M sodium chloride and 0.1 M sodium acetate pH 4.0 and exposed for 7 days to $Cs_2[V^V_2O_4(mal)_2]\cdot 2H_2O$ powder (Table 5.4). These crystals diffract X-rays at 1.46 Å and 1.18 Å resolution, respectively, and belong to the space group $P4_32_12$, with one protein molecule in the asymmetric unit (Figure 5.8). The overall structures of the protein in the two crystals are very similar to each other (RMSD < 0.35 Å) and to that of the metal-free HEWL (RMSD = 0.24-0.27 Å).

Table 5.4 – Data collection and refinement statistics.

Data collection			
	Structure A	**Structure B**	**Structure at 37°C**
PDB code	9RBG	9RBT	9RBV
Crystallization condition	1.1 M sodium chloride, 0.1 M sodium acetate pH 4.0	1.1 M sodium chloride, 0.1 M sodium acetate pH 4.0	1.1 M sodium chloride, 0.1 M sodium acetate pH 4.0
Soaking time	7 d	7 d	Few hours
Space group	$P4_32_12$	$P4_32_12$	$P4_32_12$
a (Å)	78.60	80.01	79.1
b (Å)	78.60	80.01	79.1
c (Å)	35.65	36.27	37.4
Resolution range (Å)	55.58-1.46 (1.48-1.46)	40.01-1.18 (1.20-1.18)	55.93-2.09 (2.13-2.09)
Observations	389622 (7984)	719874 (18846)	53940 (2669)
Unique reflections	17932 (542)	35010 (1939)	7102 (355)
Completeness (%)	88.9 (54.6)	89.1 (99.9)	95.7 (100.0)
Redundancy	21.7 (14.7)	20.6 (9.7)	7.6 (7.5)
Rmerge (%)	0.048 (2.964)	0.060 (4.155)	0.193 (2.494)
Average I/σ(I)	27.4 (0.8)	19.4 (0.5)	8.2 (0.9)
$CC_{1/2}$	1.000 (0.498)	0.999 (0.371)	0.997 (0.323)
Anom. completeness (%)	88.8 (55.3)	88.6 (100.0)	95.5 (100.0)
Anom. Multiplicity	11.9 (7.8)	10.9 (5.0)	4.2 (4.0)
Refinement			
Resolution (Å)	55.59-1.46	40.01-1.18	55.93-2.09
N° reflections	15647	27190	5718
N° reflections in working set	522	424	257
R-factor/Rfree	0.239/0.312	0.191/.0.235	0.213/0.293
N° non-H atoms in the refinement	1193	1184	1044
B-factor overall ($Å^2$)	27.50	25.37	38.36

Estimated occupancy of $[V^{IV}O]^{2+}$	1.00	-	1.00
Estimated occupancy of $[V^{V}_2O_5(mal)]^{2-}$	0.70	0.60	-
Estimated occupancy of $[V^{V}_{10}O_{26}]^{2-}$	0.70	-	-
Estimated occupancy of $[V^{V}_{10}O_{28}]^{6-}$	-	0.80	-
B-factor of $[V^{IV}O]^{2+}$ (Å^2)	53.5±7.2	43.2±13.3	-
B-factor of $[V^{V}_2O_5(mal)]^{2-}$ (Å^2)	44.6±4.8	-	-
B-factor of $[V^{V}_{10}O_{26}]^{2-}$ (Å^2)	-	25.1±1.8	-
B-factor of $[V^{V}_{10}O_{28}]^{6-}$ (Å^2)	53.5±7.2	43.2±13.3	-
Ramachandran values (%)			
Most favoured/Additional allowed	94.39/5.61	91.53/8.47	91.34/8.66
Outliers	0	0	1
RMSD from ideality			
RMSD bonds (Å)	0.011	0.017	0.022
RMSD angles (°)	1.900	2.414	1.569

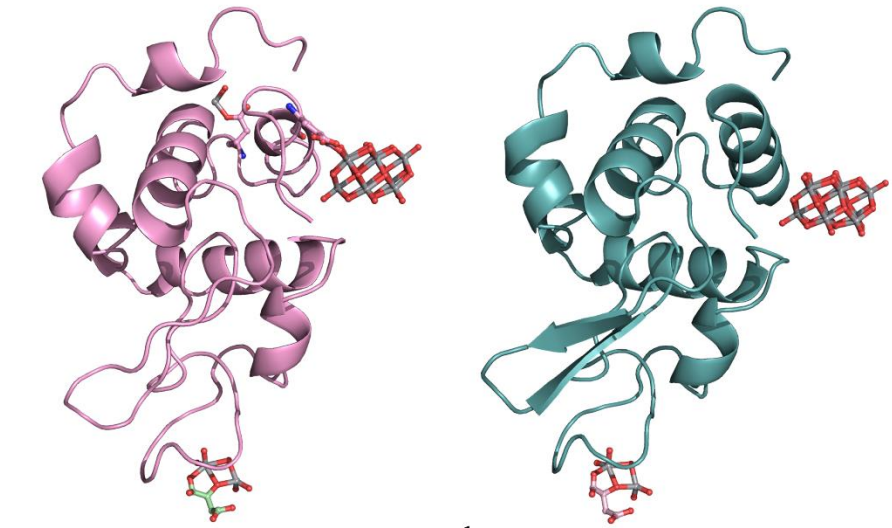

Figure 5.8 – Overall structures of V/HEWL adducts derived from two crystals of HEWL exposed to $Cs_2[V^V_2O_4(mal)_2]\cdot 2H_2O$ for 7 days: a) Structure A; b) Structure B. Vanadium atoms are in grey. Coordinates and structure factors were deposited in the PDB under the accession codes 9RBG, and 9RBT.

Interestingly, the two structures show some differences close to V binding sites.

In structure A, coordination of a VO group, assigned to $[V^{IV}O]^{2+}$, to the side chain of Asp18 (Figure 5.9a), non-covalent binding of the dinuclear oxidovanadium(V) complex $[V^V_2O_5(mal)]^{2-}$ to protein surface residues (Figure 5.9b) and covalent binding of $[V^V_{10}O_{26}]^{2-}$ to the side chain of Glu7 and its symmetry mate (Glu7*) (Figure 5.9c) are observed.

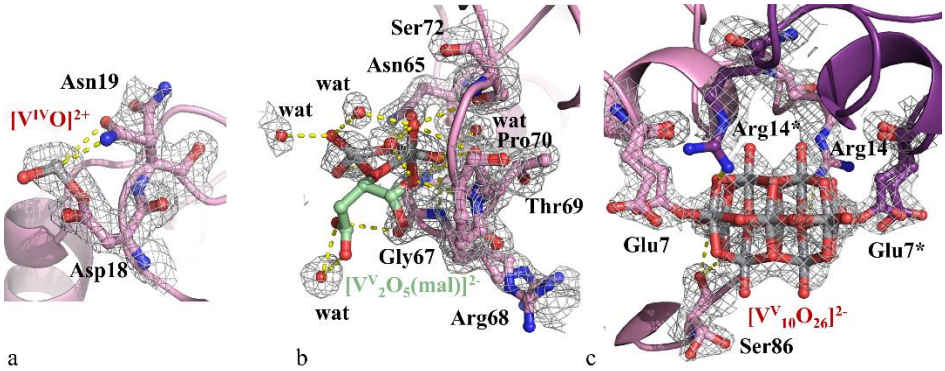

Figure 5.9 – V binding sites in the structure A: a) covalent binding of $[V^{IV}O]^{2+}$ to the side chain of Asp18; b) non-covalent interaction of the dinuclear oxidovanadium(V) complex $[V^{V}_2O_5(mal)]^{2-}$ to the protein surface; c) covalent binding of the $[V^{V}_{10}O_{26}]^{2-}$ to the side chain of Glu7 and Glu7*. 2Fo-Fc electron density maps are reported at 1.0 σ level in grey. Anomalous difference electron density map of $[V^{V}_{10}O_{26}]^{2-}$ is reported in Figure 5.12a. Asterisk refers to atoms from symmetry-related molecules (coloured in purple). Glu7 and Ser86 side chains adopt two alternative conformations.

Refinements suggest occupancy = 1.00, 0.70 and 0.70 for the $[V^{IV}O]^{2+}$, $[V^{V}_2O_5(mal)]^{2-}$ and $[V^{V}_{10}O_{26}]^{2-}$, respectively.

Surprisingly, $[V^{IV}O]^{2+}$ was not detected in the ^{51}V NMR spectra while $[V^{V}_2O_5(mal)]^{2-}$ and $[V^{V}_{10}O_{26}]^{2-}$ were observed in both ^{51}V NMR and mass spectra. The $[V^{IV}O]^{2+}$ ion, covalently bound to the OD1 atom of Asp18, is in contact with the ND2 and the OD1 atoms of Asn19 whose side chain adopts two different conformations (Figure 5.9a).

$[V^{V}_2O_5(mal)]^{2-}$ interacts non-covalently with residues Gly67-Ser72. In particular, the O1 atom of $[V^{V}_2O_5(mal)]^{2-}$ is hydrogen bonded to the O of Thr69, the N of Pro70 and a water molecule, while O4, O6 and O7 atoms of $[V^{V}_2O_5(mal)]^{2-}$ are hydrogen bonded to water molecules. O5 atom of $[V^{V}_2O_5(mal)]^{2-}$ is in contact with the O atom of Gly67 and a water molecule, while O8 atom is at hydrogen bonded distance from the O atom of Thr69, OG of Ser72 and water molecules. O9

atom of $[V^{V}_{2}O_{5}(mal)]^{2-}$ interacts with the N atom of Gly67, the N atom of Arg68, N and O atoms of Thr69 and a water molecule. O10 atom hydrogen bonds OD1 and ND2 atoms of Asn65 and N of Gly67 (Figure 5.9b).

This dinuclear oxidovanadium(V) complex $[V^{V}_{2}O_{5}(mal)]^{2-}$ is the product of the loss of one mal ligand from $[V^{V}_{2}O_{4}(mal)_{2}]^{2-}$, *i.e.*, the species observed in the ^{51}V NMR spectra. The ligand loss is in line with $[V^{V}_{2}O_{4}(mal)_{2}]^{2-}$ behaviour in aqueous solution. This anion consists of two V centres both coordinated to two oxido ligands and two bridging oxygens, one of which is part of the mal ligand. One of the two V centres binds an additional oxygen of the mal group, forming a five-membered chelated ring (Figure 5.10). The V centres are not equivalent: one is penta-coordinate and one is tetra-coordinated, at variance with what found in the structure of $Cs_{2}[V^{V}_{2}O_{4}(mal)_{2}]\cdot 2H_{2}O$, that is based on a centrosymmetric dimeric arrangement where the two metal centres show the same coordination spheres.[117]

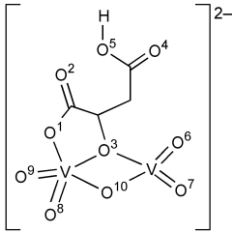

Figure 5.10 – The schematic structure of $[V^{V}_{2}O_{5}(mal)]^{2-}$.

The $[V^{V}_{10}O_{26}]^{2-}$ moiety was reconstituted by its symmetry mate and can be described as a decavanadate ion of type $[V^{V}_{10}O_{28}]^{6-}$ [165,270] that has two oxygen atoms replaced by the OE2 atoms of the side chains of Glu7 and Glu7* (that adopt two alternative conformations with occupancy 0.70 and 0.30) (Figure 5.9c). In this way, the decavanadate cross-links two protein molecules (Figure 5.11).

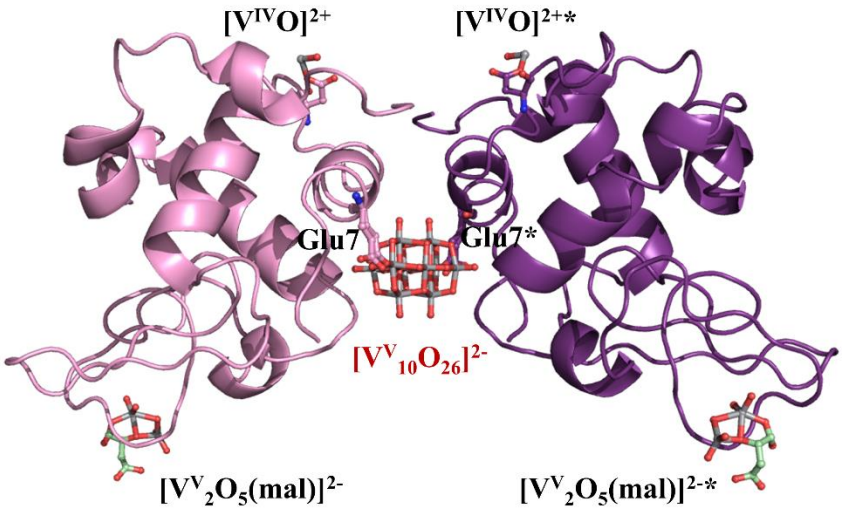

Figure 5.11 – Structure of the cross-linked HEWL dimer formed by the decavanadate covalently bound to the side chain of Glu7 and Glu7*. The symmetry-related molecule is coloured in purple and is highlighted as *.

In addition, $[V^{V}_{10}O_{26}]^{2-}$ forms hydrogen bonds with the NH2 atom of Arg14, the O atom of Ser86, water molecules and the NH2 atom of Arg14 from a symmetry-related molecule (Figure 5.9c). Anomalous difference electron density map is reported in Figure 5.12a.

The interaction of decavanadate with proteins has been already studied also by X-ray crystallography[123] and the formation of a covalent adduct between $[V^{V}_{10}O_{28}]^{6-}$ and a protein has been already hypothesized,[271] but this is the first evidence from a structural point of view.

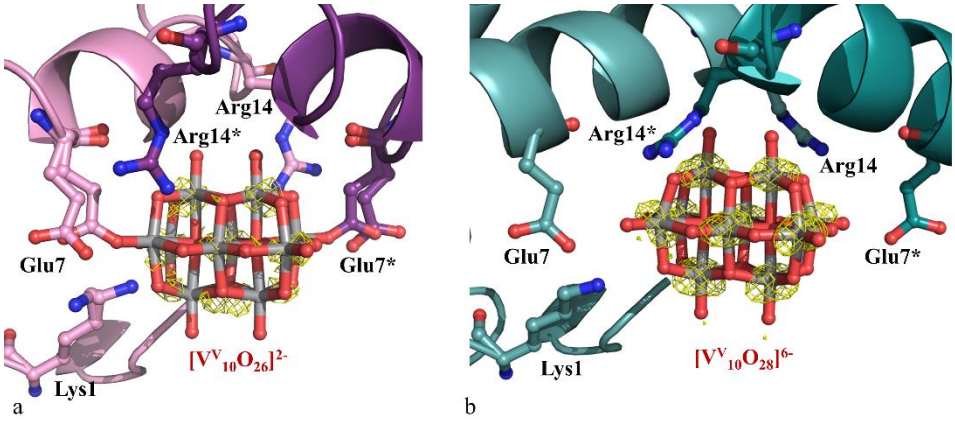

Figure 5.12 – Decavanadate binding sites in a) the structure A and b) the structure B. Anomalous difference electron density map is reported in yellow at 3.0 σ level. Asterisk (*) indicates atoms from symmetry-related molecules (purple in structure A and deep teal in structure B). In the structure A Lys1 and Glu7 adopt two different conformations.

The Cambridge Crystallographic Data Centre currently lists more than 300 X-ray structures of decavanadate ions differing for protonation state and counter-ion composition.[165] At acidic pH, decavanadate is the most stable vanadate form and at neutral pH it is kinetically inert and can persist in solution for several days.[165] Only two CCDC structures of decavanadate have two oxygen atoms of the $\{V_{10}O_{28}\}$ core replaced by other groups: the structure deposited under the accession code HEGBEB[272] and that with code TORXAA.[273] In the former structure, two methoxy groups bridge the outermost V atoms;[272] two ethoxy groups in the latter structure.[273] There are no structures in which two core oxygens are replaced by carboxylate groups.

In structure B (Figure 5.8b), non-covalent binding of the dinuclear oxidovanadium(V) complex $[V^{V}_{2}O_{5}(mal)]^{2-}$ and of $[V^{V}_{10}O_{28}]^{6-}$ are observed. $[V^{V}_{10}O_{28}]^{6-}$ is reconstructed by its symmetry mate, has occupancy equal to 0.80 and forms hydrogen bonds with the NZ atom of Lys1, the OE2 atom of Glu7, the NE2 of His15, the OD2 of Asp87, the main chain N atom of Ile88, water

molecules and the NH1 atom of Arg14 from a symmetry-related molecule (Figure 5.13).

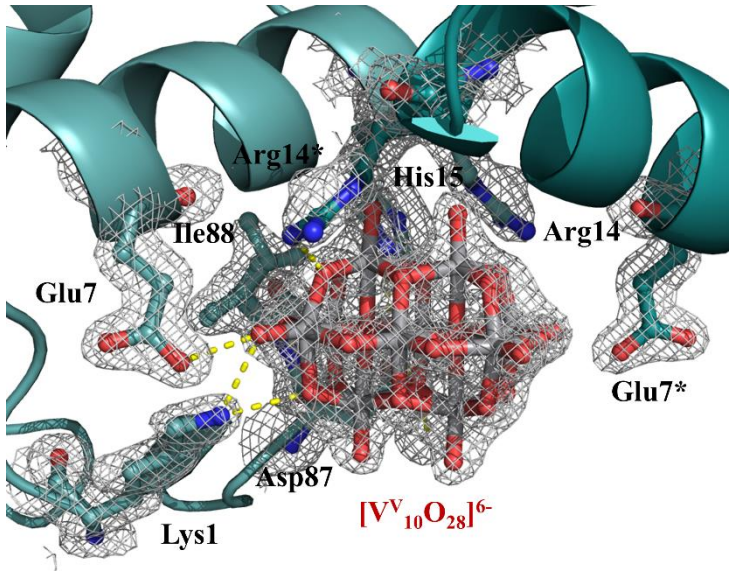

Figure 5.13 – Vanadium binding sites in structure B: non-covalent interaction of the $[V^{V}_{10}O_{28}]^{6-}$ to the protein surface. 2Fo-Fc electron density maps are reported at 1.0 σ level in grey. Asterisk refers to atoms from symmetry-related molecules (deep teal). Anomalous difference electron density map is reported in Figure 5.12b.

These interactions are favoured by conformational variations of the side chains of Lys1, Glu7, Arg14 and His15. Anomalous difference electron density map is reported in Figure 5.12b.

^{51}V NMR, ESI-MS and crystallographic results can be interpreted considering the known behaviour of $V^{V}O_2^+$ ions with *α*-hydroxycarboxylates in aqueous solution. Although stability constants for $V^{V}O_2$–mal complexes are not available, useful insights can be drawn from the corresponding $V^{V}O_2$–citr, where citr is citrate anion.[265] Malic and citric acid share a similar structure differing only for the

fourth group bound to the tetrahedral C atom which is a H atom in the first case and a $–CH_2COOH$ group in the second one (Figure 5.14).

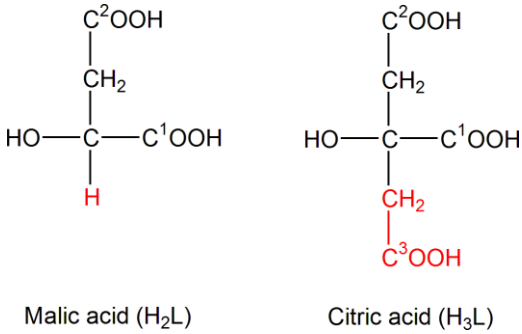

Figure 5.14 – Structure of malic and citric acid. In red the structural difference between the two bioligands is shown.

The fully protonated forms of malic and citric acids, denoted as H_2L and H_3L, have comparable pK_a values: pK_{a1} = 3.16 and pK_{a2} = 4.57 for malic acid,[274] and pK_{a1} = 2.87, pK_{a2} = 4.27 and pK_{a3} = 5.57 for citric acid,[275] and they are expected to coordinate $V^VO_2^+$ in the same way. The citrate carboxylate group is usually not involved in metal binding, and it should not influence the coordination mode.

The distribution curve of the species that citrate and $V^VO_2^+$ ion form when in a molar ratio of 1:1 and at V concentration of 100 μM (ESI-MS experiments), 0.3 mM (soaking experiments) and 5 mM (^{51}V NMR) can be calculated with the stability constants determined by Petterson et al.[265] (Figure 5.15).

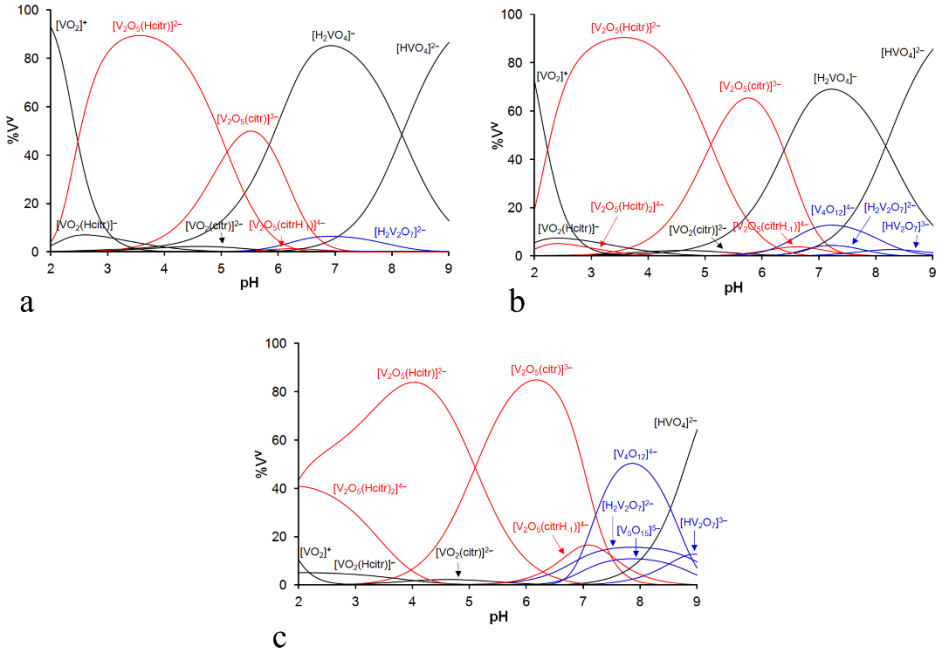

Figure 5.15 – Species distribution curves in the system V^V/citr 1:1 with V concentration: a) 100 μM; b) 300 μM; c) 5 mM. In red, blue, and black colours are shown the dinuclear complexes formed with citrate ligand, the inorganic POVs, and mononuclear species.

At pH 4.0, the species $[V^V_2O_5(Hcitr)]^{2-}$, with the (C^1OO^-, O^-) donor set bound to V^V and C^2OOH and C^3OOH groups that are still protonated, dominates in an aqueous solution. This species corresponds to $[V^V_2O_5(mal)]^{2-}$ where the coordination is (C^1OO^-, O^-) and C^2OOH is protonated. So, in aqueous solution and at pH 4.0, the transformation of $[V^V_2O_4(mal)_2]^{2-}$ to $[V^V_2O_5(mal)]^{2-}$ occurs upon the reaction $[V^V_2O_4(mal)_2]^{2-} + H_2O \rightarrow [V^V_2O_5(mal)]^{2-} + H_2mal$. This explains the non-covalent binding of $[V^V_2O_5(mal)]^{2-}$ to HEWL and the detection of this species in the ESI-MS and ^{51}V NMR spectra.

On the contrary, increasing V concentration, the amount of $[H_2V^V_2O_7]^{2-}$ and $[HV^V_2O_7]^{3-}$ increases and polynuclear species are formed. POVs with a number of V atoms higher than 5 are not expected, at least up to 5 mM, however a V_{10}

species was detected by ESI-MS and ^{51}V NMR spectroscopy. This finding could be explained by the greater stability of $[V^{V}_{2}O_5(Hcitr)]^{2-}$ than $[V^{V}_{2}O_5(mal)]^{2-}$ which could prevent the formation of decavanadate. Furthermore, it should be considered that the amount of $[V^{V}_{10}O_{28}]^{6-}$ observed in the ^{51}V NMR experiments is small and its formation could be stabilized by the presence of HEWL at RT, as can be argued from Figure 5.7 where the only adducts revealed by ESI-MS in the system formed by $Cs_2[V^{V}_{2}O_4(mal)_2]\cdot 2H_2O$ and protein is with $[H_6V^{V}_{10}O_{28}]$–HEWL.

Finally, it should be observed that, once formed, a small amount of $[V^{V}_{2}O_5(mal)]^{2-}$ can give the aquaion $[V^{V}O_2]^{+}$ according to the reaction $[V^{V}_{2}O_5(L)]^{2-} + 4\ H^{+} \rightarrow 2\ [V^{V}O_2]^{+} + LH_2 + H_2O$. Subsequently, $[V^{V}O_2]^{+}$ can be reduced to $[V^{IV}O]^{2+}$, detected in the structure A (Figure 5.8a).

5.2.4 Crystallographic studies at physiological temperature

Since ^{51}V NMR data suggest that at 37°C V_{10} is not formed in the presence of HEWL, the structure formed upon treatment of HEWL crystals grown at 37°C with $Cs_2[V^{V}_{2}O_4(mal)_2]\cdot 2H_2O$ was solved. Crystallization and data collection at 37°C are challenging. A higher protein concentration was necessary to grow HEWL crystals at 37°C and special manipulations were needed for the crystal mounting to avoid dehydration. X-ray diffraction data at 37°C of HEWL-$Cs_2[V^{V}_{2}O_4(mal)_2]\cdot 2H_2O$ crystals were collected using procedure recently developed in the Prof. Merlino's laboratory.[221]

The overall HEWL conformation in the 37°C structure is not significantly affected by the temperature, in agreement with previous observations[166,221] (RMSD with metal-free protein structure = 0.20 Å and with the structure of the V–HEWL reported in the previous paragraph = 0.27 Å and 0.35 Å). However, there are some differences close to the V binding sites. Consistently with the ^{51}V NMR results, the structure at 37°C does not show the presence of a V_{10}. Instead,

a single VO group, presumably a $[V^{IV}O]^{2+}$ ion, is bound to the side chain of Asp18 (Figure 5.16).

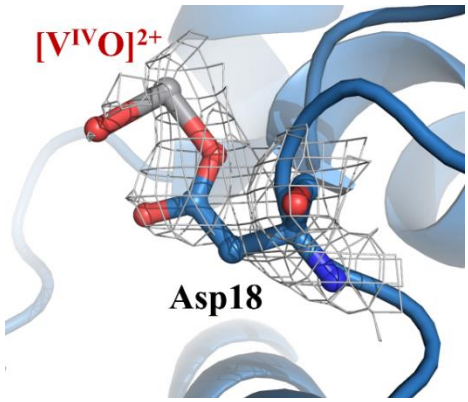

Figure 5.16 – 2Fo-Fc electron density map of the $[V^{IV}O]^{2+}$ observed in the structure at 37°C is reported at 1.0 σ level in grey.

In conclusion, results reveal that, in *crystallo*, HEWL binds a $[V^{IV}O]^{2+}$ ion, a $[V^{V}_2O_5(mal)]^{2-}$ ion and V_{10} group at 20°C, while at physiological temperature the decavanadate disappears, in strict agreement with ^{51}V NMR data, and only an adduct with $[V^{IV}O]^{2+}$ is observed.

This is the first structural observation of covalent binding of V_{10} with a protein. The interaction of $[V^{V}_{10}O_{28}]^{6-}$ with the protein is favoured by protein–protein interaction. Overall, these findings suggest that protein–protein stabilization may facilitate unexpected binding modes.[276]

5.3 Interaction of $Cs_2[V^{V}_2O_4(lact)_2]\cdot 2H_2O$ with HEWL

Given the biological relevance of lactate and its widespread occurrence in metabolic processes, $Cs_2[V^{V}_2O_4(lact)_2]\cdot 2H_2O$ represents a complementary system for studying the behaviour of dioxidovanadium(V) complexes with *α*-hydroxycarboxylic acid. As for $Cs_2[V^{V}_2O_4(mal)_2]\cdot 2H_2O$, the solution behaviour of the lactate

analogue was first examined under different conditions, followed by studies of its interaction with HEWL from a structural point of view.

5.3.1 ^{51}V NMR studies

The behaviour of $Cs_2[V^V_2O_4(lact)_2]\cdot 2H_2O$ in solution was investigated by collecting ^{51}V NMR spectra of the compound (concentration = 5 mM) in D_2O and under the conditions used to obtain its adduct with HEWL: i) 1.1 M sodium chloride, 0.1 M sodium acetate pH 4.0 and 10% D_2O; ii) 0.1 M sodium acetate pH 4.0, 20% ethylene glycol, 0.6 M sodium nitrate and 10% D_2O; iii) 0.8 M succinic acid pH 7.0 and 10% D_2O; iv) 0.1 M HEPES pH 7.5, 2.0 M sodium formate and 10% D_2O. Measurements were performed in the absence and in the presence of the protein (concentration = 13 mg/mL, 0.9 mM) after 1 hour and 7 days of incubation at RT (Figure 5.17-Figure 5.20).

The spectrum of $Cs_2[V^V_2O_4(lact)_2]\cdot 2H_2O$ collected at RT after 1 h of incubation in D_2O reveals the presence of $[V^V_2O_4(lact)_2]^{2-}$ (signal at ~–532 ppm), $[V^V_3O_7(lact)_2]^{3-}$ (signals at ~–539 ppm, –546 ppm), V_{10} (signals at ~–424 ppm, –502 ppm, –517 ppm), $[V^VO_2]^+$ (~–550 ppm) and $[H_2V^VO_4]^-$ (~–558 ppm) (Figure 5.17). After 7 d of incubation, the same species are detected except for $[H_2V^VO_4]^-$. Quantitative analysis indicates that the percentage of decavanadate significantly increases over time from ~ 11.9% (after 1 h of incubation) to ~ 35.9% (after 7 d of incubation) (Figure 5.17, Table 5.5).

The spectra collected in 1.1 M sodium chloride, 0.1 M sodium acetate pH 4.0 and 10% D_2O show the presence of $[V^V_2O_4(lact)_2]^{2-}$, $[V^V_3O_7(lact)_2]^{3-}$, V_{10} and $[V^VO_2]^+$ in both incubation times. Also in this case, the integration analysis shows that the amount of decavanadate increases over time (Figure 5.17, Table 5.5). In contrast, in the presence of the protein, only $[V^V_2O_4(lact)_2]^{2-}$, $[V^V_3O_7(lact)_2]^{3-}$ and $[V^VO_2]^+$ were detected after 1 h of incubation and only a small amount (~ 6%) of V_{10} after 7 d of incubation (Figure 5.17, Table 5.5).

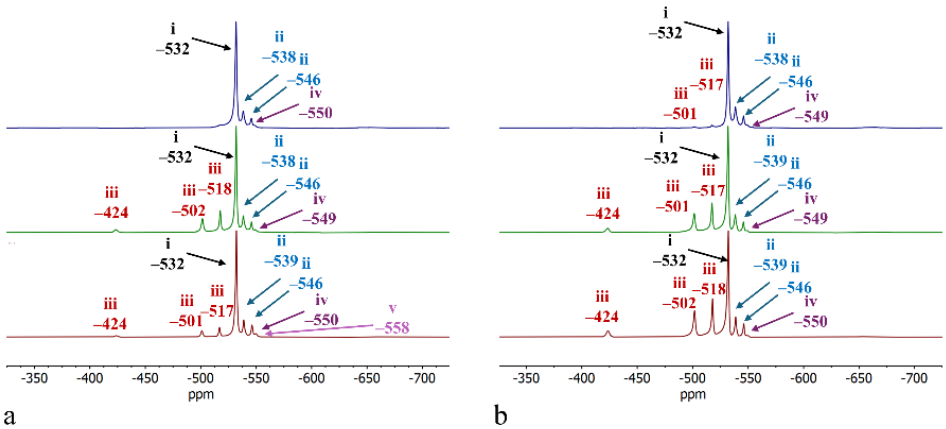

Figure 5.17 – ^{51}V NMR spectra measured at RT after a) 1 h and b) 7 d of incubation of $Cs_2[V^V_2O_4(lact)_2]\cdot 2H_2O$ (5 mM) dissolved in D_2O (red lines); in 1.1 M sodium chloride, 0.1 M sodium acetate pH 4.0 and 10% D_2O (green lines); and in 1.1 M sodium chloride, 0.1 M sodium acetate pH 4.0 and 10% D_2O in presence of HEWL (13 mg/mL) (blue lines). i indicates $[V^V_2O_4(lact)_2]^{2-}$, ii $[V^V_3O_7(lact)_2]^{3-}$, iii V_{10}, iv $[V^VO_2]^+$ and v $[H_2V^VO_4]^-$. These studies were carried out under the supervision of Prof. Annette Rompel from University of Vienna.

The ^{51}V NMR spectrum of $Cs_2[V^V_2O_4(lact)_2]\cdot 2H_2O$ was also collected at RT after 1 h of incubation in 0.1 M sodium acetate pH 4.0, 20% ethylene glycol (EG), 0.6 M sodium nitrate and 10% D_2O. Results indicate the presence of $[V^V_2O_4(lact)_2]^{2-}$ (signal at ~–532 ppm), $[V^V_3O_7(lact)_2]^{3-}$ (signals at ~–538 ppm, –546 ppm), V_{10} (signals at ~–425 ppm, –502 ppm, –519 ppm), and of a dinuclear oxidovanadium(V) complex with ethylene glycol as ligand, $[V^V_2O_4(EG)_2]^{2-}$ (signal at ~–523 ppm)[277] (Figure 5.18, Table 5.6). After 7 d of incubation, the same species are detected with the addition of $[V^VO_2(lact)(H_2O)]^-$ (signal at ~–509 ppm) and $[V^VO_2(lact)(OH)]^{2-}$ (signal at ~–520 ppm) (Figure 5.18, Table 5.6). In the presence of the protein, only $[V^V_2O_4(lact)_2]^{2-}$, $[V^V_3O_7(lact)_2]^{3-}$, $[V^V_2O_4(EG)_2]^{2-}$ and $[V^VO_2(lact)(OH)]^{2-}$ are detected (Figure 5.18, Table 5.6).

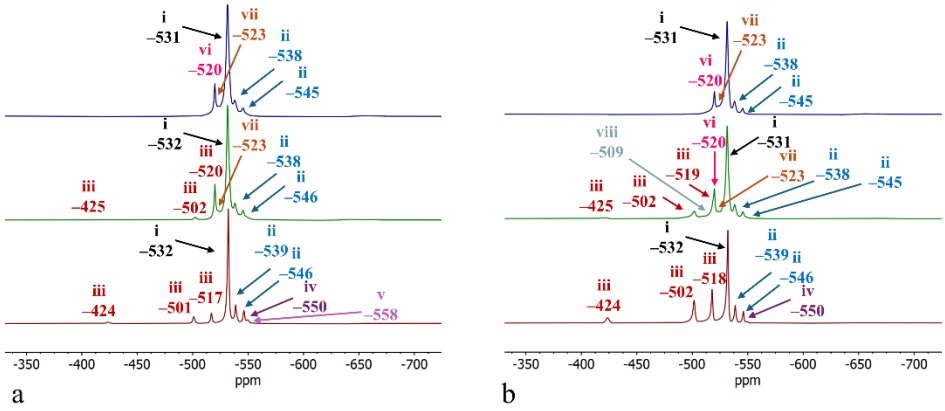

Figure 5.18 – ^{51}V NMR spectra measured at RT after a) 1 h and b) 7 d of incubation of $Cs_2[V^V_2O_4(lact)_2]\cdot 2H_2O$ (5 mM) dissolved in D_2O (red lines); in 20% ethylene glycol, 0.6 M sodium nitrate, 0.1 M sodium acetate pH 4.0 and 10% D_2O (green lines); and in 20% ethylene glycol, 0.6 M sodium nitrate, 0.1 M sodium acetate pH 4.0 and 10% D_2O in presence of HEWL (13 mg/mL) (blue lines). i indicates $[V^V_2O_4(lact)_2]^{2-}$, ii $[V^V_3O_7(lact)_2]^{3-}$, iii V_{10}, iv $[V^VO_2]^+$, v $[H_2V^VO_4]^-$, vi $[V^VO_2(lact)(OH)]^{2-}$, vii $[V^V_2O_4(EG)_2]^{2-}$ and viii $[V^VO_2(lact)(H_2O)]^-$. These studies were carried out under the supervision of Prof. Annette Rompel from University of Vienna.

The spectrum registered in 0.8 M succinic acid pH 7.0 and 10% D_2O reveals the presence of $[V^V_2O_4(lact)_2]^{2-}$ (signal at ~−532 ppm), $[V^V_3O_7(lact)_2]^{3-}$ (signals at ~−540 ppm, −548 ppm), $[H_2V^VO_4]^-$ (~−557 ppm), $[H_2V^V_2O_7]^{2-}$ (~−570 ppm), $[V^V_4O_{12}]^{4-}$ (~−574 ppm) and $[V^V_5O_{15}]^{5-}$ (~−582 ppm), both in the absence and in the presence of HEWL (Figure 5.19, Table 5.7). Similar results were obtained in 0.1 M HEPES pH 7.5, 2.0 M sodium formate and 10% D_2O. The only significant difference is a signal attributed to $[V^V_2O_4(lact)_2]^{2-}$ observed after 7 d of incubation both in the absence and in the presence of HEWL (Figure 5.20, Table 5.8).

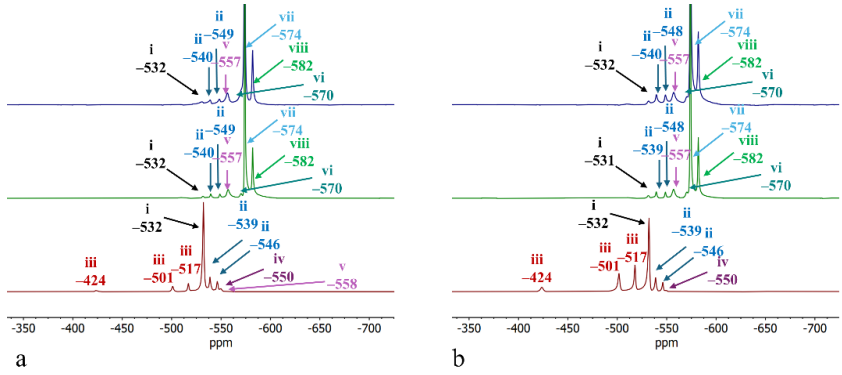

Figure 5.19 – ^{51}V NMR spectra measured at RT after a) 1 h and b) 7 d of incubation of $Cs_2[V^V_2O_4(lact)_2]\cdot 2H_2O$ (5 mM) dissolved in D_2O (red lines); in 0.8 M succinic acid pH 7.0 and 10% D_2O (green lines); and 0.8 M succinic acid pH 7.0 and 10% D_2O in presence of HEWL (13 mg/mL) (blue lines). i indicates $[V^V_2O_4(lact)_2]^{2-}$, ii $[V^V_3O_7(lact)_2]^{3-}$, iii V_{10}, iv $[V^VO_2]^+$, v $[H_2V^VO_4]^-$, vi $[H_2V^V_2O_7]^{2-}$, vii $[V^V_4O_{12}]^{4-}$ and viii $[V^V_5O_{15}]^{5-}$. These studies were carried out under the supervision of Prof. Annette Rompel from University of Vienna.

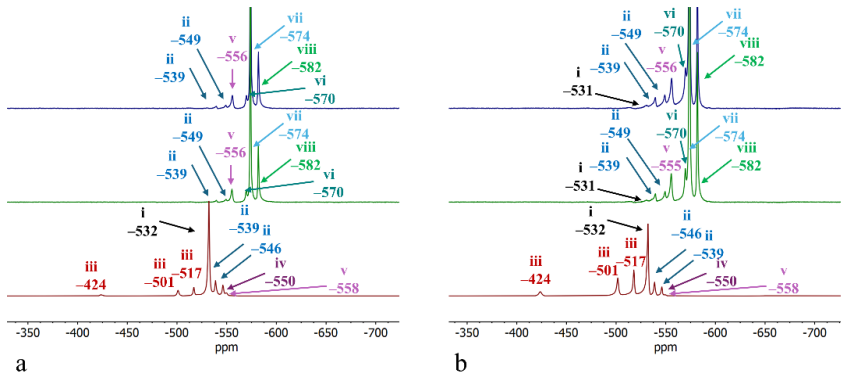

Figure 5.20 – ^{51}V NMR spectra measured at RT after a) 1 h and b) 7 d of incubation of $Cs_2[V^V_2O_4(lact)_2]\cdot 2H_2O$ (5 mM) dissolved in D_2O (red lines); in 0.1 M HEPES pH 7.5, 2.0 M sodium formate and 10% D_2O (green lines); and in 0.1 M HEPES pH 7.5, 2.0 M sodium formate and 10% D_2O in presence of HEWL (13 mg/mL) (blue lines). i indicates $[V^V_2O_4(lact)_2]^{2-}$, ii $[V^V_3O_7(lact)_2]^{3-}$, iii V_{10}, iv $[V^VO_2]^+$, v $[H_2V^VO_4]^-$, vi $[H_2V^V_2O_7]^{2-}$, vii $[V^V_4O_{12}]^{4-}$ and viii $[V^V_5O_{15}]^{5-}$. These studies were carried out under the supervision of Prof. Annette Rompel from University of Vienna.

Table 5.5 – Chemical shifts in ^{51}V NMR spectra measured in triplicate at RT after 1 h and 7 d of incubation of $Cs_2[V^V_2O_4(lact)_2]\cdot 2H_2O$ (5 mM) dissolved in (i) D_2O; (ii) 1.1 M sodium chloride, 0.1 M sodium acetate pH 4.0 and 10% D_2O; and (iii) 1.1 M sodium chloride, 0.1 M sodium acetate pH 4.0 and 10% D_2O in presence of HEWL (13 mg/mL). The relative content of species was calculated based on the integration of ^{51}V signals. Signals were assigned based on literature data. [a]

5 mM $Cs_2[V^V_2O_4(lact)_2]\cdot 2H_2O$ in D_2O (after 1 h at RT)											
^{51}V chemical shift (ppm)			**Species**	**References**	**Integration (%)**			**Sum**			**Average ± SD (%)**
Sample 1	**Sample 2**	**Sample 3**			**Sample 1**	**Sample 2**	**Sample 3**	**Sample 1**	**Sample 2**	**Sample 3**	
–425	–424	–424	V_{10}	110,263	0.7	1.3	1.3	13.1	10.8	11.8	11.9 ± 1.2
–501	–501	–501	V_{10} (or VL^-)	110,113,114,263,264,268	5.1	4.2	4.6				
–517	–517	–517	V_{10} (or VL^{2-})	110,113,114,263,264,268	7.3	5.3	5.9				
–532	–532	–532	$V_2L_2^{2-}$	110,113,114,263,264,268	65.2	65.2	67.1	65.2	65.2	67.1	65.8 ± 1.1
–539	–539	–539	$V_3L_2^{3-}$ (or V_2L^{2-})	110,113,114,263,264,268	11.7	12.9	11.6	19.5	20.5	19.1	19.7 ± 0.7
–546	–546	–546	$V_3L_2^{3-}$ (or V_2L^{2-})	110,113,114,263,264,268	7.8	7.6	7.5				
–550	–550	–550	$[V^VO_2]^+$	278	1.5	3.1	1.6	1.5	3.1	1.6	2.1 ± 0.9
–558	–558	–558	$[H_2V^VO_4]^-$	110,114,278,279,279	0.7	0.4	0.4	0.7	0.4	0.4	0.5 ± 0.2
5 mM $Cs_2[V^V_2O_4(lact)_2]\cdot 2H_2O$ in 0.1 M NaOAc pH 4.0, 1.1 M NaCl, 10% D_2O (after 1 h at RT)											
^{51}V chemical shift (ppm)			**Species**	**References**	**Integration (%)**			**Sum**			**Average ± SD (%)**
Sample 1	**Sample 2**	**Sample 3**			**Sample 1**	**Sample 2**	**Sample 3**	**Sample 1**	**Sample 2**	**Sample 3**	
–424	–424	–424	V_{10}	110,263	2.6	1.3	1.2	25.3	27.9	24.0	25.7 ± 2.0
–501	–502	–502	V_{10} (or VL^-)	110,113,114,263,264,268	10.0	10.3	9.3				

–518	–518	–517	V_{10} (or VL^{2-})	110,113,114,263,264,268	12.7	16.3	13.5				
–532	–532	–532	$V_2L_2^{2-}$	110,113,114,263,264,268	55.9	58.1	60.1	55.9	58.1	60.1	58.0 ±2.1
–538	–538	–538	$V_3L_2^{3-}$ (or V_2L^{2-})	110,113,114,263,264,268	12.1	8.7	9.9	17.4	12.7	14.8	15.0 ± 2.4
–546	–546	–546	$V_3L_2^{3-}$ (or V_2L^{2-})	110,113,114,263,264,268	5.3	4.0	4.9				
–549	–549	–549	$[V^VO_2]^+$	278	1.5	1.3	1.1	1.5	1.3	1.1	1.3 ± 0.2
5 mM $Cs_2[V^V_2O_4(lact)_2]\cdot 2H_2O$ + 13 mg/mL HEWL in 0.1 M NaOAc pH 4.0, 1.1 M NaCl, 10% D_2O (after 1 h at RT)											
^{51}V chemical shift (ppm)			**Species**	**References**	**Integration (%)**			**Sum**			**Average ± SD (%)**
Sample 1	**Sample 2**	**Sample 3**			**Sample 1**	**Sample 2**	**Sample 3**	**Sample 1**	**Sample 2**	**Sample 3**	
–532	–532	–532	$V_2L_2^{2-}$	110,113,114,263,264,268	76.4	76.1	76.6	76.4	76.1	76.6	76.4 ± 0.3
–538	–538	–538	$V_3L_2^{3-}$ (or V_2L^{2-})	110,113,114,263,264,268	15.2	15.9	15.5	22.2	22.7	21.7	22.2 ± 0.5
–546	–546	–546	$V_3L_2^{3-}$ (or V_2L^{2-})	110,113,114,263,264,268	7.0	6.8	6.2				
–550	–549	–550	$[V^VO_2]^+$	278	1.5	1.3	1.7	1.5	1.3	1.7	1.5 ± 0.2
5 mM $Cs_2[V^V_2O_4(lact)_2]\cdot 2H_2O$ in D_2O (after 7 d at RT)											
^{51}V chemical shift (ppm)			**Species**	**References**	**Integration (%)**			**Sum**			**Average ± SD (%)**
Sample 1	**Sample 2**	**Sample 3**			**Sample 1**	**Sample 2**	**Sample 3**	**Sample 1**	**Sample 2**	**Sample 3**	
–424	–425	–424	V_{10}	110,263	4.2	2.9	3.3	38.4	34.7	34.6	35.9 ± 2.2
–502	–501	–502	V_{10} (or VL^-)	110,113,114,263,264,268	15.4	13.5	13.8				
–518	–517	–518	V_{10} (or VL^{2-})	110,113,114,263,264,268	18.8	18.3	17.5				
–532	–532	–532	$V_2L_2^{2-}$	110,113,114,263,264,268	47.7	48.8	48.1	47.7	48.8	48.1	48.2 ± 0.6

–539	–539	–539	$V_3L_2^{3-}$ (or V_2L^{2-})	110,113,114,263,264,268	8.4	9.8	10.5	13.2	14.9	16.2	14.8 ±1.5
–546	–546	–546	$V_3L_2^{3-}$ (or V_2L^{2-})	110,113,114,263,264,268	4.8	5.1	5.7				
–550	–550	–550	$[V^VO_2]^+$	278	0.8	1.6	1.1	0.8	1.6	1.1	1.2 ± 0.4
5 mM $Cs_2[V^V_2O_4(lact)_2]\cdot 2H_2O$ in 0.1 M NaOAc pH 4.0, 1.1 M NaCl, 10% D_2O (after 7 d at RT)											
^{51}V chemical shift (ppm)			**Species**	**References**	**Integration (%)**			**Sum**			**Average ± SD (%)**
Sample 1	**Sample 2**	**Sample 3**			**Sample 1**	**Sample 2**	**Sample 3**	**Sample 1**	**Sample 2**	**Sample 3**	
–424	–424	–424	V_{10}	110,263	3.4	3.2	3.0	29.3	32.6	31.0	31.0 ± 1.7
–502	–501	–501	V_{10} (or VL^-)	110,113,114,263,264,268	11.5	13.3	12.1				
–518	–517	–517	V_{10} (or VL^{2-})	110,113,114,263,264,268	14.4	16.1	15.9				
–532	–532	–532	$V_2L_2^{2-}$	110,113,114,263,264,268	50.9	52.5	53.3	50.9	52.5	53.3	52.1 ± 1.2
–539	–539	–539	$V_3L_2^{3-}$ (or V_2L^{2-})	110,113,114,263,264,268	12.4	9.4	10.0	18.2	13.9	14.6	15.6 ± 2.3
–546	–546	–546	$V_3L_2^{3-}$ (or V_2L^{2-})	110,113,114,263,264,268	5.8	4.5	4.6				
–549	–549	–549	$[V^VO_2]^+$	278	1.6	0.9	1.1	1.6	0.9	1.1	1.2 ± 0.4
5 mM $Cs_2[V^V_2O_4(lact)_2]\cdot 2H_2O$ + 13 mg/mL HEWL in 0.1 M NaOAc pH 4.0, 1.1 M NaCl, 10% D_2O (after 7 d at RT)											
^{51}V chemical shift (ppm)			**Species**	**References**	**Integration (%)**			**Sum**			**Average ± SD (%)**
Sample 1	**Sample 2**	**Sample 3**			**Sample 1**	**Sample 2**	**Sample 3**	**Sample 1**	**Sample 2**	**Sample 3**	
–501	–501	–501	V_{10} (or VL^-)	110,113,114,263,264,268	0.9	3.4	1.3	3.0	9.6	5.4	6.0 ± 3.3
–517	–517	–517	V_{10} (or VL^{2-})	110,113,114,263,264,268	2.1	6.2	4.1				
–532	–532	–532	$V_2L_2^{2-}$	110,113,114,263,264,268	67.2	69.4	72.9	67.2	69.4	72.9	69.8 ± 2.9

–539	–538	–538	$V_3L_2^{3-}$ (or V_2L^{2-})	110,113,114,263,264,268	19.2	13.9	14.7	27.7	20.1	20.9	22.9 ± 4.2
–546	–546	–546	$V_3L_2^{3-}$ (or V_2L^{2-})	110,113,114,263,264,268	8.5	6.2	6.2				
–549	–549	–549	$[V^VO_2]^+$	278	2.1	0.9	0.8	2.1	0.9	0.8	1.3 ± 0.7

[a] L indicates $lact^{2-}$ ligand, VL^- indicates $[V^VO_2(lact)(H_2O)]^-$, VL^{2-} $[V^VO_2(lact)(OH)]^{2-}$, $V_2L_2^{2-}$ $[V^V_2O_4(lact)_2]^{2-}$, V_2L^{2-} $[V^V_2O_5(lact)]^{2-}$ and $V_3L_2^{3-}$ $[V^V_3O_7(lact)_2]^{3-}$.

Table 5.6 – Chemical shifts in ^{51}V NMR spectra measured in triplicate at RT after 1 h and 7 d of incubation of $Cs_2[V^V_2O_4(lact)_2]\cdot 2H_2O$ (5 mM) dissolved in (i) D_2O; (ii) 0.1 M sodium acetate pH 4.0, 20% ethylene glycol, 0.6 M sodium nitrate and 10% D_2O; and (iii) 0.1 M sodium acetate pH 4.0, 20% ethylene glycol, 0.6 M sodium nitrate and 10% D_2O in presence of HEWL (13 mg/mL). The relative content of species was calculated based on the integration of ^{51}V signals. Signals were assigned based on literature data. [a]

5 mM $Cs_2[V^V_2O_4(lact)_2]\cdot 2H_2O$ in D_2O (after 1 h at RT)											
^{51}V chemical shift (ppm)			**Species**	**References**	**Integration (%)**			**Sum**			**Aver-age ± SD (%)**
Sample 1	**Sample 2**	**Sample 3**			**Sample 1**	**Sample 2**	**Sample 3**	**Sample 1**	**Sample 2**	**Sample 3**	
–425	–424	–424	V_{10}	110,263	0.7	1.3	1.3	13.1	10.8	11.8	11.9 ± 1.2
–501	–501	–501	V_{10} (or VL^{-})	110,113,114,263,264,268	5.1	4.2	4.6				
–517	–517	–517	V_{10} (or VL^{2-})	110,113,114,263,264,268	7.3	5.3	5.9				
–532	–532	–532	$V_2L_2^{2-}$	110,113,114,263,264,268	65.2	65.2	67.1	65.2	65.2	67.1	65.8 ± 1.1
–539	–539	–539	$V_3L_2^{3-}$ (or V_2L^{2-})	110,113,114,263,264,268	11.7	12.9	11.6	19.5	20.5	19.1	19.7 ± 0.7
–546	–546	–546	$V_3L_2^{3-}$ (or V_2L^{2-})	110,113,114,263,264,268	7.8	7.6	7.5				
–550	–550	–550	$[V^VO_2]^+$	278	1.5	3.1	1.6	1.5	3.1	1.6	2.1 ± 0.9
–558	–558	–558	$[H_2V^VO_4]^-$	110,114,278,279,279	0.7	0.4	0.4	0.7	0.4	0.4	0.5 ± 0.2
5 mM $Cs_2[V^V_2O_4(lact)_2]\cdot 2H_2O$ in 0.1 M NaOAc pH 4.0, 20% ethylene glycol, 0.6 M $NaNO_3$, 10% D_2O (after 1 h at RT)											
^{51}V chemical shift (ppm)			**Species**	**References**	**Integration (%)**			**Sum**			**Aver-age ± SD (%)**
Sample 1	**Sample 2**	**Sample 3**			**Sample 1**	**Sample 2**	**Sample 3**	**Sample 1**	**Sample 2**	**Sample 3**	

–425	–425	–425	V_{10}	[110,263]	0.1	0.1	0.1	14.9	14.8	20.6	16.8 ± 3.3
–502	–502	–502	V_{10} (or VL^{-})	[110,113,114,263,264,268]	1.4	1.9	3.9				
–520	–520	–520	V_{10} (or VL^{2-})	[110,113,114,263,264,268]	13.4	12.8	16.6				
–523	–523	–523	$V_2EG_2^{2-}$	[277]	3.2	2.8	3.3	3.2	2.8	3.3	3.1 ± 0.3
–532	–532	–531	$V_2L_2^{2-}$	[110,113,114,263,264,268]	64.6	66.6	64.9	64.6	66.6	64.9	65.4 ± 1.1
–538	–538	–538	$V_3L_2^{3-}$ (or V_2L^{2-})	[110,113,114,263,264,268]	11.5	10.8	7.4	17.3	15.9	11.3	14.8 ± 3.1
–546	–546	–545	$V_3L_2^{3-}$ (or V_2L^{2-})	[110,113,114,263,264,268]	5.8	5.1	3.9				
5 mM $Cs_2[V^V_2O_4(lact)_2]\cdot 2H_2O$ + 13 mg/mL HEWL in 0.1 M NaOAc pH 4.0, 20% ethylene glycol, 0.6 M $NaNO_3$, 10% D_2O (after 1 h at RT)											
^{51}V chemical shift (ppm)			**Species**	**References**	**Integration (%)**			**Sum**			**Aver-age ± SD (%)**
Sample 1	**Sample 2**	**Sample 3**			**Sample 1**	**Sample 2**	**Sample 3**	**Sample 1**	**Sample 2**	**Sample 3**	
–520	–520	–520	VL^{2-}	[110,113,114,263,264,268]	12.0	15.9	15.0	12.0	15.9	15.0	14.3 ± 2.0
–523	–523	–523	$V_2EG_2^{2-}$	[277]	4.9	5.0	3.6	4.9	5.0	3.6	4.5 ± 0.8
–531	–531	–531	$V_2L_2^{2-}$	[110,113,114,263,264,268]	69.8	70.6	73.2	69.8	70.6	73.2	71.2 ± 1.8
–538	–538	–538	$V_3L_2^{3-}$ (or V_2L^{2-})	[110,113,114,263,264,268]	9.3	5.8	5.6	13.3	8.5	8.3	10.0 ± 2.8
–545	–545	–545	$V_3L_2^{3-}$ (or V_2L^{2-})	[110,113,114,263,264,268]	4.0	2.7	2.7				
5 mM $Cs_2[V^V_2O_4(lact)_2]\cdot 2H_2O$ in D_2O (after 7 d at RT)											
^{51}V chemical shift (ppm)			**Species**	**References**	**Integration (%)**			**Sum**			

Sample 1	Sample 2	Sample 3			Sample 1	Sample 2	Sample 3	Sample 1	Sample 2	Sample 3	Aver-age ± SD (%)
–424	–425	–424	V_{10}	[110,263]	4.2	2.9	3.3	38.4	34.7	34.6	35.9 ± 2.2
–502	–501	–502	V_{10} (or VL^{-})	[110,113,114,263,264,268]	15.4	13.5	13.8				
–518	–517	–518	V_{10} (or VL^{2-})	[110,113,114,263,264,268]	18.8	18.3	17.5				
–532	–532	–532	$V_2L_2^{2-}$	[110,113,114,263,264,268]	47.7	48.8	48.1	47.7	48.8	48.1	48.2 ± 0.6
–539	–539	–539	$V_3L_2^{3-}$ (or V_2L^{2-})	[110,113,114,263,264,268]	8.4	9.8	10.5	13.2	14.9	16.2	14.8 ±1.5
–546	–546	–546	$V_3L_2^{3-}$ (or V_2L^{2-})	[110,113,114,263,264,268]	4.8	5.1	5.7				
–550	–550	–550	$[V^{V}O_2]^{+}$	[278]	0.8	1.6	1.1	0.8	1.6	1.1	1.2 ± 0.4
5 mM $Cs_2[V^{V}_2O_4(lact)_2]\cdot 2H_2O$ in 0.1 M NaOAc pH 4.0, 20% ethylene glycol, 0.6 M $NaNO_3$, 10% D_2O (after 7 d at RT)											
^{51}V chemical shift (ppm)			**Species**	**References**	**Integration (%)**			**Sum**			**Aver-age ± SD (%)**
Sample 1	**Sample 2**	**Sample 3**			**Sample 1**	**Sample 2**	**Sample 3**	**Sample 1**	**Sample 2**	**Sample 3**	
–421	–425	–425	V_{10}	[110,263]	1.3	0.3	0.3	10.6	10.1	9.8	10.2 ± 0.4
–502	–502	–502	V_{10}	[110,263]	7.4	7.1	7.3				
–519	–519	–519	V_{10}	[110,263]	1.9	2.7	2.2				
–509	–509	–509	VL^{-}	[110,113,114,263,264,268]	7.6	11.0	7.9	7.6	11.0	7.9	8.8 ± 1.9
–520	–520	–520	VL^{2-}	[110,113,114,263,264,268]	7.7	8.6	7.8	7.7	8.6	7.8	8.0 ± 0.5
–523	–523	–523	$V_2EG_2^{2-}$	[277]	5.2	6.0	4.8	5.2	6.0	4.8	5.3 ± 0.6

–531	–531	–531	$V_2L_2^{2-}$	110,113,114,263,264,268	57.1	54.4	57.7	57.1	54.4	57.7	56.4 ± 1.8
–538	–538	–538	$V_3L_2^{3-}$ (or V_2L^{2-})	110,113,114,263,264,268	8.2	7.1	8.1	12.0	10.0	12.0	11.3 ± 1.2
–546	–545	–545	$V_3L_2^{3-}$ (or V_2L^{2-})	110,113,114,263,264,268	3.8	2.9	3.9				
5 mM $Cs_2[V^V_2O_4(lact)_2]\cdot 2H_2O$ + 13 mg/mL HEWL in 0.1 M NaOAc pH 4.0, 20% ethylene glycol, 0.6 M $NaNO_3$, 10% D_2O (after 7 d at RT)											
^{51}V chemical shift (ppm)			**Species**	**References**	**Integration (%)**			**Sum**			**Aver-age ± SD (%)**
Sample 1	**Sample 2**	**Sample 3**			**Sample 1**	**Sample 2**	**Sample 3**	**Sample 1**	**Sample 2**	**Sample 3**	
–520	–520	–520	VL^{2-}	110,113,114,263,264,268	13.6	10.7	11.0	13.6	10.7	11.0	11.8 ± 1.6
–523	–523	–523	$V_2EG_2^{2-}$	277	3.5	4.9	3.1	3.5	4.9	3.1	3.8 ± 0.9
–531	–531	–531	$V_2L_2^{2-}$	110,113,114,263,264,268	69.8	70.2	69.7	69.8	70.2	69.7	69.9 ± 0.3
–538	–538	–538	$V_3L_2^{3-}$ (or V_2L^{2-})	110,113,114,263,264,268	9.3	10.4	11.4	13.1	14.2	16.1	14.5 ± 1.5
–545	–545	–546	$V_3L_2^{3-}$ (or V_2L^{2-})	110,113,114,263,264,268	3.8	3.8	4.7				

[a] L indicates $lact^{2-}$ ligand, VL^- indicates $[V^VO_2(lact)(H_2O)]^-$, VL^{2-} $[V^VO_2(lact)(OH)]^{2-}$, $V_2L_2^{2-}$ $[V^V_2O_4(lact)_2]^{2-}$, $V_2EG_2^{2-}$ $[V^V_2O_4(EG)_2]^{2-}$, V_2L^{2-} $[V^V_2O_5(lact)]^{2-}$ and $V_3L_2^{3-}$ $[V^V_3O_7(lact)_2]^{3-}$.

Table 5.7 – Chemical shifts in ^{51}V NMR spectra measured in triplicate at RT after 1 h and 7 d of incubation of $Cs_2[V^V_2O_4(lact)_2]\cdot 2H_2O$ (5 mM) dissolved in (i) D_2O; (ii) 0.8 M succinic acid pH 7.0 and 10% D_2O; and (iii) 0.8 M succinic acid pH 7.0 and 10% D_2O in presence of HEWL (13 mg/mL). The relative content of species was calculated based on the integration of ^{51}V signals. Signals were assigned based on literature data. [a]

5 mM $Cs_2[V^V_2O_4(lact)_2]\cdot 2H_2O$ in D_2O (after 1 h at RT)											
^{51}V chemical shift (ppm)			**Species**	**References**	**Integration (%)**			**Sum**			**Aver-age ± SD (%)**
Sample 1	**Sample 2**	**Sample 3**			**Sample 1**	**Sample 2**	**Sample 3**	**Sam-ple 1**	**Sample 2**	**Sample 3**	
–425	–424	–424	V_{10}	110,263	0.7	1.3	1.3	13.1	10.8	11.8	11.9 ± 1.2
–501	–501	–501	V_{10} (or VL^{-})	110,113,114,263,264,268	5.1	4.2	4.6				
–517	–517	–517	V_{10} (or VL^{2-})	110,113,114,263,264,268	7.3	5.3	5.9				
–532	–532	–532	$V_2L_2^{2-}$	110,113,114,263,264,268	65.2	65.2	67.1	65.2	65.2	67.1	65.8 ± 1.1
–539	–539	–539	$V_3L_2^{3-}$ (or V_2L^{2-})	110,113,114,263,264,268	11.7	12.9	11.6	19.5	20.5	19.1	19.7 ± 0.7
–546	–546	–546	$V_3L_2^{3-}$ (or V_2L^{2-})	110,113,114,263,264,268	7.8	7.6	7.5				
–550	–550	–550	$[V^VO_2]^+$	278	1.5	3.1	1.6	1.5	3.1	1.6	2.1 ± 0.9
–558	–558	–558	$[H_2V^VO_4]^-$	110,114,278,279,279	0.7	0.4	0.4	0.7	0.4	0.4	0.5 ± 0.2
5 mM $Cs_2[V^V_2O_4(lact)_2]\cdot 2H_2O$ in 0.8 M succinic acid pH 7.0, 10% D_2O (after 1 h at RT)											
^{51}V chemical shift (ppm)			**Species**	**References**	**Integration (%)**			**Sum**			**Aver-age ± SD (%)**
Sample 1	**Sample 2**	**Sample 3**			**Sample 1**	**Sample 2**	**Sample 3**	**Sam-ple 1**	**Sample 2**	**Sample 3**	

–531	–532	–532	$V_2L_2^{2-}$	[110,113,114,263,264,268]	1.0	1.0	0.8	1.0	1.0	0.8	0.9 ± 0.1
–539	–540	–540	$V_3L_2^{3-}$ (or V_2L^{2-})	[110,113,114,263,264,268]	1.5	1.7	1.6	3.2	3.5	3.2	3.3 ± 0.2
–549	–549	–549	$V_3L_2^{3-}$ (or V_2L^{2-})	[110,113,114,263,264,268]	1.7	1.8	1.6				
–557	–555	–557	$[H_2V^{V}O_4]^-$	[118,268]	5.6	6.2	6.5	5.6	6.2	6.5	6.1 ± 0.5
–570	–570	–570	$[H_2V^{V}_2O_7]^{2-}$	[118,268]	3.0	2.1	2.9	3.0	2.1	2.9	2.7 ± 0.5
–574	–574	–574	$[V^{V}_4O_{12}]^{4-}$	[118,268]	71.5	69.8	70.6	71.5	69.8	70.6	70.6 ± 0.9
–583	–582	–582	$[V^{V}_5O_{15}]^{5-}$	[118,268]	15.7	17.6	16.0	15.7	17.6	16.0	16.4 ± 1.0
5 mM $Cs_2[V^{V}_2O_4(lact)_2]\cdot 2H_2O$ + 13 mg/mL HEWL in 0.8 M succinic acid pH 7.0, 10% D_2O (after 1 h at RT)											
^{51}V chemical shift (ppm)			**Species**	**References**	**Integration (%)**			**Sum**			**Aver-age ± SD (%)**
Sample 1	**Sample 2**	**Sample 3**			**Sample 1**	**Sample 2**	**Sample 3**	**Sam-ple 1**	**Sample 2**	**Sample 3**	
–532	–531	–530	$V_2L_2^{2-}$	[110,113,114,263,264,268]	1.0	1.3	1.7	1.0	1.3	1.7	1.3 ± 0.4
–540	–539	–539	$V_3L_2^{3-}$ (or V_2L^{2-})	[110,113,114,263,264,268]	1.8	1.6	1.4	3.7	3.5	3.3	3.5 ± 0.2
–549	–548	–548	$V_3L_2^{3-}$ (or V_2L^{2-})	[110,113,114,263,264,268]	1.9	1.9	1.9				
–557	–556	–556	$[H_2V^{V}O_4]^-$	[118,268]	5.8	4.7	5.3	5.8	4.7	5.3	5.3 ± 0.6
–570	–570	–570	$[H_2V^{V}_2O_7]^{2-}$	[118,268]	3.4	4.3	5.9	3.4	4.3	5.9	4.5 ± 1.3
–574	–574	–574	$[V^{V}_4O_{12}]^{4-}$	[118,268]	69.4	71.1	68.7	69.4	71.1	68.7	69.7 ± 1.2
–582	–582	–582	$[V^{V}_5O_{15}]^{5-}$	[118,268]	16.8	15.3	15.1	16.8	15.3	15.1	15.7 ± 0.9

5 mM $Cs_2[V^V_2O_4(lact)_2]\cdot 2H_2O$ in D_2O (after 7 d at RT)											
^{51}V chemical shift (ppm)			Species	References	Integration (%)			Sum			Average ± SD (%)
Sample 1	Sample 2	Sample 3			Sample 1	Sample 2	Sample 3	Sample 1	Sample 2	Sample 3	
–424	–425	–424	V_{10}	110,263	4.2	2.9	3.3	38.4	34.7	34.6	35.9 ± 2.2
–502	–501	–502	V_{10} (or VL^{-})	110,113,114,263,264,268	15.4	13.5	13.8				
–518	–517	–518	V_{10} (or VL^{2-})	110,113,114,263,264,268	18.8	18.3	17.5				
–532	–532	–532	$V_2L_2^{2-}$	110,113,114,263,264,268	47.7	48.8	48.1	47.7	48.8	48.1	48.2 ± 0.6
–539	–539	–539	$V_3L_2^{3-}$ (or V_2L^{2-})	110,113,114,263,264,268	8.4	9.8	10.5	13.2	14.9	16.2	14.8 ±1.5
–546	–546	–546	$V_3L_2^{3-}$ (or V_2L^{2-})	110,113,114,263,264,268	4.8	5.1	5.7				
–550	–550	–550	$[V^VO_2]^+$	278	0.8	1.6	1.1	0.8	1.6	1.1	1.2 ± 0.4
5 mM $Cs_2[V^V_2O_4(lact)_2]\cdot 2H_2O$ in 0.8 M succinic acid pH 7.0, 10% D_2O (after 7 d at RT)											
^{51}V chemical shift (ppm)			Species	References	Integration (%)			Sum			Average ± SD (%)
Sample 1	Sample 2	Sample 3			Sample 1	Sample 2	Sample 3	Sample 1	Sample 2	Sample 3	
–531	–531	–532	$V_2L_2^{2-}$	110,113,114,263,264,268	1.0	1.0	0.8	1.0	1.0	0.8	0.9 ± 0.1
–539	–539	–540	$V_3L_2^{3-}$ (or V_2L^{2-})	110,113,114,263,264,268	1.8	2.0	1.8	3.7	3.9	3.5	3.7 ± 0.2
–548	–549	–549	$V_3L_2^{3-}$ (or V_2L^{2-})	110,113,114,263,264,268	1.9	1.9	1.7				
–557	–557	–557	$[H_2V^VO_4]^-$	118,268	5.3	4.8	5.1	5.3	4.8	5.1	5.1 ± 0.3

–570	–570	–570	$[H_2V^V_2O_7]^{2-}$	118,268	4.1	2.4	3.0	4.1	2.4	3.0	3.2 ± 0.9
–574	–574	–574	$[V^V_4O_{12}]^{4-}$	118,268	71.2	71.9	72.3	71.2	71.9	72.3	71.8 ± 0.6
–582	–582	–582	$[V^V_5O_{15}]^{5-}$	118,268	14.8	16.1	15.2	14.8	16.1	15.2	15.4 ± 0.7
5 mM $Cs_2[V^V_2O_4(lact)_2]\cdot 2H_2O$ + 13 mg/mL HEWL in 0.8 M succinic acid pH 7.0, 10% D_2O (after 7 d at RT)											
^{51}V chemical shift (ppm)			**Species**	**References**	**Integration (%)**			**Sum**			**Aver-age ± SD (%)**
Sample 1	**Sample 2**	**Sample 3**			**Sample 1**	**Sample 2**	**Sample 3**	**Sam-ple 1**	**Sample 2**	**Sample 3**	
–532	–532	–531	$V_2L_2^{2-}$	110,113,114,263,264,268	1.3	1.3	1.2	1.3	1.3	1.2	1.3 ± 0.1
–540	–540	–539	$V_3L_2^{3-}$ (or V_2L^{2-})	110,113,114,263,264,268	3.2	2.5	2.6	6.5	5.3	5.5	5.8 ± 0.6
–549	–548	–549	$V_3L_2^{3-}$ (or V_2L^{2-})	110,113,114,263,264,268	3.3	2.8	2.9				
–557	–557	–557	$[H_2V^VO_4]^-$	118,268	5.7	4.7	5.8	5.7	4.7	5.8	5.4 ± 0.6
–570	–570	–570	$[H_2V^V_2O_7]^{2-}$	118,268	2.6	2.3	2.8	2.6	2.3	2.8	2.6 ± 0.3
–574	–574	–574	$[V^V_4O_{12}]^{4-}$	118,268	67.1	70.8	68.7	67.1	70.8	68.7	68.9 ± 1.9
–582	–5812	–582	$[V^V_5O_{15}]^{5-}$	118,268	16.8	15.6	16.1	16.8	15.6	16.1	16.2 ± 0.6

[a] L indicates $lact^{2-}$ ligand, VL^- indicates $[V^VO_2(lact)(H_2O)]^-$, VL^{2-} $[V^VO_2(lact)(OH)]^{2-}$, $V_2L_2^{2-}$ $[V^V_2O_4(lact)_2]^{2-}$, V_2L^{2-} $[V^V_2O_5(lact)]^{2-}$ and $V_3L_2^{3-}$ $[V^V_3O_7(lact)_2]^{3-}$.

Table 5.8 – Chemical shifts in ^{51}V NMR spectra measured in triplicate at RT after 1 h and 7 d of incubation of $Cs_2[V^V_2O_4(lact)_2]\cdot 2H_2O$ (5 mM) dissolved in (i) D_2O; (ii) 0.1 M HEPES pH 7.5, 2.0 M sodium formate and 10% D_2O; and (iii) 0.1 M HEPES pH 7.5, 2.0 M sodium formate and 10% D_2O in presence of HEWL (13 mg/mL). The relative content of species was calculated based on the integration of ^{51}V signals. Signals were assigned based on literature data. [a]

5 mM $Cs_2[V^V_2O_4(lact)_2]\cdot 2H_2O$ in D_2O (after 1 h at RT)											
^{51}V chemical shift (ppm)			**Species**	**References**	**Integration (%)**			**Sum**			**Aver-age ± SD (%)**
Sample 1	**Sample 2**	**Sample 3**			**Sample 1**	**Sample 2**	**Sample 3**	**Sam-ple 1**	**Sample 2**	**Sample 3**	
–425	–424	–424	V_{10}	110,263	0.7	1.3	1.3	13.1	10.8	11.8	11.9 ± 1.2
–501	–501	–501	V_{10} (or VL^{-})	110,113,114,263,264,268	5.1	4.2	4.6				
–517	–517	–517	V_{10} (or VL^{2-})	110,113,114,263,264,268	7.3	5.3	5.9				
–532	–532	–532	$V_2L_2^{2-}$	110,113,114,263,264,268	65.2	65.2	67.1	65.2	65.2	67.1	65.8 ± 1.1
–539	–539	–539	$V_3L_2^{3-}$ (or V_2L^{2-})	110,113,114,263,264,268	11.7	12.9	11.6	19.5	20.5	19.1	19.7 ± 0.7
–546	–546	–546	$V_3L_2^{3-}$ (or V_2L^{2-})	110,113,114,263,264,268	7.8	7.6	7.5				
–550	–550	–550	$[V^VO_2]^+$	278	1.5	3.1	1.6	1.5	3.1	1.6	2.1 ± 0.9
–558	–558	–558	$[H_2V^VO_4]^-$	110,114,278,279,279	0.7	0.4	0.4	0.7	0.4	0.4	0.5 ± 0.2
5 mM $Cs_2[V^V_2O_4(lact)_2]\cdot 2H_2O$ in 0.1 M HEPES pH 7.5, 2.0 M sodium formate, 10% D_2O (after 1 h at RT)											
^{51}V chemical shift (ppm)			**Species**	**References**	**Integration (%)**			**Sum**			**Aver-age ± SD (%)**
Sample 1	**Sample 2**	**Sample 3**			**Sample 1**	**Sample 2**	**Sample 3**	**Sam-ple 1**	**Sample 2**	**Sample 3**	

–539	–539	–539	$V_3L_2^{3-}$ (or V_2L^{2-})	110,113,114,263,264,268	0.6	0.7	1.0	1.4	2.1	2.5	2.0 ± 0.6
–549	–549	–549	$V_3L_2^{3-}$ (or V_2L^{2-})	110,113,114,263,264,268	0.8	1.4	1.5				
–555	–555	–556	$[H_2V^VO_4]^-$	118,268	4.9	5.5	3.7	4.9	5.5	3.7	4.7 ± 0.9
–570	–570	–570	$[H_2V^V_2O_7]^{2-}$	118,268	3.8	4.6	5.4	3.8	4.6	5.4	4.6 ± 0.8
–574	–574	–574	$[V^V_4O_{12}]^{4-}$	118,268	73.9	72.1	71.3	73.9	72.1	71.3	72.4 ± 1.3
–582	–582	–582	$[V^V_5O_{15}]^{5-}$	118,268	16.0	15.8	14.0	16.0	15.8	14.0	15.3 ± 1.1
5 mM $Cs_2[V^V_2O_4(lact)_2]\cdot 2H_2O$ + 13 mg/mL HEWL in 0.1 M HEPES pH 7.5, 2.0 M sodium formate, 10% D_2O (after 1 h at RT)											
^{51}V chemical shift (ppm)			**Species**	**References**	**Integration (%)**			**Sum**			**Aver-age ± SD (%)**
Sample 1	**Sample 2**	**Sample 3**			**Sample 1**	**Sample 2**	**Sample 3**	**Sam-ple 1**	**Sample 2**	**Sample 3**	
–539	–539	–539	$V_3L_2^{3-}$ (or V_2L^{2-})	110,113,114,263,264,268	0.6	0.7	0.7	1.7	1.9	1.8	1.8 ± 0.1
–549	–549	–549	$V_3L_2^{3-}$ (or V_2L^{2-})	110,113,114,263,264,268	1.1	1.2	1.2				
–556	–556	–556	$[H_2V^VO_4]^-$	118,268	5.3	5.4	5.0	5.3	5.4	5.0	5.2 ± 0.2
–570	–570	–570	$[H_2V^V_2O_7]^{2-}$	118,268	4.0	5.4	4.0	4.0	5.4	4.0	4.5 ± 0.8
–574	–574	–574	$[V^V_4O_{12}]^{4-}$	118,268	74.0	71.3	73.7	74.0	71.3	73.7	73.0 ± 1.5
–582	–582	–582	$[V^V_5O_{15}]^{5-}$	118,268	15.0	16.1	15.5	15.0	16.1	15.5	15.5 ± 0.6
5 mM $Cs_2[V^V_2O_4(lact)_2]\cdot 2H_2O$ in D_2O (after 7 d at RT)											
^{51}V chemical shift (ppm)			**Species**	**References**	**Integration (%)**			**Sum**			

Sample 1	Sample 2	Sample 3			Sample 1	Sample 2	Sample 3	Sam-ple 1	Sample 2	Sample 3	Aver-age ± SD (%)
–424	–425	–424	V_{10}	[110,263]	4.2	2.9	3.3	38.4	34.7	34.6	35.9 ± 2.2
–502	–501	–502	V_{10} (or VL^{-})	[110,113,114,263,264,268]	15.4	13.5	13.8				
–518	–517	–518	V_{10} (or VL^{2-})	[110,113,114,263,264,268]	18.8	18.3	17.5				
–532	–532	–532	$V_2L_2^{2-}$	[110,113,114,263,264,268]	47.7	48.8	48.1	47.7	48.8	48.1	48.2 ± 0.6
–539	–539	–539	$V_3L_2^{3-}$ (or V_2L^{2-})	[110,113,114,263,264,268]	8.4	9.8	10.5	13.2	14.9	16.2	14.8 ±1.5
–546	–546	–546	$V_3L_2^{3-}$ (or V_2L^{2-})	[110,113,114,263,264,268]	4.8	5.1	5.7				
–550	–550	–550	$[V^{V}O_2]^{+}$	[278]	0.8	1.6	1.1	0.8	1.6	1.1	1.2 ± 0.4
5 mM $Cs_2[V^{V}_2O_4(lact)_2]\cdot 2H_2O$ in 0.1 M HEPES pH 7.5, 2.0 M sodium formate, 10% D_2O (after 7 d at RT)											
^{51}V chemical shift (ppm)			**Species**	**References**	**Integration (%)**			**Sum**			**Aver-age ± SD (%)**
Sample 1	**Sample 2**	**Sample 3**			**Sample 1**	**Sample 2**	**Sample 3**	**Sam-ple 1**	**Sample 2**	**Sample 3**	
–531	–531	–531	$V_2L_2^{2-}$	[110,113,114,263,264,268]	0.1	0.4	0.7	0.1	0.4	0.7	0.4 ± 0.3
–540	–539	–539	$V_3L_2^{3-}$ (or V_2L^{2-})	[110,113,114,263,264,268]	1.0	1.3	1.5	2.3	2.8	3.3	2.8 ± 0.5
–550	–549	–549	$V_3L_2^{3-}$ (or V_2L^{2-})	[110,113,114,263,264,268]	1.3	1.5	1.8				
–555	–555	–556	$[H_2V^{V}O_4]^{-}$	[118,268]	5.3	4.9	3.6	5.3	4.9	3.6	4.6 ± 0.9
–570	–570	–570	$[H_2V^{V}_2O_7]^{2-}$	[118,268]	5.2	5.2	4.5	5.2	5.2	4.5	5.0 ± 0.4

–574	–574	–574	$[V^{V}_{4}O_{12}]^{4-}$	[118,268]	70.3	70.7	70.0	70.3	70.7	70.0	70.3 ± 0.4
–582	–582	–582	$[V^{V}_{5}O_{15}]^{5-}$	[118,268]	16.9	16.0	17.9	16.9	16.0	17.9	16.9 ± 1.0
5 mM $Cs_2[V^{V}_{2}O_4(lact)_2]\cdot 2H_2O$ + 13 mg/mL HEWL in 0.1 M HEPES pH 7.5, 2.0 M sodium formate, 10% D_2O (after 7 d at RT)											
^{51}V chemical shift (ppm)			**Species**	**References**	**Integration (%)**			**Sum**			**Aver-age ± SD (%)**
Sample 1	**Sample 2**	**Sample 3**			**Sample 1**	**Sample 2**	**Sample 3**	**Sam-ple 1**	**Sample 2**	**Sample 3**	
–531	–531	–531	$V_2L_2^{2-}$	[110,113,114,263,264,268]	0.5	0.6	0.4	0.5	0.6	0.4	0.5 ± 0.1
–539	–539	–539	$V_3L_2^{3-}$ (or V_2L^{2-})	[110,113,114,263,264,268]	1.3	1.9	1.4	3.2	4.5	3.1	3.6 ± 0.8
–549	–549	–549	$V_3L_2^{3-}$ (or V_2L^{2-})	[110,113,114,263,264,268]	1.9	2.6	1.7				
–556	–556	–556	$[H_2V^{V}O_4]^{-}$	[118,268]	5.3	6.4	4.7	5.3	6.4	4.7	5.5 ± 0.9
–570	–570	–570	$[H_2V^{V}_{2}O_7]^{2-}$	[118,268]	5.1	6.4	4.2	5.1	6.4	4.2	5.2 ± 1.1
–574	–574	–574	$[V^{V}_{4}O_{12}]^{4-}$	[118,268]	69.9	68.1	70.5	69.9	68.1	70.5	69.5 ± 1.2
–582	–582	–582	$[V^{V}_{5}O_{15}]^{5-}$	[118,268]	16.1	14.1	17.1	16.1	14.1	17.1	15.8 ± 1.5

[a] L indicates $lact^{2-}$ ligand, VL^{-} indicates $[V^{V}O_2(lact)(H_2O)]^{-}$, VL^{2-} $[V^{V}O_2(lact)(OH)]^{2-}$, $V_2L_2^{2-}$ $[V^{V}_{2}O_4(lact)_2]^{2-}$, V_2L^{2-} $[V^{V}_{2}O_5(lact)]^{2-}$ and $V_3L_2^{3-}$ $[V^{V}_{3}O_7(lact)_2]^{3-}$.

5.3.2 Mass spectrometry studies

ESI mass spectrum of $Cs_2[V^V_2O_4(lact)_2]\cdot 2H_2O$ in water in negative mode shows a series of singly charged and doubly charged species. The singly charged series includes protonated and unprotonated vanadates $[V^VO_3]^-$, $[H_2V^VO_4]^-$, $[HV^V_2O_6]^-$, $[V^V_3O_8]^-$ and $[HV^V_4O_{11}]^-$, the monoanionic lactate ligand $[C_3H_5O_3]^-$ (*i.e.*, $[lact^{2-} + H^+]^-$) and various vanadium ions with one or two metal centres: $[V^VO_2(lact)]^-$, $[V^VO(lact)_2]^-$, $[V^V_2O_4(lact) - H^+]^-$, $[V^V_2O_4(lact)(OH)]^-$, $[V^V_2O_5(lact)(H_2O)^{2-} + Na^+]^-$, $[V^V_2O_4(lact)_2^{2-} + H^+]^-$ and $[V^V_2O_4(lact)_2^{2-} + Cs^+]^-$. The only doubly charged species identified are $[V^V_{10}O_{26}]^{2-}$ and $[H_4V^V_{10}O_{28}]^{2-}$ (Figure 5.21a, Table 5.9). The negative-ion mode spectrum of $Cs_2[V^V_2O_4(lact)_2]\cdot 2H_2O$ in acetonitrile/methanol + 1% H_2O is shown in Figure 5.21b. In this spectrum, most of the species revealed in water were observed (Table 5.9) except for $[V^V_2O_4(lact) - H^+]^-$, $[V^V_3O_8]^-$, $[V^V_2O_4(lact)_2^{2-} + Cs^+]^-$ and decavanadates.

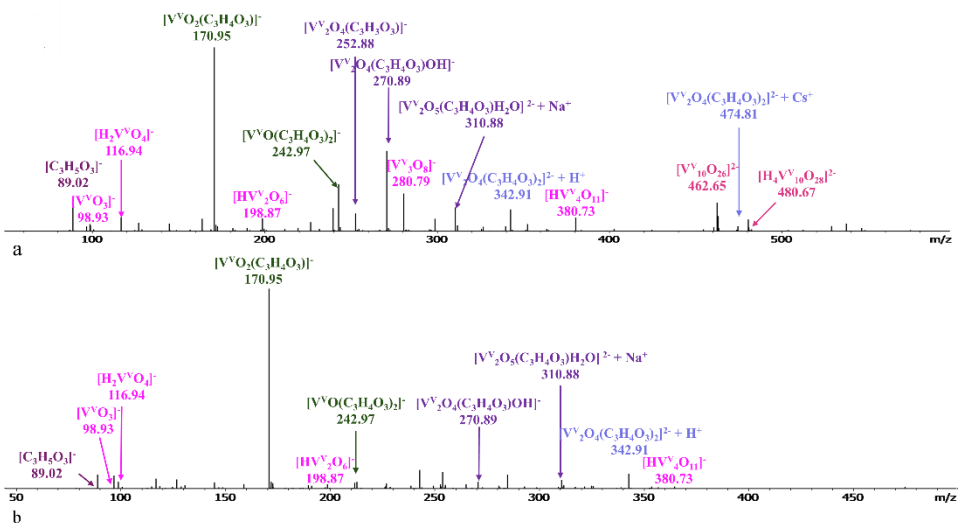

Figure 5.21 – ESI mass spectrum of $Cs_2[V^V_2O_4(lact)_2]\cdot 2H_2O$ (~ 100 µM) in a) H_2O and in b) acetonitrile/methanol + 1% H_2O. The spectra were recorded in negative ion mode within

the m/z range of 50 to 600, and the spectrometer was calibrated using the standard tunemix (Bruker Daltonik GmbH, timsTOF Pro User Manual, Bremen, Germany) to ensure an accuracy of approximately 5 ppm in the m/z region of 45-1800. These studies were carried out under the supervision of Prof. Annette Rompel from University of Vienna.

Table 5.9 – Experimental and calculated m/z values for $Cs_2[V^V_2O_4(lact)_2]\cdot 2H_2O$ dissolved in H_2O and in ACN/MeOH + 1% H_2O, recorded in negative ion mode using ESI-MS.

In H_2O		
Observed species	**Experimental m/z**	**Simulated m/z**
$[lact^{2-} + H^+]^-$	89.02	89.02
$[V^VO_3]^-$	98.93	98.93
$[H_2V^VO_4]^-$	116.94	116.94
$[V^VO_2(lact)]^-$	170.95 171.95	170.95 171.95
$[HV^V_2O_6]^-$	198.87	198.87
$[V^VO(lact)_2]^-$	242.97 243.97	242.97 243.97
$[V^V_2O_4(lact) - H^+]^-$	252.88 253.88	252.88 253.88
$[V^V_2O_4(lact)(OH)]^-$	270.89 271.89	270.89 271.89
$[V^V_3O_8]^-$	280.79	280.79
$[V^V_2O_5(lact)(H_2O)^{2-} + Na^+]^-$	310.88 311.89 312.89	310.88 311.88 312.88
$[V^V_2O_4(lact)_2{}^{2-} + H^+]^-$	342.91 343.81 344.91	342.91 343.81 344.91
$[HV^V_4O_{11}]^-$	380.73	380.73
$[V^V_{10}O_{26}]^{2-}$	462.16 462.65 463.16 463.66 464.16 464.65	462.16 462.65 463.16 463.66 464.16 464.65
$[V^V_2O_4(lact)_2{}^{2-} + Cs^+]^-$	474.81 475.81	474.81 475.81
$[H_4V^V_{10}O_{28}]^{2-}$	480.17 480.67 481.17 481.67	480.17 480.67 481.17 481.67

In ACN/MeOH + 1% H_2O		
Observed species	**Experimental m/z**	**Simulated m/z**
$[C_3H_5O_3]^-$	89.02	89.02
$[V^VO_3]^-$	98.93	98.93
$[H_2V^VO_4]^-$	116.94	116.94
$[V^VO_2(lact)]^-$	170.95 171.95	170.95 171.95
$[HV^V_2O_6]^-$	198.87	198.87
$[V^VO(lact)_2]^-$	242.97 243.97	242.97 243.97
$[V^V_2O_4(lact)(OH)]^-$	270.89 271.89	270.89 271.89
$[V^V_2O_5(lact)(H_2O)^{2-} + Na^+]^-$	310.88 311.89	310.88 311.88
$[V^V_2O_4(lact)_2^{2-} + H^+]^-$	342.91 343.81 344.91	342.91 343.81 344.91
$[HV^V_4O_{11}]^-$	380.73	380.73

The positive-ion mode ESI-MS spectrum of $Cs_2[V^V_2O_4(lact)_2]\cdot 2H_2O$ in the presence of HEWL (VC:HEWL molar ratio = 1:1) in H_2O shows two intense peaks at 14304.9 Da (metal-free protein) and at 14648.7 Da, attributed to the $[V^V_2O_4(lact)_2^{2-} + 2H^+]$–HEWL adduct (Figure 5.22b). The same spectrum upon dilution 1:100 in acetonitrile/H_2O (9/1) + 1% FA shows the peaks of metal-free protein and of an adduct of type $[V^VO(lact)_2]^-$–HEWL (Figure 5.22c).

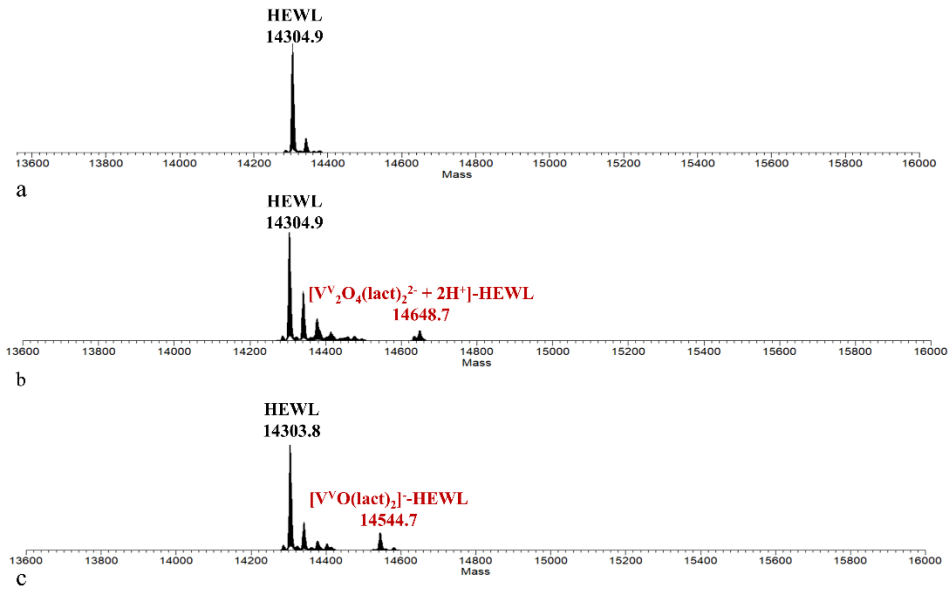

Figure 5.22 – Deconvoluted ESI-MS spectra of a) HEWL (concentration = 13 mg/mL) diluted 1:100 in acetonitrile/H_2O (9/1) + 1% FA, b) of the system containing $Cs_2[V^V_2O_4(lact)_2]\cdot 2H_2O$:HEWL in 1:1 molar ratio in H_2O and c) of the system containing $Cs_2[V^V_2O_4(lact)_2]\cdot 2H_2O$:HEWL in 1:1 molar ratio diluted 1:100 in acetonitrile/H_2O (9/1) + 1% FA. Mass is in Da. These studies were carried out under the supervision of Prof. Annette Rompel from University of Vienna.

5.3.3 Crystallographic studies

X-ray diffraction data were then collected at 100 K on crystals of HEWL grown in: i) 1.1 M sodium chloride, 0.1 M sodium acetate pH 4.0; ii) 20% ethylene glycol, 0.6 M sodium nitrate, 0.1 M sodium acetate pH 4.0; iii) 0.8 M succinic acid pH 7.0 and iv) 2.0 M sodium formate, 0.1 M HEPES pH 7.5 and exposed for 7 days to $Cs_2[V^V_2O_4(lact)_2]\cdot 2H_2O$ powder (Table 5.10). These crystals diffracted X-rays in the 1.20-1.49 Å resolution range (Figure 5.23). Data collection and refinement statistics are reported in Table 5.10.

The overall structures of the protein are very similar to each other and to the metal-free protein, with RMSD between Cα atoms in the range of 0.15-0.47 Å.

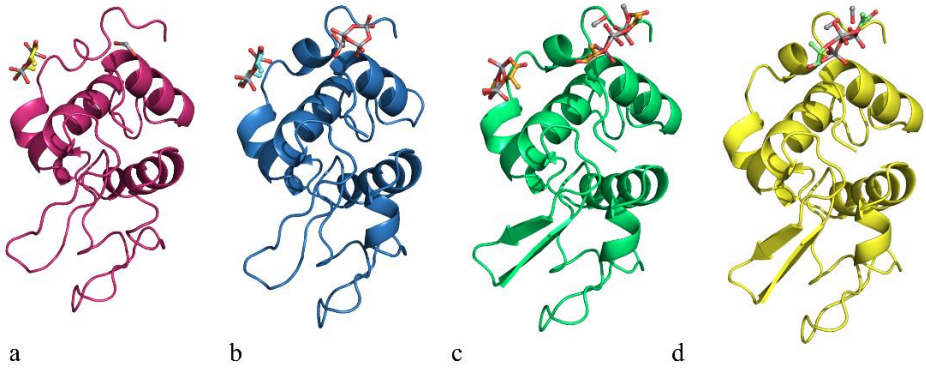

Figure 5.23 – Overall structure of the adduct formed upon reaction of $Cs_2[V^V_2O_4(lact)_2]\cdot 2H_2O$ with HEWL from crystals grown in: a) 1.1 M sodium chloride, 0.1 M sodium acetate pH 4.0 (structure A), b) 20% ethylene glycol, 0.6 M sodium nitrate, 0.1 M sodium acetate pH 4.0 (structure B), c) 0.8 M succinic acid pH 7.0 (structure C), d) 2.0 M sodium formate, 0.1 M HEPES pH 7.5 (structure D). Vanadium atoms are in grey.

Table 5.10 – Data collection and refinement statistics of structures A-D.

Data collection				
	Structure A	Structure B	Structure C	Structure D
Crystallization condition	1.1 M sodium chloride, 0.1 M sodium acetate pH 4.0	20% ethylene glycol, 0.6 M sodium nitrate, 0.1 M sodium acetate pH 4.0	0.8 M succinic acid pH 7.0	2.0 M sodium formate, 0.1 M HEPES pH 7.5
Soaking time	7 d	7 d	7 d	7 d
Space group	$P4_32_12$	$P4_32_12$	$P4_32_12$	$P4_32_12$
a (Å)	77.85	77.10	76.34	76.41
b (Å)	77.85	77.10	76.34	76.41
c (Å)	37.09	37.41	37.01	36.98
Resolution range (Å)	55.05-1.20 (1.22-1.20)	38.55-1.34 (1.37-1.34)	54.00-1.49 (1.51-1.49)	54.03-1.23 (1.25-1.23)
Observations	841373 (36231)	303896 (7644)	194724 (9282)	273116 (3394)
Unique reflections	36597 (1770)	25659 (1243)	18528 (893)	30853 (1100)
Completeness (%)	100.0 (100.0)	100.0 (100.0)	99.9 (100.0)	95.3 (69.6)
Redundancy	23.0 (20.5)	11.8 (6.1)	10.5 (10.4)	8.9 (3.1)
Rmerge (%)	0.073 (1.800)	0.116 (2.114)	0.148 (4.604)	0.084 (1.096)
Average I/σ(I)	19.7 (2.1)	7.8 (0.5)	7.7 (0.6)	12.6 (1.3)
$CC_{1/2}$	0.999 (0.856)	0.998 (0.378)	0.996 (0.398)	0.998 (0.331)
Anom. completeness (%)	100.0 (100.0)	100.0 (99.2)	100.0 (100.0)	91.0 (44.9)
Anom. Multiplicity	12.2 (10.6)	6.3 (3.2)	5.7 (5.5)	4.9 (2.0)
Refinement				
Resolution (Å)	55.05-1.20	55.31-1.36	54.01-1.52	54.03-1.23
N° reflections	34372	22388	15203	28383
N° reflections in working set	2504	418	277	1030
R-factor/Rfree	0.174/0.201	0.174/0.217	0.175/0.227	0.180/0.218
N° non-H atoms in the refinement	1256	1272	1177	1231
B-factor overall ($Å^2$)	21.04	20.79	22.69	17.48
Estimated occupancy of $[V^VO_2]^+$	0.70	0.50	-	-

Estimated occupancy of $[V^{V}_{2}O_{4}(lact)_{2}]^{2-}$	0.80	0.80	0.80	-
Estimated occupancy of $[V^{V}_{3}O_{9}]^{3-}$	-	0.50	-	-
Estimated occupancy of $[V^{IV}O]^{2+}$	-	-	0.40	0.40
Estimated occupancy of $[V^{IV}O]^{2+}$	-	-	0.40	0.40
Estimated occupancy of $[V^{V}_{3}O_{7}(lact)_{2}]^{3-}$	-	-	0.60	0.60
B-factor of $[V^{V}O_{2}]^{+}$ (Å^{2})	40.69	37.66	-	-
B-factor of $[V^{V}_{2}O_{4}(lact)_{2}]^{2-}$ (Å^{2})	23.17±3.40	28.74±4.04	36.48±3.20	-
B-factor of $[V^{V}_{3}O_{9}]^{3-}$ (Å^{2})	-	38.55±5.14	-	-
B-factor of $[V^{IV}O]^{2+}$ (Å^{2})	-	-	22.78	24.69
B-factor of $[V^{IV}O]^{2+}$ (Å^{2})	-	-	32.33	29.09
B-factor of $[V^{V}_{3}O_{7}(lact)_{2}]^{3-}$ (Å^{2})	-	-	34.47±2.43	28.60±3.85
Ramachandran values (%)				
Most favoured/Addi-tional allowed	93.75/6.25	94.64/5.36	95.97/4.03	95.16/4.84
Outliers	0	0	1	0
RMSD from ideality				
RMSD bonds (Å)	0.014	0.012	0.010	0.012
RMSD angles (°)	1.908	1.920	4.157	4.162

Structure A corresponds to the adduct of HEWL with $Cs_2[V^V_2O_4(lact)_2]\cdot 2H_2O$ crystallized in 1.1 M sodium chloride, 0.1 M sodium acetate at pH 4.0 (Figure 5.23a). The model refines at 1.20 Å. In this structure, two V-containing fragments non-covalently interact with the protein: a VO_2 group (occupancy = 0.70) and a $[V^V_2O_4(lact)_2]^{2-}$ ion (occupancy = 0.80). The VO_2 group, assigned to $[V^VO_2]^+$, is stabilized through hydrogen bonds with the N atoms of Cys6 and Glu7 and with water molecules (Figure 5.24a). $[V^V_2O_4(lact)_2]^{2-}$ interacts with the NZ atom of Lys33, water molecules and with the main chain O atom of Gly117, the O atom of Thr118, the N atom and the OE1 atom of Gln121 from a symmetry-related molecule (Figure 5.24b).

The crystallographic results obtained under this condition in part agree with the speciation trends revealed by ^{51}V NMR under the same experimental condition, which showed the presence of $[V^V_2O_4(lact)_2]^{2-}$, $[V^VO_2]^+$ and of the trimetallic species $[V^V_3O_7(lact)_2]^{3-}$ (Figure 5.17). Geometrical details of the structure $[V^V_2O_4(lact)_2]^{2-}$ are compared with those reported for the Cambridge Crystallographic Data Centre (CCDC code: QAVCOF)[117] in Table 5.11.

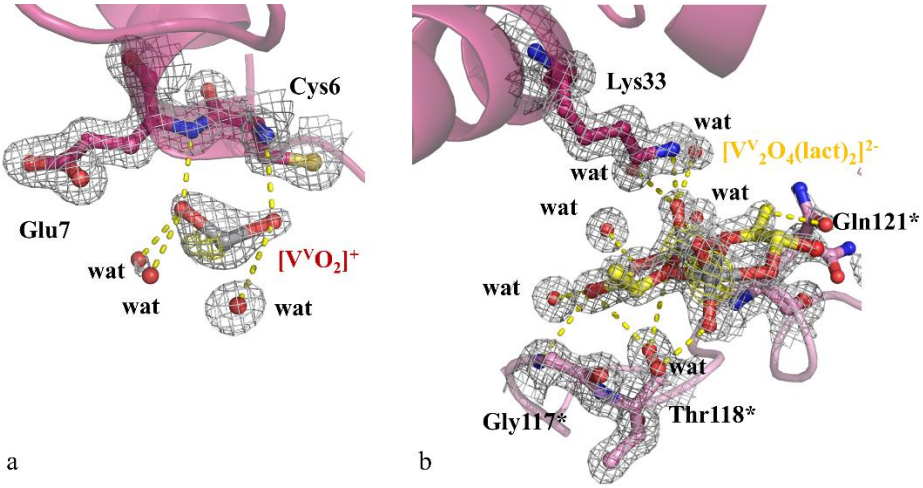

Figure 5.24 – Vanadium binding sites in the structure A non-covalent interaction of: a) $[V^{V}O_2]^{+}$ and b) $[V^{V}_2O_4(lact)_2]^{2-}$ with protein residues. 2Fo-Fc electron density maps are contoured at 1.0 σ level and depicted in grey. Anomalous difference electron density map is reported at 3.0 σ level in yellow.

Table 5.11 – Geometrical details of the structures $Cs_2[V^V_2O_4(lact)_2]\cdot 2H_2O$ compared with those reported for the Cambridge Crystallographic Data Centre (CCDC code: QAVCOF).[117]

	$Cs_2[V^V_2O_4(lact)_2]\cdot 2H_2O$ CCDC code: QAVCOF [117]		**$Cs_2[V^V_2O_4(lact)_2]\cdot 2H_2O$/HEWL Structure A**		**$Cs_2[V^V_2O_4(lact)_2]\cdot 2H_2O$/HEWL Structure B**		**$Cs_2[V^V_2O_4(lact)_2]\cdot 2H_2O$/HEWL Structure C**	
Bond	**Length (Å)**		**Length (Å)**		**Length (Å)**		**Length (Å)**	
V–O(oxo)	1.617 1.599	1.635 1.605	1.69 1.79	1.79 1.71	1.70 1.80	1.79 1.73	1.71 1.81	1.81 1.74
V–O(carb)	1.974	1.979	2.32	2.09	2.34	2.12	2.33	2.14
V–O(alc)	1.998	2.004	2.45	1.98	2.48	1.99	2.48	2.01
V–O'(alc)	1.949	1.965	2.02	1.94	2.03	1.96	2.06	1.94
Angle	**Value (°)**		**Value (°)**		**Value (°)**		**Value (°)**	
O(oxo)–V–O(oxo)	107.9	108.8	129.33	109.34	127.24	106.74	125.46	107.97
O(oxo)–V–O(alc)	121.2 124.5	130.9 126.8	96.65 121.07	133.92 129.54	99.06 123.30	133.60 129.74	117.88 128.39	116.37 123.55
O(oxo)–V–O'(alc)	99.7 99.7	102.2 101.0	92.29 89.39	97.58 94.18	93.26 92.29	97.83 94.69	90.97 87.44	107.52 95.76
O(alc)–V–O'(alc)	71.6	71.2	75.02	88.66	74.13	88.22	75.46	90.12
O(carb)–V–O(alc)	77.1	76.4	75.92	76.14	74.58	74.24	74.58	76.44
O(carb)–V–O'(alc)	148.2	147.6	149.19	164.55	147.57	162.35	148.31	161.20
V–O–V	108.8	108.8	90.28	103.12	90.57	104.41	87.84	99.09

In the structure B, obtained from crystals grown in 20% ethylene glycol, 0.6 M sodium nitrate, and 0.1 M sodium acetate at pH 4.0 (Figure 5.23b), three V-containing species were identified: $[V^{V}_{2}O_{4}(lact)_{2}]^{2-}$ (occupancy = 0.80) (Figure 5.25a), $[V^{V}O_{2}]^{+}$ and $[V^{V}_{3}O_{9}]^{3-}$ (occupancy = 0.50) (Figure 5.25b). These species non-covalently bind the protein.

As in the structure A, $[V^{V}_{2}O_{4}(lact)_{2}]^{2-}$ forms an extended network of hydrogen bonds with the NZ atom of Lys33, water molecules, and the O atom of Thr118, the N atom of Val120 and the N atom of Gln121 from a symmetry-related molecule (Figure 5.25a, Table 5.11). The $[V^{V}O_{2}]^{+}$ ion is not in the same position of the $[V^{V}O_{2}]^{+}$ ion found in the structure A. It forms hydrogen bonds only with solvent molecules (Figure 5.25b) and is alternative to $[V^{V}_{3}O_{9}]^{3-}$, which interacts with the N atoms of Arg5, Cys6, and Glu7, and with several water molecules (Figure 5.25b).

The crystallographic data are in good agreement with the speciation trends revealed by ^{51}V NMR spectra collected under the same experimental conditions, which show the presence of $[V^{V}_{2}O_{4}(lact)_{2}]^{2-}$ and $[V^{V}O_{2}]^{+}$. However, in ^{51}V NMR spectra an additional dimeric species containing ethylene glycol as a ligand and $[V^{V}_{3}O_{7}(lact)_{2}]^{3-}$ were also observed (Figure 5.18).

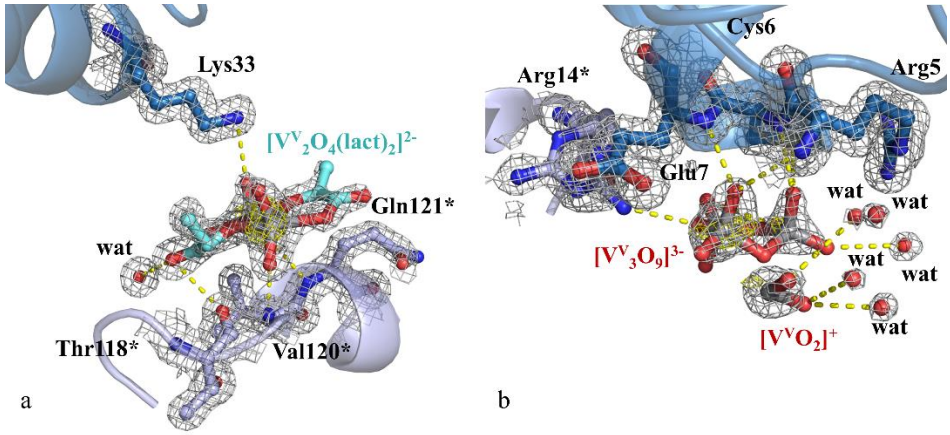

Figure 5.25 – Vanadium binding sites in the structure B non-covalent interaction with protein residues of a) $[V^{V}_2O_4(lact)_2]^{2-}$; b) $[V^{V}_3O_9]^{3-}$ and $[V^{V}O_2]^{+}$. 2Fo-Fc electron density maps are contoured at 1.0 σ level and depicted in grey. Anomalous difference electron density map is reported at 3.0 σ level in yellow.

In the structure C, obtained from crystals grown in 0.8 M succinic acid pH 7.0 (Figure 5.23c), two $[V^{IV}O]^{2+}$ ions (occupancy = 0.40), $[V^{V}_3O_7(lact)_2]^{3-}$ (occupancy = 0.60) (Figure 5.26a), and $[V^{V}_2O_4(lact)_2]^{2-}$ (occupancy = 0.80) (Figure 5.26b) were identified. The species found in the crystal structure are observed also in the ^{51}V NMR spectra (Figure 5.19). However, ^{51}V NMR data also showed the presence of $[H_2V^{V}O_4]^{-}$, $[H_2V^{V}_2O_7]^{2-}$, $[V^{V}_4O_{12}]^{4-}$, $[V^{V}_5O_{15}]^{5-}$ in 0.8 M succinic acid pH 7.0.

The trinuclear oxidovanadium(V) complex $[V^{V}_3O_7(lact)_2]^{3-}$ is observed also in the ^{51}V NMR spectra (Figure 5.19).

The structure of $[V^{V}_3O_7(lact)_2]^{3-}$ has never been reported before. It consists of three V centres, each coordinated by two terminal oxido ligands and three bridging oxygens, two of which belong to the lactate ligands (Figure 5.26a). The $[V^{V}_3O_7(lact)_2]^{3-}$ ion hydrogen bonds the N atoms of Arg5, Cys6, Glu7, the side chain of Arg128, a water molecule, the side chains of Arg14 and Lys97 from a

symmetry-related molecule, as well as the oxygen atom of a neighbouring $[V^{IV}O]^{2+}$ ion (Figure 5.26a). $[V^{IV}O]^{2+}$, in turn, interacts with one water molecule and the O atom of Gly126. Additionally, both $[V^{V}_3O_7(lact)_2]^{3-}$ and the interacting $[V^{IV}O]^{2+}$ ion are alternative to another $[V^{IV}O]^{2+}$ ion, which also interacts with the O atom of Gly126 (Figure 5.26a).

Finally, the $[V^{V}_2O_4(lact)_2]^{2-}$ unit is stabilized through an extended network of hydrogen bonds involving the side chains of Lys33 and Arg114, water molecules, the main chain of Val120 and Gln121 from a symmetry-related molecule and the side chains of Ser24, Asn27, Asp119 from a symmetry-related molecule (Figure 5.26b, Table 5.11).

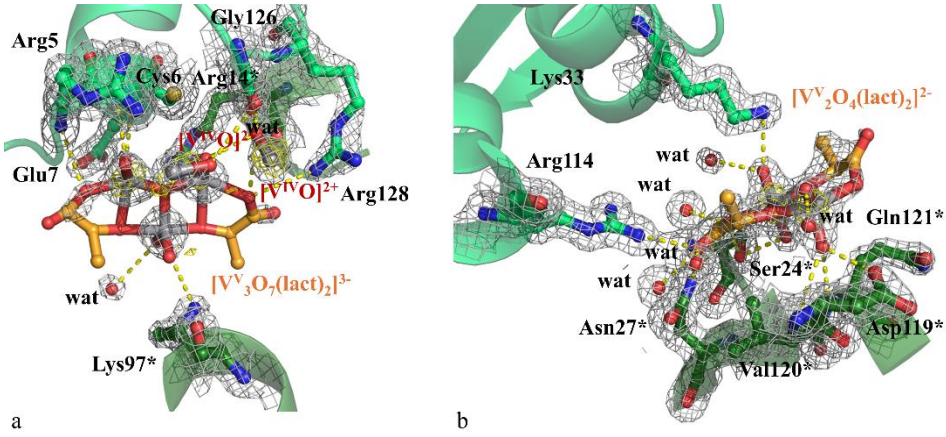

Figure 5.26 – Vanadium binding sites in the structure C: non-covalent interaction with protein residues of a) the two $[V^{IV}O]^{2+}$ ions and $[V^{V}_3O_7(lact)_2]^{3-}$, b) $[V^{V}_2O_4(lact)_2]^{2-}$. 2Fo-Fc electron density maps are contoured at 1.0 σ level and depicted in grey. Anomalous difference electron density map is reported at 3.0 σ level in yellow.

The structure D was obtained from crystals grown in 2.0 M sodium formate, 0.1 M HEPES pH 7.5 (Figure 5.23d) and refined at 1.23 Å resolution. Results revealed a binding pattern closely resembling that observed in structure C, with non-covalent binding of $[V^{IV}O]^{2+}$ (occupancy = 0.40) and $[V^{V}_3O_7(lact)_2]^{3-}$. In this

case, however, $[V^{V}_{2}O_{4}(lact)_{2}]^{2-}$ is not observed. The crystallographic findings are consistent with the ^{51}V NMR data collected under the same condition (Figure 5.20).

In conclusion, these results reveal that speciation and binding to HEWL of $Cs_{2}[V^{V}_{2}O_{4}(lact)_{2}]\cdot 2H_{2}O$ strongly depend on the experimental conditions, with the dinuclear species that predominates in acidic media, and trinuclear and mononuclear vanadates that are stabilized at higher pHs. This dynamic behaviour underscores the high complexity of V coordination chemistry in biological environments.

5.4 $Cs_{2}[V^{V}_{2}O_{4}(mal)_{2}]\cdot 2H_{2}O$ vs $Cs_{2}[V^{V}_{2}O_{4}(lact)_{2}]\cdot 2H_{2}O$

Although dinuclear complexes $Cs_{2}[V^{V}_{2}O_{4}(mal)_{2}]\cdot 2H_{2}O$ and $Cs_{2}[V^{V}_{2}O_{4}(lact)_{2}]\cdot 2H_{2}O$ share the same structure and ligands belonging to the α-hydroxycarboxylic acids (malate and lactate), they exhibit very different behaviours both in solution and in solid state in the absence and in the presence of HEWL.

Spectroscopic, spectrometric and crystallographic data reveal that $Cs_{2}[V^{V}_{2}O_{4}(mal)_{2}]\cdot 2H_{2}O$ readily transforms into a mixture of species containing two ($[V^{V}_{2}O_{4}(mal)_{2}]^{2-}$ and $[V^{V}_{2}O_{5}(mal)]^{2-}$), or ten V atoms ($V_{10}$), depending on pH, temperature, and presence of the protein. Crystallographic analysis confirms that HEWL can stabilize several of these species, including $[V^{IV}O]^{2+}$, $[V^{V}_{2}O_{5}(mal)]^{2-}$, and even the decavanadate. The latter binds to the protein both non-covalently and covalently through the carboxylate groups of Glu7 and Glu7*. At physiological temperature, however, the decavanadate does not form, and only an adduct with a $[V^{IV}O]^{2+}$ ion is detected, consistent with ^{51}V NMR data. These results highlight the influence of the temperature on speciation and interaction with proteins of these systems.

In contrast, the complex with lactate degrades forming $[V^{V}O_2]^{+}$, $[H_2V^{V}O_4]^{-}$, $[V^{V}O_2(lact)(OH)]^{2-}$ and $[V^{V}O_2(lact)(H_2O)]^{-}$, and transforms into a mixture of species containing two ($[H_2V^{V}_2O_7]^{2-}$, $[V^{V}_2O_4(lact)_2]^{2-}$), three ($[V^{V}_3O_7(lact)_2]^{3-}$), four ($[V^{V}_4O_{12}]^{4-}$), five ($[V^{V}_5O_{15}]^{5-}$), and ten V atoms ($V_{10}$).

Across the different crystallization conditions, HEWL binds $[V^{V}_2O_4(lact)_2]^{2-}$, $[V^{IV}O]^{2+}$, $[V^{V}O_2]^{+}$, $[V^{V}_3O_9]^{3-}$, and $[V^{V}_3O_7(lact)_2]^{3-}$. The interaction between V-containing fragments and proteins is mainly governed by hydrogen bonds with surface residues, indicating that the lactate ligand stabilizes the complex through non-covalent interactions.

5.5 Materials and methods

^{51}V NMR

^{51}V NMR spectra of the $Cs_2[V^{V}_2O_4(mal)_2]\cdot 2H_2O$ (concentration = 5 mM) were collected in:

- D_2O
- 1.1 M sodium chloride, 0.1 M sodium acetate pH 4.0, 10% D_2O

in the absence and in the presence of HEWL (concentration = 13 mg/mL, 0.9 mM). Spectra were collected after 1 h and 7 d of incubation at RT and after 42 h and 7 d of incubation at 37°C using a Bruker Avance Neo 500 MHz FT-NMR spectrometer at 25°C.

^{51}V NMR spectra of the $Cs_2[V^{V}_2O_4(lact)_2]\cdot 2H_2O$ (concentration = 5 mM) were collected in:

- D_2O
- 1.1 M sodium chloride, 0.1 M sodium acetate pH 4.0, 10% D_2O
- 20% ethylene glycol, 0.6 M sodium nitrate, and 0.1 M sodium acetate pH 4.0, 10% D_2O
- 0.8 M succinic acid pH 7.0, 10% D_2O

- 2.0 M sodium formate, 0.1 M HEPES pH 7.5, 10% D_2O

in the absence and in the presence of HEWL (concentration = 13 mg/mL, 0.9 mM) after 1 h and 7 d of incubation at RT using a Bruker Avance Neo 500 MHz FT-NMR spectrometer at 25°C.

Chemical shifts were referenced to $V^{V}OCl_3$ (ppm, δ). The ^{51}V NMR samples were recorded at 131.60 MHz (2000 scans, accumulation time 0.05 s, relaxation delay 0.01 s) and analysed with MestReNova (Automatic Phase Correction, Whittaker Smoother baseline).

Mass spectrometry

Mass spectra of $Cs_2[V^{V}_2O_4(mal)_2]\cdot 2H_2O$ (concentration ~100 µM) and $Cs_2[V^{V}_2O_4(lact)_2]\cdot 2H_2O$ (concentration ~100 µM) were collected in H_2O, and acetonitrile/methanol + 1% H_2O in positive (in the case of $Cs_2[V^{V}_2O_4(mal)_2]\cdot 2H_2O$) and in negative mode on Bruker timsTOF flex LC-MS System (m/z range of 90-600). The spectrometer was calibrated using the standard tunemix (accuracy ~5 ppm, m/z 50-1800, capillary voltage: 2500 V, nebulizer: 0.3 Bar, dry gas flow: 3.0 L/min Nitrogen, dry heater T: 200°C, flow rate: 3 µL/min). Spectra were analysed with Bruker Daltonics Data Analysis 4.0 software.

Mass spectra of HEWL (concentration = 13 mg/mL, 0.9 mM) in the absence and in the presence of $Cs_2[V^{V}_2O_4(mal)_2]\cdot 2H_2O$ (HEWL:VC molar ratio 1:1) and of $Cs_2[V^{V}_2O_4(lact)_2]\cdot 2H_2O$ (HEWL:VC molar ratio 1:1) were collected after diluting the sample 1:100 in acetonitrile/H_2O (9/1) + 1% formic acid and water in positive mode on Bruker timsTOF flex LC-MS System (capillary voltage: 3500 V, nebulizer: 0.3 Ba, dry gas flow: 3.0 L/min Nitrogen, dry heater T: 200°C, mass range: 300-3000 m/z). Spectra were deconvoluted with MagTran.

Crystallization, adduct formation, data collection, structure resolution and refinement

HEWL (concentration = 13 mg/mL, 0.9 mM) was crystallized using the hanging drop vapour diffusion method in:

- 1.1 M sodium chloride, 0.1 M sodium acetate pH 4.0
- 20% ethylene glycol, 0.6 M sodium nitrate, 0.1 M sodium acetate pH 4.0
- 0.8 M succinic acid pH 7.0
- 2.0 M sodium formate, 0.1 M HEPES pH 7.5

Pre-formed HEWL crystals were then exposed to stabilizing solutions containing the mother liquor saturated with $Cs_2[V^V_2O_4(mal)_2]\cdot 2H_2O$ and $Cs_2[V^V_2O_4(lact)_2]\cdot 2H_2O$ for a soaking time of 7 days and were cryopreserved for X-ray diffraction by transfer into a solution consisting of 70 % reservoir solution and 30 % glycerol. The crystals were then fished with a nylon loop, rapidly cooled in liquid nitrogen and then sent to synchrotrons. X-ray diffraction data were collected at the XRD2 Beamline at Elettra synchrotron, Trieste, Italy.

HEWL (concentration = 100 mg/mL, 6.8 mM) was also crystallized at 37°C in 1.1 M sodium chloride, 0.1 M sodium acetate pH 4.0, with crystals forming in a few hours. Pre-formed crystals were exposed to $Cs_2[V^V_2O_4(mal)_2]\cdot 2H_2O$ for a few hours. X-ray diffraction data were collected at 37°C on Beamline XRD2 at Elettra synchrotron, Trieste, Italy.

Crystals diffract at resolution in the range 1.18-1.49 Å at 100 K and 2.09 Å at 37°C. Data processing and scaling were performed using Global Phasing autoPROC pipeline.[232] The structures were solved by the Molecular Replacement method using the Phaser program from CCP4 suite[233] and the structures deposited in the PDB 193L[194] as template. Refmac5 was used for refinement.[234] Model building was carried out using Coot.[235] In all the structures, V atom position was validated using anomalous difference e.d. maps. The final models show R-factor and Rfree values in the range of 0.174-0.239 and 0.174-0.312 respectively. Ligand

positions were restrained to guide geometry optimization. Figures were generated using PyMol (www.pymol.org). The structure validation of the final models was performed using the PDB validation server.[236]

Coordinates and structure factors of the structures of HEWL treated with $Cs_2[V^V_2O_4(mal)_2]\cdot 2H_2O$ were deposited in the PDB under the accession codes 9RBG, 9RBT and 9RBV.

The results of this study were successfully published on:

M. Paolillo, G. Ferraro, N. I. Gumerova, F. Pisanu, E. Garribba, A. Rompel, A. Merlino. "Speciation and structural transformation of a V^{V}–malate complex in the absence and in the presence of a protein: from a dinuclear species to decavanadate" Inorg. Chem. Front., (2025). Advance Article. DOI: https://doi.org/10.1039/D5QI01384D

CHAPTER 6

Conclusion

6. Conclusion

The chemistry of vanadium is an important field of research. Vanadium compounds have interesting catalytic and therapeutic applications,[1–8] for example for the treatment of cancer and diabetes.[9–17] Understanding VC mechanism of action and their fate within the body is important for translation to clinical therapy of potential V-based drugs. In this respect, since proteins represent a possible VC target and are certainly involved in transport and delivery of bioactive VCs,[177,178] the interaction of proteins with VCs has to be deeply studied.

This thesis focused on the use of a combined approach, based on structural and spectroscopic techniques, to obtain insights into the interaction between members of selected classes of VCs and proteins. In particular, speciation in aqueous solution, mode of binding to proteins, and the interactions at the basis of the VC/protein recognition process were investigated. X-ray crystallography was used to obtain the structures of the adducts formed upon reaction of VCs with proteins, while ESI-MS, ^{51}V NMR and other spectroscopic techniques were used to complement the information obtained by X-ray crystallography.[168]

The first systems that were investigated during the thesis belong to the $[V^{IV}OL_2]$ class. Structural analysis of the adducts formed by these compounds with HEWL reveals variability in the V-containing fragments recognized by the protein, in their localization, occupancy and microenvironment. Furthermore, different coordination modes have been observed.

Literature data have shown that protein residue side chains can replace equatorial water molecules of the *cis*-$[V^{IV}OL_2(H_2O)]$ species formed by hydration of the starting $[V^{IV}OL_2]$ compounds, in the case of the interaction of $[V^{IV}O(malt)_2]$ with HEWL,[35] and of $[V^{IV}O(pic)_2(H_2O)]$ with HEWL,[226] RNase A[259] and trypsin.[34] Alternatively, $[V^{IV}OL_2]$ can weakly coordinate a protein at axial positions, but this mode of binding has not been observed in the structures of the adducts with proteins solved up to now. Partial ligand dissociation can also occur, as observed for

the adducts formed by $[V^{IV}O(8\text{-}HQ)_2]$ with RNase A[50] and by $[V^{IV}O(phen)_2]$ (phen = phenatroline)[34] and $[V^{IV}O(bipy)_2]$ (bipy = bipyridine) with HEWL.[34]

Results obtained in this thesis agree with this view: $[V^{IV}OL]$–protein adducts are observed in the case of $[V^{IV}O(empp)_2]$ with HEWL in 1.1 M sodium chloride, 0.1 M sodium acetate pH 4.0 and in 2.0 M sodium formate, 0.1 M HEPES pH 7.5,[280] and when $[V^{IV}O(8\text{-}HQ)_2]$ reacts with the same protein in 20% ethylene glycol, 0.6 M sodium nitrate, 0.1 M sodium acetate pH 4.5.[281] Notably, new results here reported showed that $[V^{IV}OL_2]$ complexes can also retain both their ligands. In this case, the metal centre does not change its coordination sphere and the compounds bind proteins forming non-covalent interactions, as observed for $[V^{IV}O(empp)_2]$ with HEWL in 0.8 M succinic acid pH 7.0 and in 2.0 M sodium formate, 0.1 M HEPES pH 7.5,[280] and for $[V^{IV}O(8\text{-}HQ)_2]$ with the same protein in 2.0 M sodium formate, 0.1 M HEPES pH 7.5.[281] Self-reactivity of the compounds producing oxidized dimetallic species, like $[(V^{V}O(dhp)_2)_2O]$ and $[(V^{V}O(dhp)_2)(V^{V}O(dhp)(H_2O)_2)O]^{+}$, and trimetallic species, like $[(V^{V}O_2)_3(empp)_3(H_2O)]$,[280] were also observed.

A special case is $[V^{IV}O(acac)_2]$. Since acac is a very weak ligand, it can be easily released. This facilitates the oxidation of V centre from +4 to +5 and leads to the formation of different polyoxidovanadates, containing two (as in the case of $[V^{V}_2O_6]^{2-}$ that is covalently attached to Fe_C-hTF) or four ($[V^{V}_4O_{12}]^{4-}$ non-covalently bound to HEWL) V^{V} atoms. Mixed valence species containing fifteen ($[V^{V}_7V^{IV}_8O_{36}(OH_2)]^{5-}$, $[V^{V}_7V^{IV}_8O_{36}(Cl)]^{6-}$ and $[V^{V}_7V^{IV}_8O_{33}(OH_2)]^{+}$) and twenty ($[V_{20}O_{51}(NO_3)]^{n-}$ and $[V_{20}O_{54}(H_2O)]^{n-}$) vanadium atoms are also observed in the adducts formed by $[V^{IV}O(acac)_2]$ with HEWL in 20% ethylene glycol, 0.6 M sodium nitrate, 0.1 M sodium acetate pH 4.0 and 1.1 M sodium chloride, 0.1 M sodium acetate pH 4.0 and or with human ferritin.[219–221,228]

Another class of VCs investigated in the thesis is that of the $[V^{IV}OL(H_2O)_2]$ compounds. Protein residue side chains can coordinate the metal centre of these

compounds replacing one or two water molecules. This binding mode was observed in the interaction of $[V^{IV}O(dipic)(H_2O)_2]$ with HEWL and RNase A. When $[V^{IV}O(xant)(H_2O)_2]$ and $[V^{IV}O(dipic)(H_2O)_2]$ react with HEWL, protein binding of oxidized $[V^{V}O_2L]$ species (like $[V^{V}O_2(xant)]^-$ and $[V^{V}O_2(dipic)]^-$ that non-covalently bind HEWL and $[(V^{V}O_2(xant))_2(V^{IV}O(H_2O)_2)_2]^{2+}$ that is covalently bound to the protein) is also observed.

Finally, the interaction of V^V compounds with HEWL was studied. V^V complexes with tridentate ligands (VC1, VC2 and VC3) form non-covalent interactions with proteins.[282]

Dimetallic V^V complexes with α-hydroxycarboxylic acids as ligands (formula $[V^{V}_2O_4L_2]$) also non-covalently interact with HEWL, even when they lose one ligand. Notably, these complexes can degrade forming species with three V atoms (as the $[V^{V}_3O_9]^{3-}$ and $[V^{V}_3O_7(lact)_3]^{3-}$ ions formed by $Cs_2[V^{V}_2O_4(lact)_2]\cdot 2H_2O$ in the presence of HEWL) or ten V atoms (like $[V^{V}_{10}O_{28}]^{6-}$, which non-covalently binds HEWL, and $[V^{V}_{10}O_{26}]^{2-}$ that covalently binds the protein, formed in the case of $Cs_2[V^{V}_2O_4(mal)_2]\cdot 2H_2O$).[283]

Considering the structures reported in this thesis and those available in the PDB on the interaction between $[V^{IV}OL_2]$, $[V^{IV}OL(H_2O)_2]$ and V^V complexes with proteins, a database of 44 structures can be built. The PDB codes of the database are reported in Table B.1-Table B.4 (see Appendix B).

Analysis of the structures in the Database provides general information on the binding mode of VCs to proteins. The results of this analysis are the following:

1) The binding of VCs to proteins does not significantly alter their overall conformation. RMSD of the Cα atoms of the structures of the adducts from those of the metal-free proteins are within the range 0.14-0.53 Å (see Appendix B, Table B.5).

2) VCs can interact with proteins through covalent binding, non-covalent binding or both binding modes. A statistical analysis shows that structures with only non-covalent binding are the majority (Figure 6.*1*).
   Interestingly, the number of V/protein adduct structures with non-covalent interactions is higher than that with the covalent ones, at variance with what observed in the case of other metal compounds of biomedical interest like those based on Au, Ru and Pt.[186,229,231]
3) The same compound can bind the protein both covalently and non-covalently, upon losing ligands, as observed in the case of $[V^{IV}O(empp)_2]$,[280] $[V^{IV}O(malt)_2]$[35] and $[V^{IV}O(8\text{-}HQ)_2]$[281] with HEWL, or just few atoms of its structure, as found in the case of $[V^{V}_{10}O_{26}]^{2-}$ bound to HEWL.[283]
4) Covalent and non-covalent interactions with different vanadium containing fragments can be found in the same adduct at the same time, as observed in the case of $[V^{IV}O(malt)_2]$,[35,227] $[V^{IV}O(empp)_2]$,[280] $[V^{IV}O(dhp)_2]$, $[V^{IV}O(acac)_2]$,[219–221] $[V^{IV}O(phen)_2]$,[34] $[V^{IV}O(xant)(H_2O)_2]$, $[V^{IV}O(dipic)(H_2O)_2]$ and $Cs_2[V^{V}_2O_4(mal)_2]\cdot 2H_2O$.[283]
5) Residues that are involved in the V coordination are mainly Glu, Asp and Asn side chains (Figure 6.2). V centre can bind also the C-terminal carboxylate (Figure 6.2).
6) Non-covalent binding is mediated by hydrogen bonds, electrostatic contacts, and π–π stacking interactions formed by V-containing fragments and surface residues, such as Arg, Lys, Thr, Ser, Cys, Glu, Asn, Tyr, Trp, Phe and Gln.
7) The same protein can covalently bind more than one V-containing fragment at the same time. A variety of V-containing fragments with different binding modes and occupancies are observed in the adducts formed by HEWL with $[V^{IV}O(8\text{-}HQ)_2]$,[281] $[V^{IV}O(acac)_2]$,[219–221] $[V^{IV}O(malt)_2]$,[227] $[V^{IV}O(phen)_2]$,[34] $[V^{IV}O(dipic)(H_2O)_2]$ and $Cs_2[V^{V}_2O_4(mal)_2]\cdot 2H_2O$.[283]

8) Binding of VCs to proteins depends on nature and stability of the ligands. When ligands are weak, they can be completely lost upon interaction with the protein. This favours coordination to protein residue side chains. When ligands are strong the metal compound can retain its original structure and non-covalent interactions are favoured. Thus, different ions, like $[V^{IV}O(H_2O)_3]^{2+}$, $[V^{IV}O(H_2O)_4]^{2+}$, $[V^{IV}O]^{2+}$, $[V^{V}O_2]^{+}$, $[V^{IV}OL(H_2O)]^{+}$, $[V^{IV}OL(H_2O)_2]^{+}$ can bind proteins.[35]

9) Binding of VCs to proteins depends on the experimental conditions used to study the metal compound/protein interaction. pH, ionic strength, buffer composition and temperature are important.[34,35,50,219–221,226–228,281–283]

   The binding of the same VC to the same protein under different experimental conditions leads to different V/protein adducts, as observed in the case of $[V^{IV}O(empp)_2]$,[280] $[V^{IV}O(8\text{-}HQ)_2]$,[281] $[V^{IV}O(acac)_2]$,[219–221] $[V^{IV}O(malt)_2]$,[35,227] $[V^{IV}O(xant)(H_2O)_2]$, $[V^{IV}O(dipic)(H_2O)_2]$ and $Cs_2[V^{V}{}_2O_4(lact)_2]\cdot 2H_2O$.

   The structure of the same adduct at different temperatures shows differences in the V-containing fragments that are bound to the protein, as observed in the case of $Cs_2[V^{V}{}_2O_4(mal)_2]\cdot 2H_2O$[283] and $[V^{IV}O(acac)_2]$.[221]

10) VCs can hydrolyse and/or undergo redox processes upon reaction with proteins. These modifications promote the formation of dimetallic species, as evidenced in the adducts of HEWL with $[V^{IV}O(dhp)_2]$, trimetallic species, as found in the case of HEWL with $[V^{IV}O(empp)_2]$,[280] tetrametallic species, as found in the case of HEWL with $[V^{IV}O(xant)(H_2O)_2]$, and polyoxidovanadates with two ($[V_2O_6]^{2-}$), three ($[V_3O_9]^{3-}$), four ($[V_4O_{12}]^{4-}$), ten ($[V_{10}O_{28}]^{6-}$ and $[V_{10}O_{26}]^{2-}$), fifteen ($[V_{15}O_{36}(H_2O)]^{5-}$ and $[V_{15}O_{33}(H_2O)]^{+}$) and twenty ($[V_{20}O_{51}(NO_3)]^{n-}$ and $[V_{20}O_{54}(H_2O)]^{n-}$) vanadium atoms.[219–221,283]

11) V centre can act as a protein crosslinker inducing the formation of high protein aggregates. For example, HEWL dimers covalently cross-linked through coordination to a modified Lys1 and Asp87* side chain are found upon reaction of HEWL with $[V^{IV}O(malt)_2]$.[227]

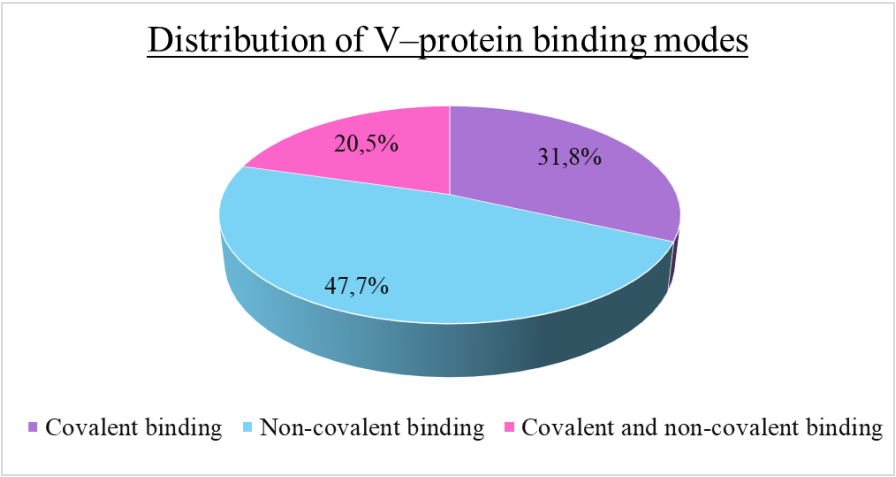

Figure 6.1 – Percentage distribution of VC–protein adducts according to their interaction mode. The chart shows the proportion of crystal structures in which V-containing fragments are bound to proteins covalently, non-covalently, or through both covalent and non-covalent interactions. The data include all VC–protein adducts reported in the PDB and those obtained during this PhD work.

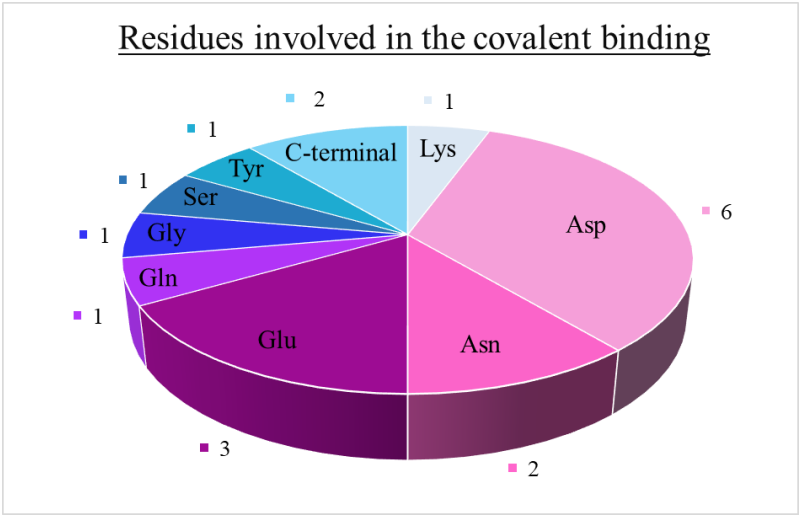

Figure 6.2 – The percentage distribution of the residues involved in the covalent binding of V-containing fragments with proteins.

Overall, the results presented in this thesis provide a comprehensive and unprecedented view of V–protein interactions. This work demonstrates how subtle variations in ligand structure, oxidation state, and experimental conditions deeply influence V compound speciation and binding to proteins. Each of the studied VCs provides valuable insights, highlighting different aspects of protein binding and potential applications. These findings not only enhance the understanding of the VC–protein interaction process but also open new perspectives for the rational design of V-based compounds. More broadly, they contribute to a deeper comprehension of the mechanism of action of V-based drugs, paving the way for the development of new therapeutic agents.

Appendix B

This appendix summarizes all the crystallographic data currently available for VC–protein adducts. A total of 44 structures, derived from the interaction between VCs and proteins, are reported in Table B.1-Table B.4. Notably, 26 of these structures were obtained during this PhD project, representing a significant expansion of the structural database on VC–protein systems. RMSD of the Cα atoms of the structures of the adducts from those of the metal-free proteins are shown in Table B.5.

Table B.1 - Details of the structures of $[V^{IV}OL_2]$–HEWL adducts, with L = bidentate ligand.

$[V^{IV}OL_2]$–HEWL adducts L= bidentate ligand																			
$[V^{IV}OL_2]$	**$[V^{IV}O(empp)_2]$**			**$[V^{IV}O(dhp)_2]$**		**$[V^{IV}O(8\text{-}HQ)_2]$**		**$[V^{IV}O(acac)_2]$**						**$[V^{IV}O(malt)_2]$**				**$[V^{IV}O(pic)_2(H_2O)]$**	**$[V^{IV}O(phen)_2]$**	**$[V^{IV}O(bipy)_2]$**
References	Structure A Para-graph 2.2 [280]	Structure B Para-graph 2.2 [280]	Structure C Para-graph 2.2 [280]	Structure A Para-graph 2.3	Structure B Para-graph 2.3	Para-graph 2.4 [281]	Para-graph 2.4 [281]	Structure at 37° C [221]	Structure A [220]	Structure B [220]	Structure C [220]	Structure A [219]	Structure B [219]	[227]	Structure A [35]	Structure A' [35]	Structure B [35]	[226]	[34]	[34]
PDB code	8OM8	8OMS	8OMT	-	-	8RTJ	8RTK	9IL8	9EX0	9EX1	9EX2	7ZU6	8PTE	9FMY	8AJ3	8AJ4	8AJ5	4C3W	7Q0V	7Q0U
Crystallization conditions	i	ii	iii	i	i	iv	iii	i	i	i	i	iii	v	i	iii	iii	v	vi	vii	vii
Covalent binding																				

Lys1 Asp87*	-	-	-	-	-	-	-	-	-	-	-	-	-	(bis) V-containing fragment (0.60)	-	-	-	-	-	-
Asp18 Gly71*	-	-	-	-	-	-	-	$[V_{15}O_{33}(OH_2)]^+$ (0.50)	-	-	$[V_{15}O_{33}(OH_2)]^+$ (0.25)	-	-	-	-	-	-	-	-	-
Glu35	-	-	-	-	-	-	-	-	-	-	-	-	-	-	-	-	$[V^{IV}O(H_2O)_3]^{2+}$ (0.35)	-	-	-
Asn46 Asp52	-	-	-	-	-	-	-	-	VO_4 (0.50)	-	VO_4 (0.30)	-	-	V^{IV} (0.30)	-	-	-	-	$[V^{IV}O(phen)(H_2O)]^{2+}$ (0.75)	$[V^{IV}O(bipy)(H_2O)]^{2+}$ (0.90)
Asp48	$[V^{IV}O(empp)(H_2O)]^+$ (0.60)	-	-	$[V^{IV}O(H_2O)_3]^{2+}$ (0.60)	$[V^{IV}O(H_2O)_3]^{2+}$ (0.50)	V^{IV} (0.60)	-	-	-	-	-	-	-	V^{IV} (0.60)	-	-	$[V^{IV}O(H_2O)_3]^{2+}$ (0.50)	-	-	-
Asp52	-	-	-	-	-	-	-	-	-	-	-	-	$[V^{IV}O(H_2O)_4]^{2+}$ (0.50)	-	-	-	-	$[V^{IV}O(pic)_2]$ (0.65)	-	-
Asn65	-	-	-	-	-	-	-	-	-	-	-	-	-	-	$[V^{IV}O(H_2$	$[V^{IV}O(m$	-	-	-	-

															$O)_4]^{2+}$ (0.50)	alt)$_2$] (0.30)				
Asp87	-	-	-	-	-	-	-	$[V_{20}O_{51}(OH_2)]^{n-}$ (0.70) Asp 87*	$[V_{20}O_{51}(OH_2)]^{n-}$ (0.80) Asp 87*	-	VO_4 (0.30)	-	$[V_{20}O_{54}(NO_3)]^{n-}$ (0.60)	-	-	-	$[V^{IV}O(H_2O)_3]^{2+}$ (0.50)	-	-	-
Asp101	-	-	-	-	-	-	-	-	-	-	-	-	-	-	-	-	-	-	$[V^{V}O_2]^{+}$ (0.50)	-
Asp119	-	-	-	-	-	$[V^{IV}O(8\text{-}HQ)(H_2O)]^{+}$ (0.60)	-	-	-	-	-	-	-	-	-	-	$[V^{IV}O]^{2+}$ (1.00)	-	-	-
C-terminal carboxylate	-	-	-	-	-	-	-	-	-	-	VO_4 (0.60)	-	-	-	-	-	V^{IV} (0.25)	-	-	-
Non-covalent binding																				
Lys1 Ser86	-	-	-	-	-	-	$[V^{IV}O]^{2+}$ (0.30)	-	-	-	-	$[V^{V}_4O_{12}]^{4-}$ (0.70) Val 2 Gln 121	-	-	-	-	-	-	-	-
	-	$[V^{IV}O$(e	$[V^{IV}O$(e	-	-	-	$[V^{IV}O]^{2+}$	-	-	-	-	$[V^{V}O_2]^{+}$	-	-	$[V^{IV}O$(m	$[V^{IV}O$(m	-	-	-	-

Arg5 Cys6 Glu7		mpp)$_2$(H_2O)] (0.40)	mpp)$_2$(H_2O)] (0.80)				(0.30) $[V^{V}O_2]^{+}$ (0.30)					(0.50)			alt)$_2$(H_2O)] (0.70)	alt)$_2$(H_2O)] (0.80)				
Arg5	$[(V^{V}O_2)_3$(emp p)$_3$(H_2O)] (0.60) Lys33 Trp123	-	-	$[(V^{V}O$(dhp)$_2)_2O]$ (0.70) Trp123 Phe38	$[(V^{V}O$(dhp)$_2$)($V^{V}O$(dhp)(H_2O)$_2$)$O]^{+}$ (0.50) Lys33 Trp123	-	-	-	-	-	-	-	-	-	-	-	-	-	-	-
Tyr20 Arg21 Lys96	-	-	-	-	-	-	-	-	-	$[V_{15}O_{36}$(OH_2)$]^{5-}$ (0.50)	$[V_{15}O_{36}$(OH_2)$]^{5-}$ (0.50)	-	-	-	-	-	-	-	-	-
Asn65 Gly67 Arg68 Thr69	-	-	-	-	-	-	-	-	-	-	-	-	-	$[V^{IV}O(H_2O)_5]^{2+}$ (0.50)	-	-	-	-	-	-
Arg73 Arg74	-	-	-	-	-	-	-	-	-	-	-	-	-	-	$[V^{IV}O$(malt)(H_2O)$_3]^{2+}$ (0.30)	$[V^{IV}O$(malt)$_2$(H_2O)] (0.30)	-	-	-	-

Asp119 Gln121	-	-	-	-	-	-	-	-	-	-	-	-	-		-	-	-	-	$V^{IV}O$ (0.50)	-
Arg125	-	-	$[V^{IV}O(empp)(H_2O)_2]$ (0.40)	-	-	-	-	-	-	-	-	-	-	-	-	-	-	-	-	-
Arg128	-	-	-	-	-	-	$[V^{IV}O(8\text{-}HQ)_2(H_2O)]$ (0.50)	-	-	-	-	-	-	-	-	-	-	-	-	-
	-	-	-	-	-	-	-	-	-	-	-	-	-	-	-	-	-	-	$[V^{V}O_2]^{+}$ (0.50)	-

i indicates 1.1 M sodium chloride, 0.1 M sodium acetate pH 4.0; ii indicates 0.8 M succinic acid pH 7.0; iii indicates 2.0 M sodium formate, 0.1 M HEPES pH 7.5; iv indicates 20% ethylene glycol, 0.6 M sodium nitrate, 0.1 M sodium acetate pH 4.5; v indicates 20% ethylene glycol, 0.6 M sodium nitrate, 0.1 M sodium acetate pH 4.0; vi indicates 4-8% (M/V) sodium chloride, 0.1 M sodium acetate pH 4.5; vii indicates 6-8% (M/V) sodium chloride, 0.1 M sodium acetate pH 4.5.

Table B.2 – Details of the structures of $[V^{IV}OL_2]$–protein adducts, with L = bidentate ligand and $[V^{IV}OL(H_2O)_2]$–RNase A adduct, with L = tridentate ligand.

Adducts	**$[V^{IV}OL_2]$–RNase A adducts L = bidentate ligands**		**$[V^{IV}OL_2]$–Trypsin adducts L = bidentate ligands**		**$[V^{IV}OL_2]$–human H-chain Ferritin adduct L = bidentate ligand**	**$[V^{IV}OL_2]$–hFt adduct L = bidentate ligand**	**$[V^{IV}OL(H_2O)_2]$–RNase A adduct L = tridentate ligand**
Vanadium compounds	**$[V^{IV}O(pic)_2(H_2O)]$**	**$[V^{IV}O(8\text{-}HQ)_2]$**	**$[V^{IV}O(pic)_2(H_2O)]$**	**$[V^{IV}O(phen)_2]$**	**$[V^{IV}O(acac)_2]$**	**$[V^{IV}O(acac)_2]$**	**$[V^{IV}O(dipic)(H_2O)_2]$**
Reference	[259]	[50]	[34]	[34]	[228]	Paragraph 2.5	Paragraph 3.5
PDB code	7P8R	7QWH	7Q0X	7Q0W	9RGH, 9RGJ, 9RGI	9RTB	-
Crystallization conditions	22% PEG 4K 10 mM sodium citrate pH 5.1	22% PEG 4K 10 mM sodium citrate pH 5.1	30% PEG 4K 0.2 M ammonium sulphate	10% (m/v) PEG8000, 0.1 M imidazole pH 8.0	2.0 M $MgCl_2$ 0.1 M bicine buffer pH 9.0	15% (w/v) PEG 3350 16% (v/v) glycerol 8 mM disodium malonate 150 mM Na-PIPES pH 6.5	22% PEG 4K 10 mM sodium citrate pH 5.1
V-containing fragment bound to the protein	$[V^{IV}O(pic)_2]$ (0.75)	$[V^{IV}O(8\text{-}HQ)(H_2O)_2]^+$ (0.70)	$[V^{IV}O(pic)_2]$ (0.80)	$[V^{IV}O(phen)(imidazole)(H_2O)]$ (0.70)	$[V_{15}O_{36}(Cl)]^{6-}$ (0.50)	$[V^{V}{}_2O_6]^{2-}$ (0.70)	$[V^{IV}O(dipic)(H_2O)]$ (0.75)
Covalent binding							
Binding site	Glu111	Glu111	Ser195	Ser195	-	Tyr188	C-terminal tail of chain A
Non-covalent binding							
Binding site	-	-	-	-	Thr5, Arg9, Gln10, Asn11, Tyr12, His13 and Gln14	-	-

Table B.3 – Details of the structures of $[V^{IV}OL(H_2O)_2]$–HEWL adduct, with L = tridentate ligand.

$[V^{IV}OL(H_2O)_2]$–HEWL adducts L = tridentate ligand							
$[V^{IV}OL(H_2O)_2]$	**$[V^{IV}O(xant)(H_2O)_2]$**					**$[V^{IV}O(dipic)(H_2O)_2]$**	
References	Structure A Paragraph 3.3	Structure B Paragraph 3.3	Structure C Paragraph 3.3	Structure D Paragraph 3.3	Structure E Paragraph 3.3	Structure A Paragraph 3.4	Structure B Paragraph 3.4
PDB code	-	-	-	-	-	-	-
Crystallization conditions	1.1 M sodium chloride 0.1 M sodium acetate pH 4.0	20% ethylene glycol 0.6 M sodium nitrate 0.1 M sodium acetate pH 4.0	14% PEG 8000, 0.1 M sodium citrate, 0.05 M sodium cacodylate pH 6.5	0.8 M succinic acid pH 7.0	2.0 M sodium formate 0.1 M HEPES pH 7.5	1.1 M sodium chloride 0.1 M sodium acetate pH 4.0	20% ethylene glycol 0.6 M sodium nitrate 0.1 M sodium acetate pH 4.0
Covalent binding							
Glu7 Glu7*	$[(V^{V}O_2(xant))_2(V^{IV}O(H_2O)_2)_2]^{2+}$ (0.85)	-	-	-	-	-	-
Asp18	-	-	-	-	-	$[V^{IV}O(dipic)(H_2O)]$ (0.80)	-
Asp119	-	-	-	-	-	$[V^{IV}O(dipic)]$ (0.95)	-
Gln121	-	-	-	-	-	-	$[V^{IV}O(dipic)(H_2O)]$ (0.90)
C-terminal carboxylate	-	-	-	-	-	V^{IV} (0.20)	-
Non-covalent binding							
Arg14	-	-	-	-	-	-	$[V^{V}O_2(dipic)]^{-}$ (0.40)
Asp101	-	-	-	-	-	$[V^{V}O(dipic)(CH_3COO)]$	-

						(0.70) Ala107 Trp108	
Trp123	$[V^{V}O_2(xant)]^-$ (0.60) Ala122 Asp119*	$[V^{V}O_2(xant)]^-$ (0.60) Ala122 Asp119* Lys33	$[V^{V}O_2(xant)]^-$ (0.50) Ala122 Asp119* Lys33	$[V^{V}O_2(xant)]^-$ (0.50) Ala122 Asp119* Lys33	$[V^{V}O_2(xant)]^-$ (0.50) Ala122 Asp119* Lys33	$[V^{V}O_2(dipic)]^-$ (0.70) Arg5 Arg125	$[V^{V}O_2(dipic)]^-$ (0.50) Arg125
Arg125	$[V^{V}O_2(xant)]^-$ (0.50) Asp119*	-	-	-	-	-	-
Asn103* Asn106* Arg112*	$[V^{V}O_2(xant)]^-$ (0.50)	-	-	-	-	-	-

Table B.4 – Details of the structures of VC–HEWL adducts (V^V complexes).

VC–HEWL adduct (V^V complexes)										
VC (V^V complexes)	**VC1**	**VC2**	**VC3**	**$Cs_2[V^V_2O_4(mal)_2]\cdot 2H_2O$**			**$Cs_2[V^V_2O_4(lact)_2]\cdot 2H_2O$**			
References	Paragraph 4.2[282]	Paragraph 4.2[282]	Paragraph 4.3	Structure A Paragraph 5.2[283]	Structure B Paragraph 5.2[283]	Structure at 37°C Paragraph 5.2[283]	Structure A Paragraph 5.3	Structure B Paragraph 5.3	Structure C Paragraph 5.3	Structure D Paragraph 5.3
PDB code	9GOG	9GOK	9SA2	9RBG	9RBT	9RBV	-	-	-	-
Crystallization conditions	1.1 M sodium chloride 0.1 M sodium acetate pH 4.0	1.1 M sodium chloride 0.1 M sodium acetate pH 4.0	1.1 M sodium chloride 0.1 M sodium acetate pH 4.0	1.1 M sodium chloride 0.1 M sodium acetate pH 4.0	1.1 M sodium chloride 0.1 M sodium acetate pH 4.0	1.1 M sodium chloride 0.1 M sodium acetate pH 4.0	1.1 M sodium chloride 0.1 M sodium acetate pH 4.0	20% ethylene glycol 0.6 M sodium nitrate 0.1 M sodium acetate pH 4.0	0.8 M succinic acid pH 7.0	2.0 M sodium formate 0.1 M HEPES pH 7.5
Covalent binding										
Glu7 Glu7*	-	-	-	$[V^V_{10}O_{26}]^{2-}$ (0.70)	-	-	-	-	-	-
Asp18	-	-	-	$[V^{IV}O]^{2+}$ (1.00)	-	$[V^{IV}O]^{2+}$ (1.00)	-	-	-	-
Non-covalent binding										

Glu7	$[V^{V}O_2]^{+}$ (0.70) Cys6	-	-	-	$[V^{V}_{10}O_{28}]^{6-}$ (0.80) Lys1 Arg14	-	$[V^{V}O_2]^{+}$ (0.70) Cys6	$[V^{V}_3O_9]^{3-}$ (0.50) Arg5 Cys6	$[V^{V}_3O_7(lact)_2]^{3-}$ (0.60) Arg5 Cys6 Arg14 Gly126 Arg128	$[V^{V}_3O_7(lact)_2]^{3-}$ (0.60) Arg5 Cys6 Arg14 Gly126 Arg128
								$[V^{V}O_2]^{+}$ (0.50)	$[V^{IV}O]^{2+}$ (0.40)	$[V^{IV}O]^{2+}$ (0.40)
									$[V^{IV}O]^{2+}$ (0.40)	$[V^{IV}O]^{2+}$ (0.40)
Lys33	VC1 (1) (0.70)	VC2 (1) (0.60)	VC3 (1) (0.70)	-	-	-	$[V^{V}_2O_4(lact)_2]^{2-}$ (0.80)	$[V^{V}_2O_4(lact)_2]^{2-}$ (0.80)	$[V^{V}_2O_4(lact)_2]^{2-}$ (0.80) Arg114	-
	VC1 (2) (0.70) Arg5	VC2 (2) (0.60)	VC3 (2) (0.70) Trp123							
Asn65 Gly67 Arg68 Thr69 Pro70 Ser72	-	-	-	$[V^{V}_2O_5(mal)]^{2-}$ (0.70)	$[V^{V}_2O_5(mal)]^{2-}$ (0.60)	-	-	-	-	-

Table B.5 – RMSD of the Cα atoms of the structures of the adducts from those of the metal-free proteins.

$[V^{IV}OL_2]$–HEWL adducts L= bidentate ligand			
$[V^{IV}OL_2]$	**References**	**PDB code**	**RMSD (Å)**
$[V^{IV}O(empp)_2]$	Structure A Paragraph 2.2[280]	8OM8	0.19
	Structure B Paragraph 2.2[280]	8OMS	0.19
	Structure C Paragraph 2.2[280]	8OMT	0.22
$[V^{IV}O(dhp)_2]$	Structure A Paragraph 2.3	-	0.18
	Structure B Paragraph 2.3	-	0.14
$[V^{IV}O(8\text{-}HQ)_2]$	Paragraph 2.4[281]	8RTJ	0.21
	Paragraph 2.4[281]	8RTK	0.21
$[V^{IV}O(acac)_2]$	Structure A[219]	7ZU6	0.19
	Structure B[219]	8PTE	0.22
	Structure A[220]	9EX0	0.22
	Structure B[220]	9EX1	0.42
	Structure C[220]	9EX2	0.26
	Structure at 37°C[221]	9IL8	0.26
$[V^{IV}O(malt)_2]$	Structure A[35]	8AJ3	0.20
	Structure A'[35]	8AJ4	0.20
	Structure B[35]	8AJ5	0.24
	[227]	9FMY	0.22
$[V^{IV}O(pic)_2(H_2O)]$	[226]	4C3W	0.16
$[V^{IV}O(phen)_2]$	[34]	7Q0V	0.16
$[V^{IV}O(bipy)_2]$	[34]	7Q0U	0.17
$[V^{IV}OL_2]$–RNase A adducts L = bidentate ligands			
$[V^{IV}OL_2]$	**References**	**PDB code**	**RMSD (Å)**
$[V^{IV}O(pic)_2(H_2O)]$	[259]	7P8R	0.35
$[V^{IV}O(8\text{-}HQ)_2]$	[50]	7QWH	0.30
$[V^{IV}OL_2]$–Trypsin adducts L = bidentate ligands			

$[V^{IV}OL_2]$	References	PDB code	RMSD (Å)
$[V^{IV}O(pic)_2(H_2O)]$	[34]	7Q0X	0.45
$[V^{IV}O(phen)_2]$	[34]	7Q0W	0.45
$[V^{IV}OL_2]$–human H-chain Ferritin adduct L = bidentate ligand			
$[V^{IV}OL_2]$	References	PDB code	RMSD (Å)
$[V^{IV}O(acac)_2]$	[228]	9RGH, 9RGJ, 9RGI	0.41-0.53
$[V^{IV}OL_2]$–hFt adduct L = bidentate ligand			
$[V^{IV}OL_2]$	References	PDB code	RMSD (Å)
$[V^{IV}O(acac)_2]$	Paragraph 2.5	9RTB	0.27
$[V^{IV}OL(H_2O)_2]$–HEWL adducts L = tridentate ligand			
$[V^{IV}OL(H_2O)_2]$	References	PDB code	RMSD (Å)
$[V^{IV}O(xant)(H_2O)_2]$	Structure A Paragraph 3.3	-	0.37
	Structure B Paragraph 3.3	-	0.29
	Structure C Paragraph 3.3	-	0.29
	Structure D Paragraph 3.3	-	0.24
	Structure E Paragraph 3.3	-	0.35
$[V^{IV}O(dipic)(H_2O)_2]$	Structure A Paragraph 3.4	-	0.25
	Structure B Paragraph 3.4	-	0.31
$[V^{IV}OL(H_2O)_2]$–RNase A adduct L = tridentate ligand			
$[V^{IV}OL(H_2O)_2]$	References	PDB code	RMSD (Å)
$[V^{IV}O(dipic)(H_2O)_2]$	Paragraph 3.5	-	0.47
VC–HEWL adduct (V^V complexes)			
VC (V^V complexes)	References	PDB code	RMSD (Å)
VC1	Paragraph 4.2[282]	9GOG	0.42
VC2	Paragraph 4.2[282]	9GOK	0.35

VC3	Paragraph 4.3	9SA2	0.35
$Cs_2[V^V_2O_4(mal)_2]\cdot 2H_2O$	Structure A Paragraph 5.2[283]	9RBG	0.24
	Structure B Paragraph 5.2[283]	9RBT	0.27
	Structure at 37°C Paragraph 5.2[283]	9RBV	0.20
$Cs_2[V^V_2O_4(lact)_2]\cdot 2H_2O$	Structure A Paragraph 5.3	-	0.15
	Structure B Paragraph 5.3	-	0.19
	Structure C Paragraph 5.3	-	0.47
	Structure D Paragraph 5.3	-	0.38

References

1 W. Plass, Chiral and supramolecular model complexes for vanadium haloperoxidases: Host–guest systems and hydrogen bonding relays for vanadate species, *Coord. Chem. Rev.*, 2011, **255**, 2378–2387.

2 M. V. Kirillova, M. L. Kuznetsov, J. A. L. da Silva, M. F. C. Guedes da Silva, J. J. R. Fraústo da Silva and A. J. L. Pombeiro, Amavadin and Other Vanadium Complexes as Remarkably Efficient Catalysts for One-Pot Conversion of Ethane to Propionic and Acetic Acids, *Chem. – Eur. J.*, 2008, **14**, 1828–1842.

3 T. Hirao, Selective synthetic methods using vanadium-mediated redox reactions, *Pure Appl. Chem.*, 2005, **77**, 1539–1557.

4 D. C. Crans, J. J. Smee, E. Gaidamauskas and L. Yang, The Chemistry and Biochemistry of Vanadium and the Biological Activities Exerted by Vanadium Compounds, *Chem. Rev.*, 2004, **104**, 849–902.

5 D. Rehder, The future of/for vanadium, *Dalton Trans.*, 2013, **42**, 11749.

6 D. Rehder, The role of vanadium in biology, *Metallomics*, 2015, **7**, 730–742.

7 D. Rehder, Implications of vanadium in technical applications and pharmaceutical issues, *Inorganica Chim. Acta*, 2017, **455**, 378–389.

8 R. R. Langeslay, D. M. Kaphan, C. L. Marshall, P. C. Stair, A. P. Sattelberger and M. Delferro, Catalytic Applications of Vanadium: A Mechanistic Perspective, *Chem. Rev.*, 2019, **119**, 2128–2191.

9 J. C. Pessoa, S. Etcheverry and D. Gambino, Vanadium compounds in medicine, *Coord. Chem. Rev.*, 2015, **301–302**, 24–48.

10 D. Rehder, Perspectives for Vanadium in Health Issues, *Future Med. Chem.*, 2016, **8**, 325–338.

11 D. Rehder, Vanadium in health issues, *ChemTexts*, 2018, **4**, 20.

12 S. Treviño, A. Díaz, E. Sánchez-Lara, B. L. Sanchez-Gaytan, J. M. Perez-Aguilar and E. González-Vergara, Vanadium in Biological Action: Chemical, Pharmacological Aspects, and Metabolic Implications in Diabetes Mellitus, *Biol. Trace Elem. Res.*, 2019, **188**, 68–98.

13 D. Rehder, The potentiality of vanadium in medicinal applications, *Inorganica Chim. Acta*, 2020, **504**, 119445.

14 A. Ścibior, Ł. Pietrzyk, Z. Plewa and A. Skiba, Vanadium: Risks and possible benefits in the light of a comprehensive overview of its pharmacotoxicological mechanisms and multi-applications with a summary of further research trends, *J. Trace Elem. Med. Biol.*, 2020, **61**, 126508.

15 A. A. Sharfalddin, I. M. Al-Younis, H. A. Mohammed, M. Dhahri, F. Mouffouk, H. Abu Ali, Md. J. Anwar, K. A. Qureshi, M. A. Hussien, M. Alghrably, M. Jaremko, N. Alasmael, J. I.

Lachowicz and A.-H. Emwas, Therapeutic Properties of Vanadium Complexes, *Inorganics*, 2022, **10**, 244.

16 S. Semiz, Vanadium as potential therapeutic agent for COVID-19: A focus on its antiviral, antiinflamatory, and antihyperglycemic effects, *J. Trace Elem. Med. Biol.*, 2022, **69**, 126887.

17 A. P. Singh, S. Roy and I. C. Maurya, Vanadium complexes: potential candidates for therapeutic applications, *Transit. Met. Chem.*, 2024, **49**, 101–119.

18 H. Sakurai, Y. Kojima, Y. Yoshikawa, K. Kawabe and H. Yasui, Antidiabetic vanadium(IV) and zinc(II) complexes, *Coord. Chem. Rev.*, 2002, **226**, 187–198.

19 K. H. Thompson and C. Orvig, Vanadium in diabetes: 100 years from Phase 0 to Phase I, *J. Inorg. Biochem.*, 2006, **100**, 1925–1935.

20 K. H. Thompson, J. Lichter, C. LeBel, M. C. Scaife, J. H. McNeill and C. Orvig, Vanadium treatment of type 2 diabetes: A view to the future, *J. Inorg. Biochem.*, 2009, **103**, 554–558.

21 S. Treviño and A. Diaz, Vanadium and insulin: Partners in metabolic regulation, *J. Inorg. Biochem.*, 2020, **208**, 111094.

22 L. M. P. F. Amaral, T. Moniz, A. M. N. Silva and M. Rangel, Vanadium Compounds with Antidiabetic Potential, *Int. J. Mol. Sci.*, 2023, **24**, 15675.

23 V. Nischwitz, J. T. Davies, D. Marshall, M. González, J. L. Gómez Ariza and H. Goenaga-Infante, Speciation studies of vanadium in human liver (HepG2) cells after in vitro exposure to bis(maltolato)oxovanadium(iv) using HPLC online with elemental and molecular mass spectrometry, *Metallomics*, 2013, **5**, 1685.

24 K. H. Thompson and C. Orvig, Boon and Bane of Metal Ions in Medicine, *Science*, 2003, **300**, 936–939.

25 J. Szklarzewicz, A. Jurowska, M. Hodorowicz, G. Kazek, M. Głuch-Lutwin and J. Sapa, Ligand role on insulin-mimetic properties of vanadium complexes. Structural and biological studies, *Inorganica Chim. Acta*, 2021, **516**, 120135.

26 Md. N. Islam, A. A. Kumbhar, A. S. Kumbhar, M. Zeller, R. J. Butcher, M. B. Dusane and B. N. Joshi, Bis(maltolato)vanadium(III)-Polypyridyl Complexes: Synthesis, Characterization, DNA Cleavage, and Insulin Mimetic Activity, *Inorg. Chem.*, 2010, **49**, 8237–8246.

27 V. Badmaev, S. Prakash and M. Majeed, Vanadium: A Review of its Potential Role in the Fight Against Diabetes, *J. Altern. Complement. Med.*, 1999, **5**, 273–291.

28 X.-Q. Cong, M.-H. Piao, Y. Li, L. Xie and Y. Liu, Bis(maltolato)oxovanadium(IV) (BMOV) Attenuates Apoptosis in High Glucose-Treated Cardiac Cells and Diabetic Rat Hearts by Regulating the Unfolded Protein Responses (UPRs), *Biol. Trace Elem. Res.*, 2016, **173**, 390–398.

29 C. Orvig, P. Caravan, L. Gelmini, N. Glover, F. G. Herring, H. Li, J. H. McNeill, S. J. Rettig and I. A. Setyawati, Reaction chemistry of BMOV, bis(maltolato)oxovanadium(IV), a potent insulin mimetic agent, *J. Am. Chem. Soc.*, 1995, **117**, 12759–12770.

30 C. M. Krejsa, S. G. Nadler, J. M. Esselstyn, T. J. Kavanagh, J. A. Ledbetter and G. L. Schieven, Role of Oxidative Stress in the Action of Vanadium Phosphotyrosine Phosphatase Inhibitors, *J. Biol. Chem.*, 1997, **272**, 11541–11549.

31 D. I. Shah and M. Singh, Inhibition of protein tyrosin phosphatase improves vascular endothelial dysfunction, *Vascul. Pharmacol.*, 2006, **44**, 177–182.

32 D. Sanna and E. Garribba, Pharmacologically Active Vanadium Species: Distribution in Biological Media and Interaction with Molecular Targets, *Curr. Med. Chem.*, 2021, **28**, 7339–7384.

33 V. Ugone, D. Sanna, G. Sciortino, D. C. Crans and E. Garribba, ESI-MS Study of the Interaction of Potential Oxidovanadium(IV) Drugs and Amavadin with Model Proteins, *Inorg. Chem.*, 2020, **59**, 9739–9755.

34 M. F. A. Santos, G. Sciortino, I. Correia, A. C. P. Fernandes, T. Santos-Silva, F. Pisanu, E. Garribba and J. Costa Pessoa, Binding of $V^{IV}O^{2+}$, $V^{IV}OL$, $V^{IV}OL_2$ and $V^{V}O_2L$ Moieties to Proteins: X-ray/Theoretical Characterization and Biological Implications, *Chem. – Eur. J.*, DOI:10.1002/chem.202200105.

35 G. Ferraro, M. Paolillo, G. Sciortino, E. Garribba and A. Merlino, Multiple and Variable Binding of Pharmacologically Active Bis(maltolato)oxidovanadium(IV) to Lysozyme, *Inorg. Chem.*, 2022, **61**, 16458–16467.

36 V. G. Yuen, C. Orvig and J. H. McNeill, Glucose-lowering effects of a new organic vanadium complex, bis(maltolato)oxovanadium(IV), *Can. J. Physiol. Pharmacol.*, 1993, **71**, 263–269.

37 J. Costa Pessoa and I. Tomaz, Transport of Therapeutic Vanadium and Ruthenium Complexes by Blood Plasma Components, *Curr. Med. Chem.*, 2010, **17**, 3701–3738.

38 K. D. Mjos and C. Orvig, Metallodrugs in Medicinal Inorganic Chemistry, *Chem. Rev.*, 2014, **114**, 4540–4563.

39 B. V. Rotterdam, .

40 Y.-B. Wei and X.-D. Yang, Synthesis, characterization and anti-diabetic therapeutic potential of a new benzyl acid-derivatized kojic acid vanadyl complex, *BioMetals*, 2012, **25**, 1261–1268.

41 R. C. Hider and A. V. Hoffbrand, The Role of Deferiprone in Iron Chelation, *N. Engl. J. Med.*, 2018, **379**, 2140–2150.

42 M. Rangel, A. Tamura, C. Fukushima and H. Sakurai, *In vitro* study of the insulin-like action of vanadyl-pyrone and -pyridinone complexes with a VO(O4) coordination mode, *JBIC J. Biol. Inorg. Chem.*, 2001, **6**, 128–132.

43 H. Sakurai, H. Yasui and Y. Adachi, The therapeutic potential of insulin-mimetic vanadium complexes, *Expert Opin. Investig. Drugs*, 2003, **12**, 1189–1203.

44 C. Rozzo, D. Sanna, E. Garribba, M. Serra, A. Cantara, G. Palmieri and M. Pisano, Antitumoral effect of vanadium compounds in malignant melanoma cell lines, *J. Inorg. Biochem.*, 2017, **174**, 14–24.

45 J.-C. Liu, Y. Yu, G. Wang, K. Wang and X.-G. Yang, Bis(acetylacetonato)-oxovanadium(iv), bis(maltolato)-oxovanadium(iv) and sodium metavanadate induce antilipolytic effects by regulating hormone-sensitive lipase and perilipin via activation of Akt, *Metallomics*, 2013, **5**, 813.

46 I. Correia, P. Adão, S. Roy, M. Wahba, C. Matos, M. R. Maurya, F. Marques, F. R. Pavan, C. Q. F. Leite, F. Avecilla and J. Costa Pessoa, Hydroxyquinoline derived vanadium(IV and V) and copper(II) complexes as potential anti-tuberculosis and anti-tumor agents, *J. Inorg. Biochem.*, 2014, **141**, 83–93.

47 G. Scalese, I. Machado, C. Fontana, G. Risi, G. Salinas, L. Pérez-Díaz and D. Gambino, New heteroleptic oxidovanadium(V) complexes: synthesis, characterization and biological evaluation as potential agents against Trypanosoma cruzi, *JBIC J. Biol. Inorg. Chem.*, 2018, **23**, 1265–1281.

48 G. Scalese, I. Machado, I. Correia, J. C. Pessoa, L. Bilbao, L. Pérez-Diaz and D. Gambino, Exploring oxidovanadium(IV) homoleptic complexes with 8-hydroxyquinoline derivatives as prospective antitrypanosomal agents, *New J. Chem.*, 2019, **43**, 17756–17773.

49 K. Choroba, L. R. Raposo, J. Palion-Gazda, E. Malicka, K. Erfurt, B. Machura and A. R. Fernandes, *In vitro* antiproliferative effect of vanadium complexes bearing 8-hydroxyquinoline-based ligands – the substituent effect, *Dalton Trans.*, 2020, **49**, 6596–6606.

50 G. Ferraro, L. Vitale, G. Sciortino, F. Pisanu, E. Garribba and A. Merlino, Interaction of $V^{IV}O$–8-hydroxyquinoline species with RNase A: the effect of metal ligands in the protein adduct stabilization, *Inorg. Chem. Front.*, 2023, **10**, 5186–5198.

51 N. Ribeiro, I. Bulut, V. Pósa, B. Sergi, G. Sciortino, J. C. Pessoa, L. B. Maia, V. Ugone, E. Garribba, É. A. Enyedy, C. Acilan and I. Correia, Solution chemical properties and anticancer potential of 8-hydroxyquinoline hydrazones and their oxidovanadium(IV) complexes, *J. Inorg. Biochem.*, 2022, **235**, 111932.

52 G. Sciortino, V. Ugone, D. Sanna, G. Lubinu, S. Ruggiu, J.-D. Maréchal and E. Garribba, Biospeciation of Potential Vanadium Drugs of Acetylacetonate in the Presence of Proteins, *Front. Chem.*, 2020, **8**, 345.

53 M. W. Makinen and M. J. Brady, Structural Origins of the Insulin-mimetic Activity of Bis(acetylacetonato)oxovanadium(IV), *J. Biol. Chem.*, 2002, **277**, 12215–12220.

54 B. A. Reul, S. S. Amin, J. Buchet, L. N. Ongemba, D. C. Crans and S. M. Brichard, Effects of vanadium complexes with organic ligands on glucose metabolism: a comparison study in diabetic rats, *Br. J. Pharmacol.*, 1999, **126**, 467–477.

55 M. W. Makinen and M. Salehitazangi, The structural basis of action of vanadyl (VO^{2+}) chelates in cells, *Coord. Chem. Rev.*, 2014, **279**, 1–22.

56 Y. Fu, Q. Wang, X.-G. Yang, X.-D. Yang and K. Wang, Vanadyl bisacetylacetonate induced G1/S cell cycle arrest via high-intensity ERK phosphorylation in HepG2 cells, *JBIC J. Biol. Inorg. Chem.*, 2008, **13**, 1001–1009.

57 J.-X. Wu, Y.-H. Hong and X.-G. Yang, Bis(acetylacetonato)-oxidovanadium(IV) and sodium metavanadate inhibit cell proliferation via ROS-induced sustained MAPK/ERK activation but with elevated AKT activity in human pancreatic cancer AsPC-1 cells, *JBIC J. Biol. Inorg. Chem.*, 2016, **21**, 919–929.

58 R. Dinda, P. Sengupta, S. Ghosh and T. C. W. Mak, Valence Delocalization in a Mixed-Oxidation Divanadium (IV, V) Complex Electrogenerated from Its Structurally Characterized Divanadium (V) Analogue with a Tridentate (ONO) Ligand, *Inorg. Chem.*, 2002, **41**, 1684–1688.

59 C. Slebodnick, B. J. Hamstra and V. L. Pecoraro, in *Metal Sites in Proteins and Models*, eds H. A. O. Hill, P. J. Sadler and A. J. Thomson, Springer Berlin Heidelberg, Berlin, Heidelberg, 1997, vol. 89, pp. 51–108.

60 C. Djordjevic and G. L. Wampler, Antitumor activity and toxicity of peroxo heteroligand vanadates(V) in relation to biochemistry of vanadium, *J. Inorg. Biochem.*, 1985, **25**, 51–55.

61 D. Rehder, The coordination chemistry of vanadium as related to its biological functions, *Coord. Chem. Rev.*, 1999, **182**, 297–322.

62 H. Zhang, A. Zhang, J. Miao, H. Sun, G. Yan, F. Wu and X. Wang, Targeting regulation of tryptophan metabolism for colorectal cancer therapy: a systematic review, *RSC Adv.*, 2019, **9**, 3072–3080.

63 L. Kubicova, F. Hadacek, G. Bachmann, W. Weckwerth and V. Chobot, Coordination Complex Formation and Redox Properties of Kynurenic and Xanthurenic Acid Can Affect Brain Tissue Homeodynamics, *Antioxidants*, 2019, **8**, 476.

64 E. Wirthgen, A. Hoeflich, A. Rebl and J. Günther, Kynurenic Acid: The Janus-Faced Role of an Immunomodulatory Tryptophan Metabolite and Its Link to Pathological Conditions, *Front. Immunol.*, 2018, **8**, 1957.

65 E. Langner, K. Walczak, W. Jeleniewicz, W. A. Turski and G. Rajtar, Quinaldic acid inhibits proliferation of colon cancer HT-29 cells in vitro: Effects on signaling pathways, *Eur. J. Pharmacol.*, 2015, **757**, 21–27.

66 C.-H. Lee, Growth Inhibiting Activity of Quinaldic Acid Isolated from Ephedra pachyclada against Intestinal Bacteria, *J. Korean Soc. Appl. Biol. Chem.*, 2009, **52**, 331–335.

67 G. C. Capodagli, W. G. Sedhom, M. Jackson, K. A. Ahrendt and S. D. Pegan, A Noncompetitive Inhibitor for *Mycobacterium tuberculosis* 's Class IIa Fructose 1,6-Bisphosphate Aldolase, *Biochemistry*, 2014, **53**, 202–213.

68 K. Walczak, E. Langner, K. Szalast, A. Makuch-Kocka, P. Pożarowski and T. Plech, A Tryptophan Metabolite, 8-Hydroxyquinaldic Acid, Exerts Antiproliferative and Anti-Migratory Effects on Colorectal Cancer Cells, *Molecules*, 2020, **25**, 1655.

69 E. G. Ferrer, M. V. Salinas, M. J. Correa, L. Naso, D. A. Barrio, S. B. Etcheverry, L. Lezama, T. Rojo and P. A. M. Williams, Synthesis, characterization, antitumoral and osteogenic activities of quercetin vanadyl(IV) complexes, *JBIC J. Biol. Inorg. Chem.*, 2006, **11**, 791–801.

70 A. L. Di Virgilio, I. E. León, C. A. Franca, I. Henao, G. Tobón and S. B. Etcheverry, $Cu(Nor)_2 \cdot 5H_2O$, a complex of Cu(II) with Norfloxacin: theoretic approach and biological studies. Cytotoxicity and genotoxicity in cell cultures, *Mol. Cell. Biochem.*, 2013, **376**, 53–61.

71 L. G. Naso, L. Lezama, T. Rojo, S. B. Etcheverry, M. Valcarcel, M. Roura, C. Salado, E. G. Ferrer and P. A. M. Williams, Biological evaluation of morin and its new oxovanadium(IV) complex as antio-xidant and specific anti-cancer agents, *Chem. Biol. Interact.*, 2013, **206**, 289–301.

72 I. E. Leon, V. Porro, A. L. Di Virgilio, L. G. Naso, P. A. M. Williams, M. Bollati-Fogolín and S. B. Etcheverry, Antiproliferative and apoptosis-inducing activity of an oxidovanadium(IV) complex with the flavonoid silibinin against osteosarcoma cells, *JBIC J. Biol. Inorg. Chem.*, 2014, **19**, 59–74.

73 I. E. León, P. Díez, E. J. Baran, S. B. Etcheverry and M. Fuentes, Decoding the anticancer activity of VO-clioquinol compound: the mechanism of action and cell death pathways in human osteosarcoma cells, *Metallomics*, 2017, **9**, 891–901.

74 D. Biswal, N. R. Pramanik, S. Chakrabarti, M. G. B. Drew, K. Acharya and S. Chandra, Syntheses, crystal structures, DFT calculations, protein interaction and anticancer activities of water soluble dipicolinic acid-imidazole based oxidovanadium(IV) complexes, *Dalton Trans.*, 2017, **46**, 16682–16702.

75 D. C. Crans, Chemistry and insulin-like properties of vanadium(IV) and vanadium(V) compounds1This manuscript summarizes the presentation given at the symposium 'Biological Aspects of Vanadium Chemistry — Chemistry, Biochemistry and Therapeutic Applications of Vanadium Compounds' and recently communicated in original research articles. The original

research articles describing the experimental details of this work are given in Refs: [1–5].1, *J. Inorg. Biochem.*, 2000, **80**, 123–131.

76 K. Choroba, B. Filipe, A. Świtlicka, M. Penkala, B. Machura, A. Bieńko, S. Cordeiro, P. V. Baptista and A. R. Fernandes, *In Vitro* and *In Vivo* Biological Activities of Dipicolinate Oxovanadium(IV) Complexes, *J. Med. Chem.*, 2023, **66**, 8580–8599.

77 D. Biswal, N. R. Pramanik, M. G. B. Drew, N. Jangra, M. R. Maurya, M. Kundu, P. C. Sil and S. Chakrabarti, Synthesis, crystal structure, DFT calculations, protein interaction, anticancer potential and bromoperoxidase mimicking activity of oxidoalkoxidovanadium(V) complexes, *New J. Chem.*, 2019, **43**, 17783–17800.

78 A. Banerjee, S. A. Patra, G. Sahu, G. Sciortino, F. Pisanu, E. Garribba, M. F. N. N. Carvalho, I. Correia, J. C. Pessoa, H. Reuter and R. Dinda, A Series of Non-Oxido V^{IV} Complexes of Dibasic ONS Donor Ligands: Solution Stability, Chemical Transformations, Protein Interactions, and Antiproliferative Activity, *Inorg. Chem.*, 2023, **62**, 7932–7953.

79 S. Kundu, D. Mondal, K. Bhattacharya, A. Endo, D. Sanna, E. Garribba and M. Chaudhury, Nonoxido Vanadium(IV) Compounds Involving Dithiocarbazate-Based Tridentate ONS Ligands: Synthesis, Electronic and Molecular Structure, Spectroscopic and Redox Properties, *Inorg. Chem.*, 2015, **54**, 6203–6215.

80 T. K. Paine, T. Weyhermüller, L. D. Slep, F. Neese, E. Bill, E. Bothe, K. Wieghardt and P. Chaudhuri, Nonoxovanadium(IV) and Oxovanadium(V) Complexes with Mixed O, X, O-Donor Ligands (X = S, Se, P, or PO), *Inorg. Chem.*, 2004, **43**, 7324–7338.

81 H. Michibata, Ed., *Vanadium: Biochemical and Molecular Biological Approaches*, Springer Netherlands, Dordrecht, 2012.

82 Y. Yoshikawa, H. Sakurai, D. C. Crans, G. Micera and E. Garribba, Structural and redox requirements for the action of anti-diabetic vanadium compounds, *Dalton Trans*, 2014, **43**, 6965–6972.

83 A. S. Tracey and M. J. Gresser, Interaction of vanadate with phenol and tyrosine: implications for the effects of vanadate on systems regulated by tyrosine phosphorylation., *Proc. Natl. Acad. Sci.*, 1986, **83**, 609–613.

84 D. Sanna, V. Ugone, G. Micera, T. Pivetta, E. Valletta and E. Garribba, Speciation of the Potential Antitumor Agent Vanadocene Dichloride in the Blood Plasma and Model Systems, *Inorg. Chem.*, 2015, **54**, 8237–8250.

85 P. Köpf-Maier and D. Krahl, Tumor inhibition by metallocenes: Ultrastructural localization of titanium and vanadium in treated tumor cells by electron energy loss spectroscopy, *Chem. Biol. Interact.*, 1983, **44**, 317–328.

86 P. Ghosh, O. J. D'Cruz, R. K. Narla and F. M. Uckun, Apoptosis-inducing vanadocene compounds against human testicular cancer, *Clin. Cancer Res. Off. J. Am. Assoc. Cancer Res.*, 2000, **6**, 1536–1545.

87 B. Gleeson, J. Claffey, M. Hogan, H. Müller-Bunz, D. Wallis and M. Tacke, Novel benzyl-substituted vanadocene anticancer drugs, *J. Organomet. Chem.*, 2009, **694**, 1369–1374.

88 B. Gleeson, A. Deally, H. Müller-Bunz, S. Patil and M. Tacke, Novel Achiral Aryl-Substituted Vanadocenes: Synthesisand Preliminary Cytotoxicity Studies, *Aust. J. Chem.*, 2010, **63**, 1514.

89 J. Honzíček, I. Klepalová, J. Vinklárek, Z. Padělková, I. Císařová, P. Šiman and M. Řezáčová, Synthesis, characterization and cytotoxic effect of ring-substituted and ansa-bridged vanadocene complexes, *Inorganica Chim. Acta*, 2011, **373**, 1–7.

90 D. C. Crans, J. T. Koehn, S. M. Petry, C. M. Glover, A. Wijetunga, R. Kaur, A. Levina and P. A. Lay, Hydrophobicity may enhance membrane affinity and anti-cancer effects of Schiff base vanadium(V) catecholate complexes, *Dalton Trans.*, 2019, **48**, 6383–6395.

91 H. A. Murakami, C. Uslan, A. A. Haase, J. T. Koehn, A. P. Vieira, D. J. Gaebler, J. Hagan, C. N. Beuning, N. Proschogo, A. Levina, P. A. Lay and D. C. Crans, Vanadium Chloro-Substituted Schiff Base Catecholate Complexes are Reducible, Lipophilic, Water Stable, and Have Anticancer Activities, *Inorg. Chem.*, 2022, **61**, 20757–20773.

92 E. Griffin, A. Levina and P. A. Lay, Vanadium(V) tris-3,5-di-tert-butylcatecholato complex: Links between speciation and anti-proliferative activity in human pancreatic cancer cells, *J. Inorg. Biochem.*, 2019, **201**, 110815.

93 A. Levina, A. Pires Vieira, A. Wijetunga, R. Kaur, J. T. Koehn, D. C. Crans and P. A. Lay, A Short-Lived but Highly Cytotoxic Vanadium(V) Complex as a Potential Drug Lead for Brain Cancer Treatment by Intratumoral Injections, *Angew. Chem. Int. Ed.*, 2020, **59**, 15834–15838.

94 K. Kostenkova, A. Levina, D. A. Walters, H. A. Murakami, P. A. Lay and D. C. Crans, Vanadium(V) Pyridine-Containing Schiff Base Catecholate Complexes are Lipophilic, Redox-Active and Selectively Cytotoxic in Glioblastoma (T98G) Cells, *Chem. – Eur. J.*, 2023, **29**, e202302271.

95 G. Sahu, A. Banerjee, R. Samanta, M. Mohanty, S. Lima, E. R. T. Tiekink and R. Dinda, Water-Soluble Dioxidovanadium(V) Complexes of Aroylhydrazones: DNA/BSA Interactions, Hydrophobicity, and Cell-Selective Anticancer Potential, *Inorg. Chem.*, 2021, **60**, 15291–15309.

96 J. Benítez, L. Becco, I. Correia, S. M. Leal, H. Guiset, J. C. Pessoa, J. Lorenzo, S. Tanco, P. Escobar, V. Moreno, B. Garat and D. Gambino, Vanadium polypyridyl compounds as potential antiparasitic and antitumoral agents: New achievements, *J. Inorg. Biochem.*, 2011, **105**, 303–312.

97 V. Gomathi Sankareswari, D. Vinod, A. Mahalakshmi, M. Alamelu, G. Kumaresan, R. Ramaraj and S. Rajagopal, Interaction of oxovanadium(IV)–salphen complexes with bovine serum albumin and their cytotoxicity against cancer, *Dalton Trans*, 2014, **43**, 3260–3272.

98 D. Sanna, V. Ugone, G. Lubinu, G. Micera and E. Garribba, Behavior of the potential antitumor $V^{IV}O$ complexes formed by flavonoid ligands. 1. Coordination modes and geometry in solution and at the physiological pH, *J. Inorg. Biochem.*, 2014, **140**, 173–184.

99 L. Reytman, O. Braitbard, J. Hochman and E. Y. Tshuva, Highly Effective and Hydrolytically Stable Vanadium(V) Amino Phenolato Antitumor Agents, *Inorg. Chem.*, 2016, **55**, 610–618.

100 D. Patra, S. Paul, I. Majumder, N. Sepay, S. Bera, R. Kundu, M. G. B. Drew and T. Ghosh, Exploring the effect of substituent in the hydrazone ligand of a family of μ-oxidodivanadium(V) hydrazone complexes on structure, DNA binding and anticancer activity, *Dalton Trans.*, 2017, **46**, 16276–16293.

101 L. Ni, H. Zhao, L. Tao, X. Li, Z. Zhou, Y. Sun, C. Chen, D. Wei, Y. Liu and G. Diao, Synthesis, *in vitro* cytotoxicity, and structure–activity relationships (SAR) of multidentate oxidovanadium(IV) complexes as anticancer agents, *Dalton Trans.*, 2018, **47**, 10035–10045.

102 A. Sinha, K. Banerjee, A. Banerjee, S. Das and S. K. Choudhuri, Synthesis, characterization and biological evaluation of a novel vanadium complex as a possible anticancer agent, *J. Organomet. Chem.*, 2014, **772–773**, 34–41.

103 D. C. Crans, Fifteen years of dancing with vanadium, *Pure Appl. Chem.*, 2005, **77**, 1497–1527.

104 D. C. Crans, K. A. Woll, K. Prusinskas, M. D. Johnson and E. Norkus, Metal Speciation in Health and Medicine Represented by Iron and Vanadium, *Inorg. Chem.*, 2013, **52**, 12262–12275.

105 M. A. Malik, O. A. Dar, P. Gull, M. Y. Wani and A. A. Hashmi, Heterocyclic Schiff base transition metal complexes in antimicrobial and anticancer chemotherapy, *MedChemComm*, 2018, **9**, 409–436.

106 P. Krishnamoorthy, P. Sathyadevi, R. R. Butorac, A. H. Cowley, N. S. P. Bhuvanesh and N. Dharmaraj, Copper(I) and nickel(II) complexes with 1 : 1 vs. 1 : 2 coordination of ferrocenyl hydrazone ligands: Do the geometry and composition of complexes affect DNA binding/cleavage, protein binding, antioxidant and cytotoxic activities?, *Dalton Trans.*, 2012, **41**, 4423.

107 P. Krishnamoorthy, P. Sathyadevi, R. R. Butorac, A. H. Cowley, N. S. P. Bhuvanesh and N. Dharmaraj, Variation in the biomolecular interactions of nickel(ii) hydrazone complexes upon tuning the hydrazide fragment, *Dalton Trans.*, 2012, **41**, 6842.

108 A. K. Renfrew, Transition metal complexes with bioactive ligands: mechanisms for selective ligand release and applications for drug delivery, *Metallomics*, 2014, **6**, 1324–1335.

109 L. H. Beatriz, A. Ángel, E.-B. Ana and H. Sonsoles, Metal-Based Compounds as Promising Anticancer Agents: An Overview on the Recent Literature, *Anti-Cancer Agents Med. Chem.*, **19**, 48–66.

110 F. Zechel, P. Schwendt, R. Gyepes, J. Šimunek, J. Tatiersky and L. Krivosudský, Vanadium(V) complexes of mandelic acid, *New J. Chem.*, 2019, **43**, 17696–17702.

111 E. Bermejo, R. Carballo, A. Castiñeiras and A. B. Lago, Coordination of α-hydroxycarboxylic acids with first-row transition ions, *Coord. Chem. Rev.*, 2013, **257**, 2639–2651.

112 P. Schwendt, J. Tatiersky, L. Krivosudský and M. Šimuneková, Peroxido complexes of vanadium, *Coord. Chem. Rev.*, 2016, **318**, 135–157.

113 A. S. Tracey, M. J. Gresser and K. M. Parkinson, Vanadium(V) Oxyanions. Interactions of Vanadate with Oxalate, Lactate, and Glycerate, *Inorg. Chem.*, 1987, **26**, 629–638.

114 S. Hati, R. J. Batchelor, F. W. B. Einstein and A. S. Tracey, Vanadium(V) Complexes of α-Hydroxycarboxylic Acids in Aqueous Solution, *Inorg. Chem.*, 2001, **40**, 6258–6265.

115 M. Tsaramyrsi, D. Kavousanaki, C. P. Raptopoulou, A. Terzis and A. Salifoglou, Systematic synthesis, structural characterization, and reactivity studies of vanadium(V)–citrate anions $[VO_2(C_6H_6O_7)]_2^{2-}$, isolated from aqueous solutions in the presence of different cations, *Inorganica Chim. Acta*, 2001, **320**, 47–59.

116 A. Kövilein, C. Kubisch, L. Cai and K. Ochsenreither, Malic acid production from renewables: a review, *J. Chem. Technol. Biotechnol.*, 2020, **95**, 513–526.

117 M. Biagioli, L. Strinna-Erre, G. Micera, A. Panzanelli and M. Zema, Molecular structure, characterization and reactivity of dioxo complexes formed by vanadium(V) with α-hydroxycarboxylate ligands, *Inorganica Chim. Acta*, 2000, **310**, 1–9.

118 A. Gorzsás, I. Andersson and L. Pettersson, Speciation in the aqueous $H^+/H_2VO_4^-/H_2O_2/$L -(+)-lactate system, *Dalton Trans*, 2003, 2503–2511.

119 S.-M. Wang, J. Hwang and E. Kim, Polyoxometalates as promising materials for electrochromic devices, *J. Mater. Chem. C*, 2019, **7**, 7828–7850.

120 S.-S. Wang and G.-Y. Yang, Recent Advances in Polyoxometalate-Catalyzed Reactions, *Chem. Rev.*, 2015, **115**, 4893–4962.

121 S. Y. Lai, K. H. Ng, C. K. Cheng, H. Nur, M. Nurhadi and M. Arumugam, Photocatalytic remediation of organic waste over Keggin-based polyoxometalate materials: A review, *Chemosphere*, 2021, **263**, 128244.

122 Y.-F. Song and R. Tsunashima, Recent advances on polyoxometalate-based molecular and composite materials, *Chem. Soc. Rev.*, 2012, **41**, 7384.

123 M. Aureliano, N. I. Gumerova, G. Sciortino, E. Garribba, C. C. McLauchlan, A. Rompel and D. C. Crans, Polyoxidovanadates' interactions with proteins: An overview, *Coord. Chem. Rev.*, 2022, **454**, 214344.

124 D. C. Crans, Enzyme Interactions with Labile Oxovanadates and Other Polyoxometalates, *Comments Inorg. Chem.*, 1994, **16**, 35–76.

125 Y. Hayashi, Hetero and lacunary polyoxovanadate chemistry: Synthesis, reactivity and structural aspects, *Coord. Chem. Rev.*, 2011, **255**, 2270–2280.

126 A. Bijelic, M. Aureliano and A. Rompel, Polyoxometalates as Potential Next-Generation Metallodrugs in the Combat Against Cancer, *Angew. Chem. Int. Ed.*, 2019, **58**, 2980–2999.

127 A. Bijelic, M. Aureliano and A. Rompel, The antibacterial activity of polyoxometalates: structures, antibiotic effects and future perspectives, *Chem. Commun.*, 2018, **54**, 1153–1169.

128 A. Bijelic and A. Rompel, The use of polyoxometalates in protein crystallography – An attempt to widen a well-known bottleneck, *Coord. Chem. Rev.*, 2015, **299**, 22–38.

129 J. M. Missina, L. B. P. Leme, K. Postal, F. S. Santana, D. L. Hughes, E. L. De Sá, R. R. Ribeiro and G. G. Nunes, Accessing decavanadate chemistry with tris(hydroxymethyl)aminomethane, and evaluation of methylene blue bleaching, *Polyhedron*, 2020, **180**, 114414.

130 A. Bijelic and A. Rompel, Polyoxometalates: more than a phasing tool in protein crystallography, *ChemTexts*, DOI:10.1007/s40828-018-0064-1.

131 M. B. Čolović, M. Lacković, J. Lalatović, A. S. Mougharbel, U. Kortz and D. Z. Krstić, Polyoxometalates in Biomedicine: Update and Overview, *Curr. Med. Chem.*, 2020, **27**, 362–379.

132 J. T. Rhule, C. L. Hill, D. A. Judd and R. F. Schinazi, Polyoxometalates in Medicine, *Chem. Rev.*, 1998, **98**, 327–358.

133 M. Aureliano, N. I. Gumerova, G. Sciortino, E. Garribba, A. Rompel and D. C. Crans, Polyoxovanadates with emerging biomedical activities, *Coord. Chem. Rev.*, 2021, **447**, 214143.

134 H. Stephan, M. Kubeil, F. Emmerling and C. E. Müller, Polyoxometalates as Versatile Enzyme Inhibitors, *Eur. J. Inorg. Chem.*, 2013, **2013**, 1585–1594.

135 T. L. Turner, V. H. Nguyen, C. C. McLauchlan, Z. Dymon, B. M. Dorsey, J. D. Hooker and M. A. Jones, Inhibitory effects of decavanadate on several enzymes and Leishmania tarentolae In Vitro, *J. Inorg. Biochem.*, 2012, **108**, 96–104.

136 S.-Y. Lee, A. Fiene, W. Li, T. Hanck, K. A. Brylev, V. E. Fedorov, J. Lecka, A. Haider, H.-J. Pietzsch, H. Zimmermann, J. Sévigny, U. Kortz, H. Stephan and C. E. Müller, Polyoxometalates—Potent and selective ecto-nucleotidase inhibitors, *Biochem. Pharmacol.*, 2015, **93**, 171–181.

137 H. S. Shah, R. Al-Oweini, A. Haider, U. Kortz and J. Iqbal, Cytotoxicity and enzyme inhibition studies of polyoxometalates and their chitosan nanoassemblies, *Toxicol. Rep.*, 2014, **1**, 341–352.

138 Ş. Bâlici, S. Şuşman, D. Rusu, G. Z. Nicula, O. Soriţău, M. Rusu, A. S. Biris and H. Matei, Differentiation of stem cells into insulin-producing cells under the influence of nanostructural polyoxometalates, *J. Appl. Toxicol.*, 2016, **36**, 373–384.

139 M. J. Pereira, E. Carvalho, J. W. Eriksson, D. C. Crans and M. Aureliano, Effects of decavanadate and insulin enhancing vanadium compounds on glucose uptake in isolated rat adipocytes, *J. Inorg. Biochem.*, 2009, **103**, 1687–1692.

140 S. García-Vicente, F. Yraola, L. Marti, E. González-Muñoz, M. J. García-Barrado, C. Cantó, A. Abella, S. Bour, R. Artuch, C. Sierra, N. Brandi, C. Carpéné, J. Moratinos, M. Camps, M. Palacín, X. Testar, A. Gumà, F. Albericio, M. Royo, A. Mian and A. Zorzano, Oral Insulin-Mimetic Compounds That Act Independently of Insulin, *Diabetes*, 2007, **56**, 486–493.

141 J. Zhao, K. Li, K. Wan, T. Sun, N. Zheng, F. Zhu, J. Ma, J. Jiao, T. Li, J. Ni, X. Shi, H. Wang, Q. Peng, J. Ai, W. Xu and S. Liu, Organoplatinum-Substituted Polyoxometalate Inhibits β-amyloid Aggregation for Alzheimer's Therapy, *Angew. Chem. Int. Ed.*, 2019, **58**, 18032–18039.

142 J. Iqbal, M. Barsukova-Stuckart, M. Ibrahim, S. U. Ali, A. A. Khan and U. Kortz, Polyoxometalates as potent inhibitors for acetyl and butyrylcholinesterases and as potential drugs for the treatment of Alzheimer's disease, *Med. Chem. Res.*, 2013, **22**, 1224–1228.

143 E. E. Hamilton, P. E. Fanwick and J. J. Wilker, The Elusive Vanadate $(V_3O_9)^{3-}$: Isolation, Crystal Structure, and Nonaqueous Solution Behavior, *J. Am. Chem. Soc.*, 2002, **124**, 78–82.

144 N. I. Gumerova and A. Rompel, Polyoxometalates in solution: speciation under spotlight, *Chem. Soc. Rev.*, 2020, **49**, 7568–7601.

145 J. Fuchs, S. Mahjour and J. Pickardt, Structure of the "True" Metavanadate Ion, *Angew. Chem. Int. Ed. Engl.*, 1976, **15**, 374–375.

146 V. W. Day, W. G. Klemperer and O. M. Yaghi, A new structure type in polyoxoanion chemistry: synthesis and structure of the $V_5O_{14}^{3-}$ anion, *J. Am. Chem. Soc.*, 1989, **111**, 4518–4519.

147 P. Y. Zavalij, T. Chirayil, M. S. Whittingham, V. K. Pecharsky and R. A. Jacobson, A New Decavanadate with Mixed Cations, $[Li(H_2O)_4]_2[N(CH_3)_4]_4[V_{10}O_{28}].4H_2O$, *Acta Crystallogr. C*, 1997, **53**, 170–171.

148 V. W. Day, W. G. Klemperer and O. M. Yaghi, Synthesis and characterization of a soluble oxide inclusion complex, $[CH_3CN\subset(V_{12}O_{32}^{4-})]$, *J. Am. Chem. Soc.*, 1989, **111**, 5959–5961.

149 D. Hou, K. S. Hagen and C. L. Hill, Tridecavanadate, $[V_{13}O_{34}]^{3-}$, a new high-potential isopolyvanadate, *J. Am. Chem. Soc.*, 1992, **114**, 5864–5866.

150 D. Hou, K. S. Hagen and C. L. Hill, Pentadecavanadate, $V_{15}O_{42}^{9-}$, a new highly condensed fully oxidized isopolyvanadate with kinetic stability in water, *J Chem Soc Chem Commun*, 1993, **0**, 426–428.

151 L. Pettersson, Equilibria of polyoxometalates in aqueous solution, *Mol. Eng.*, 1993, **3**, 29–42.

152 In *Advances in Chemistry*, American Chemical Society, Washington, DC, 1996, pp. 303–328.

153 A. S. Tracey, J. S. Jaswal and S. J. Angus-Dunne, Influences of pH and Ionic Strength on Aqueous Vanadate Equilibria, *Inorg. Chem.*, 1995, **34**, 5680–5685.

154 K. Elvingson, A. González Baró and L. Pettersson, Speciation in Vanadium Bioinorganic Systems. 2. An NMR, ESR, and Potentiometric Study of the Aqueous H^+−Vanadate−Maltol System, *Inorg. Chem.*, 1996, **35**, 3388–3393.

155 R. Crumb, Vanadium and its role in life Metal ions in biological systems volume 31, *Biochem. Educ.*, 1995, **23**, 180.

156 N. McCann, M. Wagner and H. Hasse, A thermodynamic model for vanadate in aqueous solution – equilibria and reaction enthalpies, *Dalton Trans*, 2013, **42**, 2622–2628.

157 E. Heath and O. W. Howarth, Vanadium-51 and oxygen-17 nuclear magnetic resonance study of vanadate(V) equilibria and kinetics, *J. Chem. Soc. Dalton Trans.*, 1981, 1105.

158 D. C. Crans, B. J. Peters, X. Wu and C. C. McLauchlan, Does anion-cation organization in Na^+-containing X-ray crystal structures relate to solution interactions in inhomogeneous nanoscale environments: Sodium-decavanadate in solid state materials, minerals, and microemulsions, *Coord. Chem. Rev.*, 2017, **344**, 115–130.

159 D. K. Walanda, R. C. Burns, G. A. Lawrance and E. I. Von Nagy-Felsobuki, New isopolyoxovanadate ions identified by electrospray mass spectrometry, *Inorg. Chem. Commun.*, 1999, **2**, 487–489.

160 D. K. Walanda, R. C. Burns, G. A. Lawrance and E. I. Von Nagy-Felsobuki, Unknown isopolyoxovanadate species detected by electrospray mass spectrometry, *Inorganica Chim. Acta*, 2000, **305**, 118–126.

161 D. C. Crans, C. D. Rithner and L. A. Theisen, Application of time-resolved vanadium-51 2D NMR for quantitation of kinetic exchange pathways between vanadate monomer, dimer, tetramer, and pentamer, *J. Am. Chem. Soc.*, 1990, **112**, 2901–2908.

162 I. Andersson, L. Pettersson, J. J. Hastings and O. W. Howarth, Oxygen and vanadium exchange processes in linear vanadate oligomers, *J. Chem. Soc. Dalton Trans.*, 1996, 3357.

163 M. Aureliano, C. A. Ohlin, M. O. Vieira, M. P. M. Marques, W. H. Casey and L. A. E. Batista De Carvalho, Characterization of decavanadate and decaniobate solutions by Raman spectroscopy, *Dalton Trans.*, 2016, **45**, 7391–7399.

164 O. W. Howarth and M. Jarrold, Protonation of the decavanadate(6–) ion: a vanadium-51 nuclear magnetic resonance study, *J Chem Soc Dalton Trans*, 1978, 503–506.

165 M. Aureliano and D. C. Crans, Decavanadate ($V_{10}O_{28}^{6-}$) and oxovanadates: Oxometalates with many biological activities, *J. Inorg. Biochem.*, 2009, **103**, 536–546.

166 A. Merlino, Recent advances in protein metalation: structural studies, *Chem. Commun.*, 2021, **57**, 1295–1307.

167 In *Encyclopedia of Inorganic and Bioinorganic Chemistry*, Wiley, 2nd edn., 2020, pp. 1–17.

168 G. Ferraro and A. Merlino, Investigation of metallodrug/protein interaction by X-ray crystallography and complementary biophysical techniques, *Inorg. Chem. Front.*, 2025, **12**, 3345–3366.

169 A. Rilak Simović, R. Masnikosa, I. Bratsos and E. Alessio, Chemistry and reactivity of ruthenium(II) complexes: DNA/protein binding mode and anticancer activity are related to the complex structure, *Coord. Chem. Rev.*, 2019, **398**, 113011.

170 H. Peng, H. Jin, H. Zhuo and H. Huang, Enhanced antitumor efficacy of cisplatin for treating ovarian cancer *in vitro* and *in vivo* via transferrin binding, *Oncotarget*, 2017, **8**, 45597–45611.

171 D. M. Monti, G. Ferraro and A. Merlino, Ferritin-based anticancer metallodrug delivery: Crystallographic, analytical and cytotoxicity studies, *Nanomedicine Nanotechnol. Biol. Med.*, 2019, **20**, 101997.

172 C. R. Park, H. Y. Kim, M. G. Song, Y.-S. Lee, H. Youn, J.-K. Chung, G. J. Cheon and K. W. Kang, Efficacy and Safety of Human Serum Albumin–Cisplatin Complex in U87MG Xenograft Mouse Models, *Int. J. Mol. Sci.*, 2020, **21**, 7932.

173 T. Matsuo, T. Miyake and S. Hirota, Recent developments on creation of artificial metalloenzymes, *Tetrahedron Lett.*, 2019, **60**, 151226.

174 B. Bertrand and A. Casini, A golden future in medicinal inorganic chemistry: the promise of anticancer gold organometallic compounds, *Dalton Trans*, 2014, **43**, 4209–4219.

175 F. Arnesano and G. Natile, 'Platinum on the road': Interactions of antitumoral cisplatin with proteins, *Pure Appl. Chem.*, 2008, **80**, 2715–2725.

176 O. Pinato, C. Musetti and C. Sissi, Pt-based drugs: the spotlight will be on proteins, *Metallomics*, 2014, **6**, 380–395.

177 J. C. Pessoa, M. F. A. Santos, I. Correia, D. Sanna, G. Sciortino and E. Garribba, Binding of vanadium ions and complexes to proteins and enzymes in aqueous solution, *Coord. Chem. Rev.*, 2021, **449**, 214192.

178 G. Sciortino, J. Rodríguez-Guerra Pedregal, A. Lledós, E. Garribba and J. Maréchal, Prediction of the interaction of metallic moieties with proteins: An update for protein-ligand docking techniques, *J. Comput. Chem.*, 2018, **39**, 42–51.

179 I. Russo Krauss, A. Merlino, A. Vergara and F. Sica, An Overview of Biological Macromolecule Crystallization, *Int. J. Mol. Sci.*, 2013, **14**, 11643–11691.

180 I. Russo Krauss, G. Ferraro, A. Pica, J. A. Márquez, J. R. Helliwell and A. Merlino, Principles and methods used to grow and optimize crystals of protein–metallodrug adducts, to determine metal binding sites and to assign metal ligands, *Metallomics*, 2017, **9**, 1534–1547.

181 C. G. Hartinger, M. Groessl, S. M. Meier, A. Casini and P. J. Dyson, Application of mass spectrometric techniques to delineate the modes-of-action of anticancer metallodrugs, *Chem. Soc. Rev.*, 2013, **42**, 6186.

182 S. Theiner, A. Schoeberl, A. Schweikert, B. K. Keppler and G. Koellensperger, Mass spectrometry techniques for imaging and detection of metallodrugs, *Curr. Opin. Chem. Biol.*, 2021, **61**, 123–134.

183 M. Wenzel and A. Casini, Mass spectrometry as a powerful tool to study therapeutic metallodrugs speciation mechanisms: Current frontiers and perspectives, *Coord. Chem. Rev.*, 2017, **352**, 432–460.

184 L. Messori and A. Merlino, Protein metalation by metal-based drugs: X-ray crystallography and mass spectrometry studies, *Chem Commun*, 2017, **53**, 11622–11633.

185 A. Merlino, Metallodrug binding to serum albumin: Lessons from biophysical and structural studies, *Coord. Chem. Rev.*, 2023, **480**, 215026.

186 D. Loreto, G. Ferraro and A. Merlino, Protein-metallodrugs interactions: Effects on the overall protein structure and characterization of Au, Ru and Pt binding sites, *Int. J. Biol. Macromol.*, 2020, **163**, 970–976.

187 J. Burgess, B. De Castro, C. Oliveira, M. Rangel and W. Schlindweind, Synthesis and characterization of 3-hydroxy-4pyridinone-oxovanadium(IV) complexes, *Polyhedron*, 1997, **16**, 789–794.

188 M. Rangel, A. Leite, M. João Amorim, E. Garribba, G. Micera and E. Lodyga-Chruscinska, Spectroscopic and Potentiometric Characterization of Oxovanadium(IV) Complexes Formed by 3-Hydroxy-4-Pyridinones. Rationalization of the Influence of Basicity and Electronic Structure of the Ligand on the Properties of $V^{IV}O$ Species in Aqueous Solution, *Inorg. Chem.*, 2006, **45**, 8086–8097.

189 P. Buglyó, T. Kiss, E. Kiss, D. Sanna, E. Garribba and G. Micera, Interaction between the low molecular mass components of blood serum and the VO(IV)–DHP system (DHP = 1,2-dimethyl-3-hydroxy-4(1H)-pyridinone), *J. Chem. Soc. Dalton Trans.*, 2002, 2275–2282.

190 F. Avecilla, C. F. G. C. Geraldes and M. M. C. A. Castro, A New Trinuclear Oxovanadium(V) Complex with DMPP Ligands − Synthesis and Structural Characterization in the Solid State and in Aqueous Solution, *Eur. J. Inorg. Chem.*, 2001, **2001**, 3135–3142.

191 T. Jakusch, É. A. Enyedy, K. Kozma, Z. Paár, A. Bényei and T. Kiss, Vanadate complexes of 3-hydroxy-1,2-dimethyl-pyridinone: Speciation, structure and redox properties, *Inorganica Chim. Acta*, 2014, **420**, 92–102.

192 D. Sanna, P. Buglyó, G. Micera and E. Garribba, A quantitative study of the biotransformation of insulin-enhancing VO^{2+} compounds, *JBIC J. Biol. Inorg. Chem.*, 2010, **15**, 825–839.

193 G. Sciortino, D. Sanna, V. Ugone, J.-D. Maréchal, M. Alemany-Chavarria and E. Garribba, Effect of secondary interactions, steric hindrance and electric charge on the interaction of $V^{IV}O$ species with proteins, *New J. Chem.*, 2019, **43**, 17647–17660.

194 M. C. Vaney, S. Maignan, M. Riès-Kautt and A. Ducruix, High-Resolution Structure (1.33 Å) of a HEW Lysozyme Tetragonal Crystal Grown in the APCF Apparatus. Data and Structural Comparison with a Crystal Grown under Microgravity from SpaceHab-01 Mission, *Acta Crystallogr. D Biol. Crystallogr.*, 1996, **52**, 505–517.

195 D. Marasco, L. Messori, T. Marzo and A. Merlino, Oxaliplatin vs. cisplatin: competition experiments on their binding to lysozyme, *Dalton Trans.*, 2015, **44**, 10392–10398.

196 L. Messori, T. Marzo and A. Merlino, The X-ray structure of the complex formed in the reaction between oxaliplatin and lysozyme, *Chem. Commun.*, 2014, **50**, 8360.

197 C. R. Martinez and B. L. Iverson, Rethinking the term “pi-stacking”, *Chem. Sci.*, 2012, **3**, 2191.

198 L. F. Vilas Boas and J. Costa Pessoa, Pergamon Press, Oxford, G. Wilkinson, R. D. Gillard, J. A. McCleverty., 1987, vol. 3, pp. 453–583.

199 E. Garribba, G. Micera, D. Sanna and E. Lodyga-Chruscinska, Oxovanadium(IV) complexes of quinoline derivatives, *Inorganica Chim. Acta*, 2003, **348**, 97–106.

200 N. C. Giri, Role of Transferrin in Iron Metabolism, *Iron Metabolism - A Double-Edged Sword; IntechOpen*, DOI:10.5772/intechopen.100488.

201 J. Wang and K. Pantopoulos, Regulation of cellular iron metabolism, *Biochem. J.*, 2011, **434**, 365–381.

202 In *Current Topics in Membranes*, Elsevier, 2012, pp. 3–35.

203 N. C. Andrews and P. J. Schmidt, Iron Homeostasis, *Annu. Rev. Physiol.*, 2007, **69**, 69–85.

204 A. M. N. Silva, T. Moniz, B. De Castro and M. Rangel, Human transferrin: An inorganic biochemistry perspective, *Coord. Chem. Rev.*, 2021, **449**, 214186.

205 J. Williams and K. Moreton, The distribution of iron between the metal-binding sites of transferrin human serum, *Biochem. J.*, 1980, **185**, 483–488.

206 In *Structure and Bonding*, Springer Berlin Heidelberg, Berlin, Heidelberg, 1997, pp. 71–102.

207 D. R. Hall, J. M. Hadden, G. A. Leonard, S. Bailey, M. Neu, M. Winn and P. F. Lindley, The crystal and molecular structures of diferric porcine and rabbit serum transferrins at resolutions of 2.15 and 2.60 Å, respectively, *Acta Crystallogr. D Biol. Crystallogr.*, 2002, **58**, 70–80.

208 J. Wally, P. J. Halbrooks, C. Vonrhein, M. A. Rould, S. J. Everse, A. B. Mason and S. K. Buchanan, The Crystal Structure of Iron-free Human Serum Transferrin Provides Insight into Inter-lobe Communication and Receptor Binding, *J. Biol. Chem.*, 2006, **281**, 24934–24944.

209 W. Harris, Binding of Vanadate to Human Serum Transferrin, *J. Inorg. Biochem.*, 1984, **22**, 201–218.

210 A. Levina, C. Uslan, H. Murakami, D. C. Crans and P. A. Lay, Substitution Kinetics, Albumin and Transferrin Affinities, and Hypoxia All Affect the Biological Activities of Anticancer Vanadium(V) Complexes, *Inorg. Chem.*, 2023, **62**, 17804–17817.

211 G. C. Justino, E. Garribba and J. C. Pessoa, Binding of $V^{IV}O^{2+}$ to the Fe binding sites of human serum transferrin. A theoretical study, *JBIC J. Biol. Inorg. Chem.*, 2013, **18**, 803–813.

212 A.-K. Bordbar, A. L. Creagh, F. Mohammadi, C. A. Haynes and C. Orvig, Calorimetric studies of the interaction between the insulin-enhancing drug candidate bis(maltolato)oxovanadium(IV) (BMOV) and human serum apo-transferrin, *J. Inorg. Biochem.*, 2009, **103**, 643–647.

213 D. Sanna, E. Garribba and G. Micera, Interaction of VO^{2+} ion with human serum transferrin and albumin, *J. Inorg. Biochem.*, 2009, **103**, 648–655.

214 I. Correia, I. Chorna, I. Cavaco, S. Roy, M. L. Kuznetsov, N. Ribeiro, G. Justino, F. Marques, T. Santos-Silva, M. F. A. Santos, H. M. Santos, J. L. Capelo, J. Doutch and J. C. Pessoa, Interaction of $[V^{IV}O(acac)_2]$ with Human Serum Transferrin and Albumin, *Chem. – Asian J.*, 2017, **12**, 2062–2084.

215 J. Costa Pessoa, G. Gonçalves, S. Roy, I. Correia, S. Mehtab, M. F. A. Santos and T. Santos-Silva, New insights on vanadium binding to human serum transferrin, *Inorganica Chim. Acta*, 2014, **420**, 60–68.

216 D. Sanna, V. Ugone, M. Serra and E. Garribba, Speciation of potential anti-diabetic vanadium complexes in real serum samples, *J. Inorg. Biochem.*, 2017, **173**, 52–65.

217 T. Kiss, T. Jakusch, D. Hollender, Á. Dörnyei, É. A. Enyedy, J. C. Pessoa, H. Sakurai and A. Sanz-Medel, Biospeciation of antidiabetic VO(IV) complexes, *Coord. Chem. Rev.*, 2008, **252**, 1153–1162.

218 A. Levina and P. A. Lay, Vanadium(V/IV)–Transferrin Binding Disrupts the Transferrin Cycle and Reduces Vanadium Uptake and Antiproliferative Activity in Human Lung Cancer Cells, *Inorg. Chem.*, 2020, **59**, 16143–16153.

219 G. Ferraro, G. Tito, G. Sciortino, E. Garribba and A. Merlino, Stabilization and Binding of $[V_4O_{12}]^{4-}$ and Unprecedented $[V_{20}O_{54}(NO_3)]^{n-}$ to Lysozyme upon Loss of Ligands and Oxidation of the Potential Drug $V^{IV}O$(acetylacetonato)$_2$, *Angew. Chem.*, 2023, **135**, e202310655.

220 G. Tito, G. Ferraro, F. Pisanu, E. Garribba and A. Merlino, Non-Covalent and Covalent Binding of New Mixed-Valence Cage-like Polyoxidovanadate Clusters to Lysozyme, *Angew. Chem. Int. Ed.*, 2024, e202406669.

221 G. Tito, G. Ferraro, E. Garribba and A. Merlino, Formation of Mixed-Valence Cage-Like Polyoxidovanadates at 37°C Upon Reaction of $V^{IV}O$(acetylacetonato)$_2$ With Lysozyme, *Chem. – Eur. J.*, DOI:10.1002/chem.202500488.

222 R. Troisi, F. Galardo, G. Ferraro, F. Sica and A. Merlino, Cisplatin Binding to Human Serum Transferrin: A Crystallographic Study, *Inorg. Chem.*, 2023, **62**, 675–678.

223 H. Schmidt, I. Andersson, D. Rehder and L. Pettersson, A Potentiometric and ^{51}V NMR Study of the Aqueous $H^+/H_2VO_4^-/H_2O_2$/L-α-Alanyl-L-histidine System, *Chemistry*, 2001, **7**, 251–257.

224 J. Costa Pessoa, E. Garribba, M. F. A. Santos and T. Santos-Silva, Vanadium and proteins: Uptake, transport, structure, activity and function, *Coord. Chem. Rev.*, 2015, **301–302**, 49–86.

225 R. Troisi, F. Galardo, G. Ferraro, R. Lucignano, D. Picone, A. Marano, M. Trifuoggi, F. Sica and A. Merlino, Cisplatin/Apo-Transferrin Adduct: X-ray Structure and Binding to the Transferrin Receptor 1, *Inorg. Chem.*, 2025, **64**, 761–765.

226 M. F. A. Santos, I. Correia, A. R. Oliveira, E. Garribba, J. C. Pessoa and T. Santos-Silva, Vanadium Complexes as Prospective Therapeutics: Structural Characterization of a V^{IV} Lysozyme Adduct, *Eur. J. Inorg. Chem.*, 2014, **2014**, 3293–3297.

227 M. Paolillo, G. Ferraro, I. Cipollone, E. Garribba, M. Monti and A. Merlino, Unexpected *in crystallo* reactivity of the potential drug bis(maltolato)oxidovanadium(IV) with lysozyme, *Inorg. Chem. Front.*, 2024, **11**, 6307–6315.

228 R. Lucignano, G. Tito, G. Ferraro, D. Picone, F. Pisanu, E. Garribba and A. Merlino, Spherical mixed-valence pentadecavanadate binding to human H-chain ferritin, *Inorg. Chem. Front.*, 2025, 10.1039.D5QI01694K.

229 G. Ferraro, D. Loreto and A. Merlino, Interaction of Platinum-based Drugs with Proteins: An Overview of Representative Crystallographic Studies, *Curr. Top. Med. Chem.*, 2021, **21**, 6–27.

230 D. Loreto and A. Merlino, The interaction of rhodium compounds with proteins: A structural overview, *Coord. Chem. Rev.*, 2021, **442**, 213999.

231 A. Giorgio and A. Merlino, Gold metalation of proteins: Structural studies, *Coord. Chem. Rev.*, 2020, **407**, 213175.

232 C. Vonrhein, C. Flensburg, P. Keller, A. Sharff, O. Smart, W. Paciorek, T. Womack and G. Bricogne, Data processing and analysis with the *autoPROC* toolbox, *Acta Crystallogr. D Biol. Crystallogr.*, 2011, **67**, 293–302.

233 McCoy, A. J., Storoni, L. C., Bunkoczi, G., Oeffner, R. D., Read, R. J., Grosse-Kunstleve, R. W., ... & Winn, M. D., Phaser (CCP4: supported program) NAME phaser-2.5. 0-maximum likelihood analysis and phasing. SYNOPSIS phaser, *J. Appl. Cryst.*, 2007, **40**, 658–674.

234 G. N. Murshudov, A. A. Vagin and E. J. Dodson, Refinement of Macromolecular Structures by the Maximum-Likelihood Method, *Acta Crystallogr. D Biol. Crystallogr.*, 1997, **53**, 240–255.

235 P. Emsley and K. Cowtan, *Coot* : model-building tools for molecular graphics, *Acta Crystallogr. D Biol. Crystallogr.*, 2004, **60**, 2126–2132.

236 H. Berman, K. Henrick and H. Nakamura, Announcing the worldwide Protein Data Bank, *Nat. Struct. Mol. Biol.*, 2003, **10**, 980–980.

237 Bruker Analytische Messtechnik GmbH, 1996.

238 M. J. Frisch, G. W. Trucks, H. B. Schlegel, G. E. Scuseria, M. A. Robb, J. R. Cheeseman, G. Scalmani, V. Barone, B. Mennucci, G. A. Petersson, H. Nakatsuji, M. Caricato, X. Li, H. P. Hratchian, A. F. Izmaylov, J. Bloino, G. Zheng, J. L. Sonnenberg, M. Hada, M. Ehara, K. Toyota, R. Fukuda, J. Hasegawa, M. Ishida, T. Nakajima, Y. Honda, O. Kitao, H. Nakai, T. Vreven, A. J. Montgomery, Jr. Peralta J. E., F. Ogliaro, M. Bearpark, J. J. Heyd, E. Brothers, K. N. Kudin, V. N. Staroverov, T. Keith, R. Kobayashi, J. Normand, K. Raghavachari, A. Rendell, J. C. Burant, S. S. Iyengar, J. Tomasi, M. Cossi, N. Rega, J. M. Millam, M. Klene, J. E. Knox, J. B. Cross, V. Bakken, C. Adamo, J. Jaramillo, R. Gomperts, R. E. Stratmann, O. Yazyev, A. J. Austin, R. Cammi, C. Pomelli, J. W. Ochterski, R. L. Martin, K. Morokuma, V. G. Zakrzewski, G. A. Voth, P. Salvador, J. J. Dannenberg, S. Dapprich, A. D. Daniels, Ö. Farkas, J. B. Foresman, J. V. Ortiz, J. Cioslowski and D. J. Fox, 2010.

239 R. Diamond, Real-space refinement of the structure of hen egg-white lysozyme, *J. Mol. Biol.*, 1974, **82**, 371–391.

240 M. T. Marty, A. J. Baldwin, E. G. Marklund, G. K. A. Hochberg, J. L. P. Benesch and C. V. Robinson, Bayesian Deconvolution of Mass and Ion Mobility Spectra: From Binary Interactions to Polydisperse Ensembles, *Anal. Chem.*, 2015, **87**, 4370–4376.

241 A. D. Becke, Density-functional thermochemistry. III. The role of exact exchange, *J. Chem. Phys.*, 1993, **98**, 5648–5652.

242 S. Grimme, J. Antony, S. Ehrlich and H. Krieg, A consistent and accurate *ab initio* parametrization of density functional dispersion correction (DFT-D) for the 94 elements H-Pu, *J. Chem. Phys.*, 2010, **132**, 154104.

243 A. W. Ehlers, M. Böhme, S. Dapprich, A. Gobbi, A. Höllwarth, V. Jonas, K. F. Köhler, R. Stegmann, A. Veldkamp and G. Frenking, A set of f-polarization functions for pseudo-potential basis sets of the transition metals Sc□Cu, Y□Ag and La□Au, *Chem. Phys. Lett.*, 1993, **208**, 111–114.

244 A. V. Marenich, C. J. Cramer and D. G. Truhlar, Universal Solvation Model Based on Solute Electron Density and on a Continuum Model of the Solvent Defined by the Bulk Dielectric Constant and Atomic Surface Tensions, *J. Phys. Chem. B*, 2009, **113**, 6378–6396.

245 G. Jones, P. Willett, R. C. Glen, A. R. Leach and R. Taylor, Development and validation of a genetic algorithm for flexible docking 1 1Edited by F. E. Cohen, *J. Mol. Biol.*, 1997, **267**, 727–748.

246 G. Sciortino, D. Sanna, V. Ugone, A. Lledós, J.-D. Maréchal and E. Garribba, Decoding Surface Interaction of $V^{IV}O$ Metallodrug Candidates with Lysozyme, *Inorg. Chem.*, 2018, **57**, 4456–4469.

247 S. Al-Harthi, J. I. Lachowicz, M. E. Nowakowski, M. Jaremko and Ł. Jaremko, Towards the functional high-resolution coordination chemistry of blood plasma human serum albumin, *J. Inorg. Biochem.*, 2019, **198**, 110716.

248 G. Sciortino, D. Sanna, G. Lubinu, J. Maréchal and E. Garribba, Unveiling $V^{IV}O^{2+}$ Binding Modes to Human Serum Albumins by an Integrated Spectroscopic–Computational Approach, *Chem. – Eur. J.*, 2020, **26**, 11316–11326.

249 B. D. Liboiron, K. H. Thompson, G. R. Hanson, E. Lam, N. Aebischer and C. Orvig, New Insights into the Interactions of Serum Proteins with Bis(maltolato)oxovanadium(IV): Transport and Biotransformation of Insulin-Enhancing Vanadium Pharmaceuticals, *J. Am. Chem. Soc.*, 2005, **127**, 5104–5115.

250 D. Sanna, G. Micera and E. Garribba, New Developments in the Comprehension of the Biotransformation and Transport of Insulin-Enhancing Vanadium Compounds in the Blood Serum, *Inorg. Chem.*, 2010, **49**, 174–187.

251 D. Sanna, L. Bíró, P. Buglyó, G. Micera and E. Garribba, Biotransformation of BMOV in the presence of blood serum proteins, *Metallomics*, 2012, **4**, 33–36.

252 T. Moriuchi, M. Nishiyama, T. Beppu, T. Hirao and D. Rehder, Structural Characterization of a Dioxovanadium(V) Complex with 4,8-Dihydroxyquinoline-2-carboxylic Acid, *Bull. Chem. Soc. Jpn.*, 2007, **80**, 957–959.

253 S. Suku and R. Ravindran, Synthesis, characterization, biological and dielectric studies of a proton transfer compound of pyridine-2,6-dicarboxylic acid with 1H-benzimidazole-2-amine and its vanadium and iron complexes, *J. Mol. Struct.*, 2023, **1283**, 135217.

254 M. Tabatabaee, H. Mahmoodikhah, G. Ahadiat, M. Dušek and M. Pojarová, Synthesis, crystal structure, and spectroscopic characterization of two new binuclear complexes of manganese(II) and vanadium(V) with dipicolinate ligands containing 2-aminopyrimidinium as a counter cation, *Monatshefte Für Chem. - Chem. Mon.*, 2013, **144**, 621–626.

255 F. Ghasemi, A. R. Rezvani, K. Ghasemi and C. Graiff, Glycine and metformin as new counter ions for mono and dinuclear vanadium(V)-dipicolinic acid complexes based on the insulin-enhancing anions: Synthesis, spectroscopic characterization and crystal structure, *J. Mol. Struct.*, 2018, **1154**, 319–326.

256 A. C. Gonzalez-Baró, E. E. Castellano, O. E. Piro and B. S. Parajón-Costa, Synthesis, crystal structure and spectroscopic characterization of a novel bis (oxo-bridged) dinuclear vanadium(V)–dipicolinic acid complex, *Polyhedron*, 2005, **24**, 49–55.

257 M. Trivedi, R. Nagarajan, A. Kumar and N. P. Rath, A new single pot synthesis of μ-bis(oxido)bis{oxidovanadium(V)} dipicolinato complex with 2-aminopyridinium as counter cation: Spectroscopic, structural, catalytic and theoretical studies, *J. Organomet. Chem.*, 2010, **695**, 1722–1728.

258 R. J. Batrice, J. N. Wacker, E. N. Glass, S. Z. Jilani, Y. J. Tong, M. Nyman and K. E. Knope, Template-free cyclic hexavanadate: Synthesis, characterization, solid-state structure, and solution-state dynamics, *Polyhedron*, 2019, **169**, 266–277.

259 G. Ferraro, N. Demitri, L. Vitale, G. Sciortino, D. Sanna, V. Ugone, E. Garribba and A. Merlino, Spectroscopic/Computational Characterization and the X-ray Structure of the Adduct of the $V^{IV}O$–Picolinato Complex with RNase A, *Inorg. Chem.*, 2021, **60**, 19098–19109.

260 Vitagliano, L., Berisio, R., Mazzarella, L., & Zagari, A., *Biopolym. ISSN 0006-3525 0006-6352 0006-3525print*, 2001, 459–464.

261 E. Krissinel and K. Henrick, Secondary-structure matching (SSM), a new tool for fast protein structure alignment in three dimensions, *Acta Crystallogr. D Biol. Crystallogr.*, 2004, **60**, 2256–2268.

262 E. F. Pettersen, T. D. Goddard, C. C. Huang, E. C. Meng, G. S. Couch, T. I. Croll, J. H. Morris and T. E. Ferrin, UCSF CHIMERAX : Structure visualization for researchers, educators, and developers, *Protein Sci.*, 2021, **30**, 70–82.

263 M. M. Caldeira, M. L. Ramos, N. C. Oliveira and V. M. S. Gil, Complexes of vanadium(V) with α-hydroxycarboxylic acids studied by^{1} H,^{13} C, and^{51} V nuclear magnetic resonance spectroscopy, *Can. J. Chem.*, 1987, **65**, 2434–2440.

264 M.-H. Lee and I.-W. Kim, ^{13}C and ^{51}V Nuclear Magnetic Resonance Studies of Vanadium (V)-α-Hydroxycarboxylate Complexes, *Bull. Korean Chem. Soc.*, 1993, **14**, 557–561.

265 A. Gorzsás, K. Getty, I. Andersson and L. Pettersson, Speciation in the aqueous $H^{+}/H_2VO_4^{-}/H_2O_2$/citrate system of biomedical interest, *Dalton Trans.*, 2004, 2873.

266 B. Baruah, J. M. Roden, M. Sedgwick, N. M. Correa, D. C. Crans and N. E. Levinger, When Is Water Not Water? Exploring Water Confined in Large Reverse Micelles Using a Highly Charged Inorganic Molecular Probe, *J. Am. Chem. Soc.*, 2006, **128**, 12758–12765.

267 G. Ferraro, E. Garribba and A. Merlino, Exploring polyoxidovanadate–protein interaction, *Trends Chem.*

268 A. Tracey, Applications of ^{51}V NMR spectroscopy to studies of the complexation of vanadium(V) by α-hydroxycarboxylic acids, *Coord. Chem. Rev.*, 2003, **237**, 113–121.

269 C. Slebodnick and V. L. Pecoraro, Solvent effects on ^{51}V NMR chemical shifts: characterization of vanadate and peroxovanadate complexes in mixed water/acetonitrile solvent, *Inorganica Chim. Acta*, 1998, **283**, 37–43.

270 H. T. Evans Jr., The Molecular Structure of theIsopoly Complex Ion, Decavanadate ($V_{10}O_{28}^{6-}$), *Inorg. Chem.*, 1966, **5(6)**, 967–977.

271 M. P. M. Marques, D. Gianolio, S. Ramos, L. A. E. Batista De Carvalho and M. Aureliano, An EXAFS Approach to the Study of Polyoxometalate–Protein Interactions: The Case of Decavanadate–Actin, *Inorg. Chem.*, 2017, **56**, 10893–10903.

272 F. Sun, Y.-T. Li, Z.-Y. Wu, D.-Q. Wang and J.-M. Dou, Tetrapiperidinium di-μ-methoxy-di-μ_5 -oxo-tetra-μ_3 -oxo-dodeca-μ_2 -oxo-octaoxodecavanadate, *Acta Crystallogr. C*, 2006, **62**, m60–m62.

273 Y. Li, F. Sun, Z. Wu and Z. Zhang, Synthesis, Crystal Structure and Properties of Tetra(piperidinium)bis(ethanolate) Decavanadate, *Pol. J. Chem.*, 2007, **81(8)**, 1379–1386.

274 T. Kiss, I. Sóvágó, R. B. Martin and J. Pursiainen, Ternary complex formation between Al(III)-adenosine-5′-phosphates and carboxylic acid derivatives, *J. Inorg. Biochem.*, 1994, **55**, 53–65.

275 T. Kiss, P. Buglyó, D. Sanna, G. Micera, P. Decock and D. Dewaele, Oxovanadium(IV) complexes of citric and tartaric acids in aqueous solution, *Inorganica Chim. Acta*, 1995, **239**, 145–153.

276 S. Ramos, M. Manuel, T. Tiago, R. Duarte, J. Martins, C. Gutiérrez-Merino, J. J. G. Moura and M. Aureliano, Decavanadate interactions with actin: Inhibition of G-actin polymerization and stabilization of decameric vanadate, *J. Inorg. Biochem.*, 2006, **100**, 1734–1743.

277 W. J. Ray, D. C. Crans, J. Zheng, J. W. Burgner, H. Deng and M. Mahroof-Tahir, Structure of the Dimeric Ethylene Glycol-Vanadate Complex and Other 1,2-Diol-Vanadate Complexes in Aqueous Solution: Vanadate-Derived Transition-State Analog Complexes of Phosphotransferases, *J. Am. Chem. Soc.*, 1995, **117**, 6015–6026.

278 D. Rehder, The (biological) speciation of vanadate(V) as revealed by ^{51}V NMR: A tribute on Lage Pettersson and his work, *J. Inorg. Biochem.*, 2015, **147**, 25–31.

279 L. Pettersson, B. Hedman, A.-M. Nenner, I. Andersson and E. Hoyer, Multicomponent Polyanions. Hydrolysis and Redox Equilibria of the H(+)--HVO4(2-) System in 0.6 M Na(Cl). A Complementary Potentiometric and 51V NMR Study at Low Vanadium Concentrations in Acid Solution., *Acta Chem. Scand.*, 1985, **39a**, 499–506.

280 G. Ferraro, M. Paolillo, G. Sciortino, F. Pisanu, E. Garribba and A. Merlino, Implications of Protein Interaction in the Speciation of Potential $V^{IV}O$–Pyridinone Drugs, *Inorg. Chem.*, 2023, **62**, 8407–8417.

281 M. Paolillo, G. Ferraro, F. Pisanu, J. Maréchal, G. Sciortino, E. Garribba and A. Merlino, Protein-Protein Stabilization in $V^{IV}O$/8-Hydroxyquinoline–Lysozyme Adducts, *Chem. – Eur. J.*, 2024, e202401712.

282 M. Paolillo, G. Ferraro, G. Sahu, P. D. Pattanayak, E. Garribba, S. Halder, R. Ghosh, B. Mondal, P. B. Chatterjee, R. Dinda and A. Merlino, Interaction of $V^{V}O_2$−hydrazonates with lysozyme, *J. Inorg. Biochem.*, 2025, **264**, 112787.

283 M. Paolillo, G. Ferraro, N. I. Gumerova, F. Pisanu, E. Garribba, A. Rompel and A. Merlino, Speciation and structural transformation of a V^{V}–malate complex in the absence and in the presence of a protein: from a dinuclear species to decavanadate, *Inorg. Chem. Front.*, 2025, **12**, 6503–6518.